Open Access Dissertations

Theses and Dissertations

12-2016

Gravity-assist trajectories to Venus, Mars, and the ice giants: Mission design with human and robotic applications

Kyle M. Hughes
Purdue University

Follow this and additional works at: https://docs.lib.purdue.edu/open_access_dissertations

Part of the Aerospace Engineering Commons, and the Physics Commons

GRAVITY-ASSIST TRAJECTORIES TO VENUS, MARS, AND THE ICE

GIANTS: MISSION DESIGN WITH HUMAN AND ROBOTIC APPLICATIONS

A Dissertation

Submitted to the Faculty

of

Purdue University

by

Kyle M. Hughes

In Partial Fulfillment of the

Requirements for the Degree

of

Doctor of Philosophy

December 2016

Purdue University

West Lafayette, Indiana

PURDUE UNIVERSITY
GRADUATE SCHOOL
Thesis/Dissertation Acceptance

This is to certify that the thesis/dissertation prepared

By Kyle M. Hughes

Entitled
Gravity-Assist Trajectories to Venus, Mars, and the Ice Giants: Mission Design with Human and Robotic Applications

For the degree of Doctor of Philosophy

Is approved by the final examining committee:

James M. Longuski
Chair

Kathleen C. Howell

Martin J. Corless

William A. Crossley

To the best of my knowledge and as understood by the student in the Thesis/Dissertation Agreement, Publication Delay, and Certification Disclaimer (Graduate School Form 32), this thesis/dissertation adheres to the provisions of Purdue University's "Policy of Integrity in Research" and the use of copyright material.

Approved by Major Professor(s): James M. Longuski

Approved by: Weinong Wayne Chen   12/7/2016

Head of the Departmental Graduate Program   Date

ACKNOWLEDGMENTS

I would like to thank my advisor Jim Longuski for his invaluable insight through-
out this entire work, and more generally, for teaching me how to be a researcher and
astrodynamicist. Working in his research group has been an invaluable experience
and a great positive influence my life and future career. I am, to say the least, grateful
for having the opportunity to work with Professor Longuski, and I will aim to follow
his example throughout my career. I would also like to thank my committee members
Professors William Crossley, Martin Corless, and Kathleen Howell for their support
and feedback. Professor Howell's very memorable course on advanced orbital dynam-
ics was the most fascinating and fun experience I've had in a classroom. I would also
like to thank my colleagues Sarag Saikia, Jim Moore, Blake Rogers, and Alec Mudek
for all of their help and insight, often through long discussions at Armstrong Hall and
on the phone, which significantly improved in many ways the quality of this thesis.

I would like to thank my collaborators Parul Agrawal, Gary Allen, Helen Hwang,
and Raj Venkatapathy at Ames Research Center for pushing my research into the
atmospheres of the Gas and Ice Giants; Mike Loucks, John Carrico, and Dennis Tito
for their support and interest in my contribution to Inspiration Mars; and Buzz Aldrin
for sharing so many hours of his time with me and our research group, and allowing
me to contribute to his vision for putting a permanent human presence on Mars. I
would also like to thank Alinda Mashiku, Trevor Williams, and Jacob Englander at
Goddard Space Flight Center for letting me pester them with endless questions, and
helping me to find the next step in my career path.

I would like to thank my mom and dad, Paulette and Mike, who many times
helped me financially during this work, and have always given their support and en-
couragement, without which this work may never have taken place. I would especially
like to acknowledge my mom, who we lost in 2013. Her sense of humor, delightful

cynicism, and unfailing ability to help me put things in perspective, helped keep me sane through most of my life and especially during graduate school. I continually work to follow her example in all aspects of my life, and be mindful of the advice I may only speculate she would give. I would also like to thank my sister Laura for our long phone conversations that helped me get through difficult times of loss and stress.

Most importantly, I would like to thank my wife Mariah for her support, encouragement, and infinite patience with me, which I depend on daily. I will be forever grateful to her for her sacrifice in leaving her home and effectively postponing her career so that I may pursue this degree.

TABLE OF CONTENTS

LIST OF TABLES

LIST OF FIGURES

ABSTRACT

Hughes, Kyle M. PhD, Purdue University, December 2016. Gravity-Assist Trajectories to Venus, Mars, and the Ice Giants: Mission Design with Human and Robotic Applications. Major Professor: James Longuski.

Gravity-assist trajectories to Uranus and Neptune are found (with the allowance of impulsive maneuvers using chemical propulsion) for launch dates ranging from 2024 to 2038 for Uranus and 2020 to 2070 for Neptune. Solutions are found using a patched conic model with analytical ephemeris via the Satellite Tour Design Program (STOUR), originally developed at the Jet Propulsion Laboratory (JPL). Delivered payload mass is computed for all solutions for select launch vehicles, and attractive solutions are identified as those that deliver a specified amount of payload mass into orbit at the target body in minimum time. The best cases for each launch year are cataloged for orbiter missions to Uranus and Neptune. Solutions with sufficient delivered payload for a multi-planet mission (e.g. sending a probe to Saturn on the way to delivering an orbiter at Uranus) become available when the Space Launch System (SLS) launch vehicle is employed. A set of possible approach trajectories are modeled at the target planet to assess what (if any) adjustments are needed for ring avoidance, and to determine the probe entry conditions.

Mars free-return trajectories are found with an emphasis on short flight times for application to near-term human flyby missions (similar to that of Inspiration Mars). Venus free-returns are also investigated and proposed as an alternative to a human Mars flyby mission. Attractive Earth-Mars free-return opportunities are identified that use an intermediate Venus flyby. One such opportunity, in 2021, has been adopted by the Inspiration Mars Foundation as a backup to the currently considered 2018 Mars free-return opportunity.

Methods to establish spacecraft into Earth-Mars cycler trajectories are also investigated to reduce the propellant cost required to inject a 95-metric ton spacecraft into a cycler orbit. The establishment trajectories considered use either a V-infinity leveraging maneuver or low thrust. The V-infinity leveraging establishment trajectories are validated using patched conics via the STOUR program. Establishment trajectories that use low-thrust were investigated with particular focus on validating the patched-conic based solutions at instances where Earth encounter times are not negligible.

1. THE PATCHED-CONIC METHOD OF COMPUTING GRAVITY-ASSIST TRAJECTORIES

For heliocentric trajectories, the spacecraft will be primarily under the influence of the Sun's gravity for the vast majority of time spent on the trajectory. Compared to the overall time spent on such trajectory, any time taken for the spacecraft to fly by a celestial body in the Solar System (which in practice may take several hours) is often approximated as happening instantaneously. This in principle is the patched-conic approximation (as applied to heliocentric trajectories), and is often used for early phase mission design to estimate ΔV and propellant mass required for a mission.

For most heliocentric, interplanetary, gravity-assist trajectories, the only other gravitational bodies that need to be considered are those of the encounter bodies used for gravity-assist. The patched-conic model assumes that only the gravity of Sun influences the spacecraft throughout its trajectory, except during a flyby of a gravity-assist body. During the gravity assist, only the gravity of that body is assumed to have influence on the spacecraft, and the amount of bending on the spacecraft's velocity vector do to the hyperbolic flyby can be computed for a given closest approach distance. With this approximation, the 2-body gravity model can be used for the heliocentric trajectory, as well as for the gravity-assist encounters, whereby the trajectories between gravity-assists are "patched" together to create an approximation to a complete (n-body) heliocentric, gravity-assist trajectory.

In this work, the patched-conic approximation is used for purposes of identifying the existence of a heliocentric, gravity-assist trajectory, and to determine the feasibility of the trajectory for use in a mission, by estimating key values such as: $DeltaV$, delivered mass, flight times, planet-relative velocities, and encounter geometries. Of course the specific values of interest vary depending on the mission requirements, but

the values considered in this work are among a typical set of important values in determining mission feasibility. Since these results are based on the patched-conic approximation, any continued work on such trajectories will eventually need to be computed in a high-fidelity force model, such as from the General Mission Analysis Tool (GMAT) or the Systems Tool Kit (STK). For the heliocentric trajectories presented in this work, it is assumed that the patched-conic solutions are of medium-fidelity, which we describe as being sufficiently close to the high-fidelity solution that they may be used as an initial guess for the high-fidelity tool to converge on a trajectory with similar characteristics.

Finding a patched-conic solution typically begins with finding a desired heliocentric trajectory between two Planets (or other celestial bodies), or between a sequence of Planets for gravity-assist trajectories. If an impulsive maneuver is planned, a heliocentric arc may go from a Planet to a point in space where the maneuver is to be implemented. For the case of gravity-assist trajectories, if the flyby is to be ballistic (without assistance by a maneuver) the V_∞ at the arrival body on the incoming heliocentric arc, must match (in magnitude) the departure V_∞ of the outgoing heliocentric arc. Additionally, the amount the $\mathbf{V}_\infty$ vector rotates between the incoming and outgoing heliocentric arcs, must have a feasible closest approach to the gravity-assist body—that is, without colliding with the Planet, and in most cases, without significantly interacting with a Planet's atmosphere or rings.

In trajectory design, the challenge is to find a desirable heliocentric solution, that: encounters the desired targets at the correct times (according to an ephemeris model), is feasible for a spacecraft to fly given technology limitations (for example due to available launch vehicles and thrusters), and meets mission requirements (such as specified launch date spans, maximum flight times, encounter conditions for a probe or orbiter, etc.). One such approach to finding these solutions, is to compute the heliocentric arcs in the ephemeris model by solving Lambert's problem.

1.1 Lambert's Problem

In orbital mechanics, the problem of computing a trajectory that connects two position vectors (i.e. at departure and arrival) in a specified amount of time, is often referred to as Lambert's problem (and sometimes as the Gauss problem). Solving Lambert's problem is fundamental to the computation of interplanetary trajectories (using the patched-conic model), especially when multiple gravity-assist trajectories are desired.

For example, take two celestial bodies orbiting the Sun. If we know the date we wish to depart the first celestial body, and the date we wish to arrive at the second celestial body, then an ephemeris model of each body's motion would reveal their positions on those dates, and the difference in time would reveal a specific time of flight to travel between the bodies. With such information, we could compute one or more trajectories between the two bodies by solving Lambert's problem. Additionally, if we wanted to then depart the second body and go to a third body, we could compute a trajectory that would take the spacecraft there by choosing a date of arrival at (or time of flight to) the third body, and solving Lambert's problem again for the subsequent heliocentric arc. Further analysis is required to determine if such trajectories are feasible (or desirable) to fly using available technology; however, regardless of these additional computations, Lambert's problem is at the heart of nearly all of the interplanetary trajectories presented in this thesis.

There are several methods for solving Lambert's problem in literature; however, for this work, the patched-conic solutions are computed using the Satellite TOUR design program (STOUR), which solves Lambert's problem using the Lancaster-Blanchard method [1]. The ephemeris model used by STOUR to solve Lambert's problem and the patched-conic solutions is an analytical model presented by Sturms [2].

Another factor that must be considered in using Lambert's problem to solve for heliocentric arcs (or Lambert arcs) between bodies, is matching the incoming and outgoing V_∞ magnitude at a gravity assist. For a ballistic flyby (i.e. where no

maneuver is applied during the encounter), the incoming V_∞ must equal the outgoing V_∞. The direction of the $\mathbf{V}_\infty$ vector will change (which is what causes the energy change for the heliocentric trajectory), but the magnitude remains the same. In STOUR, this constraint is considered by computing hundreds of outgoing Lambert arcs (given a fixed incoming Lambert arc) at an encounter, whereby a root solving method is used to find the all outgoing trajectories that have an outgoing V_∞ that equals the incoming V_∞ within a specified tolerance. A complete description of this C_3-matching technique (as implemented in STOUR) is given by Williams in Ref. [3].

1.2 The Tisserand Graph

The Tisserand graph is implemented in this work as a plot of orbital specific energy versus radius of periapsis, and provides a graphical means of identifying potential gravity-assist combinations (or "paths"). A detailed description of the theory behind this graphical method, and how it is developed using Tisserand's criterion, is provided by Strange and Longuski [4] and Labunsky et al. [5]. The Tisserand graph has since been adapted by Johnson and Longuski in 2002 for aerogravity-assist trajectories [6], by Chen et al. in 2008 for low-thrust gravity-assist trajectories [7], and more recently by Campagnola and Russell in 2010 for gravity-assist trajectories that implement V_∞-leveraging maneuvers [8], as well as for application to the circular-restricted three-body problem [9].

In simple terms, the Tisserand graph can be described as follows: The lines on the Tisserand graph represent the locus of orbits with the same energy relative to a given planet. The intersection of lines of one planet with those of another indicates that there exist orbits about each planet with the same heliocentric energy. Thus, a transfer from one planet to another is possible from an energy standpoint (though the planet may not be in the correct location at the time the spacecraft crosses the planet's orbit). Knowledge of the planetary ephemerides and the solution of

Lambert's problem are then required for pathsolving, in order to find out when in time the transfer orbit occurs.

In this work, the Tisserand graph is used to primarily to identify candidate trajectory paths to the Ice Giants, Uranus and Neptune (discussed in chapters 3 and 4). The Tisserand graph is also useful for screening out flyby combinations that are not feasible within the desired launch V_∞ bounds, and thus avoid the computational effort that would otherwise be required to consider such a path.

In this work, the problem of identifying candidate gravity-assist paths based on orbital energy (i.e. using the Tisserand graph), will be referred to as "pathfinding." Whereas, the problem of identifying real trajectories on those paths in the ephemeris model will be referred to as "pathsolving."

1.2.1 Selecting Candidate Paths: Pathfinding

To illustrate the use of the Tisserand graph, an example case is shown in Figure 1.1 for the path Venus-Earth-Earth-Jupiter-Neptune (VEEJN). The specific energy of the orbit is shown on the vertical axis and the radius of periapsis is shown on a logarithmic scale on the horizontal axis. In this example, lines are shown for Venus, Earth, Jupiter, and Neptune. The rightmost line for each planet represents a V_∞ of 1 km/s. V_∞ increases by 2 km/s with each line to the left (i.e. moving from right to left, the lines represent V_∞s of 1 km/s, 3 km/s, 5 km/s, etc.). The dots (or small circles if obstructed by a line in bold) along the V_∞ lines provide reference points for the amount of energy change that can be accomplished with a single flyby of the planet, with a closest approach of 200 km altitude. This energy change is based on the maximum possible amount that the planet can rotate (or bend) the V_∞ vector.

A potential VEEJN path is highlighted by the bold lines in Figure 1.1. The path begins at Earth with 3 km/s as the chosen V_∞ of launch. By traversing this line down and to the left, an intersection with Venus is found at the line representing a V_∞ of 5 km/s. Following this line upward, several other V_∞ lines for Earth are encountered.
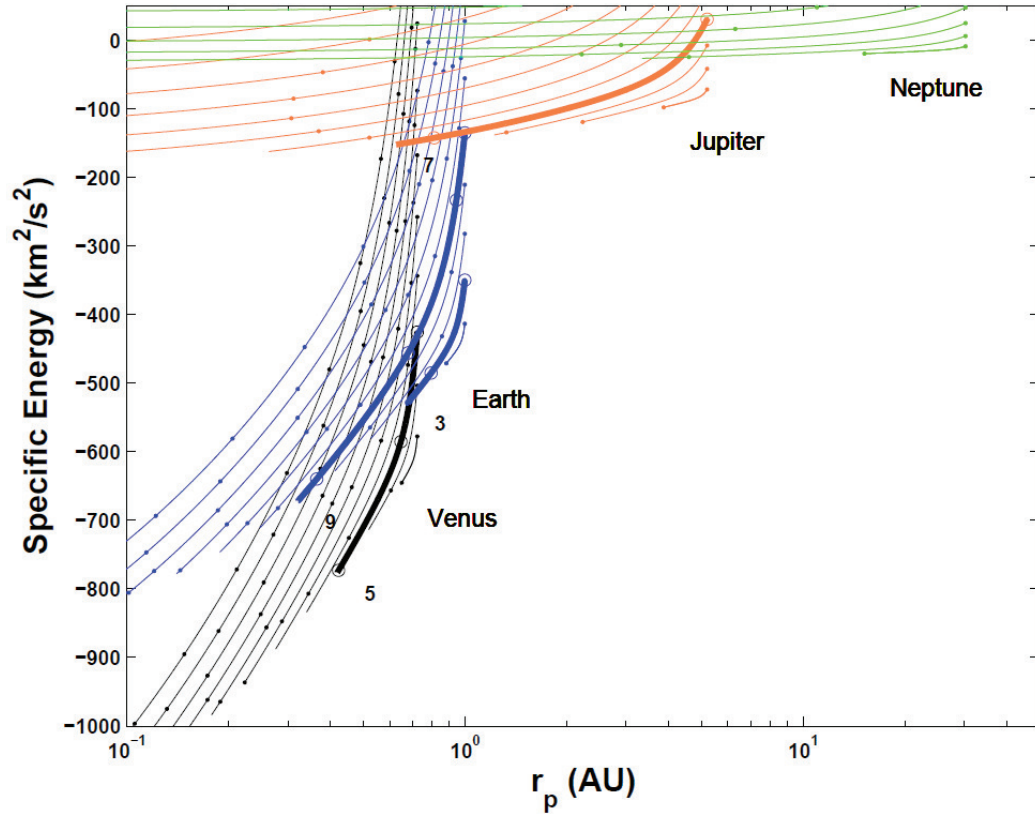
Figure 1.1.: Tisserand graph with the example path Venus-Earth-Earth-Jupiter-Neptune (VEEJN) indicated by the lines in bold.

The 9 km/s V_∞ line for Earth is of particular interest because it also intersects a Jupiter V_∞ line. The Earth V_∞ line for 9 km/s is then followed up and to the right (past the small circle), and on to an intersection with the Jupiter V_∞ line for 7 km/s. Surpassing the full distance between the two small circles on the Earth V_∞ line (while on route to the Jupiter line at 7 km/s), indicates that the amount of energy required is more than what can be achieved in a single Earth flyby. Therefore, two Earth flybys are required to get from Venus to Jupiter on this path. Finally, the Jupiter V_∞ line for 7 km/s is followed up and to the right until it intersects the Neptune V_∞ line at 3 km/s. The overall implication of this result is that a spacecraft with launch V_∞ of 3 km/s is capable of reaching Neptune by means of the flyby sequence Venus-Earth-Earth-Jupiter, and then arriving at Neptune with a V_∞ of 3 km/s.

In this work, powered flybys are also considered, but only at one of the flyby bodies (to reduce computational time). We assume the maneuver is performed 3 days after the point of closest approach so that navigators have time to determine the location of the spacecraft before implementing the powered flyby maneuver. As a result of this delay, we conservatively assume that the burn occurs along the departure asymptote—taking no advantage of the additional energy boost gained by implementing the maneuver within the planets gravity well.

Identifying which flyby body will be most beneficial for a powered flyby is done by inspection of the Tisserand graph. Since the giant planets provide a substantial energy boost without a maneuver, powered flybys are only considered at the inner planets. To approximate the energy boost provided by such a maneuver, we shift vertically upwards on the Tisserand graph just after a flyby. The amount of the shift is determined by the maximum allowed maneuver ΔV. For this work, we assume a maximum ΔV of 3 km/s, which (if applied along the departure asymptote) provides a +3 km/s V_∞ boost to the flyby. This 3-km/s V_∞ increase equates to a vertical shift on the Tisserand graph by 1.5 V_∞ curves. For each gravity assist path, the flyby chosen to implement the powered flyby, is the one that provides the largest heliocentric orbital energy boost. It was found that this often occurs when the powered flyby is implemented at the last inner planet flyby.

2. INTERPLANETARY HYPERBOLIC ENCOUNTERS: APPROACH AND DEPARTURE TRAJECTORIES NEAR A TARGET BODY

2.1 Planetocentric Equatorial Frames

To model trajectories near a target body, it is useful to us a coordinate frame centered at the target body, with the xy-plane of that frame chosen to be the body's equatorial plane. In this analysis, two frames are used.

The "body-inertial" frame is defined as follows:

- The frame is centered at the body's center of mass.
- The x-axis is along the line formed by the intersection of the body's equator and the equator of the International Celestial Reference Frame (ICRF) defined by the International Astronomical Union (IAU) [10].
- The z-axis is along the body's spin axis.
- The y-axis completes the triad (using the "right hand rule").

The ICRF is a precisely defined inertial frame centered at the barycenter of the Solar System. To help visualize the ICRF, its axes are oriented nearly identically to those in the Earth J2000 equatorial frame, with ICRF equator and z-axis, approximately equal to Earth's equatorial plane and spin axis, respectively. The ICRF x-axis is directed towards the Vernal Equinox. The spin axis orientation for a target planet is defined relative to the ICRF by right ascension angle, α_0, and declination angle, δ_0, as defined by the IAU in Ref. [10]. The body-inertial frame is visually depicted in Fig. 2.1, which has been adapted from a figure in Ref. [10].
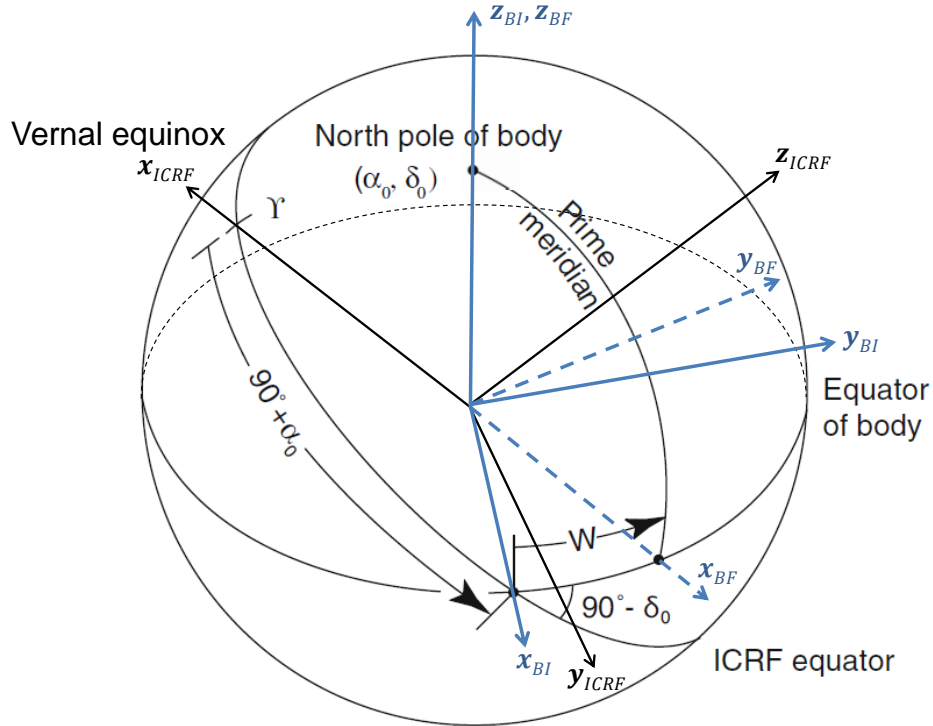
Figure 2.1.: Body-inertial and body-fixed equatorial frames centered at the target body. Both body frames are shown relative to the ICRF, by the angles $90° + \alpha_0$, $90° - \delta_0$, and for the body-fixed frame, the additional angle W. This figure was adapted from a figure in Ref. [10], which also provides the values of α_0, δ_0, and W for each planet.

To compute the coordinates of a vector in the body-inertial frame, given a vector in the ICRF, the following rotation matrices are first defined. The direction cosine matrix for a rotation about the x-axis by angle θ is given by

$$R_1(\theta) = \begin{bmatrix} 1 & 0 & 0 \\ 0 & \cos\theta & \sin\theta \\ 0 & -\sin\theta & \cos\theta \end{bmatrix} \tag{2.1}$$

Similarly, for a rotation about the z-axis by angle θ, the direction cosine matrix is

$$R_3(\theta) = \begin{bmatrix} \cos\theta & \sin\theta & 0 \\ -\sin\theta & \cos\theta & 0 \\ 0 & 0 & 1 \end{bmatrix} \tag{2.2}$$

Given a vector in the ICRF, two rotations are required to compute such a vector's equivalent in the body-inertial frame. First, a rotation about the z-axis by angle $90° + \alpha_0$ is required, and second, a rotation about the x-axis by angle $90° - \delta_0$ is required. The calculation is given by

$$\mathbf{r}_{BI} = R_1(90° - \delta_0)R_3(90° + \alpha_0)\mathbf{r}_{ICRF} \tag{2.3}$$

where $\mathbf{r}_{BI}$ is a column vector in the body-inertial frame, and $\mathbf{r}_{ICRF}$ is the equivalent column vector expressed in the ICRF.

The "body-fixed" frame, rotates with the target body about its spin axis, and is defined as follows:

- The frame is centered at the body's center of mass.
- The x-axis is within the body's equatorial plane, in the direction of the body's prime meridian (which lies in the x-z plane).
- The z-axis is along the body's spin axis.
- The y-axis completes the triad (using the "right hand rule").

Given a vector in the body-inertial frame, that vector's equivalent in the body-fixed frame is found via a rotation about the z-axis by angle W. The computation is

$$\mathbf{r}_{BF} = R_3(W)\mathbf{r}_{BI} \tag{2.4}$$

where $\mathbf{r}_{BF}$ is a column vector in the body-fixed frame. Depending on how the north pole is defined, a planet may spin prograde about it's north pole (i.e. appear to spin counterclockwise to an observer looking down onto the north pole), or retrograde

(i.e. appear to spin clockwise to an observer looking down onto the north pole). In the body-fixed and body-inertial frames defined above, the positive z-axis is directed along the spin axis towards the north pole. For the parameters α_0, δ_0, and W used in this study to define a body's orientation (as defined by [10]), the rotation is prograde if W increases with time, and retrograde if W decreases with time. Of the eight planets, only Venus and Uranus spin retrograde according to this definition.

Given a vector in ICRF coordinates, the calculation to body-fixed coordinates is found by substituting Eq. 2.3 into Eq. 2.4, giving

$$\mathbf{r}_{BF} = R_3(W)R_1(90° - \delta_0)R_3(90° + \alpha_0)\mathbf{r}_{ICRF} \qquad (2.5)$$

For some software tools such as STOUR and MALTO, it is more convenient to compute vectors in the J2000 ecliptic frame. To compute such a vector's equivalent in either the body-inertial frame, or the body-fixed frame, one must first express that vector in the ICRF. Since, in this work, this calculation is only used for V_∞ vectors found from the low- to mid-fidelity STOUR or MALTO solutions, it is assumed that the ICRF and the J2000 equatorial frame are equal. With this assumption, the rotation from the J2000 ecliptic frame, to the ICRF, is simply a rotation about their mutually shares x-axis by Earth's axial tilt of 23.44°, giving

$$\mathbf{r}_{ICRF} = R_1(23.44°)\mathbf{r}_{J2K,Ec} \qquad (2.6)$$

where $\mathbf{r}_{J2K,Ec}$ is a column vector in the J2000 ecliptic frame.

2.2 Hyperbolic Approach Trajectories

When identifying an interplanetary trajectory, the characteristics of the approach trajectory to a target body can play a key role in assessing whether or not that trajectory is feasible. Visualizing the approach can also be insightful for identifying trajectories that pass through a planet's rings, identifying whether or not line-of-sight

is maintained between the spacecraft (or probe) and the Earth or Sun, or simply communicating the available approach options to the scientific community. The significance of the approach trajectory parameters depend on the mission application, but the consequences of the approach trajectory (which are dependent on the corresponding interplanetary trajectory) can be just as important to the mission's feasibility as the interplanetary trajectory characteristics themselves (e.g. flight time, delivered payload mass, and arrival V_∞).

For example, consider a mission to Uranus, where we are assessing the possible approach trajectories for an atmospheric probe. Since Uranus has rings and a large axial tilt (of about 98°to its own orbit), factors such as a high declination angle, or ring avoidance, may result in approach trajectories with high atmospheric entry speeds. Depending on the available thermal protection systems for the probe, the approach trajectories may turn out to be infeasible, and therefore, the corresponding interplanetary trajectory would not be suitable for such a mission.

2.2.1 Locus of Possible Solutions

Given a $\mathbf{V}_\infty$ vector in body-inertial coordinates (as defined in Sec. 2.1), the "locus" of possible hyperbolic approach trajectories can be derived. An example of the possible approach trajectories for a particular $\mathbf{V}_\infty$ vector at Saturn is visualized in Fig. 2.2. The approach trajectories are all constrained by the interplanetary arrival $\mathbf{V}_\infty$ vector, and the span of possible approach trajectories is computed by selecting a range of hyperbolic periapsis radii magnitudes, and a step size for the span of angles about the ring created by the locus of periapses (shown in green in Fig. 2.2). The angular position, ψ, on the ring of periapsis radii is defined in Fig. 2.3. With the $\mathbf{V}_\infty$ vector already given, a chosen periapsis magnitude and value of ψ defines a particular approach trajectory, which can therefore be calculated from these values.

The equation to express a column vector, $\mathbf{r}_{xyz}$ (in xyz-frame coordinates), as an equivalent vector, $\mathbf{r}_{x'y'z'}$ (in $x'y'z'$-frame coordinates) is
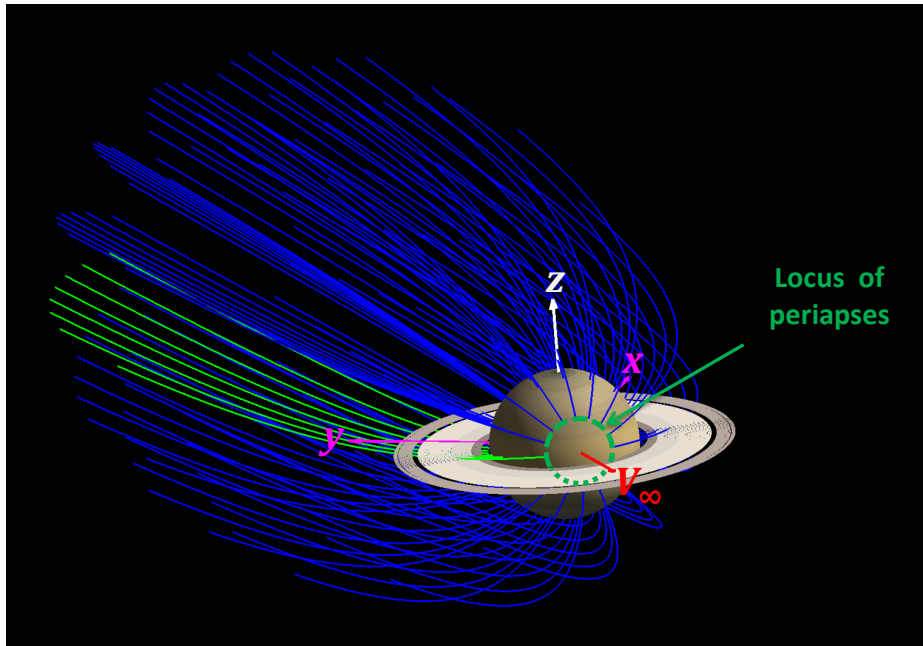
Figure 2.2.: Locus of approach trajectories at Saturn for a particular $\mathbf{V}_\infty$ vector. The approach trajectories shown span all available inclinations with a range of periapsis radii. The trajectories shown in light green have the minimum possible inclination for a ballistic approach (given this particular $\mathbf{V}_\infty$ vector).

$$\mathbf{r}_{x'y'z'} = R_3(\phi_1)\mathbf{r}_{xyz} \qquad (2.7)$$

Similarly, to compute a column vector, $\mathbf{r}_{x''y''z''}$ in $x''y''z''$-frame coordinates, from an equivalent vector $\mathbf{r}_{x'y'z'}$, the equation is

$$\mathbf{r}_{x''y''z''} = R_2(\phi_2)\mathbf{r}_{x'y'z'} \qquad (2.8)$$

where

$$R_2(\theta) = \begin{bmatrix} \cos\theta & 0 & -\sin\theta \\ 0 & 1 & 0 \\ \sin\theta & 0 & \cos\theta \end{bmatrix} \qquad (2.9)$$

and by plugging Eq. 2.7 into Eq. 2.8 gives
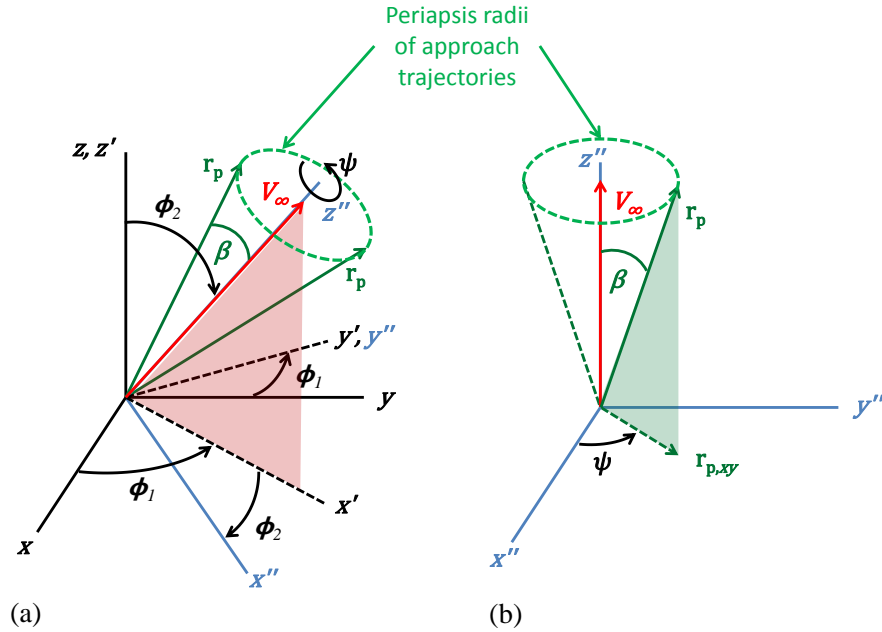
Figure 2.3.: (a) Coordinate frame rotations from body-inertial equatorial frame and a frame with z'' axis aligned with the incoming $\mathbf{V}_\infty$ vector. (b) Inertial frame used to identify a particular hyperbolic approach trajectory, given values for the $\mathbf{V}_\infty$ vector, r_p (magnitude), and ψ.

$$\mathbf{r}_{x''y''z''} = R_2(\phi_2)R_3(\phi_1)\mathbf{r}_{xyz} \tag{2.10}$$

For probe entry, it is often the goal pick the approach trajectory with the minimum possible inclination (i.e. the approach trajectory with minimum inclination relative to the equatorial plane of the encounter body). The minimum inclination trajectory is desired to take the most advantage of the rotation of the planet's atmosphere, to reduce the entry "air" speed of the probe, and therefore, the entry heating. By observation of Fig. 2.3a, it can be found that the minimum inclination approach trajectories correspond to a value of $\psi = 3\pi/2$. This is illustrated more clearly in Fig. 2.4, which shows a plane containing the approach $\mathbf{V}_\infty$ vector, the y'' axis, and the approach trajectory corresponding to the minimum inclination solution. The solution opposite the minimum inclination solution (and in the same plane) at $\psi = \pi/2$,

is the maximum inclination solution, and represents a retrograde solution closest to the equatorial plane, which minimizes the entry "air" speed for planets such as Venus and Uranus which spin retrograde about their north pole (as defined by [10]). Alternatively, a ψ values of $\pi/2$ maximizes the air speed for entry at all other planets (which spin prograde with respect to their north pole). Quantitatively, the minimum inclination angle is equal to the absolute value of the declination angle, δ (where $-\pi/2 \leq \delta \leq \pi/2$), which is the angle between the $\mathbf{V}_\infty$ vector and the equatorial plane (i.e. between $\mathbf{V}_\infty$ and the x' axis). In other words,

$$i_{\min} = |\delta| \tag{2.11}$$

where $i_{\min}$ is the minimum possible orbit inclination (without the use of a maneuver or perturbation forces) for the hyperbolic approach trajectory.
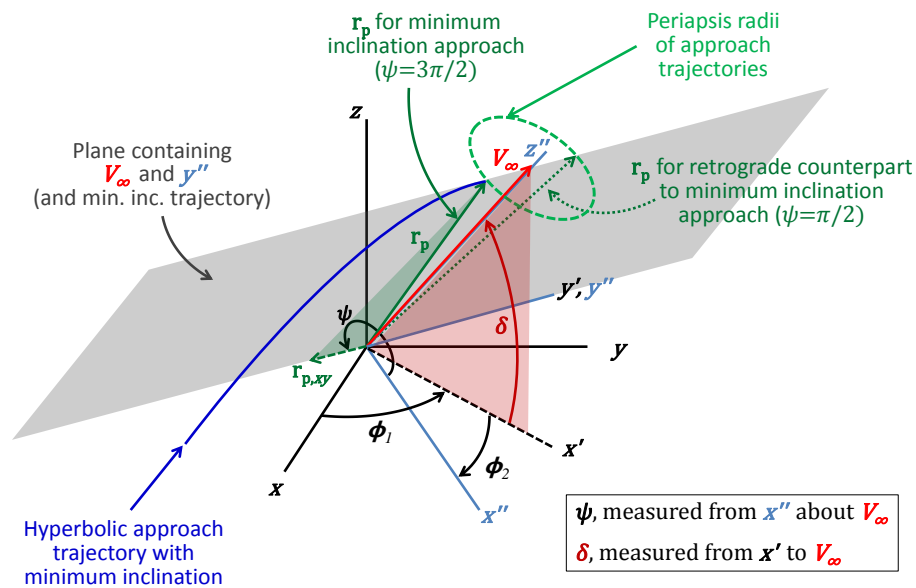
Figure 2.4.: Hyperbolic approach trajectory with minimum inclination relative to encounter planet's equatorial planet (at $\psi = 3\pi/2$). The retrograde counterpart to this solution (i.e. the approach trajectory opposite the minimum inclination solution, and in the same plane) occurs at $\psi = \pi/2$, and represents the maximum inclination solution. The absolute value of the declination angle, δ, of the approach, is equal to the minimum inclination.

To compute the orbital elements for an approach trajectory (given $\mathbf{V}_\infty$ (vector), r_p (magnitude), and ψ), the semimajor axis, eccentricity, and angle β are first calculated, given by

$$a = -\mu/V_\infty^2 \tag{2.12}$$

$$e = 1 - r_p/a \tag{2.13}$$

$$\beta = \cos^{-1}(1/e), \;\; 0 < \beta < \pi/2 \tag{2.14}$$

where μ is the gravitational parameter of the encounter body (i.e. the gravitational constant multiplied by the mass of the encounter body), and the angle β is the supplement to the true anomaly of the hyperbolic trajectory at infinity (i.e. the true anomaly of the outgoing asymptote).

The radius, r, at a specified true anomaly, θ^*, can now be computed from

$$r = \frac{a(1 - e^2)}{1 + e\cos\theta^*} \tag{2.15}$$

To get the remaining orbital elements, the periapsis vector, $\mathbf{r}_p$ is computed. To calculate $\mathbf{r}_p$, the rotation angles ϕ_1 and ϕ_2 are first found from the components of the $\mathbf{V}_\infty$ vector as follows:

$$\phi_1 = \tan^{-1}\left(\frac{V_{\infty,y}}{V_{\infty,x}}\right) \tag{2.16}$$

$$\phi_2 = \tan^{-1}\left(\frac{V_{\infty,x'}}{V_{\infty,z'}}\right) \tag{2.17}$$

When computing trajectories in this study (e.g. with STOUR or MALTO), the $\mathbf{V}_\infty$ vector is typically found in J2000 ecliptic-frame coordinates. From Eqs. 2.6 and 2.3 (using the δ_0 and α_0 values in Ref. [10] for the desired planet), the $\mathbf{V}_\infty$ vector

coordinates can be quickly converted to body-inertial frame coordinates. Since the body-inertial coordinates represent the planetocentric equatorial xyz-frame, computing ϕ_1 from Eq. 2.16 is straightforward. To find an expression for the $\mathbf{V}_\infty$ components in $x'y'z'$-frame coordinates (shown in Fig. 2.3), we use Eq. 2.7, with ϕ_1 and $\mathbf{V}_\infty$ substituted for θ and $\mathbf{r}_{xyz}$, respectively. The resulting expressions for the $V_{\infty,x'}$ and $V_{\infty,z'}$ components can then be plugged into Eq. 2.17, giving

$$\phi_2 = \tan^{-1}\left(\frac{V_{\infty,x}\cos\phi_1 + V_{\infty,y}\sin\phi_1}{V_{\infty,z}}\right) \tag{2.18}$$

With ϕ_1 and ϕ_2 known, the periapsis vector, $\mathbf{r}_p$ can be computed. By inspection of Fig. 2.3b, $\mathbf{r}_p$ can be expressed in terms of β and ψ as

$$\mathbf{r}_p = r_p\sin\beta\cos\psi\hat{x}'' + r_p\sin\beta\sin\psi\hat{y}'' + r_p\cos\beta\hat{z}'' \tag{2.19}$$

where $\hat{x}''$, $\hat{y}''$, and $\hat{z}''$ are unit vectors along the x, y, and z axes, respectively. From Eq. 2.10, the $\hat{x}''$, $\hat{y}''$, and $\hat{z}''$ components of $\mathbf{r}_p$ can be written in $\hat{x}$, $\hat{y}$, and $\hat{z}$ coordinates (via the ϕ_1 and ϕ_2 rotations as shown in Fig. 2.3a), giving

$$
\begin{aligned}
\mathbf{r}_p = \ & r_p\{[\cos\phi_1\,(\sin\beta\cos\psi\cos\phi_2 + \cos\beta\sin\phi_2) - \sin\phi_1\sin\beta\sin\psi]\,\hat{x} \\
& + [\sin\phi_1\,(\sin\beta\cos\psi\cos\phi_2 + \cos\beta\sin\phi_2) + \cos\phi_1\sin\beta\sin\psi]\,\hat{y} \\
& + (\cos\beta\cos\phi_2 - \sin\beta\cos\psi\sin\phi_2)\,\hat{z}\}
\end{aligned}
\tag{2.20}
$$

which is expressed entirely in terms of known values.

With $\mathbf{r}_p$ known, the remaining orbital elements for the hyperbolic approach trajectory can be computed from,

$$\mathbf{e} = e\frac{\mathbf{r_p}}{r_p} = e_x\hat{x} + e_y\hat{y} + e_z\hat{z} \tag{2.21}$$

$$h = \sqrt{a\mu(1 - e^2)} \tag{2.22}$$

$$\hat{h} = \frac{\mathbf{r}_p \times \mathbf{V}_\infty}{|\mathbf{r}_p \times \mathbf{V}_\infty|} \tag{2.23}$$

$$\mathbf{h} = h\hat{h} = h_x\hat{x} + h_y\hat{y} + h_z\hat{z} \tag{2.24}$$

$$i = \cos^{-1}\left(\frac{h_z}{h}\right) \tag{2.25}$$

where h is the specific angular momentum, and i is the inclination of the orbit with respect to the encounter body's equatorial plane. If we define $\mathbf{N}$ as the "node vector" (i.e. the vector directed from the origin to the ascending node of the approach trajectory), given by

$$\mathbf{N} = \hat{z} \times \mathbf{h} = N_x\hat{x} + N_y\hat{y} + N_z\hat{z} \tag{2.26}$$

then the right ascension of the ascending node, Ω, and the argument of periapsis, ω, can be computed from

$$\Omega = \begin{cases} \cos^{-1}\left(\frac{N_x}{N}\right) & \text{for } N_y \geq 0 \\ 2\pi - \cos^{-1}\left(\frac{N_x}{N}\right) & \text{for } N_y < 0 \end{cases} \tag{2.27}$$

$$\omega = \begin{cases} \cos^{-1}\left(\frac{\mathbf{N}\cdot\mathbf{e}}{Ne}\right) & \text{for } e_z \geq 0 \\ 2\pi - \cos^{-1}\left(\frac{\mathbf{N}\cdot\mathbf{e}}{Ne}\right) & \text{for } e_z < 0 \end{cases} \tag{2.28}$$

The x'', y'', z'' frame can be related to the more commonly used B-plane frame, for a reference normal vector $\hat{N}_{ref} = \hat{z}$ (the planet's spin axis). The relationship to B-plane is illustrated in Fig. 2.5, and given by the following equations

$$\mathbf{B} = b\hat{\mathbf{B}} \tag{2.29}$$
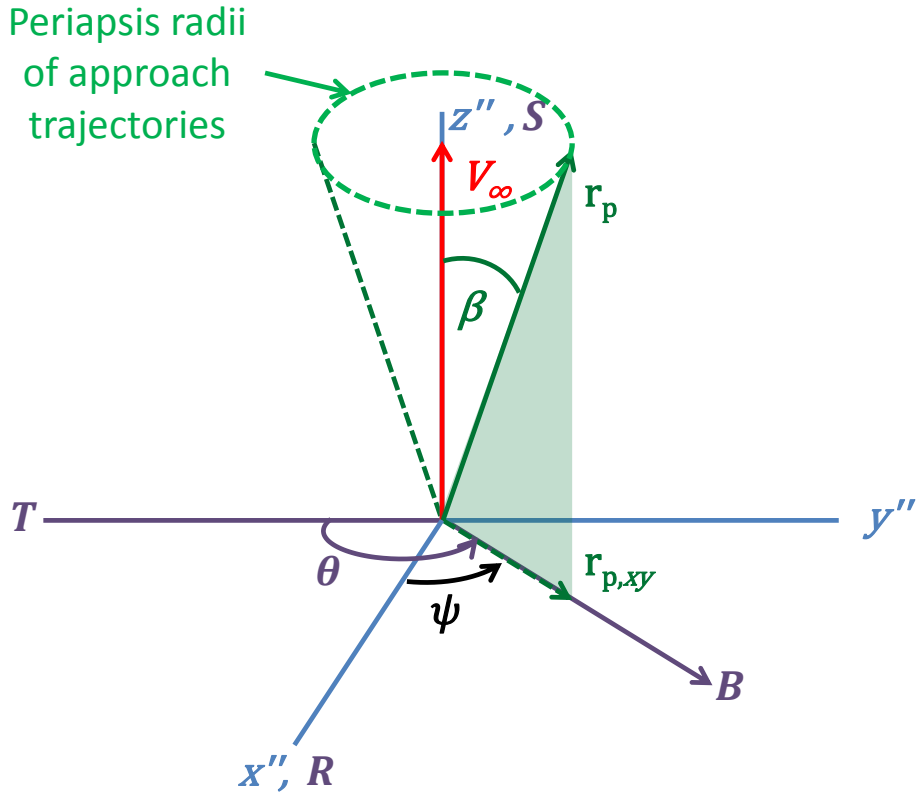
Figure 2.5.: Relationship between the inertial x'', y'', z'' frame, and the B-plane $\mathbf{T}$, $\mathbf{R}$, $\mathbf{S}$ frame. The vectors $\mathbf{B}$ and $\mathbf{r}_{p,xy}$ are parallel.

$$b = |a|\sqrt{e^2 - 1} \tag{2.30}$$

$$\hat{\mathbf{B}} = \hat{\mathbf{S}} \times \hat{\mathbf{h}} \tag{2.31}$$

where $\hat{\mathbf{h}}$ is the angular momentum of the trajectory and

$$\hat{\mathbf{S}} = \hat{\mathbf{z}} = \hat{\mathbf{V}}_\infty \tag{2.32}$$

Additionally, the unit vectors $\hat{\mathbf{T}}$ and $\hat{\mathbf{R}}$ can be expressed as

$$\hat{\mathbf{T}} = \frac{\hat{\mathbf{S}} \times \hat{\mathbf{N}}_{\mathbf{ref}}}{|\hat{\mathbf{S}} \times \hat{\mathbf{N}}_{\mathbf{ref}}|} = -\hat{\mathbf{y}}'' \tag{2.33}$$

$$\hat{\mathbf{R}} = \hat{\mathbf{S}} \times \hat{\mathbf{T}} = \hat{\mathbf{x}}'' \tag{2.34}$$

The B-plane angle θ can be related to the design parameter ψ by the simple relation

$$\theta = \psi + \pi/2 = \psi + 90° \tag{2.35}$$

2.2.2 Probe Entry Parameters for an Oblate Body

When approaching and entering the atmosphere of a planet or moon, the oblateness (bulge) of the body may significantly impact the entry conditions, such as entry flight path angle and entry latitude. The cause is both geometric and gravitational. The geometric impact is due to the fact that the entry point on the surface of an oblate spheroid at a specified radius will differ from a corresponding entry point on that of a sphere. The gravity field of an oblate body will also cause perturbations on the orbital elements (compared to the gravity field if a spherical body is assumed). One such change is the precession of the right ascension of the ascending node.

For the Gas-Giant and Ice-Giant planets, the oblateness is particularly pronounced. For this analysis, the shapes of the giant planets are assumed to be oblate spheroids, defined by their mean equatorial radius and polar radius. Additionally, only the geometric consequences of entry on an oblate body are considered. Since the approach hyperbolic trajectory is only in the vicinity of the planet from (approximately) the point of entry into the planet's sphere of influence, to atmospheric entry, any precession of the elements is assumed small is this relatively short period of time (compared to the time scale of a spacecraft orbiting the planet).

This work also does not include an analysis of the probe during entry; rather, the purpose is to compute the probe's states upon entry into the atmosphere.

In this section, a method is presented for computing the following parameters at the point of atmospheric entry on an oblate spheroid, for a known hyperbolic approach trajectory:

- Inertial velocity magnitude (i.e. orbital velocity in "body inertial" frame)
- Entry flight path angle
- Heading angle
- Latitude
- Longitude
- Atmosphere-relative entry velocity

To understand whether or not such entry conditions are feasible for a particular probe design, an entry analysis will need to be conducted. Since entry analyses often fall outside the expertise of many mission designers, the following derivation computes entry parameters that are convenient for an entry analysis team to simulate entry. This process will likely be iterative, where the mission designers adjust the approach trajectories (or possibly the interplanetary trajectory) and send updated entry parameters, until a feasible probe design can be found. In this work, much of the entry insight came from a collaboration with the entry analysis team at NASA Ames Research Center, who's entry analysis tools required the entry parameters derived in this section. One exception is the derivation of the atmospheric-relative entry velocity. This parameter is more intuitive for the non-entry expert to interpret, and by comparison to atmosphere-relative entry speeds in the literature for other probe entry designs, can be used to gauge the feasibility of probe entry, when a complete entry analysis has yet to be done, or is unavailable.

For the following derivation of the entry parameters, it is assumed that the hyperbolic approach trajectory is completely known. The approach trajectory parameters that are used in this derivation include: $\mathbf{r}_P$, $\mathbf{V}_\infty$, ψ, $\mathbf{h}$, i, Ω, $\mathbf{e}$, and ω. Where $\mathbf{h}$ is the orbital angular momentum vector, i is the inclination, Ω is the right ascension of the ascending node, $\mathbf{e}$ is the eccentricity vector (which points from the focus of the hyperbolic or elliptical trajectory to the periapsis), and ω is the argument of periapsis.

If an approach trajectory has not yet been selected, the following method can still be used to calculate the entry parameters, but the process must be iterative; where several approach trajectories are selected and the various entry parameters are assessed to choose a feasible approach trajectory. (This iterative process was the primary method used to select an approach trajectory in this work.)

Point of Entry and Inertial Velocity at Entry

The planet shape including its atmosphere is assumed to be an oblate spheroid. A point on the surface of this oblate spheroid is defined by,

$$\frac{r_x^2 + r_y^2}{a^2} + \frac{r_z^2}{b^2} = 1 \qquad (2.36)$$

where $\mathbf{r}$ is the position vector pointing to the specified point on the surface of an oblate spheroid (centered about the origin) expressed in Cartesian coordinates. (For this derivation, the x-y-z frame refers to the body-inertial frame.) Since the surface of the oblate spheroid defined for this derivation includes the planet and its atmosphere,

$$a = R_{Eq} + EntryAlt \qquad (2.37)$$

$$b = R_{Pol} + EntryAlt \qquad (2.38)$$

where R_{Eq} and R_{Pol} are the planet's mean equatorial radius and polar radius, and *EntryAlt* is the altitude where the entry is defined to occur (i.e. the "edge" of the planet's atmosphere). In this work, the point of entry is assumed to be 1000 km at Saturn, and 3000 km at Uranus and Neptune. For all giant planets, the "surface" is often defined as the point where the atmospheric pressure is 1 bar.

To find the point of entry on an approach trajectory, the position vector $\mathbf{r}$ in Eq. (2.36), must also be a position vector on the approach trajectory. Identifying such a vector represents the point on the approach trajectory that intersects the surface

of the oblate spheroid. Since the approach trajectory is known, identifying the true anomaly at this intersection will give the entry point. To find the true anomaly, $\mathbf{r}$ is expressed in Cartesian coordinates (in the body-inertial frame) in terms of the orbital elements Ω, i, and θ,

$$
\begin{aligned}
\mathbf{r} = \ & r\{(\cos\Omega\cos\theta - \sin\Omega\cos i\sin\theta)\,\hat{x} \\
& + (\sin\Omega\cos\theta + \cos\Omega\cos i\sin\theta)\,\hat{y} \\
& + \sin i\sin\theta\hat{z}\} \\
= \ & r_x\hat{x} + r_y\hat{y} + r_z\hat{z}
\end{aligned}
\tag{2.39}
$$

and

$$
\theta = \theta^* + \omega
\tag{2.40}
$$

were θ^* is the true anomaly.

Plugging r_x, r_y, and r_z, into Eq. (2.36), replacing θ using Eq. (2.40), and expressing r using the conic equation (expressed in terms of h), given by

$$
r = \frac{h^2/\mu}{1 + e\cos\theta^*}
\tag{2.41}
$$

produces the transcendental equation

$$
\frac{\mu^2(1 + e\cos\theta^*)}{h^4} = \frac{\cos^2(\theta^* + \omega) + \cos^2 i\sin^2(\theta^* + \omega)}{a^2} + \frac{\sin^2 i\sin^2(\theta^* + \omega)}{b^2}
\tag{2.42}
$$

Equation (2.42) can be solved for the entry θ^* using a root solver. A recommended initial guess, is the entry true anomaly for a spherical body (using either the equatorial radius as done below, or the polar radius, or an average of the two to define the sphere), given by

$$
\theta^*_{Sphere} = -\cos^{-1}\left[\frac{1}{e}\left(\frac{h^2}{\mu r} - 1\right)\right]
\tag{2.43}
$$

where the negative solution of $\cos^{-1}(*)$ is taken since the approach trajectory is incoming, and therefore entry occurs before periapsis passage.

With θ^* at entry known, it can be plugged into Eq. (2.39) to compute $\mathbf{r}_{Entry}$.

The inertial velocity magnitude at the point of entry is then computed from

$$V_{Entry} = \sqrt{V_\infty^2 + 2\mu/r_{Entry}} \tag{2.44}$$

where $r_{Entry} = |\mathbf{r}_{Entry}|$.

The velocity vector, $\mathbf{V}_{Entry}$ can be computed from the orbital flight path angle at entry, which should not be confused with the entry flight path angle on an oblate spheroid. The orbital flight path angle is the angle between the velocity vector, and the $\hat{\theta}$ direction (in $\hat{r}$-$\hat{\theta}$-$\hat{h}$ coordinates). The entry flight path angle on an oblate spheroid is the minimum angle between the velocity vector at entry, and a plane tangent to the surface of the oblate spheroid at the point of entry (i.e. the angle of decent into the atmosphere). Only for a spherical atmosphere are these two angles the same.

The orbital flight path angle at entry is given by

$$\gamma_{Entry} = -\cos^{-1}\left(\frac{h}{r_{Entry}V_{Entry}}\right) \tag{2.45}$$

Thus, in $\hat{r}$-$\hat{\theta}$-$\hat{h}$ coordinates, the entry velocity vector can be expressed as

$$\begin{aligned}
\mathbf{V}_{Entry} &= V_{Entry}r_{Entry}\left(\sin\gamma_{Entry}\hat{r} + \cos\gamma_{Entry}\hat{\theta}\right) \\
&= V_r\hat{r} + V_\theta\hat{\theta}
\end{aligned} \tag{2.46}$$

where the $\hat{h}$ component of the velocity vector is zero by definition.

Converting to Cartesian coordinates (in the body-inertial frame) using Ω, i, and θ, gives

$$
\begin{aligned}
\mathbf{V}_{Entry} &= \left[V_r \left(\cos\theta \cos\Omega - \sin\theta \cos i \sin\Omega \right) + V_\theta \left(-\sin\theta \cos\Omega - \cos\theta \cos i \sin\Omega \right) \right] \hat{x} \\
&\quad + \left[V_r \left(\cos\theta \sin\Omega + \sin\theta \cos i \cos\Omega \right) + V_\theta \left(\cos\theta \cos i \cos\Omega - \sin\theta \sin\Omega \right) \right] \hat{y} \\
&\quad + \left[V_r \sin\theta \sin i + V_\theta \cos\theta \sin i \right] \hat{z} \\
&= V_x \hat{x} + V_y \hat{y} + V_z \hat{z}
\end{aligned}
$$

$$(2.47)$$

where V_r and V_θ are the $\hat{r}$ and $\hat{\theta}$ components of $\mathbf{V}_{Entry}$ in Eq. (2.46).

Entry Heading Angle

Heading angle at entry may have several definitions in the literature depending on the reference direction for which the heading angle is measured. In this work, the heading angle is defined to be zero degrees if the velocity vector is directed to the south at entry, and 90 degrees if the velocity is directed to the east. To compute the heading angle, two new coordinate frames are defined. The frame rotations and the heading angle are all depicted in Fig. 2.6 relative to the Cartesian x-y-z coordinates of the body-inertial frame. (The third frame rotation, into the x'''-y'''-z''' frame, will be used in the next section to compute the entry flight path angle.) The vector $\mathbf{n}$ represents the surface normal vector on the oblate spheroid at the point of entry.

From Fig. 2.6, it is apparent that the heading angle, $\mathcal{H}$, can be computed from the inertial entry velocity vector, using

$$
\mathcal{H} = \tan^{-1} \left(\frac{V_{y''}}{V_{x''}} \right)
$$

$$(2.48)$$

where $V_{x''}$ and $V_{y''}$ are components of the inertial velocity vector written in the x''-y''-z'' coordinates. From Eq. (2.44), the entry velocity vector is known in body-inertial coordinates, and so to compute the heading angle, the x-y-z and x''-y''-z'' frames need to be related.

To relate the x-y-z and x'-y'-z' frames, note that the primed frame is a rotation about the z axis by angle ξ_1, giving the relations

Figure 2.6.: Coordinate frames used to define heading angle of (inertial) entry velocity vector. The x-y-z axes represent the body-fixed frame, and the vector $\mathbf{n}$ represents the surface normal vector on the oblate spheroid at the point of entry.

$$
\begin{aligned}
\hat{x}' &= \cos \xi_1 \hat{x} + \sin \xi_1 \hat{y} \\
\hat{y}' &= -\sin \xi_1 \hat{x} + \cos \xi_1 \hat{y} \\
\hat{z}' &= \hat{z}
\end{aligned}
\tag{2.49}
$$

To relate the x'-y'-z' and x''-y''-z'' frames, the double-primed frame is a rotation about the y' axis by angle ξ_2, giving

$$
\begin{aligned}
\hat{x}'' &= \cos \xi_2 \hat{x}' - \sin \xi_2 \hat{z}' \\
\hat{y}'' &= \hat{y}' \\
\hat{z}'' &= \sin \xi_2 \hat{x}' + \cos \xi_2 \hat{z}'
\end{aligned}
\tag{2.50}
$$

Rearranging Eqs. (2.49) and (2.50) provides their inverse, giving

$$
\begin{aligned}
\hat{x} &= \cos \xi_1 \hat{x}' - \sin \xi_1 \hat{y}' \\
\hat{y} &= \sin \xi_1 \hat{x}' + \cos \xi_1 \hat{y}' \\
\hat{z} &= \hat{z}'
\end{aligned}
\tag{2.51}
$$

and

$$\begin{aligned}
\hat{x}' &= \cos\xi_2 \hat{x}'' + \sin\xi_2 \hat{z}'' \\
\hat{y}' &= \hat{y}'' \\
\hat{z}' &= -\sin\xi_2 \hat{x}'' + \cos\xi_2 \hat{z}''
\end{aligned} \tag{2.52}$$

The entry velocity vector can be expressed in the x''-y''-z'' frame coordinates by first plugging Eq. (2.51) followed by (2.52) into Eq. (2.44), giving

$$\begin{aligned}
V_{Entry} &= \left(V_x \cos\xi_1 + V_y \sin\xi_1\right)\hat{x}' + \left(V_y \cos\xi_1 - V_x \sin\xi_1\right)\hat{y}' + V_z \hat{z}' \\
&= V_{x'}\hat{x}' + V_{y'}\hat{y}' + V_{z'}\hat{z}'
\end{aligned} \tag{2.53}$$

and

$$\begin{aligned}
V_{Entry} &= \left[\left(V_x \cos\xi_1 + V_y \sin\xi_1\right)\cos\xi_2 - V_z \sin\xi_2\right]\hat{x}'' \\
&\quad + \left(V_y \cos\xi_1 - V_x \sin\xi_1\right)\hat{y}'' \\
&\quad + \left[\left(V_x \cos\xi_1 + V_y \sin\xi_1\right)\sin\xi_2 + V_z \cos\xi_2\right]\hat{z}'' \\
&= V_{x''}\hat{x}'' + V_{y''}\hat{y}'' + V_{z''}\hat{z}''
\end{aligned} \tag{2.54}$$

The angle ξ_1 can be computed from the components of $\mathbf{r}_{Entry}$,

$$\xi_1 = \tan^{-1}\left(\frac{r_y}{r_x}\right) \tag{2.55}$$

where r_y and r_x are the components of $\mathbf{r}_{Entry}$ in the body-inertial frame.

To compute the angle ξ_2, the surface normal vector $\mathbf{n}$ must first be computed, which can be computed by taking the gradient of the surface of the oblate spheroid at the point of entry. First, the variable terms in the equation for an oblate spheroid are expressed as the function f, given by

$$f(x,y,z) = \frac{x^2}{a^2} + \frac{y^2}{a^2} + \frac{z^2}{b^2} \tag{2.56}$$

The gradient of f is then computed, and evaluated at the point of entry, given by

$$
\begin{aligned}
\mathbf{n} &= \nabla f(x, y, z)|_{x=r_x, y=r_y, z=r_z} \\
&= \frac{2r_x}{a^2}\hat{x} + \frac{2r_y}{a^2}\hat{y} + \frac{2r_z}{b^2}\hat{z} \\
&= n_x\hat{x} + n_y\hat{y} + n_z\hat{z}
\end{aligned}
\tag{2.57}
$$

where r_x, r_y, and r_z are the components of the position vector $\mathbf{r}_{Entry}$ in body-inertial coordinates.

The angle ξ_2 can now be expressed (by observation of Fig. 2.6a), as

$$
\xi_2 = \tan^{-1}\left(\frac{n'_x}{n'_y}\right)
\tag{2.58}
$$

The components of $\mathbf{n}$ can be expressed in the primed frame of Fig. 2.6 using Eq. (2.49), giving

$$
\begin{aligned}
\mathbf{n} &= \left(n_x \cos\xi_1 + n_y \sin\xi_1\right)\hat{x}' + \left(n_y \cos\xi_1 - n_x \sin\xi_1\right)\hat{y}' + n_z\hat{z}' \\
&= n_{x'}\hat{x}' + n_{y'}\hat{y}' + n_{z'}\hat{z}'
\end{aligned}
\tag{2.59}
$$

Plugging $n_{x'}$ and $n_{z'}$ into Eq. (2.58), gives

$$
\begin{aligned}
\xi_2 &= \tan^{-1}\left(\frac{n_x \cos\xi_1 + n_y \sin\xi_1}{n_z}\right) \\
&= \tan^{-1}\left[\frac{b^2}{a^2}\left(\frac{r_x \cos\xi_1 + r_y \sin\xi_1}{r_z}\right)\right]
\end{aligned}
\tag{2.60}
$$

With ξ_1 and ξ_2 defined, the heading angle can now be expressed in known terms, by plugging Eqs. (2.54), (2.55), and (2.60) into (2.48), giving

$$
\mathcal{H} = \tan^{-1}\left[\frac{V_y \cos\xi_1 - V_x \sin\xi_1}{(V_x \cos\xi_1 + V_y \sin\xi_1)\cos\xi_2 - V_z \sin\xi_2}\right]
\tag{2.61}
$$

Entry Flight Path Angle on Oblate Spheroid

To compute the entry flight path angle, we first define the x'''-y'''-z''' frame, illustrated in Fig. 2.6. The rotation is about the surface normal, $\mathbf{n}$, by the heading angle, $\mathcal{H}$.

The entry flight path angle on an oblate spheroid can then be expressed as

$$\gamma_{Entry,Ob} = \tan^{-1}\left(\frac{V_{z'''}}{V_{x'''}}\right) \tag{2.62}$$

The relation between the double-prime and triple-prime frames is given by,

$$\begin{aligned}
\hat{x}'' &= \cos\mathcal{H}\hat{x}''' - \sin\mathcal{H}\hat{y}''' \\
\hat{y}'' &= \sin\mathcal{H}\hat{x}''' + \cos\mathcal{H}\hat{y}''' \\
\hat{z}'' &= \hat{z}'''
\end{aligned} \tag{2.63}$$

Plugging Eq. (2.63) into (2.54) gives

$$\begin{aligned}
V_{Entry} &= \{[(V_x\cos\xi_1 + V_y\sin\xi_1)\cos\xi_2 - V_z\sin\xi_2]\cos\mathcal{H} \\
&\quad + [V_y\cos\xi_1 - V_x\sin\xi_1]\sin\mathcal{H}\}V_{x'''} \\
&+ \{(V_y\cos\xi_1 - V_x\sin\xi_1)\cos\mathcal{H} \\
&\quad - [(V_x\cos\xi_1 + V_y\sin\xi_1)\cos\xi_2 - V_z\sin\xi_2]\sin\mathcal{H}\}V_{y'''} \\
&+ [(V_x\cos\xi_1 + V_y\sin\xi_1)\sin\xi_2 + V_z\cos\xi_2]V_{z'''} \\
&= V_{x'''}\hat{x}''' + V_{y'''}\hat{y}''' + V_{z'''}\hat{z}'''
\end{aligned} \tag{2.64}$$

Plugging the $V_{z'''}$ and $V_{x'''}$ components into Eq. (2.62) gives

$$\gamma_{Entry,Ob} = \tan^{-1}\left(\frac{(V_x\cos\xi_1 + V_y\sin\xi_1)\sin\xi_2 + V_z\cos\xi_2}{[(V_x\cos\xi_1 + V_y\sin\xi_1)\cos\xi_2 - V_z\sin\xi_2]\cos\mathcal{H} + [V_y\cos\xi_1 - V_x\sin\xi_1]\sin\mathcal{H}}\right) \tag{2.65}$$

Entry Latitude and Longitude

To compute the latitude at the point of entry, we use the components of the entry position vector, r_{Entry}, in the primed frame (as illustrated in Fig. 2.6), given by

$$\text{Latitude} = \tan^{-1}\left(\frac{r_{z'}}{r_{x'}}\right) \tag{2.66}$$

Plugging the expressions for x', y', and z' from Eq. (2.51) into Eq. (2.39) gives

$$\begin{aligned}
\mathbf{r} &= \left(r_x \cos\xi_1 + r_y \sin\xi_1\right)\hat{x}' + \left(r_y \cos\xi_1 - r_x \sin\xi_1\right)\hat{y}' + r_z\hat{z}' \\
&= r_{x'}\hat{x}' + r_{y'}\hat{y}' + r_{z'}\hat{z}'
\end{aligned} \tag{2.67}$$

and plugging the expressions for $r_{x'}$ and $r_{z'}$ into Eq. (2.66) gives

$$\text{Latitude} = \tan^{-1}\left(\frac{r_z}{r_x \cos\xi_1 + r_y \sin\xi_1}\right) \tag{2.68}$$

To compute the longitude at entry, recall that the prime meridian of the body lies in the x-z plane (on the positive x side) in the Body-Fixed coordinate system, illustrated in Fig. 2.1. Thus far in this section, the x-y-z coordinates are in the Body-Inertial frame. To convert from Body-Inertial coordinates to Body-Fixed coordinates, we use Eq. (2.4). Thus, the entry position vector in Body-Fixed coordinates is given by

$$\begin{aligned}
\mathbf{r}_{BF} &= R_3(W)\mathbf{r}_{BI} \\
&= r_{xBF}\hat{x}_{BF} + r_{yBF}\hat{y}_{BF} + r_{zBF}\hat{z}_{BF}
\end{aligned} \tag{2.69}$$

The longitude can then be computed as the angle between $\mathbf{r}$ and the x_{BF}-z_{BF} plane (i.e. the prime meridian), given by

$$\text{Longitude} = \tan^{-1}\left(\frac{r_{yBF}}{r_{xBF}}\right) \tag{2.70}$$

Atmosphere-Relative Entry Velocity

To compute the entry velocity relative to the planet's rotating atmosphere, we first compute the velocity of the planet's atmosphere at the point of entry. For this calculation, it is assumed that the planet's atmosphere rotates uniformly about the body's spin axis.

In the primed frame illustrated in Fig. 2.6, the velocity of the atmosphere, $\mathbf{V}_{Atm}$, at the point of entry can be expressed as

$$\mathbf{V}_{Atm} = V_{Atm}\hat{y}' \tag{2.71}$$

where $\hat{y}'$ can be expressed in unprimed (i.e. Body-Inertial) coordinates from Eq. (2.49). The magnitude of the atmosphere velocity V_{Atm} is given by

$$V_{Atm} = r\cos(\text{Latitude})\omega_{Rot} \tag{2.72}$$

where ω_{Rot} is the rotation rate of the planet's atmosphere, which has a positive value for prograde rotation, and a negative value for retrograde rotation.

The velocity of the atmosphere at entry can thus be expressed as

$$\mathbf{V}_{Atm} = r\cos(\text{Latitude})\omega_{Rot}\left(-\sin\xi_1\hat{x} + \cos\xi_1\hat{y}\right) \tag{2.73}$$

The atmosphere-relative entry velocity is then given by

$$\mathbf{V}_{Entry,AtmRel} = \mathbf{V}_{Entry} - \mathbf{V}_{Atm} \tag{2.74}$$

where $\mathbf{V}_{Entry}$ is given by Eq. (2.47) and $\mathbf{V}_{Atm}$ is given by Eq. (2.73).

2.2.3 Consequences of Interplanetary Trajectory Design on Launch

In this section, the discussion of the approach trajectory is expanded to relate it to the launch problem. In principle, departure and approach on a hyperbolic trajectory

are identical, with time running in opposite directions. A consequence of this, is that for any departure hyperbolic trajectory, the declination of the departure asymptote, constrains the inclination of the departure hyperbola (just as it does with approach) as expressed in Eq. (2.11) restated here as $i_{min} = |\delta|$.

For example, if a rocket is to be launched from Kennedy Space Center and depart Earth on a hyperbolic trajectory, the minimum inclination (of the departure hyperbola) that can be achieved without a plane change is 28.5°, and the maximum inclination (due to restrictions on avoiding flight over populated areas) is about 57°. However, any inclination larger than 28.5° results in launch performance losses, since the velocity direction is not taking full advantage of the Earth's rotation. Thus, any interplanetary departure with declination magnitude, $|\delta|$, less than 28.5° can be launched into without requiring a plane change. If $|\delta|$ is greater than 28.5°, however, then the launch inclination must be greater than 28.5° since the minimum departure hyperbolic inclination, $i_{min} = |\delta|$. If the declination magnitude exceeds 57°, a plane change is required during departure (to avoid flight over populated areas), which may be feasible for a particular design, but will incur additional launch performance losses in terms of delivered payload injected into the interplanetary trajectory. In some cases, the interplanetary trajectory may need to be redesigned to reduce the declination magnitude.

2.2.4 Spacecraft Deflection Maneuver for Probe Release During Flyby

When a probe is released by a spacecraft, the spacecraft (in previous designs such as Galileo[*]) approaches the target body on an approach trajectory designed for the probe to enter the atmosphere. This is because the probe does not have its own propulsion system to target the body, and so the spacecraft then must put itself back on course for its target (e.g. for orbit insertion or to target fly by conditions to continue on to another body). The spacecraft's course adjustment is called a

---

[*]http://nssdc.gsfc.nasa.gov/planetary/galileo.html

deflection maneuver. In this work, the ΔV required for such a maneuver is estimated, for a spacecraft that flies by a body while releasing a probe. In this section, the model used to estimate the deflection maneuver ΔV is derived.

For this derivation, it is assumed that the approach trajectory for the probe is known, and the following terms are assumed given: the periapsis vector of the probe approach trajectory, $\mathbf{r}_{p,probe}$, the approach V_∞ (assumed same for both probe and spacecraft), semimajor axis, a (also same for both probe and spacecraft), and the probe approach trajectory eccentricity, e_{probe}, angular momentum, h_{probe}, argument of periapsis, ω_{probe}, right ascension of the ascending node, Ω_{probe}, and inclination, i_{probe}. It is also assumed that the approach trajectory of the spacecraft is known; however, the spacecraft trajectory will be changed slightly to accommodate the probe release and (in a single maneuver) return to a nearly identical trajectory to the originally designed spacecraft approach trajectory (i.e. the trajectory of the spacecraft if it approached the body from its designed approach trajectory, rather than the probe's). In this analysis, we use the periapsis vector of the spacecraft trajectory, $\mathbf{r}_{p,sc}$, from the (originally designed spacecraft approach), which we target using Lambert's method from the position of probe release.

The radius of the deflection maneuver, $r_{\Delta V}$, is also assumed known and is chosen by the designer. Physically, the deflection maneuver will decrease as $r_{\Delta V}$ increases (i.e. the maneuver is performed as far from the planet as possible); however, the precision limitation of the navigation design (to target the correct entry point for the probe) limits how far away the probe can be released. Without conducting a precise navigation analysis, in this study we choose the $r_{\Delta V}$ value, so that the time of flight of the probe is approximately 150 days to closely match the flight time of the Galileo probe, which was released 147 days prior to atmospheric entry[†]. This is determined iteratively by choosing a value for $r_{\Delta V}$ and then calculating the TOF from probe release to probe periapsis passage (which is approximately the same as the TOF to probe entry for this analysis).

[†]http://nssdc.gsfc.nasa.gov/planetary/galileo.html

To estimate the deflection maneuver δV, we first calculate the true anomaly, angle θ, and the vector components of $r_\Delta V$, at the point of probe release, given by

$$\theta^*_{\Delta V,probe} = -\cos^{-1}\left[\frac{1}{e_{probe}}\left(\frac{h^2_{probe}}{\mu r_{\Delta V}} - 1\right)\right] \tag{2.75}$$

$$\theta_{\Delta V,probe} = \theta^*_{\Delta V,probe} + \omega_{probe} \tag{2.76}$$

Plugging $\theta_{\Delta V,probe}$, Ω_{probe}, and i_{probe} into Eq: (2.39) gives the position vector, $\mathbf{r}_{\Delta V}$, at probe release.

The transfer angle, $\Delta\theta^*_{probe}$, between the position of probe release and probe trajectory periapsis, and the transfer angle $\Delta\theta^*_{sc}$, between the position of probe release and the spacecraft trajectory periapsis, are given by

$$\Delta\theta^*_{probe} = \left|\theta^*_{probe}\right| \tag{2.77}$$

$$\Delta\theta^*_{sc} = \cos^{-1}\left(\frac{\mathbf{r}_{p,sc} \bullet \mathbf{r}_{\Delta V}}{r_{p,sc}r_{\delta V}}\right) \tag{2.78}$$

Next, the velocity vector on the probe's trajectory at the release point is computed from the f and g functions

$$f_{probe} = 1 - \frac{r_{p,probe}}{P_{probe}}\left(1 - \cos\Delta\theta^*_{probe}\right) \tag{2.79}$$

$$g_{probe} = \frac{r_{\Delta V}r_{p,probe}}{\sqrt{\mu P_{probe}}}\sin\Delta\theta^*_{probe} \tag{2.80}$$

where the parameter P_{probe} is the semi-lattice rectum of the approach trajectory, given by

$$P_{probe} = a(1 - e^2_{probe}) \tag{2.81}$$

The probe velocity vector at the release point is then given by

$$\mathbf{V}_{\Delta V,probe} = \left(\mathbf{r}_{p,probe} - f_{probe}\mathbf{r}_{\Delta V}\right)/g_{probe} \tag{2.82}$$

To compute the velocity vector of the spacecraft at the point of probe release (immediately after the deflection maneuver has been performed), Lambert's method is used to compute the parameter P_{sc}, and then f and g functions are again used to calculate the spacecraft velocity vector at probe release.

Using Lambert's method, the P_{sc} is computed from

$$P_{sc} = \frac{4|a|\left(S - r_{p,sc}\right)\left(S - r_{\Delta V}\right)}{C^2} \sinh^2\left(\frac{\alpha' \pm \beta'}{2}\right) \tag{2.83}$$

where C is the chord length that connects the two position vectors at probe release and periapsis of the spacecraft trajectory, which is computed using the law of cosines, given by

$$C = \sqrt{r_{p,sc}^2 + r_{\Delta V}^2 - 2r_{p,sc}r_{\Delta V}\cos\Delta\theta_{sc}^*} \tag{2.84}$$

S is the semi-perimeter of the position vectors and the chord length, given by

$$S = \frac{1}{2}\left(r_{p,sc} + r_{\Delta V} + C\right) \tag{2.85}$$

and the angles α' and β' are given by

$$\alpha' = 2\sinh^{-1}\sqrt{\frac{S}{2|a|}} \tag{2.86}$$

$$\beta' = 2\sinh^{-1}\sqrt{\frac{S-C}{2|a|}} \tag{2.87}$$

The choice of $+$ or $-$ in Eq. (2.83), was found by calculating both solutions and identifying the $+$ solution as correct. (We expect the deflection maneuver size to be on the order of 10s to 100s of m/s. If the $-$ solution is used for an example case, the maneuver size is on the order of 10s of km/s.)

To compute the spacecraft velocity at the point of probe release (just after the deflection maneuver is performed), the f and g functions are again used, giving

$$f_{sc} = 1 - \frac{r_{p,sc}}{P_{sc}} \left(1 - \cos \Delta\theta^*_{sc}\right) \tag{2.88}$$

$$g_{sc} = \frac{r_{\Delta V} r_{p,sc}}{\sqrt{\mu P_{sc}}} \sin \Delta\theta^*_{sc} \tag{2.89}$$

and the spacecraft velocity, $\mathbf{V}_{\Delta V,sc}$, at probe release is computed from

$$\mathbf{V}_{\Delta V,sc} = \left(\mathbf{r}_{p,sc} - f_{sc}\mathbf{r}_{\Delta V}\right)/g_{sc} \tag{2.90}$$

From Eq. (2.82) and Eq. (2.90), the orbit deflection maneuver is given by

$$\Delta V_{Defl} = |\mathbf{V}_{\Delta V,sc} - \mathbf{V}_{\Delta V,probe}| \tag{2.91}$$

To compute the flight time of the probe from the point of release to the point of periapsis passage (which is approximately the same flight time as probe release to atmospheric entry), we use Kepler's time equation, giving

$$\text{TOF}_{probe} = \sqrt{\frac{|a|^3}{\mu}} \left|e_{probe} \sinh \text{H}_{\Delta V,probe} - \text{H}_{\Delta V,probe}\right| \tag{2.92}$$

where $\text{H}_{\Delta V,probe}$ is the hyperbolic anomaly of the probe trajectory at the point of release, given by

$$\text{H}_{\Delta V,probe} = 2 \tanh^{-1} \left[\sqrt{\frac{e_{probe} - 1}{e_{probe} + 1}} \tan\left(\frac{\theta^*_{\Delta V,probe}}{2}\right)\right] \tag{2.93}$$

If the time of flight of the spacecraft from probe release to the spacecraft's periapsis is desired, it can be computed from Lambert's equation, given by

$$\text{TOF}_{sc} = \frac{|a|^{3/2}}{\sqrt{\mu}} \left\{[\sinh(\alpha') - \alpha'] - [\sinh(\beta') - \beta']\right\} \tag{2.94}$$

2.2.5   Launch Vehicle Performance

In this work, the maximum launch mass (for a given launch vehicle) is determined for a particular launch V_∞ (or C_3), in order to compute the maximum delivered mass at a target body. The launch vehicles considered in this work are the Atlas V 551, Delta IV Heavy, and the Space Launch System (SLS) Block 1B. The performance curves for the Atlas V 551 and Delta IV Heavy are available on NASA's Launch Vehicle Performance website[‡]. The SLS performance data are not yet available on the NASA website, and so the performance curves presented in Ref. [35] are used.

In post processing the thousands of results found using the trajectory design tool STOUR, as well as to compute optimal (or low-thrust) trajectories in MALTO, it is convenient to fit a polynomial curve to the performance data for a particular launch vehicle. Of the performance curve fits used in this work, the SLS curve fit has the largest error, which has a maximum error of about 10 kg. The data itself is subject to human error, however, since the data was obtained by visually inspecting the performance curve plot given in Ref. [35].

The polynomial curve fits for each of the three launch vehicles considered are provided below.

$$
\begin{aligned}
m_{L,AV551} = {} & 6106.286412675735 - 110.6762537571361 C_{3,AV551} \\
& + 0.617132837063155 C_{3,AV551}^2 + 1.655556918721937(10^{-4}) C_{3,AV551}^3 \\
& - 1.764489380594721(10^{-6}) C_{3,AV551}^4
\end{aligned}
\tag{2.95}
$$

which is valid for C_3 from -10 to 60 km^2/s^2,

$$
\begin{aligned}
m_{L,DIVH} = {} & 10598.68546670721 - 186.4563475807183 C_{3,DIVH} \\
& + 1.377092176829015 C_{3,DIVH}^2 - 0.004579784822348 C_{3,DIVH}^3 \\
& - 1.007433959379602(10^{-6}) C_{3,DIVH}^4
\end{aligned}
\tag{2.96}
$$

[‡]https://elvperf.ksc.nasa.gov/Pages/Default.aspx

which is valid for C_3 from -10 to 100 km^2/s^2, and

$$
\begin{aligned}
m_{L,SLS} &= 35722.46358080152 - 510.5138820643374 C_{3,SLS} \\
&+ 2.932563746865676 C_{3,SLS}^2 - 0.011030421338031 C_{3,SLS}^3 \\
&+ 2.287772444084514(10^{-5}) C_{3,SLS}^4
\end{aligned}
\tag{2.97}
$$

which is valid for C_3 from -8 to 140 km^2/s^2. Note that any of the performance functions can be written in terms of launch V_∞ using the relation $C_3 = V_\infty^2$.

In this work, it was found that bi-exponential curve fits often worked well, but polynomial fits are used exclusively in this study, since this is the only format accepted by the Mission Analysis Low-Thrust Optimization (MALTO) tool.

For some trajectories with high launch V_∞, an additional upper stage is used, such as a STAR 48. In this analysis, we consider the STAR 48 for the Atlas V 551, Delta IV Heavy, and the SLS Block 1B. To be conservative regarding delivered mass at the target body, it is assumed that the STAR 48 burn occurs on the departure asymptote (since a burn closer to periapsis will improve the performance of the STAR 48 burn). The parameters assumed for the STAR 48 are for the STAR 48A, with an effective $I_{sp} = 183$ s, a wet mass of 2574 kg, with propellant mass of 2430 kg (leaving a dry mass of 144 kg) [11].

To compute the modified performance curve with the STAR 48 additional upper stage, we first define the following terms:

- m_L = maximum launch mass by the launch vehicle with STAR 48 (on modified performance curve, which excludes the wet mass of the STAR 48)

- V_∞ = launch V_∞ corresponding to m_{PL} on modified performance curve with STAR 48 additional upper stage

- $m_{L,LV}$ = maximum launch mass of standard launch vehicle (using unmodified performance curve)

- $V_{\infty,LV}$ launch V_∞ corresponding to $m_{L,LV}$ on unmodified performance curve (without STAR 48 additional upper stage)

- m_{STAR48} = total (wet) mass of the STAR 48

- $m_{STAR48,prop}$ = propellant mass of STAR 48

- $m_{STAR48,dry}$ = dry mass of STAR 48

It is assumed that the polynomial (or other function form) fit of the unmodified launch vehicle performance curve is known, i.e.

$$m_{L,LV} = f(V_{\infty,LV}) \tag{2.98}$$

where $f(V_{\infty,LV})$ is the known polynomial-fit function, and the STAR 48 characteristics (m_{STAR48}, $m_{STAR48,prop}$, and $m_{STAR48,dry}$) are also known.

The launch mass for a launch vehicle with unmodified performance curve in Eq. (2.98), can be modified to account for the STAR 48 mass, giving

$$m_{L,LV} = m_L + m_{STAR48} \tag{2.99}$$

or inversely

$$m_L = m_{L,LV} - m_{STAR48} \tag{2.100}$$

To compute the boost in velocity provided by the STAR 48, we use the rocket equation

$$\Delta V = g_0 I_{sp} \ln\left(\frac{m_0}{m_f}\right) \tag{2.101}$$

where $g_0 = 9.80665 m/s^2$ (standard gravity), I_{sp} is the specific impulse of the STAR 48, and

$$m_0 = m_{L,LV} \tag{2.102}$$

$$m_f = m_{L,LV} - m_{STAR48,prop} \tag{2.103}$$

Since the STAR 48 burn is (for this study) assumed to burn along the departure asymptote, the ΔV due too the STAR 48 can be interpreted as a ΔV_∞, where the boost in velocity is simply added to the departure V_∞, given by

$$\Delta V = V_\infty - V_{\infty,LV} \tag{2.104}$$

Plugging Eq. (2.98), (2.102), (2.103), and (2.104) into (2.101), gives

$$V_\infty = V_{\infty,LV} + g_0 I_{sp} \ln\left[\frac{f(V_{\infty,LF})}{f(V_{\infty,LF}) - m_{STAR48,prop}}\right] \tag{2.105}$$

The modified performance curve for a launch vehicle with the additional STAR 48 upper stage can now be computed using the following method:

1. Choose a range of values of $V_{\infty,LV}$ for a launch vehicle of choice. Be sure to not choose values outside the listed performance of your chosen launch vehicle.

2. Compute the corresponding $m_{L,LV}$ from Eq. (2.98). These, along with the $V_{\infty,LV}$ values, are the unmodified performance values for the chosen launch vehicle. (Equation (2.95), (2.96), or (2.97) can be used if the reader is interested in the Atlas V 551, Delta IV Heavy, or SLS Block 1B, respectively. The reader is warned, however, that the performance of these vehicles may have been changed since the time of writing this document.)

3. For each value of $V_{\infty,LV}$, compute V_∞ from Eq. (2.105).

4. For each value of $m_{L,LV}$, compute m_L from Eq. (2.100). The values of V_∞ and m_L make up the performance data for the modified performance curve with the STAR 48 additional upper stage.

5. Fit a curve to the m_L and V_∞ performance data, with polynomial-fit function $m_L = f(V_\infty)$. Since most performance curves use C_3 rather than V_∞ it is recommended that the V_∞ be converted to C_3 (using $C_3 = V_\infty^2$), to make the fit function $m_L = f(C_3)$.

The modified (and unmodified) performance curve fits for the Atlas V 551 and SLS Block 1B launch vehicles are given in Figs. 2.8 and 2.8. For each modified curve, only a portion of the modified data is used to fit a curve, due to the difficulty in fitting an accurate curve for the shape produced by the modified performance data. For the Atlas V 551, the unmodified performance is better (i.e. delivers more mass) than the modified data; however, the modified data provides solutions for higher C_3. Thus, only the modified data greater than a C_3 of 60 km^2/s^2 is considered for the modified performance curve fit. Similarly, the modified SLS data outperforms the unmodified data at a C_3 of about 80 km^2/s^2; and therefore, only the modified data greater than (just under) 80 km^2/s^2 is used for the modified performance curve fit.
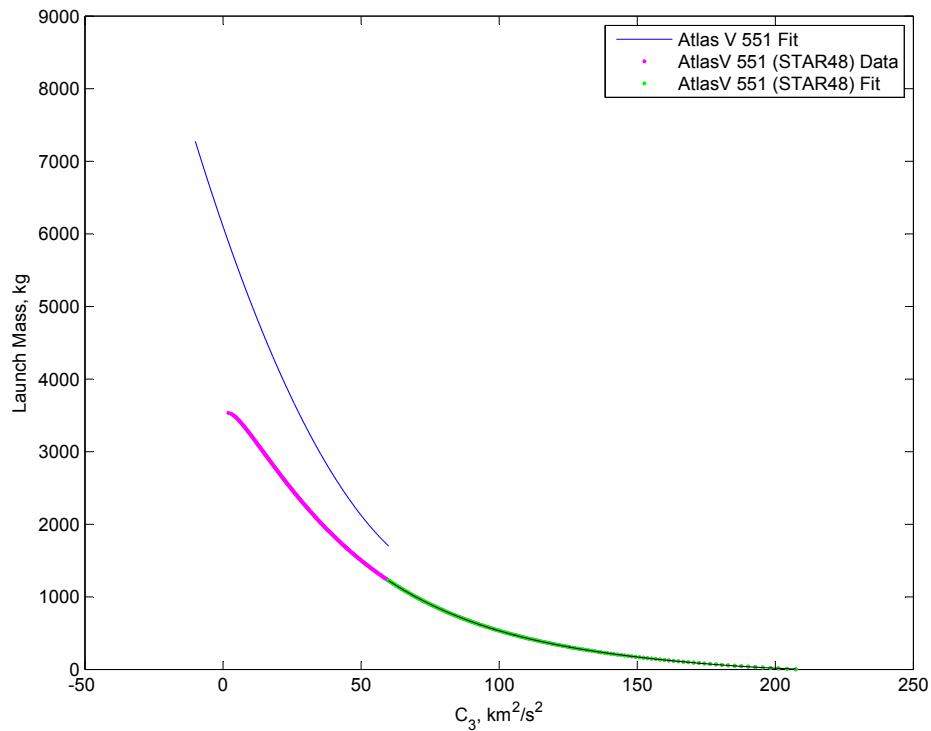
Figure 2.7.: Performance curve for the Atlas V 551 launch vehicle. The blue curve is the unmodified performance curve, and the magenta and green points represent the modified performance data with the STAR 48 additional upper stage. The green portion of the modified performance data represents the portion used to fit a 4th-order polynomial curve.
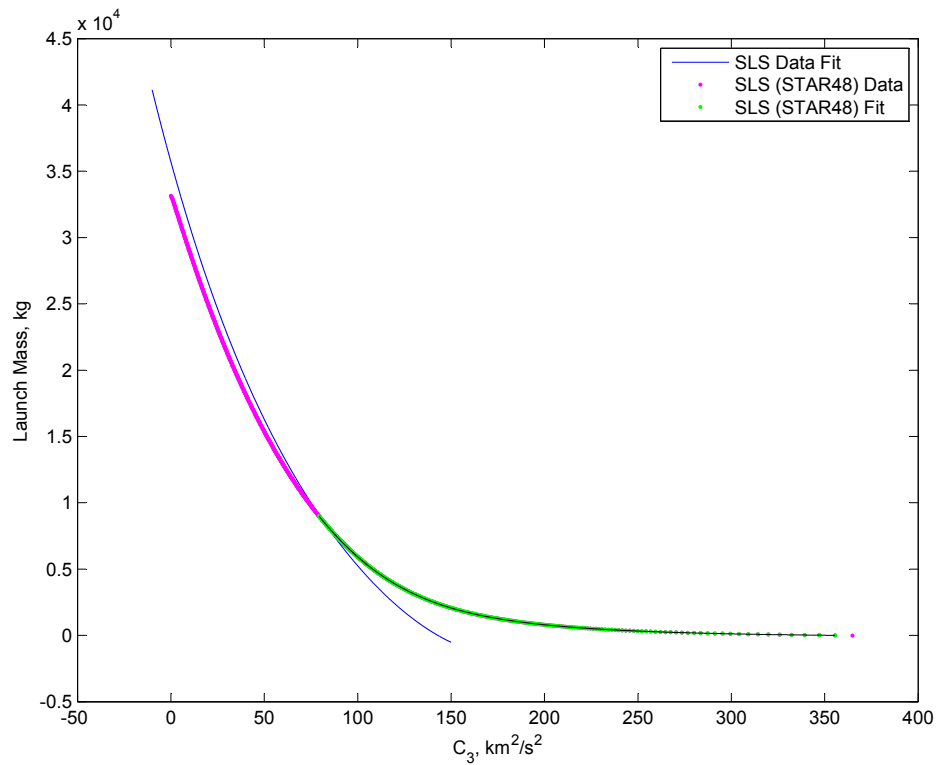
Figure 2.8.: Performance curve for SLS Block 1B launch vehicle. The blue curve is the unmodified performance curve, and the magenta and green points represent the modified performance data with the STAR 48 additional upper stage. The green portion of the modified performance data represents the portion used to fit an 8th-order polynomial curve.

3. CATALOG OF TRAJECTORIES TO URANUS FROM 2024 TO 2038 INCLUDING AN OPPORTUNITY FOR A SATURN PROBE

In 1986, the Voyager 2 spacecraft achieved the only close encounter with Uranus, followed in 1989 by a flyby of Neptune. These two Ice Giants remain among the least known planets of our Solar System, and are the only class of planet never to have been explored in detail. In this chapter, we investigate multiple gravity-assist trajectories (with impulsive, chemical propulsion maneuvers) to Uranus that explore 89 combinations of gravity-assist paths, using Venus, Earth, Mars, Jupiter, and Saturn. We consider launch dates spanning from January 2024 to December 2038 with step sizes of 5 days. We use a patched-conic model with an analytic planetary ephemeris to calculate the trajectories. The launch vehicles considered are the Space Launch System (SLS) Block 1B, Atlas V 551, and Delta IV Heavy. Trajectories that can deliver at least 2000 kg of payload in orbit about Uranus in minimum time are cataloged for each launch year. A preliminary catalog of candidate trajectories that use aerocapture at Uranus is also provided. Of the 89 total gravity-assist paths searched, 26 include a flyby of Saturn. The alignment of Saturn and Uranus only occurs every 45 years, and provides a rare opportunity for a Saturn-Uranus mission. A trajectory in 2028 is identified as an attractive candidate for such a mission—delivering a probe at Saturn, as well as a probe and orbiter at Uranus.

3.1 Background

A Uranus orbiter and probe mission (with no solar electric propulsion stage) is stated in the Decadal Survey for 2013–2022 [12] to be the third highest priority for

a Flagship-class mission, and it is recommended (in the survey) that such a mission should be selected even if the other two higher-priority missions are selected. The two higher-priority missions, now called Mars 2020 and the Europa Clipper (or Flyby) have indeed been selected by the time of writing this thesis, and it is likely that the Uranus orbiter and probe mission will be one of the highest (if not the highest) priority for a Flagship-class mission for the next Decadal Survey (beyond 2022).

More recently (to the time of writing this work), at the August 2015 meeting of the Outer Planets Assessment Group, NASA's Planetary Science Division announced the initiation of an Ice Giants Study for a Flagship-class mission. The JPL-lead study is to be part of the next Decadal Survey (beyond 2022) [13].

The announcement of the Ice Giants Study specified, as part of its objectives, to identify enabling technologies, and assess the capabilities afforded by the SLS [13]. This work identifies mission opportunities to Saturn and Uranus, which would be enabled with the use of the SLS Block 1B, without the use of technologies such as low thrust or aerocapture. This mission would not only send a probe and orbiter to Uranus, but also a probe to Saturn.

In 2011, Spreen et al. [14] investigated ballistic trajectories to Uranus between 2020 and 2060. In their paper, they state that their best case is a trajectory with launch date on Feb. 14, 2044 that, using an Atlas V 551 launch vehicle, can deliver just over 2.1 Mg of payload into a 200-day orbit about Uranus, with an Earth-Uranus flight time of 15.0 years. Between the launch dates of 2024 and 2038 (the years under consideration for this paper), the best case found by Spreen et al. can deliver 1.4 Mg of payload to Uranus (into a 200-day orbit) in 14.7 years, with launch date Oct. 5, 2029. Although the trajectories found by Spreen et al. are capable of delivering a sufficient amount of payload for a Uranus orbiter, the time to reach Uranus (of about 15 years) is long.

Also in 2011, Dankanich and McAdams [15] investigated low-thrust trajectories to Uranus for the 2013-2022 decadal survey. The recommended trajectory found in their study, launched in 2019, had a 13-year Earth-Uranus transfer time, and was

capable of delivering over 2 Mg into orbit about Uranus. This trajectory used solar electric propulsion (SEP) and an Atlas V 551 launch vehicle.

In 2009, Landau et al. [16] conducted a search of low-thrust trajectories to Uranus and Neptune with launch dates ranging from 2015 and 2035. Using SEP and an Atlas V 551 launch vehicle, they found trajectories launching in 2020 that could deliver as much as 1.5 Mg into an orbit about Uranus, with an Earth-Uranus transfer time of 10 years. Their study also estimated that, if aerocapture were used (assuming the thermal protection system, or TPS, takes up 50% of the spacecraft mass at Uranus arrival) over 2 Mg of delivered mass could be placed in orbit at Uranus within a flight time of 10 years. These aerocapture trajectories also use SEP, and an Atlas V 551 launch vehicle.

Several other Uranus mission studies have been conducted that investigate both ballistic, chemical-propulsion trajectories, and low-thrust trajectories [17–27].

3.2   Methods

3.2.1   Computing the Trajectory Design Space

The sweeping search of trajectories that are used to construct the catalogs presented in this paper, are computed using the program STOUR [3, 28, 29]. STOUR is a patched-conic propagator with an analytic planetary ephemeris that can rapidly calculate thousands gravity-assist trajectories. The program imposes a grid search of all candidate trajectories by stepping through specified launch V_∞ and launch dates (between January of 2024 through December of 2038 in 5-day increments).

When selecting the combinations of flyby bodies in this work, Venus, Earth, Mars, Jupiter, and Saturn are considered. Mercury is not, however, since its low mass and close proximity to the Sun make it a poor body for useful gravity assist. Only Venus, Earth and Mars are considered for repeated flybys of the same body, since doing so at the outer planets would result in TOFs exceeding our imposed constraint of 15

years. Once a flyby of an outer planet has occurred, only planets farther out from that body are considered for subsequent flybys.

Within the rules specified in the previous paragraph, all combinations of flyby bodies are investigated for up to 3 total flybys (excluding Earth launch and Uranus arrival). For sequences of four flyby bodies, only paths from previous studies were considered. For example, all paths from the work by Petropoulos et al. [53] (for trajectories to Jupiter) were investigated, with the modification of adding Neptune as the final body after the Jupiter encounter. Flyby paths from Spreen et al. [14] were also investigated. The complete list of gravity-assist paths investigated is:

Direct, V0, 0E0, M0, J, S, VV0, VE0, VM0, V0J, V0S, 0EV0, 0EE0, 0E0M, 0E0J, 0E0S, MV0, ME0, MM0, M0J, M0S, JS, VVV0, VVE0, VVM0, VV0J, VV0S, VEV0, VEE0, VEM0, VE0J, VE0S, VMV0, VME0, VMM0, VM0J, VM0S, V0JS, 0EE0J, 0E0MJ, 0E0MS, 0E0JS, MVV0, MVE0, MVM0, MV0J, MV0S, MEV0, MEE0, ME0M, ME0J, ME0S, MMV0, MME0, MMM0, MM0J, MM0S, M0JS, VVV0J, VVV0S, VVE0J, VVE0S, VVMV0, VV0MJ, VV0MS, VEEE0, VEEM0, VEE0J, VEE0S, VEME0, VEM0J, VMV0J, MEE0J, MEE0S, VVEE0J, VEVE0J, VEVE0S, VEEE0J, VEEE0S, VEE0MJ, VEE0MS, VEME0J, VEME0S, VMVE0J, VMEE0J, VMEE0S, MEVE0J, MEME0J, and MEME0S

where "Direct" denotes a direct launch to Uranus from Earth, and V, E, M, J, and S denote a flyby of Venus, Earth, Mars, Jupiter, and Saturn, respectively. All paths launch from Earth and arrive at Uranus. A "0" between two flybys, or between the last flyby and Uranus arrival, denotes an impulsive maneuver, which is implemented by STOUR's "maneuver algorithm" developed by Patel [29]. The maneuver algorithm applies powered flybys and broken plane or "mid-course" maneuvers [29]. A "0" at the start of the path indicates a maneuver is done before the first encounter; specifically, at aphelion of a near resonant orbit to leverage the energy change at the subsequent gravity assist: a maneuver called "V_∞ leveraging" [31–33].

Before analyzing a gravity-assist path in STOUR, it is first checked using a Tisserand graph, to determine whether the path is possible with regards to orbital energy

(i.e. to see if it has sufficient energy to reach Uranus). All flyby paths identified as infeasible by the Tisserand graph are eliminated from the list of possible candidates.

For the remaining possible candidate gravity-assist paths, STOUR is used to solve the phasing problem, and determine which of these paths produce trajectories to Uranus.

In practice, there are several constraints that limit the solution space, such as minimum flyby altitude for a given flyby body, maximum TOF for the full trajectory to Uranus, and maximum launch V_∞. A summary of the constraints imposed on the trajectories considered for this broad search study are shown in Table 3.1.

Table 3.1.: Trajectory Search Constraints

Parameter	Value
Minimum flyby altitude	300 km (Venus and Earth), 200 km (Mars), 100k km (Jupiter), 50k km (Saturn and Uranus)
Maximum TOF	15 yr
Maximum launch V_∞	20 km/s (Direct Launch), 17 km/s (1 flyby), 12 km/s (2 flybys), 9 km/s (3 flybys), 7 (4 and 5 flybys)
Maximum maneuver ΔV	3 km/s

For the case of minimum flyby altitudes used, our goal is to avoid interaction with the flyby body's atmosphere, as well as collisions with the body's rings (whenever applicable). Since the outer planets can potentially provide a significant energy increase during a flyby, minimum altitudes were chosen just below the outer most (prominent) ring altitude to ensure that no trajectory opportunities are missed. The total TOF for each trajectory was limited to 15 years based on previous decadal studies [22,34].

To determine the maximum allowed launch V_∞, many factors were considered. First and foremost, the goal in choosing these launch values is to encompass all foreseeable mission types to Neptune during the 2020 to 2070 time frame. Such mission types include both flyby and capture missions (although capture missions are

the focus of this work), as well as low and high payload mass missions. Additionally, the general reason for using gravity assist bodies (and adding the complexity to the interplanetary trajectory) is to reduce the required launch V_∞ while still gaining sufficient orbital energy to reach the target body (provided by the gravity assists). Therefore, the maximum launch V_∞ considered is reduced for this analysis as more flyby bodies are added to the path.

As an example of a single flyby body path, the New Horizons spacecraft trajectory (an earlier version of which is noted by Patel [29]) launched with a V_∞ of about 16 km/s, and then flew by Jupiter on its way to Pluto. Using New Horizons as a reference, a maximum launch V_∞ of 17 km/s was chosen for all paths with only one flyby body, and 20 km/s was used for direct launch to Uranus. For two, three, and four flyby bodies, the maximum launch V_∞ values used by Landau et al. [16] were first considered for this study; however, for the case of three and four flyby bodies, some example simulations indicated that slightly larger launch V_∞ values provided a sizable increase in opportunities to the Ice Giants. Thus, for paths containing three or four flyby bodies, the maximum launch V_∞ values chosen are slightly larger than those used by Landau et al. All cases considered for 5 flyby bodies are modifications of select 4-flyby body paths (e.g. adding a Mars flyby after an Earth or Venus flyby on route to an outer planet); and thus, use the same launch V_∞ as paths with 4 flyby bodies, of 7 km/s.

We note that STOUR is not an optimization tool. It does not find the optimal deep-space maneuver (DSM) locations and encounter dates to maximize delivered mass. STOUR computes thousands of trajectories to reveal a grid of the solution space. Attractive trajectories are then initially characterized by those that can deliver a targeted amount of mass in orbit at Uranus in minimum time (of the solutions found in STOUR). We do this by plotting all solutions' TOF versus delivered mass, and identifying the best cases from the plot. This optimization can be more formally described as identifying the nondominated Pareto optimal set of solutions, with flight time and delivered mass as the optimization objectives.

3.2.2 Defining the Capture Science Orbit and Estimating the Delivered Mass

The launch vehicles we consider for the trajectories found are the Space Launch System (SLS) Block 1B, Atlas V 551, and Delta IV Heavy. The launch data for the Atlas V 551 and Delta IV Heavy are available on the NASA Launch Vehicle Performance website*. The performance of the SLS is approximated based on the data provided in [35].

To compute the delivered mass in orbit at Uranus, a science orbit is assumed with an orbital period of 20 days, and a periapsis of 52,000 km to avoid Uranus' rings. The 20-day science orbit is chosen based on previous decadal studies [22, 34], as well as our own assessment, by observing the variations in capture ΔV for various orbit sizes and various arrival V_∞ at Uranus. Figure 3.1 illustrates the ΔV required for capture at Uranus for various science orbit sizes and various arrival V_∞. The solid lines represent capture inside the rings of Uranus, at an altitude of 3000 km. The dotted lines represent capture at a radius of 52000 km, just outside the major rings (as done in Ref. [22]). At the time of writing this work, it was not yet known if the risks of capture inside the rings would be tolerable for a Uranus mission. Thus, to be conservative regarding delivered mass values, (an to be consistent with Ref. [22]) only capture outside the rings was considered. The figure shows that for all arrival V_∞, the capture ΔV spikes for capture orbits just below about 20-days. From these results (and to be consistent with Refs. [22] and [34]), a 20-day science orbit is used for all capture orbits in this work.

The thruster characteristics used for the impulsive DSMs and capture at Uranus, are based on those used by Landau et al. [16], with an Isp = 323 s, and a propellant mass penalty (to estimate the tank and structure mass) of 12%.

---

*https://elvperf.ksc.nasa.gov/Pages/Default.aspx
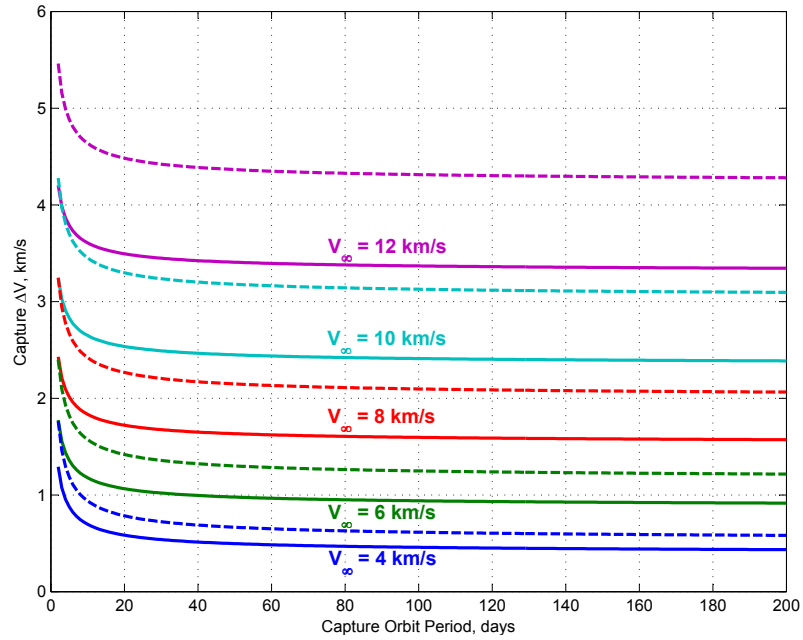
Figure 3.1.: Capture ΔV at Uranus for various science orbit sizes and arrival V_∞. The solid lines represent capture inside the rings of Uranus, at an altitude of 3000 km. The dotted lines represent capture outside the major rings, at a radius of 52000 km.

3.2.3 Investigating Select Cases

Once attractive trajectories are identified, the maneuver locations and encounter dates are optimized using trajectory optimization tools such as the Mission Analysis Low-Thrust Optimization (MALTO) tool [36, 37], or the Evolutionary Mission Trajectory Generator (EMTG) [38–46], to improve the solution in terms of delivering the maximum mass in minimum time.

Next, the encounter conditions for an orbiter and probe are modeled using MATLAB to compute and visualize the design space of hyperbolic approach trajectories. The goal is to quickly assess the feasibility of a selected trajectory when considering factors such as ring avoidance, probe entry speed, line of sight between probe and orbiter, as well as between the orbiter and Earth. For the case of ring avoidance for probe entry, the visualization allows the designer to quickly adjust the approach trajectory, by adjusting the angle (ψ) about the arrival-V_∞ vector. This adjustment

is illustrated in Fig. 3.2, where the approach trajectory must be rotated slightly below the minimum inclination approach (which would provide the minimum entry speed) in order to ensure that the probe enters before crossing the ring plane—all of which can be adjusted by inspection. By providing a visualization, one does not need to understand the formulation of the trajectories to spot potential issues with the design, which is conducive for collaborative mission designs with contributors from a diverse set of disciplines.
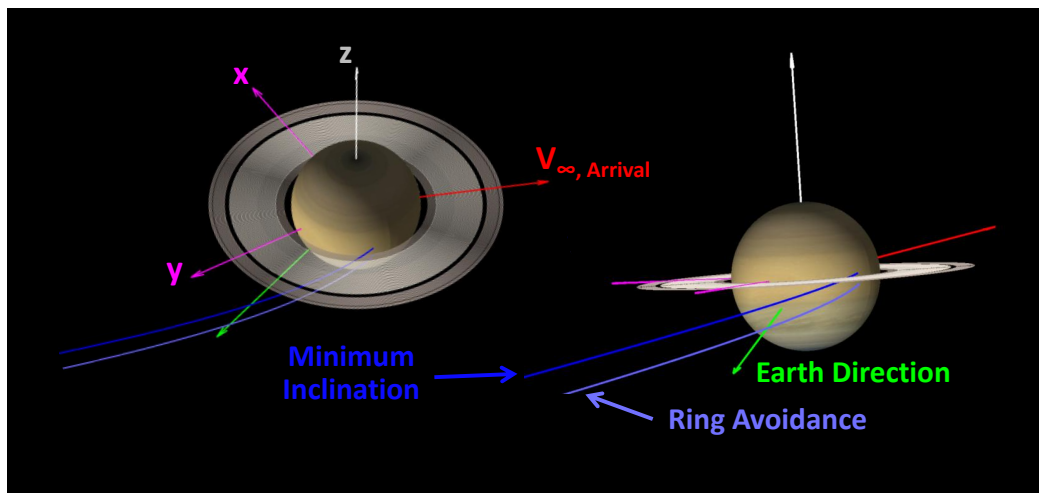
Figure 3.2.: Using visualization tool to adjust a Saturn probe approach trajectory for ring avoidance by inspection.

The visualization is a useful learning tool to better understand the challenges for a mission, as well as serve as a "sanity check" for any major issues with the encounter. For example, the two trajectories shown in Fig. 3.3 illustrate two different trajectories that fly by Saturn on route to Uranus. For both trajectories, the probe must approach Saturn so that it enters prograde with Saturn's spin, to reduce its atmosphere-relative entry speed. The spacecraft on the other hand, must fly by depending on the conditions required by its interplanetary trajectory, to encounter Uranus. For the trajectory in Fig. 3.3(a) however, the flyby conditions require the spacecraft to approach Saturn on the opposite side of the planet as the probe. This interference in line-of-sight between probe and spacecraft will prevent the probe from

sending its data to the spacecraft as it enters Saturn. To mitigate such an issue, the probe must send its data directly to Earth, which requires more transmission power, and possibly a much larger antenna, which may not be possible to accommodate. The geometry in Fig. 3.3(b) however, allows the spacecraft to approach Saturn on the same side as the probe, and; therefore, maintain line-of-sight between the probe and spacecraft throughout probe entry and descent into Saturn's atmosphere.

(a)	(b)
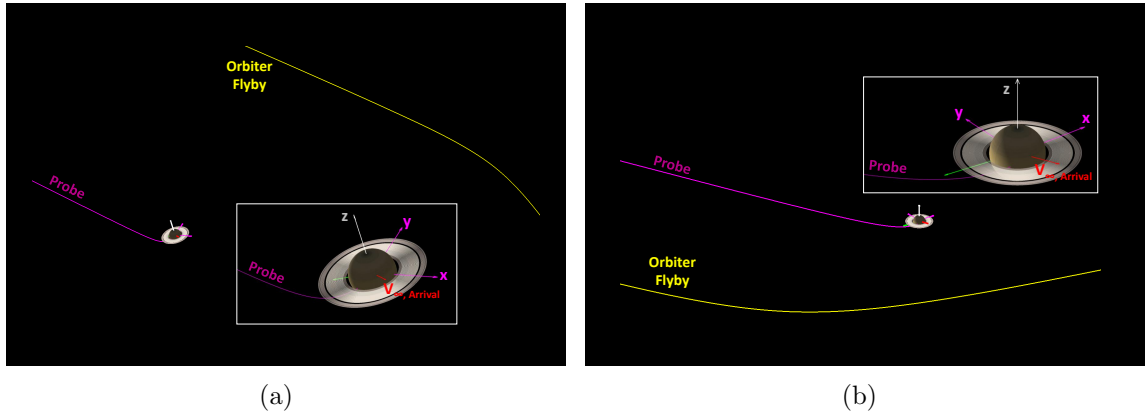
Figure 3.3.: Saturn flyby trajectories with atmospheric probes. The visualization shows that the probe-spacecraft line-of-sight is lost for the trajectory on the left, causing data link difficulties that may have no feasible design solution.

We will show in this work that the trajectory search results find solutions that can deliver over 2000 kg into a capture orbit at Uranus, and many of these trajectories fly by Saturn. Using this knowledge, we target a mass of about 2000 kg in orbit at Uranus with 600 kg reserved for a Uranus and Saturn probe, which we estimate to be conservative (based on estimates for a Uranus orbiter and probe in Ref. [22] and Saturn probe in Ref. [47]) for a multi-planet, Saturn-Uranus mission. In such a mission, a probe can be delivered at Saturn during the flyby, and a probe and orbiter can be delivered at Uranus. For these trajectories, the hyperbolic approach trajectories at both Saturn and Uranus are modeled to assess the feasibility of the trajectory for such a mission.

3.3   Cataloging Trajectories to Uranus

For each trajectory found using STOUR, the mass the trajectory can deliver into orbit at Uranus is calculated for a specified launch vehicle. To give a sense of the trajectory solution space, Fig. 3.4 shows the TOF vs. delivered mass using the SLS Block 1B launch vehicle. In the figure, each dot represents a trajectory to Uranus, and the color corresponds to the gravity-assist path in the legend, where, the "U" at the end of each path represents arrival at Uranus (rather than a flyby).

Due to the large number of paths found, the colors in Fig. 3.4 are difficult to distinguish between adjacent paths in the legend; however, the purpose in showing this legend is more to give a sense of which paths found results, rather than to identify which path corresponds to a particular dot. Regardless of the specific path used, the figure shows that using the SLS, trajectories that deliver 2000 kg will take about 9 years to capture at Uranus; however, if a TOF of 14 years is acceptable, about 15,000 kg can be delivered. In general, the trajectories of interest on this plot are those that lie on the right diagonal edge of the data set (called the Pareto front), since these are the cases that can deliver a specified amount of mass in the least amount of time. The overall trend of this front, suggests that longer flight times are required to deliver more mass (for up to a 15-year TOF).

We note that if an additional upper stage is used (such as a STAR 48 engine), trajectories become avail-able that have higher launch C3 than those shown in Fig. 3.4. These high C3 trajectories are shown in Fig. 3.5. We also note that because the SLS launch vehicle is by far the most capable considered in this study, a subset of the trajectories found using the SLS (with smaller delivered mass values) are available if other launch vehicles are used, such as the Delta IV Heavy or the Atlas V 551.

One difficulty with the results shown in Figs. 3.4 and 3.5, is that the launch date is not visible. Furthermore, many mission proposal calls require that launch occurs during a specified year. To resolve this issue, Tables 3.2–3.4 show catalogs of the most attractive trajectories (in terms of delivered mass and TOF) for each launch year. In
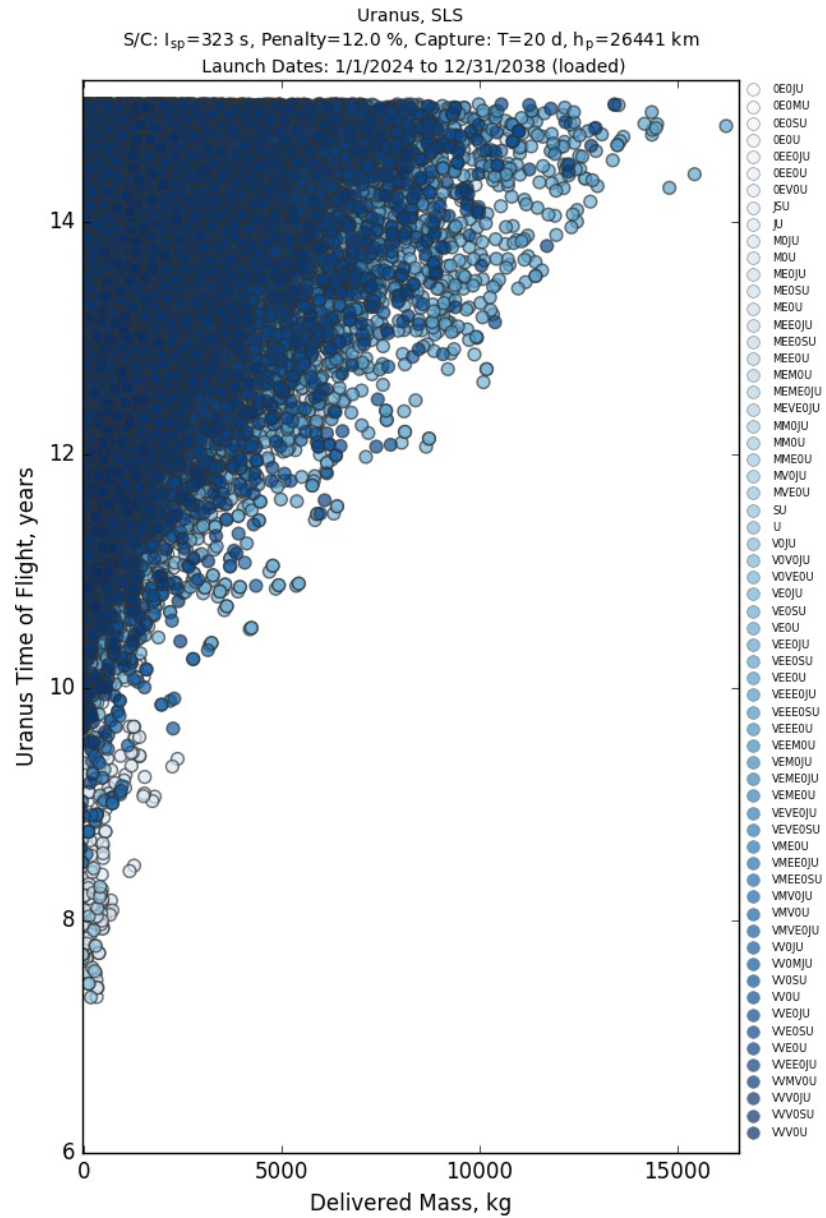
Figure 3.4.: Trajectories to Uranus using SLS Block 1B.

these tables, we select for each launch year, the trajectory(ies) that can deliver at least a mass of about 2000 kg to Uranus in minimum time. These trajectories are found by first computing the delivered mass for a selected launch vehicle, for all trajectories found. We then isolate the data to only contain solutions within a selected launch year, and then compare the TOF and delivered mass for that subset.
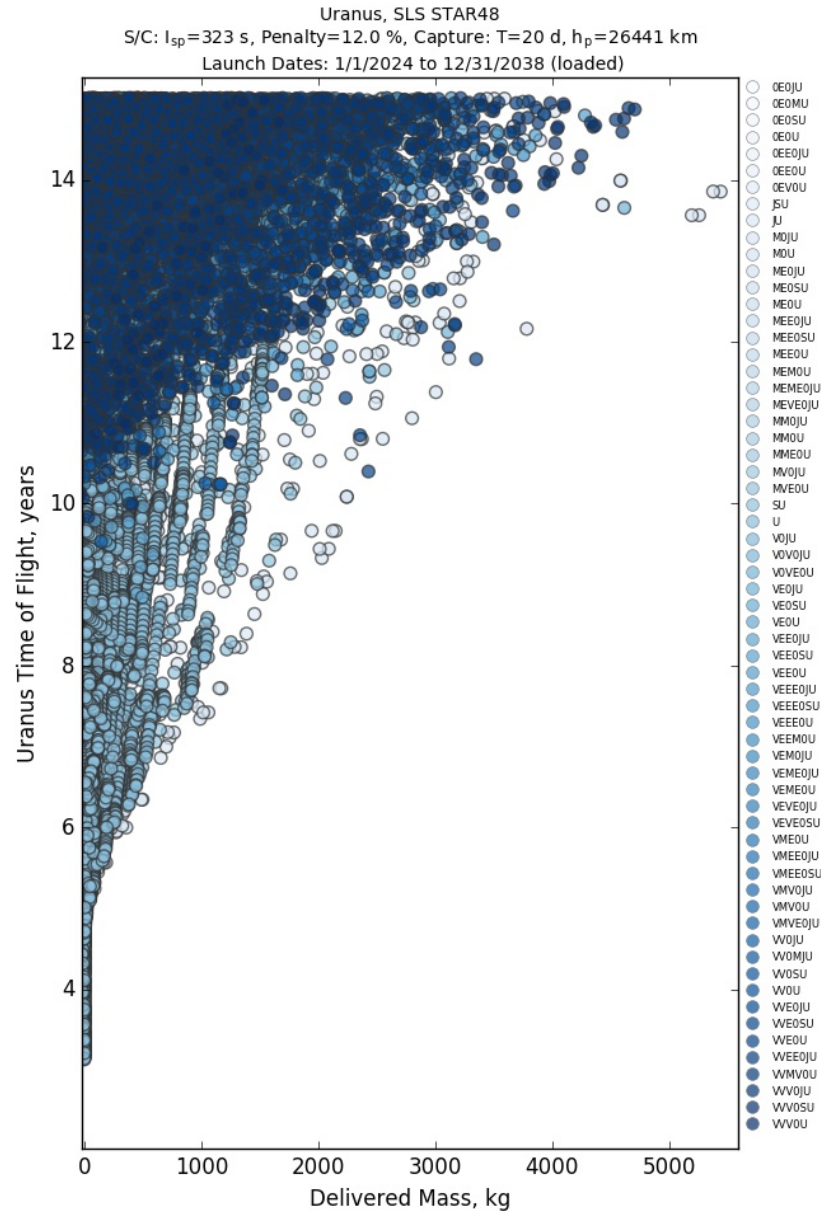
Figure 3.5.: Trajectories to Uranus using SLS Block 1B with STAR-48 as additional upper stage.

We note that for some years, the case(s) that can deliver at least 2000 kg with the shortest TOF, may deliver much more than the desired 2000 kg. In other cases, masses of about 1500 kg could be delivered for significantly less TOF (than those requiring 2000 kg), and are also recorded in the table. Of course, these lower delivered-mass trajectories would be for a mission that allows for a less massive spacecraft design.

Table 3.2.: Uranus Trajectory Catalog: SLS Block 1B

Launch Date	Flyby Path	TOF, yrs	Mass, Mg	Prop. Mass, Mg
05/20/2024	0E0SU	12.1	3.0	12.9
02/19/2025	VEE0SU	11.4	2.4	22.2
03/01/2025	VEE0U	11.5	2.9	21.7
04/01/2026	VEE0SU	11.8	2.0	24.5
06/19/2026	0E0SU	11.9	4.1	11.7
07/09/2026	0E0SU	10.9	**1.3	10.3
07/04/2027	0E0SU	12.4	3.8	12.0
03/20/2028	VEE0U	11.9	2.4	22.2
09/21/2028	0E0SU	11.3	2.0	14.2
07/25/2029	*SU	9.5	**1.6	1.4
10/26/2029	VEE0JU	11.2	2.1	26.1
01/24/2030	VEE0JU	11.1	2.0	22.6
08/04/2030	*SU	9.5	**1.6	1.4
12/20/2030	VE0JU	11.2	2.6	23.9
07/08/2031	VE0JU	10.4	3.2	19.5
12/11/2032	VV0JU	9.6	2.3	16.4
04/28/2033	M0JU	9.3	2.2	14.3
08/03/2034	0E0U	11.1	2.1	13.7
08/08/2035	0E0U	11.1	2.1	13.8
08/12/2036	0E0U	11.0	2.0	13.8
08/28/2036	*JU	11.2	2.5	1.3
08/23/2036	*JU	8.6	**1.5	1.5
08/05/2037	ME0U	10.9	2.6	11.9
08/22/2037	*M0U	9.3	2.0	1.8
09/11/2037	*M0U	9.0	**1.6	1.4
02/08/2038	VVE0U	11.4	2.1	18.6
08/22/2038	0E0U	11.0	2.0	13.9

*Uses STAR 48 as additional upper stage.
**Delivers well under 2 Mg.

Delivered masses of about 1800 kg or more may be reported as well that are expected to meet or exceed 2000 kg after optimization in a program such as MALTO.

The purpose of these tables is to allow systems engineers, scientists, and any other interested individuals the ability to quickly get a sense of what flight times and masses are feasible (using chemical propulsion) for a Uranus orbiter mission within a given launch year. For mission designers, these results may help to identify rare planetary

Table 3.3.: Uranus Trajectory Catalog: Delta IV Heavy

Launch Date	Flyby Path	TOF, yrs	Mass, Mg
12/21/2024	VEE0U	13.6	2.1
06/04/2025	0E0SU	14.6	2.1
10/02/2026	VEE0U	12.7	**1.5
10/02/2026	VEE0U	13.4	2.5
11/26/2027	VVEE0JU	14.5	2.3
02/24/2028	VEE0U	13.8	1.9
04/14/2028	VE0JU	14.2	2.2
10/16/2029	VEE0JU	11.8	**1.4
10/16/2029	VEEE0JU	12.4	1.9
01/04/2030	VEE0JU	13.1	2.3
12/10/2030	VVE0JU	12.1	**1.6
07/18/2031	VE0JU	10.9	**1.5
07/23/2031	VE0JU	12.1	2.4
11/19/2032	VEEM0U	12.4	**1.4
12/16/2032	VV0JU	13.2	2.0
03/19/2033	VEE0JU	13.6	2.0
04/08/2033	VEEM0U	12.2	**1.4
01/28/2034	VEE0U	13.8	2.2
04/05/2034	VEE0U	13.0	**1.6
12/26/2035	VEE0U	13.7	2.0
01/08/2036	VEME0U	13.8	2.0
08/17/2036	0E0U	12.2	**1.3
11/08/2037	VEE0U	13.0	2.1
01/19/2038	VVE0U	12.9	1.9
02/23/2038	VEE0U	12.2	**1.4

*Uses STAR 48 as additional upper stage.
**Delivers well under 2 Mg.

alignments for gravity assist (such as an alignment of Mars with Jupiter, Saturn, or Uranus) that may have otherwise gone unnoticed.

Some launch years contain multiple solutions for a few reasons. One reason is that different gravity-assist paths may be more or less desirable depending on the details of the mission design; therefore, multiple trajectories may be listed for a given launch year if the solutions in question can deliver a similar amount of mass in a similar (minimum) time, but have differing gravity-assist paths. Another reason for

Table 3.4.: Uranus Trajectory Catalog: Atlas V 551

Launch Date	Flyby Path	TOF, yrs	Mass, Mg
11/26/2024	VEE0SU	14.8	**1.4
11/11/2025	VEE0U	15.0	**1.2
10/07/2026	VEE0U	14.3	1.9
11/16/2027	VVEE0JU	14.9	**1.4
02/29/2028	VEEE0JU	14.5	**1.4
10/31/2029	VEE0JU	14.3	2.4
01/04/2030	VEE0JU	14.8	2.0
02/23/2031	VEE0JU	14.4	2.4
07/28/2031	VE0JU	14.2	2.0
06/07/2032	VEEM0U	14.7	1.8
12/24/2033	VEE0U	14.6	**1.4
01/03/2034	VEE0U	14.8	**1.5
12/26/2035	VEE0U	14.9	**1.3
01/25/2036	VEE0U	14.7	**1.4
11/13/2037	VEE0U	14.4	1.9
02/08/2038	VEE0U	15.0	**1.4

*Uses STAR 48 as additional upper stage.
**Delivers well under 2 Mg.

listing multiple trajectories for the same launch year is due to the fact that the solutions in the tables are not optimized in terms of DSM location or encounter date. Since each individual trajectory may be improved using an optimization tool such as MALTO, additional solutions may be listed within the same launch year if significant improvement is expected (after optimization in MALTO) for a trajectory that may otherwise appear less capable than other "best case" STOUR results listed in the table for that year. Lastly, targeting a mass of 2000 kg is a best estimate of an orbiter and probe mass based on previous decadal studies (such as in Ref. [22]). If trajectories are identifies in a particular launch year that can deliver substantially more mass with a moderate increase in flight time (over the 2000 kg case), then such a trajectory will also be recorded in the table. For example, one such case in Table 3.2 with 6/19/2026 launch date can deliver about 2100 kg more than the targeted

2000 kg case (on 4/1/2026) with only 0.1 more years of flight time using a different gravity assist path.

To build the catalogs and select the best cases, we use a Python script (which we call the STOUR Utility) that reads in and stores the output data from all STOUR runs and allows us to sort the data in post and calculate delivered mass (for an assumed launch vehicle, DSM I_{sp}, and capture orbit). The STOUR Utility also allows us to generate plots, such as those shown in Figs. 3.4 and 3.5, where a point can be selected in the figure to examine the complete list of trajectory characteristics, such as encounter dates and velocities, ΔV magnitudes, etc. When selecting the cases for the catalog, the plotted data is isolated to a single launch year.

Examining the results in Tables 3.2–3.4, if a delivered mass of 2000 kg or more is required, the shortest TOF provided by the SLS is 9.3 years, which occurs both in 2033 and 2037. For the Delta IV Heavy, the shortest TOF solution is 12.1 years with launch in 2031. If a smaller delivered mass can be designed for a given mission, the SLS can deliver 1500 kg in only 8.6 years launching in 2036, and the Delta IV Heavy can deliver 1500 kg in 10.9 years, launching in 2031. For the Atlas V 551, a TOF of 14–15 years is required regardless of whether 1500 kg or 2000 kg of delivered mass is desired. In all cases, these solutions may be improved after being optimized in a tool such as MALTO.

Since many of the solutions that launch using the SLS require a large amount of propellant mass, we include this value for the SLS results in 3.2. The amount in the table ranges from 1.3 Mg to 26.1 Mg, which is directly related to the required launch C_3 for the trajectory. For lower C_3 trajectories, the SLS can lift more mass, and since we are targeting a delivered mass of 2000 kg, the rest of the launch mass is then devoted to propellant. Additionally, the lower C_3 solutions (and thus high propellant mass solutions) are more common for trajectories with multiple gravity assists (particularly of the inner planets), where the gravity assists and DSMs are increasing the spacecraft's energy—work that would otherwise be done by the launch vehicle. Thus, if the propellant mass must be limited for a particular mission design,

the SLS is most effective when launching into trajectories that require high C_3, which typically occurs for solutions that only have one flyby (at Jupiter or Saturn) on route to Neptune. Since the high C_3 solutions are also those where the STAR 48 is most effective, trajectories that use a STAR 48 require less propellant mass than those without a STAR 48.

To accommodate missions that may require smaller propellant mass values, Table 3.5 shows the catalog of trajectories to Uranus with solutions restricted to only those with a propellant mass of 5000 kg or less (including the imposed 12% propellant mass penalty). An interesting trend in the results is that a gravity assist at Saturn and sometimes no gravity assist provides the better solution, even during years when Jupiter is available. This trend is suspected to be a direct consequence of needing higher C_3 solutions to reduce the amount of propellant mass required, as a Saturn flyby (and no flybys) will certainly more often require higher C_3 than that of a Jupiter flyby trajectory. Another factor that may be at play is the logic used in this study to select attractive trajectories, where we search for solutions with minimum flight time, and short flight-time solutions often require high C_3. Short flight time solutions also typically have higher arrival V_∞ as well; however, since we are capping the allowed amount of propellant used, the capture maneuver is indirectly limited, which in turn limits the solution set to those with smaller arrival V_∞.

The delivered mass calculations also assume that the launch vehicle is delivering the maximum amount of mass for a given launch C_3; which may not be implemented in practice if the total amount of propellant mass is constrained. For example, the trajectory shown in Table 3.5 delivers 4.0 Mg of payload in orbit at Uranus, which is well over the target value of 2 Mg. If the delivered mass for this same trajectory were to be fixed at 2 Mg, the corresponding launch mass required to deliver the 2 Mg (rather than the 4.0 Mg shown in the table) will be reduced; thereby reducing the required propellant mass, without modifying any of the trajectory characteristics.

The catalogs in Tables 3.2–3.4 also reveal when certain bodies are available for gravity assist. For example, if Uranus is to be reached in less than 14 years using

Table 3.5.: Uranus Trajectory Catalog: SLS Block 1B—5 Mg or Less of Propellant

Launch Date	Flyby Path	TOF, yrs	Mass, Mg	Prop. Mass, Mg
07/24/2024	*U	11.3	**1.5	0.9
05/30/2025	*SU	11.2	**1.5	1.5
12/16/2025	*VEEE0U	14.7	2.5	4.7
06/05/2026	*SU	10.4	**1.5	1.5
06/10/2026	*SU	13.8	2.2	0.8
06/15/2027	*SU	11.1	1.8	1.2
07/04/2028	*SU	11.6	2.6	1.2
07/14/2028	*SU	10.5	1.8	1.2
07/10/2029	*SU	9.0	**1.5	1.5
07/15/2029	*SU	12.1	2.7	1.1
11/25/2029	VVV0JU	13.9	4.0	4.8
07/30/2030	*SU	9.3	**1.6	1.4
08/09/2030	*SU	11.4	2.0	1.0
11/15/2030	VE0JU	13.6	4.6	4.1
03/15/2031	*M0JU	12.0	2.7	4.5
08/14/2031	*SU	11.0	1.9	1.1
08/28/2032	*SU	13.5	2.0	1.0
08/31/2032	*U	11.7	**1.5	0.8
12/11/2032	VEE0U	14.8	4.3	4.4
09/05/2033	*U	11.8	**1.5	0.8
11/24/2033	*VEEM0U	14.3	3.8	4.9
01/23/2034	*VEE0U	14.5	3.9	4.8
09/10/2034	*U	11.6	**1.5	0.8
09/15/2035	*U	11.7	**1.5	0.8
08/23/2036	*JU	8.6	**1.5	1.5
08/28/2036	*JU	11.2	2.5	1.3
08/22/2037	*M0U	9.3	2.0	1.8
09/29/2038	*U	11.4	**1.5	0.8
10/19/2038	*ME0U	14.5	2.5	4.7

*Uses STAR 48 as additional upper stage.
**Delivers well under 2 Mg.

either the SLS or the Delta IV Heavy, Jupiter is not available for gravity assist until about 2029, where it then remains available until the early to mid 2030s. While Jupiter is unavailable in the near term, Saturn happens to be in good position for gravity-assist (using the SLS Block 1B) from the early 2020s until about 2029.

From the synodic period of Saturn and Uranus, the favorable alignment of these two planets for gravity assist only occurs about every 45 years. Considering this rare, near-term opportunity, which has trajectories in the 2020s capable of delivering over 2000 kg at Uranus, a two-planet mission may be possible, using current or near-term technology. Such a mission could deliver a probe at Saturn, as well as a probe and orbiter at Uranus.

Of course, other two-planet opportunities could be considered, such as a Jupiter-Uranus or a Venus-Uranus mission; however, the Jupiter-Uranus and Venus-Uranus alignments are much more frequent than that of Saturn-Uranus. The Jupiter-Uranus and Venus-Uranus alignments repeat about every 14 years, and every 2 to 3 years, respectively. By comparison, the Saturn-Uranus alignment is much more rare (occurring nearly once in a lifetime), and so we focus on the Saturn-Uranus trajectories for such a two-planet mission in this paper.

If we select Saturn as our flyby target of scientific interest, we then only consider Uranus trajectories that include Saturn as a flyby body. The best of these trajectories (in terms of shortest TOF to deliver at least 2000 kg of mass) are given in the catalogs shown in Tables 3.6 and 3.7, for the SLS Block 1B and the Delta IV Heavy, respectively.

In Tables 3.6 and 3.7, the reported delivered mass is the mass leftover for an orbiter, after Uranus orbit insertion (UOI). In calculating this adjusted delivered mass number, we assume that 600 kg is dropped prior to UOI, which is allocated to a combined probe mass for the Saturn probe and Uranus probe (which are both released prior to UOI). This 600-kg combined probe mass is expected to be conservative, based on a 230-kg Saturn probe mass estimate in Ref. [47].

For some years, there are no trajectories that can deliver an orbiter mass of about 2000 kg. In these cases, we report the trajectory that delivers the most mass for that year. No solution is reported if the computed orbiter mass is below 1000 kg. For this reason, some years for the SLS Block 1B and Delta IV Heavy have no reported

Table 3.6.: Saturn-Uranus Trajectory Catalog: SLS Block 1B

Launch Date	Flyby Path	TOF, yrs	Mass, Mg	Prop. Mass, Mg
05/15/2024	0E0SU	11.5	**1.6	14.4
05/20/2024	0E0SU	12.2	2.8	13.0
02/24/2025	VEE0SU	11.3	2.0	24.5
06/24/2025	0E0SU	11.2	1.7	10.0
06/19/2026	0E0SU	11.8	3.8	12.1
06/15/2027	*SU	11.1	**1.5	1.5
07/04/2027	0E0SU	12.3	3.4	12.4
07/04/2028	*SU	11.6	2.2	1.6
07/14/2028	*SU	10.5	**1.4	1.5
09/21/2028	0E0SU	11.2	**1.6	14.5
07/10/2029	*SU	9.0	**1.2	1.8
07/15/2029	*SU	12.1	2.2	1.6
08/04/2030	*SU	9.5	**1.3	1.7
08/09/2030	*SU	11.4	**1.6	1.4
08/09/2031	*SU	12.0	**1.6	1.4
08/28/2032	*SU	13.5	**1.6	1.4
09/22/2033	*SU	13.7	**1.1	1.3
09/27/2034	*SU	14.6	**1.0	1.3
09/26/2037	*JSU	14.3	**1.5	3.2

*Uses STAR 48 as additional upper stage.
**Delivers well under 2 Mg.

Table 3.7.: Saturn-Uranus Trajectory Catalog: Delta IV Heavy

Launch Date	Flyby Path	TOF, yrs	Mass, Mg
12/31/2024	VEE0SU	14.3	1.8
01/05/2025	VEE0SU	14.8	1.8
06/04/2025	0E0SU	14.6	1.7
03/26/2026	VEE0SU	13.9	1.8
03/05/2028	VEE0SU	14.8	**1.4

*Uses STAR 48 as additional upper stage.
**Delivers well under 2 Mg.

solution. For the Atlas V 551 no solutions were found that provide sufficient delivered mass.

3.4 Catalogs for Trajectories that Capture Inside the Rings of Uranus

Since it has yet to be confirmed (at the time of writing this work) that capture inside the rings of Uranus will not be permitted (for risk of colliding with debris), in this section we present a set of catalogs for each the Atlas V 551, Delta IV Heavy, and SLS Block 1B with capture inside Uranus' rings. The capture periapsis altitude for this analysis is assumed to be 3000 km, with a capture orbital period of 20 days. The catalogs are presented in Tables 3.8–3.10.

Table 3.8.: Uranus Trajectory Catalog: Atlas V 551—Capture Inside Rings

Launch Date	Flyby Path	TOF, yrs	Mass, Mg
11/26/2024	VEE0SU	14.8	1.7
11/11/2025	VEE0U	15.0	**1.5
10/07/2026	VEE0U	14.1	2.2
10/17/2027	VVEE0JU	14.8	1.9
02/29/2028	VEEE0JU	14.5	1.9
10/26/2029	VEE0JU	12.7	2.0
01/24/2030	VEE0JU	14.7	2.1
05/29/2031	VEEE0JU	13.5	2.0
08/12/2031	VE0JU	12.6	1.9
06/07/2032	VEEM0U	14.6	2.1
12/24/2033	VEE0U	14.6	1.7
01/03/2034	VEE0U	14.8	1.9
12/26/2035	VEE0U	14.9	**1.5
01/25/2036	VEE0U	14.7	1.7
11/13/2037	VEE0U	13.8	2.1
02/08/2038	VEE0U	15.0	**1.5

*Uses STAR 48 as additional upper stage.
**Delivers well under 2 Mg.

As with the case for capture outside the rings of Uranus, the SLS may require a large amount of propellant mass (due to its ability to have very high launch mass). For capture inside the rings, the propellant mass in Table 3.10 ranges from 0.9 Mg to 24.4 kg. If we limit the maximum amount of propellant mass to that of 5000 kg or less, a completely different catalog of trajectories arises (given the selection criteria of this study) shown in Table 3.11.

Table 3.9.: Uranus Trajectory Catalog: Delta IV Heavy—Capture Inside Rings

Launch Date	Flyby Path	TOF, yrs	Mass, Mg
12/06/2024	VEE0U	13.3	2.1
01/05/2025	VEEE0U	14.4	2.0
10/02/2026	VEE0U	12.7	1.9
09/17/2027	VVEE0JU	13.9	2.1
04/19/2028	VE0JU	13.5	2.1
12/30/2029	VEE0JU	11.7	2.0
11/05/2030	MEE0JU	11.7	1.8
12/10/2030	VVE0JU	12.1	2.1
07/18/2031	VE0JU	10.9	2.1
11/19/2032	VEEM0U	12.4	1.9
12/16/2032	VV0JU	13.2	2.3
01/05/2033	VEE0U	13.4	2.0
04/08/2033	VEEM0U	12.2	1.8
03/26/2034	VVE0U	13.0	2.0
12/21/2035	VEE0U	13.1	1.8
02/09/2036	VVE0U	13.2	2.1
11/10/2037	VEE0U	12.6	2.0
02/08/2038	VEE0U	12.8	2.1

*Uses STAR 48 as additional upper stage.
**Delivers well under 2 Mg.

3.5 Candidate Trajectory for a Saturn-Uranus Mission

We assume in this study that, of the Saturn-Uranus trajectories available, the more desirable solutions are those with flight times less than 14 or 15 years, which leaves only the SLS as a usable launch vehicle (of the trajectories found in this study) for a Saturn-Uranus mission. Additionally, we assume that such a mission will fall into the flagship class category of NASA missions. Given this assumption, to avoid overlapping (due to limited funds) with the Europa flyby mission in the early 2020s, we put preference on launch dates that occur in the late 2020s. With these considerations in mind, we selected the July 4, 2028 Saturn-Uranus trajectory (from Table 3.6) for further analysis.

Table 3.10.: Uranus Trajectory Catalog: SLS Block 1B—Capture Inside Rings

Launch Date	Flyby Path	TOF, yrs	Mass, Mg	Prop. Mass, Mg
07/19/2024	*U	9.5	**1.5	0.9
05/20/2024	0E0SU	10.6	2.0	13.9
12/16/2024	VEE0SU	10.9	2.1	24.4
07/24/2025	*U	9.5	**1.4	0.9
03/11/2025	VEE0U	10.8	2.4	24.1
07/29/2026	*U	9.7	**1.5	0.9
07/09/2026	0E0SU	10.9	2.1	9.5
06/30/2027	*SU	9.1	**1.5	1.4
06/15/2027	*SU	11.1	2.1	0.9
07/14/2027	0E0U	11.4	2.1	9.5
08/07/2028	*U	9.8	**1.5	0.8
07/14/2028	*SU	10.5	2.1	0.9
09/21/2028	0E0SU	11.3	2.7	13.5
07/15/2029	*SU	8.2	**1.5	1.5
07/25/2029	*SU	9.5	1.9	1.1
11/30/2029	VEE0JU	10.6	2.1	22.6
07/30/2030	*SU	9.3	1.9	1.1
09/13/2031	VV0JU	9.8	2.0	16.6
11/09/2032	VMV0JU	9.1	2.1	18.6
12/01/2032	*VVE0U	10.4	3.0	5.7
04/23/2033	M0JU	8.4	2.2	14.4
08/21/2034	*U	9.5	**1.5	0.8
06/22/2034	VEE0U	10.8	2.4	10.2
08/26/2035	*U	9.4	**1.5	0.9
08/08/2035	0E0U	11.1	2.9	13.0
08/28/2036	*JU	8.4	1.7	1.3
08/12/2036	0E0U	11.0	2.8	13.1
09/01/2037	*M0U	7.7	**1.5	1.5
08/17/2037	*M0U	9.1	2.1	1.7
09/09/2038	*U	9.2	**1.5	0.9
08/22/2038	0E0U	11.0	2.7	13.2

*Uses STAR 48 as additional upper stage.
**Delivers well under 2 Mg.

First, we use the optimization tool MALTO to ad-just the encounter dates, in an attempt to improve the STOUR solution. In MALTO, we maximize delivered mass with a maximum TOF constraint set to the value found in STOUR. Since no DSMs

are implemented for this trajectory, the MALTO solution found was very similar to the solution found in STOUR, with the MALTO solution's launch date now occurring on July 3, 2028.

To assess the hyperbolic approach conditions, we use MATLAB to model the solution space of approach trajectories at Saturn and Uranus. These models allow us to calculate the probe entry conditions, and estimate the required deflection maneuver needed for the probe to be released at Saturn. The approach trajectory models also allow us to visually inspect and adjust the approach trajectories for ring avoidance, and inspect the line of sight visibility (between the probe and orbiter, and the orbiter with Earth) for communications. The goal of this analysis is to quickly identify any "red flags" in the approach conditions (such as high probe entry speed, or loss of line of sight for communication) that may result in an infeasible trajectory design: the purpose being to catch these issues early on, and avoid running into them in later stages of a future, more in-depth conceptual design.

The possible approach trajectories at Saturn and Uranus are illustrated in Figs. 3.6a and 3.6b for the July 3, 2028 MALTO solution. The only inputs to the visualization required from the MALTO solution are the planet-relative velocity vector (i.e. V_∞), and the en-counter date and time. The set of approach trajectories shown in the figures are computed for various specified periapsis radii, and for various specified angular values (ψ) about the V_∞ vector (shown in red).

The set of bright blue trajectories in Figs. 3.6a and 3.6b represent the trajectories that have an inclination closest to the equatorial plane, and thus have orbital velocities (at entry) directed as much as possible in the direction of the planet's rotating atmosphere. For Saturn, this is the set of minimum inclination solutions (since Saturn is defined to spin prograde), and for Uranus, this is the set of maximum inclination solutions (since Uranus is defined to spin retrograde). If no other factors impact the trajectory (such as ring avoidance, communications, etc.) then these bright blue trajectories potentially provide the minimum probe entry speed. The choice in which blue approach trajectory to use for the probe depends on the required entry flight

a)   b)
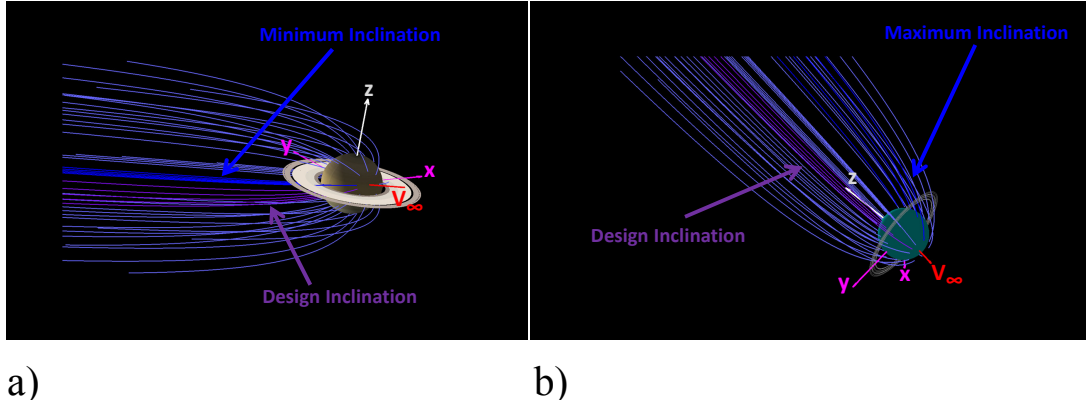
Figure 3.6.: Hyperbolic approach trajectories at (a) Saturn, and (b) Uranus, for the optimized version of the July 4, 2028 opportunity in Table 3.6.

path angle, which for the final design comes from a more detailed entry analysis. For this study, we provide a set of approach trajectories over a range of entry flight path angles.

The probe entry conditions for a rotating atmosphere are computed for a select set of approach trajectories. The "design" approach trajectories are selected by adjusting (via trial and error) the angle ψ, until the (approximate) minimum inclination approach at Saturn, and maximum inclination approach at Uranus, is found without passing through the planets' rings. These solutions correspond to the approximate minimum atmosphere-relative entry speed for a range of entry flight path angles. The approximate maximum atmosphere-relative entry speed for each design is about 27 km/s at Saturn and 22 km/s at Uranus. The entry speed bounds are based on the previous Saturn and Uranus mission decadal studies in Refs. [47] and [22], respectively. We assume entry occurs at 1000 km altitude at Saturn, and 3000 km altitude at Uranus (where the "surface" is defined at an atmospheric pres-sure of 1 bar).

The entry flight path angle is primarily determined by the choice in approach periapsis. For this study a range of entry flight path angles is provided from -25°to -40°at Uranus (from Ref. [18]) and from -8°to -30°at Saturn (from Ref. [48] and personal correspondence with Parul Agrawal Ph.D. and Gary Allen Ph.D at NASA Ames Research Center). These flight path angles (along with corresponding atmosphere-

relative entry speeds withing the maximum stated values) are estimates of what is needed for a feasible probe entry design, with respect to maximum acceleration loads and heating. A more detailed entry analysis however is needed to confirm that such a design is feasible (and is beyond the scope of this work).

The purple set of trajectories in Figs. 3.6a and 3.6b represent the inclination chosen for the final design in this preliminary analysis. Notice that the min (Saturn) and max (Uranus) inclination solutions were not selected for either the Saturn approach or the Uranus approach, which (in both cases) was to avoid passing through the planets' rings. We note that the approach trajectories at Uranus are all highly inclined, which is common at Uranus due to its large axial tilt, and can require large maneuvers after capture if an equatorial science orbit is desired.

The final approach trajectories along with the interplanetary trajectory solution from MALTO (plotted using MATLAB) are shown in Fig. 3.7. The 130 m/s ΔV listed at the Saturn encounter is an estimate for the orbit deflection maneuver. This maneuver is required for the orbiter to release the probe, and then burn its engine to put itself back on course for the Saturn flyby to continue on to Uranus. Since the two trajectories converge as the distance from Saturn increases, the earlier the probe is released, the lower the ΔV required; however, this also requires very precise navigation to ensure that the probe enters the atmosphere with the desired conditions. For this analysis, we assume the probe is released 150 days prior to the Saturn encounter, based on the 147-day release time used by the Galileo spacecraft[†].

The masses at each encounter for the 2028 Saturn-Uranus trajectory are adjusted from the MALTO solution to account for 300 kg dropped at Saturn for the probe, plus an additional 140 kg for the propellant estimated for the deflection maneuver (calculated after the Saturn probe mass is dropped). Another 300 kg is assumed released prior to UOI for the Uranus probe. In total, 740 kg is assumed to be dropped before the propellant mass is calculated for the UOI maneuver. The remaining mass in orbit at Uranus then receives the reduction of 12% of the propellant mass used for

---

[†]http://nssdc.gsfc.nasa.gov/planetary/galileo.html

all DSMs and capture. The remaining mass after the 12% reduction is the reported orbiter capture mass in Fig. 3.7, of 2.1 Mg.

A range of entry conditions are given in Table 3.12 for entry at Saturn and Table 3.13 for entry at Uranus, where $V_{Inertial}$ is the body-inertial velocity, FPA is the flight path angle, Lat is the latitude, Long is the longitude, and $V_{Atm-Rel}$ is the atmosphere-relative entry velocity.
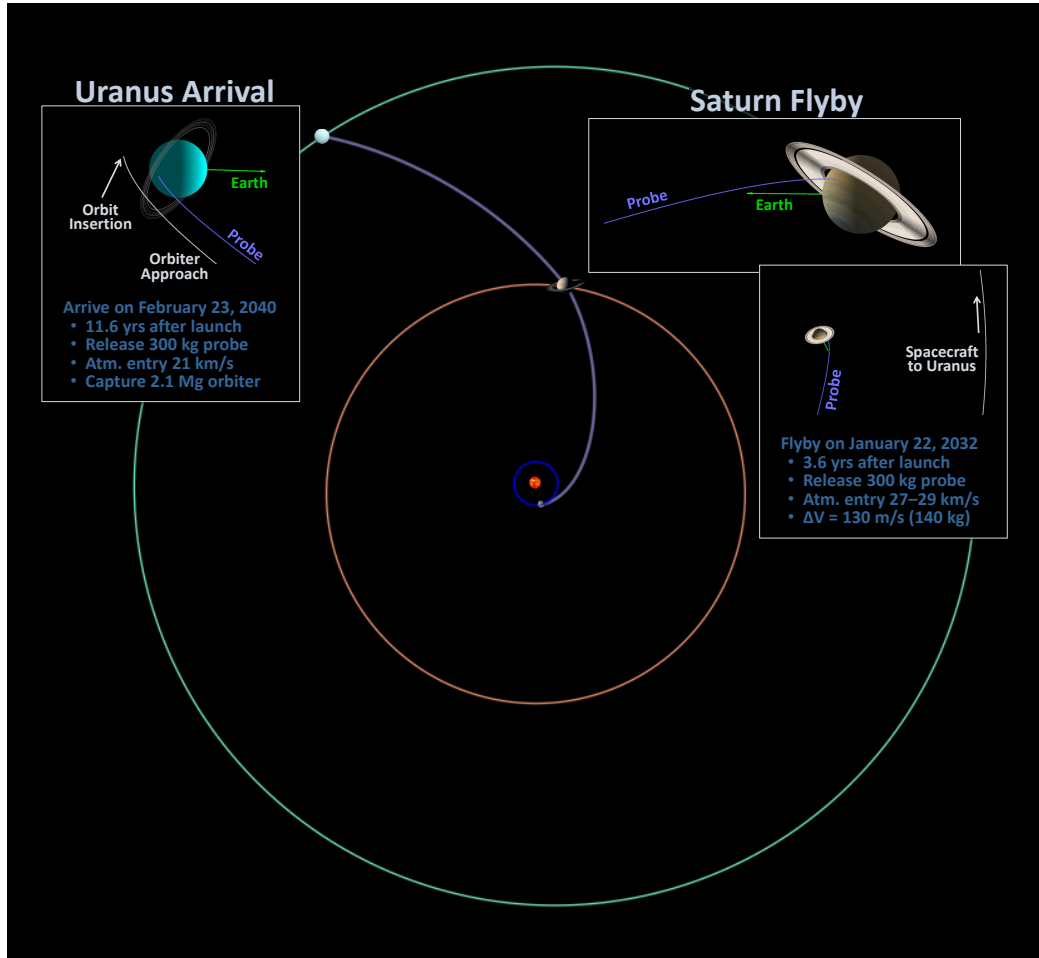
Figure 3.7.: MALTO-optimized Saturn-Uranus trajectory. Launch date on July 3, 2028, using SLS Block 1B with STAR 48 additional upper stage.

As a final remark to this section, we note that the trajectory analysis presented in this paper contributed to the foundational work of a much more thorough Saturn-Uranus mission concept design, presented by Kolencherry et al. [49]. In their study,

they conclude that a mission to deliver a Saturn probe followed by a Uranus probe and orbiter is feasible, using the 2028 Saturn-Uranus opportunity in Fig. 3.7.

3.6 Aerocapture

So far in this analysis, it appears that heavy lift launch vehicles (such as the SLS and the Delta IV Heavy) are required for flight times on the order of a decade to be achievable. The Atlas V 551 is indeed capable of delivering sufficient mass to Uranus, but the flight times required are much longer: on the order of 15 years. One means to reduce the flight times for smaller launch vehicles is to employ aerocapture.

Aerocapture uses the atmosphere of a planet or moon to reduce the spacecraft's relative velocity enough to enter into orbit about the target body. This capture maneuver is achieved with the use of a TPS, similar in principle to that used for atmospheric probes and entry capsules for human missions.

Because aerocapture may be an enabling technology to reduce flight times to the outer planets, we present a very brief and preliminary analysis to identify candidate trajectories that may prove to be attractive for aerocapture. A key advantage of aerocapture is its capability to capture with arrival speeds much larger than what a chemical propulsion system can provide. Since trajectories with short flight times often have high encounter velocities, aerocapture is a possible solution for "fast" trajectories to Uranus. Additionally, because propulsive capture is a proven technology in space travel, any trajectory that is attractive for propulsive capture will likely not be a good candidate for aerocapture; the point being, the trajectories shown in Tables 3.2–3.4, 3.6 and 3.7 are not attractive for aerocapture.

In this paper, we consider an attractive aerocapture trajectory to be one that can deliver at least 1500 kg at Uranus (excluding the TPS mass) in under 10 years. Since these conditions can be met using chemical capture with the SLS Block 1B, we only consider the Atlas V 551 and Delta IV Heavy launch vehicles (which may be the only vehicles available if the development of the SLS does not continue).

A challenge then is to identify trajectories that are not attractive for propulsive capture, but may be attractive for aerocapture, without performing a detailed hypersonic entry analysis. In this preliminary analysis, we assume (as done by Landau et al. [16]) that the mass of the TPS is uniformly 50% of the delivered mass before capture. This mass fraction is by no means guaranteed for any particular aerocapture trajectory, but is similar to the TPS mass fraction in a Neptune aerocapture study by Lockwood [50].

The candidate aerocapture trajectories to Uranus are presented in Tables 3.14 and 3.15. The trajectories were found using the same methods as described for all other trajectories presented in this paper, with the single change that the delivered mass is now calculated to be 50% of the arrival mass at Uranus (before UOI). As a result of our blanketed assumption of 50% TPS mass fraction, the delivered mass values presented in Tables 3.14 and 3.15 are preliminary. We stress that our goal in this analysis is only to identify candidate trajectories that may be attractive for aerocapture. We merely point to such trajectories for future detailed aerocapture studies, where the delivered mass estimates can be refined.

The results in Tables 3.14 and 3.15 indicate that there are several attractive candidate opportunities for aerocapture at Uranus in the late 2020s and early 2030s using either the Atlas V 551 or Delta IV Heavy launch vehicles. Since no hypersonic analysis was done on these trajectories to indicate their feasibility, the arrival V_∞ at Uranus is also listed, for future aerocapture designers to more judiciously select candidates from these catalogs.

In addition to aerocapture, we note that low thrust may also provide significant flight time savings with smaller launch vehicles. For the case of solar electric propulsion (SEP), energy from a solar array (sufficient for an electric propulsion thruster) becomes unavailable around Jupiter's orbital distance due to the reduced sunlight intensity. Therefore, such a spacecraft would either need to bring with it a chemical engine, or use aerocapture, for UOI. We do not present a low-thrust analysis in this

paper; however, a thorough low-thrust analysis (such as those in [15, 16]) is highly recommended for continuing Uranus orbiter mission studies.

3.7   Conclusion

The catalogs presented in this paper indicate that the SLS could provide regular opportunities for capture missions to Uranus with flight times between 9 and 12 years, using a chemical propulsion system. Smaller launch vehicles (compared to the SLS) can also deliver an orbiter at Uranus using chemical propulsion, but with longer flight times: 12-15 years for the Delta IV Heavy, and about 15 years for the Atlas V 551.

Although Jupiter is unavailable for gravity assist in the near term, Saturn is available until the early 2030s, and may allow for an interesting Saturn-Uranus mission. One such trajectory is presented in 2028 that delivers a Saturn probe, followed by a Uranus probe and orbiter: a rare opportunity, since the Saturn-Uranus alignment only repeats every 45 years.

If a less expensive Saturn-Uranus mission is desired (e.g. for the New Frontiers program) another potentially attractive mission concept using the Saturn-Uranus alignment, is to use it for a Saturn probe mission. In such a mission, a spacecraft could continue on to fly by Uranus (and possibly deliver a Uranus probe), after delivering the Saturn probe.

If shorter flight times are desired using smaller launch vehicles than the SLS, several trajectory candidates for aerocapture are found in the late 2020s and early 2030s using an Atlas V 551 or Delta IV Heavy, with flight times under 10 years.

With growing interest in missions to the Ice Giants, it is important for scientists, systems engineers, and mission designers, to be able to quickly and easily get a sense of the feasible trajectories to our outermost planets. The catalogs we present in this work are intended to make identifying realistic trajectory parameters quick and easy for professionals working on future missions to the Ice Giants. We emphasize that the trajectories presented in this work are of medium fidelity, and are not ready for flight;

however, they are expected to serve as good estimates for delivered mass, flight time, and launch date. Additionally, since only flight time, delivered mass, and launch date are used to select attractive cases, the feasibility of the trajectories presented in this work for any particular mission cannot completely be verified without a full end-to-end mission concept study, that considers the specific requirements of such a mission.

One key result of this study is quantifying (in terms of delivered mass to orbit and flight time) the advantages provided by the SLS. The SLS also provides a means to enable a complex Uranus orbiter mission (such as the Saturn-Uranus mission concept), using current, heritage technology, such as chemical propulsion, without requiring new technology such as aerocapture, or less-flown technology such as low thrust. The SLS will change how we think about what is feasible for future space exploration missions, and the Saturn-Uranus opportunity presented in this paper highlights one such game-changing mission concept.

Table 3.11.: Uranus Trajectory Catalog: SLS Block 1B—Capture Inside Rings with 5 Mg or Less of Propellant

Launch Date	Flyby Path	TOF, yrs	Mass, Mg	Prop. Mass, Mg
07/19/2024	*U	9.5	**1.5	0.9
06/29/2024	VEEE0U	14.4	2.1	4.9
07/24/2025	*U	9.5	**1.4	0.9
05/30/2025	*SU	11.2	1.8	1.2
12/21/2025	*VEEE0U	14.4	2.4	4.9
07/29/2026	*U	9.7	**1.5	0.9
06/05/2026	*SU	10.4	1.8	1.2
06/20/2026	*SU	11.9	2.1	0.9
06/30/2027	*SU	9.1	**1.5	1.4
06/15/2027	*SU	11.1	2.1	0.9
08/07/2028	*U	9.8	**1.5	0.8
07/14/2028	*SU	10.5	2.1	0.9
07/04/2028	*SU	11.6	2.8	1.0
07/15/2029	*SU	8.2	**1.5	1.5
07/25/2029	*SU	9.5	1.9	1.1
07/15/2029	*SU	12.1	2.9	0.9
07/30/2030	*SU	9.3	1.9	1.1
11/10/2030	*VE0JU	12.1	4.0	4.7
08/09/2031	*SU	9.3	**1.4	0.9
08/14/2031	*SU	11.0	2.1	0.9
03/10/2031	M0JU	12.2	4.6	4.1
08/11/2032	*U	9.7	**1.5	0.8
01/26/2032	*VVE0U	11.8	4.0	4.7
08/16/2033	*U	9.6	**1.5	0.8
11/29/2033	*VEEM0U	13.2	3.7	5.0
08/21/2034	*U	9.5	**1.5	0.8
04/03/2034	*VEE0U	13.7	3.9	4.8
08/26/2035	*U	9.4	**1.5	0.9
06/02/2035	*VEE0U	14.4	4.0	4.7
08/28/2036	*JU	8.4	1.7	1.3
08/28/2036	*JU	11.2	2.8	1.0
09/01/2037	*M0U	7.7	**1.5	1.5
08/17/2037	*M0U	9.1	2.1	1.7
09/09/2038	*U	9.2	**1.5	0.9
12/23/2038	*VEEE0U	13.9	2.3	4.9

*Uses STAR 48 as additional upper stage.

**Delivers well under 2 Mg.

Table 3.12.: July 3, 2028 Trajectory: Entry Parameters at Saturn

$V_{Inertial}$, km/s	FPA, deg	Heading, deg	Lat, deg	Long, deg	$V_{Atm-Rel}$, km/s
36.204	-30.028	110.736	-12.105	0.804	28.873
36.191	-28.528	111.401	-11.140	3.199	28.730
36.179	-26.961	112.035	-10.115	5.677	28.588
36.167	-25.316	112.635	-9.021	8.257	28.447
36.155	-23.576	113.198	-7.845	10.966	28.308
36.145	-21.716	113.718	-6.571	13.842	28.169
36.135	-19.703	114.187	-5.173	16.939	28.031
36.127	-17.485	114.590	-3.614	20.340	27.894
36.122	-14.971	114.903	-1.826	24.192	27.758
36.120	-11.979	115.076	0.323	28.792	27.623
36.126	-8.000	114.964	3.206	34.981	27.491

Table 3.13.: July 3, 2028 Trajectory: Entry Parameters at Uranus

$V_{Inertial}$, km/s	FPA, deg	Heading, deg	Lat, deg	Long, deg	$V_{Atm-Rel}$, km/s
20.777	-40.037	-5.019	18.417	-78.449	20.774
20.772	-38.697	-4.953	16.282	-78.642	20.770
20.768	-37.333	-4.895	14.112	-78.834	20.767
20.765	-35.944	-4.845	11.899	-79.026	20.764
20.762	-34.523	-4.802	9.636	-79.219	20.761
20.759	-33.067	-4.767	7.314	-79.415	20.758
20.758	-31.570	-4.739	4.923	-79.614	20.755
20.756	-30.025	-4.721	2.449	-79.819	20.752
20.756	-28.424	-4.711	-0.121	-80.031	20.749
20.757	-26.756	-4.712	-2.809	-80.253	20.746
20.758	-25.009	-4.725	-5.639	-80.487	20.743

Table 3.14.: Preliminary Uranus Aerocapture Trajectory Catalog: Atlas V 551

Launch Date	Flyby Path	TOF, yrs	Mass, Mg	$V_{\infty, Uranus}$, km/s
11/25/2029	VEE0JU	9.84	2.0	18.7
12/10/2029	VEE0JU	9.57	1.6	19.8
01/14/2030	VEE0JU	9.22	1.9	21.2

Table 3.15.: Preliminary Uranus Aerocapture Trajectory Catalog: Delta IV Heavy

Launch Date	Flyby Path	TOF, yrs	Mass, Mg	$V_{\infty,Uranus}$, km/s
12/11/2029	VEE0JU	9.57	2.9	19.8
10/06/2029	VEE0JU	9.44	1.8	21.6
01/14/2030	VEE0JU	9.22	3.4	21.2
03/05/2031	VEE0JU	9.85	2.0	15.1
05/21/2031	0E0JU	8.53	1.6	17.9
06/24/2032	0E0JU	8.95	1.6	13.7

4. 50-YEAR CATALOG OF GRAVITY-ASSIST TRAJECTORIES TO NEPTUNE

In this study, a similar analysis is performed for trajectories to Neptune, as was done in the previous chapter for trajectories to Uranus. We investigate ballistic gravity-assist trajectories to Neptune with launch dates ranging from the years 2020 to 2070. Impulsive maneuvers are considered, with up to 3 km/s ΔV, for each maneuver. Trajectories are calculated using the patched-conic propagator STOUR, with an analytical ephemeris model. A total of 84 different flyby combinations are considered and compared, including less conventional flybys of Mars, Saturn and Uranus. Trajectories are constrained to flight times of 15 years or less, and desirable trajectories with regard to parameters such as time of flight and delivered mass are selected and discussed. The more desirable of these trajectories include a flyby of Jupiter; however, for launch dates when Jupiter is unavailable (such as around 2022 to 2030), direct launch to Neptune or a flyby of Saturn can be used.

4.1   Introduction

Mission concept studies for the 2010 decadal survey have indicated much interest in the last two outer planets—Uranus and Neptune [22, 34]. For the case of Neptune, missions for both flyby of and capture into the Neptune system are proposed—including studies of Neptune's largest moon Triton. Some of these proposed missions go beyond the Neptune system to investigate Kuiper Belt Objects (KBOs). Trajectories to Neptune typically require high launch energies, long times of flight (TOF), and high arrival energies. As a result, nearly all proposed trajectories to Neptune involve a Jupiter gravity assist (JGA), which in turn restricts most Neptune-bound missions to take place during periods of time when Jupiter is available.

Broad searches for trajectory opportunities to the outer planets have been studied in previous years. In 1991, Longuski and Williams [51] investigated ballistic trajectories to Pluto, and discovered a four-planet grand tour opportunity in 1996, with flybys of Jupiter, Uranus, Neptune and Pluto. Ballistic trajectories to Pluto were also investigated by Sims et al. [52] in 1997, for the Pluto Express mission. These trajectories were constrained to arrive at Pluto within 12 years, and contain no flybys of Earth. To obtain such trajectories, Sims et al. allowed for the implementation of impulsive deep-space maneuvers. All of the trajectories found by Sims et al. included JGAs, and some allowed for flybys of asteroids such as Seraphina.

In 2000, Petropoulos et al. [53] investigated ballistic trajectories to Jupiter over a large span of launch dates ranging from 1999 to 2030. In their paper, 'classical' sequences of flyby bodies (or 'paths') were found, such as of Venus and Earth, respectively, as well as nonconventional paths, such as Venus-Mars-Venus-Earth. In 2011, Spreen et al. [14] conducted a similar investigation (to that of Petropoulos et al.) for ballistic trajectories to Uranus for Earth launch dates ranging from the years 2020 to 2060.

In all of these previously mentioned studies, the broad search of trajectories was done using a patched-conic propagator with analytic ephemeris. Optimization techniques, however, have also been applied to ballistic gravity-assist trajectories, such as by Melman et al. [54], who implemented genetic algorithms to find an optimal trajectory to Neptune, as well as an optimal tour of the Neptune system.

Broad searches for low-thrust opportunities to the outer planets have also been investigated, such as by Landau et al. [16], who found a variety of solar electric propulsion (SEP) low-thrust trajectories, with launch dates spanning from 2015 to 2035. The SEP trajectories were found using the low-thrust optimization tool MALTO [37] developed at the Jet Propulsion Laboratory (JPL). Other methods for the design of optimal low-thrust gravity-assist trajectories have been proposed, such as by Casalino et al. [65], who focused on low-thrust trajectories to escape the Solar System, and Zimmer and Ocampo [56], who applied analytical gradients to optimize low-thrust

trajectories. More recently, Yam et al. [57] used global optimization techniques for low-thrust gravity-assist trajectories to Jupiter.

4.2   Methods

The overall method of analysis in this study is the same as that followed in the previous chapter, regarding trajectories to Uranus; however when going to Neptune, Uranus can now be considered for gravity assist. As in the Uranus trajectory study, the launch vehicles considered are the Atlas V 551, Delta IV Heavy, and SLS Block 1B; each of which could use a STAR 48 additional upper stage (assumed to be burned along the departure asymptote). Trajectories are sorted in terms of flight time and delivered mass, and the most attractive cases are identified as those that can deliver a specified amount of mass in minimum time. Further analysis is need to determine whether or not such trajectories meet any mission-particular requirements of interest to the reader.

The list of gravity-assist paths considered to Neptune is identical to those considered for missions to Uranus (see Ch. 3), with a few exceptions. Several paths are investigated that fly by Uranus (denoted "U"), specifically: U, V0U, M0U, JU, SU, VJU, and VSU. Additionally, the paths VVV0S, VVE0S, VVMV0, VV0MS, VEEE0, MEE0S, VEVE0S, VEEE0S, VEE0MS, VEME0S, VMEE0S, and MEME0S took nearly 15 years to arrive at Uranus (as discovered by the search of trajectories to Uranus in Ch. 3) and are not considered for Neptune, since they would exceed the 15-year flight time constraint.

The capture orbit at Neptune is sized based on the Neptune-Triton-KBO decadal study [34], with 20-day orbital period, and periapsis of 2.5 Neptune (mean equatorial) radii. The decision in capture orbit size is also informed by investigating the variation in capture ΔV for various arrival V_∞, shown in 4.1.

Each curve shown in Figure 4.1 represents a particular arrival V_∞ at Neptune, as indicated by the annotations. The solid lines represent capture at a periapsis outside
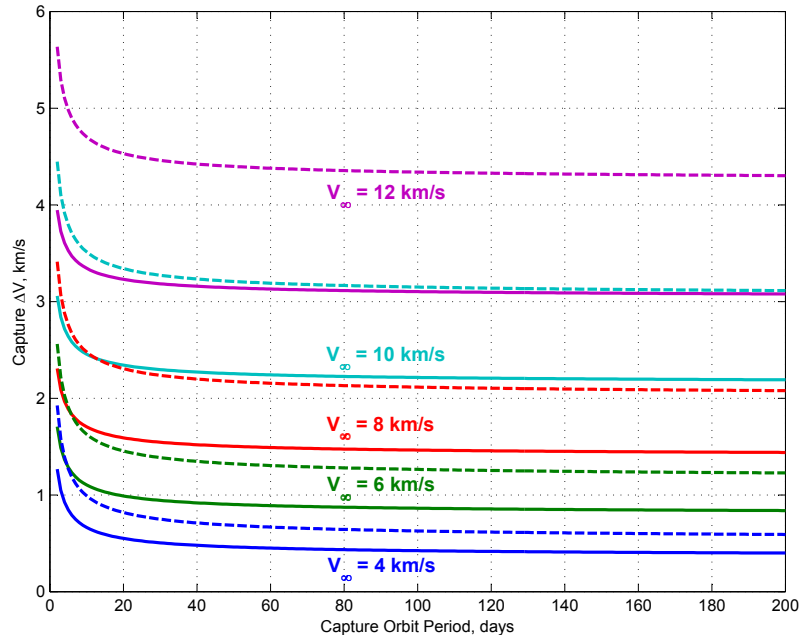
Figure 4.1.: Capture ΔV at Neptune for various science orbit sizes and arrival V_∞. The solid lines represent capture inside the rings of Neptune, at an altitude of 3000 km. The dotted lines represent capture outside the major rings, at a radius of 2.5 Neptune (mean equatorial) radii.

the rings, at 2.5 Neptune radii; whereas, the dotted lines represent capture inside the rings at an altitude of 3000 km. In this work, we assume capture occurs outside the rings, since this may be the only option for capture, and such an assumption provides more conservative results (with regards to delivered mass at Neptune). We point out however that capture inside the rings can potentially save significant ΔV (and thus provide substantially more delivered mass); especially for the higher arrival V_∞ values shown in Fig. 4.1. The figure shows each curve approaching a horizontal asymptote as the orbit size increases—the limiting case being capture into a parabolic orbit. The figure also shows that the capture ΔV is essentially at a minimum (for all V_∞ curves) once the orbit period exceeds about 40 to 60 days; however, the majority of ΔV reduction is achieved around a period of 20 days.

4.3 Uranus-Neptune Alignment

Before presenting the catalog of trajectories to Neptune, we note that no trajectories were found that fly by Uranus on route to Neptune. The issue is the poor relative alignment of Uranus and Neptune for the years 2020 (the earliest launch year) through 2085 (the latest launch year plus a 15-year TOF). The locations of Uranus and Neptune on 1/1/2020 and 12/31/2085 are shown in Figure 4.2, where (for orbital motion in a counterclockwise direction), an encounter with Neptune after a flyby of Uranus requires traversing a large section of the outer solar system, which is much too far to complete withing the 15-year TOF constraint. To put this in context, the orbital period of Uranus is about 84 years, and that of Neptune is about 165 years. Another issue with the Uranus-Neptune alignment is that for the 2020s (and the few following decades), a large bending angle is required if the spacecraft is to avoid completing nearly a full revolution about the Sun at an orbital distance of Uranus and greater (which would take about a century to complete). This large bending angle is apparent in Fig. 4.2 where a clockwise trajectory approaching Uranus at 1/1/2020 must rotate (in the Sun-centered frame shown) by about 270°. To verify that trajectories with paths containing consecutive Uranus-Neptune encounters are infeasible, the gravity-assist path UN is propagated (in the patched-conic model) with a minimum flyby altitude at Uranus of only 300 km, and found no trajectories (within the 15-year TOF constraint).

4.4 Catalog of Trajectories to Neptune

The launch vehicles considered for this study are the Atlas V 551, Delta IV Heavy, and SLS Block 1B. In each case the option of an additional STAR 48 upper stage is considered for high launch C_3 trajectories. As with the Uranus trajectory analysis, a delivered mass of 2000 kg is desired, however lower mass values are also presented if they provide a substantial reduction in TOF (compared to the 2000-kg solution). If
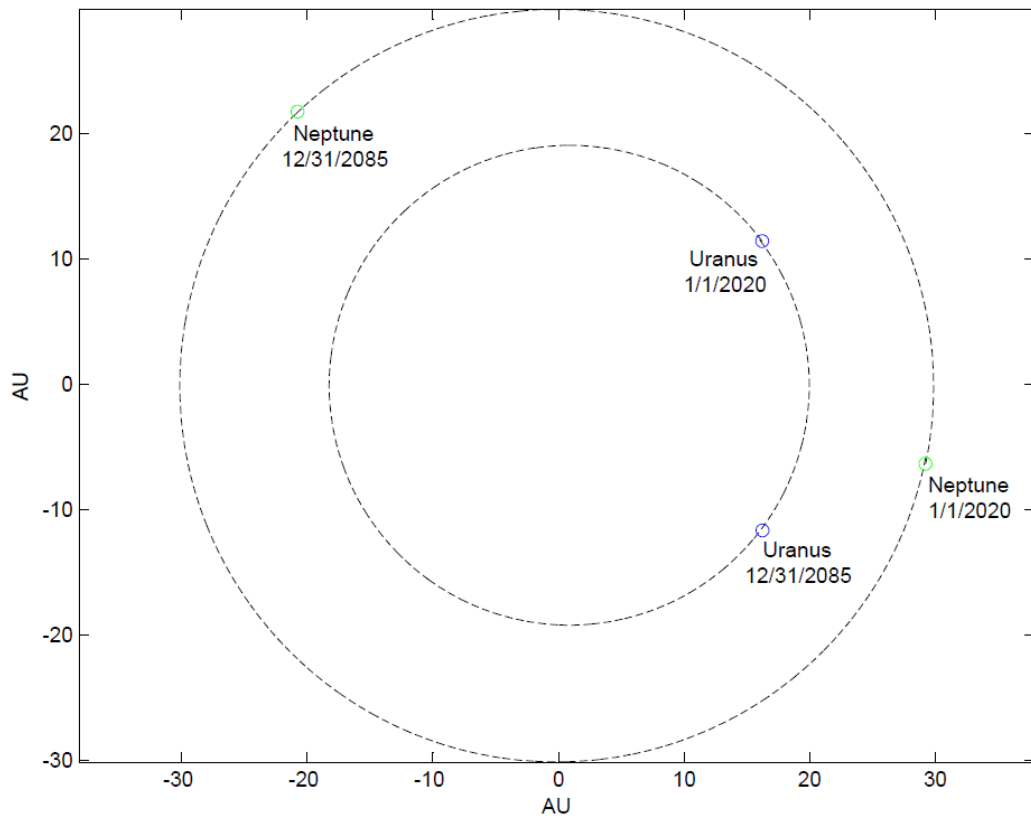
Figure 4.2.: The relative positions of Uranus (inner orbit) and Neptune (outer orbit) on 1/1/2020 and 12/31/2070 illustrates that a long flight times (across much of outer solar system), or possibly large flyby bending angle, is required to consecutively fly by Uranus and Neptune, respectively.

no solutions are found for a particular launch year that deliver 2000 kg, the maximum delivered mass is presented, if it is larger than 1000 kg.

For the Atlas V 551, no solutions are found that deliver over 1000 kg in orbit at Neptune. The maximum delivered mass solutions for the only three launch years capable of delivering 500 kg or more are presented in Table 4.1. None of the three solutions are near term (with the earliest launch date in 2040), all use a Jupiter gravity assist, and all have long TOFs (with the shortest being 14.0 years). Table 4.2 shows the solutions capable of delivering mass of 1000 kg or more, if we allow the capture periapsis to be located inside Neptune's rings at an altitude of 3000 km. The 2042 and 2053 solutions are the only two launch years that provide a delivered mass of at least 1000 kg, which is still well below the desired delivered-mass value of 2000 kg. If a flight time longer than 15 years can be tolerated for a particular mission design, solutions with larger delivered mass values are likely to be found (which may make the Atlas V 551 a feasible option for a chemical trajectory to Neptune).

Table 4.1.: Neptune Trajectory Catalog: Atlas V 551—Capture Outside Rings

Launch Date	Flyby Path	TOF, yrs	Mass, Mg
08/13/2040	VE0JN	14.9	0.5
07/29/2042	VVE0JN	14.0	0.6
10/14/2053	VEE0JN	14.8	0.6

Table 4.2.: Neptune Trajectory Catalog: Atlas V 551—Capture Inside Rings

Launch Date	Flyby Path	TOF, yrs	Mass, Mg
07/29/2042	VVE0JN	14.0	1.0
10/14/2053	VEE0JN	14.8	1.2

The trajectory catalog for the Delta IV Heavy is shown in Table 4.3 below. No solutions are found that deliver our target delivered mass of 2000 kg, and only two solutions are found that deliver greater than 1000 kg (shown in the table. Since so

few solutions are found assuming capture periapsis outside the rings, a second catalog is provided in Table 4.4 assuming a capture periapsis altitude of 3000 km (with same capture orbit period of 20 days). Likewise, the trajectory catalog for the SLS Block 1B is given in Table 4.5, using a capture periapsis outside Neptune's rings. We also present a catalog of SLS Block 1B trajectories that have capture periapsis inside the rings, provided in Table 4.6. Even though the SLS is capable of delivering the desired mass of 2000 kg, capture solutions inside the rings are of interest since they may provide solutions that can deliver 2000 kg with significantly reduced flight times. As is the case for the trajectories to Uranus that launched with the SLS, many of the solutions require a large amount of propellant mass.

Table 4.3.: Neptune Trajectory Catalog: Delta IV Heavy—Capture Outside Rings

Launch Date	Flyby Path	TOF, yrs	Mass, Mg
07/29/2042	VVE0JN	14.7	**1.2
10/14/2053	VEE0JN	14.8	**1.1

*Uses STAR 48 as additional upper stage.
**Delivers well under 2 Mg.

Table 4.4.: Neptune Trajectory Catalog: Delta IV Heavy—Capture Inside Rings

Launch Date	Flyby Path	TOF, yrs	Mass, Mg
7/13/2026	VEE0JN	14.8	**1.3
10/31/2027	VEE0JN	14.9	**1.2
01/24/2028	VVE0JN	14.7	**1.3
09/20/2029	VE0JN	14.3	**1.0
02/12/2031	M0JN	14.1	**1.3
05/11/2039	VEEE0JN	14.8	**1.1
06/29/2040	VE0JN	14.9	1.7
01/15/2041	VVE0JN	14.7	**1.5
07/29/2042	VVE0JN	14.0	1.8
03/01/2043	JN	14.6	**1.0
10/08/2051	VEE0JN	14.8	**1.1
01/31/2052	VEE0JN	14.9	**1.2
11/03/2053	VEE0JN	14.7	2.1
02/21/2054	VEE0JN	14.7	**1.3
12/03/2064	VMVE0JN	15.0	**1.2
01/19/2065	VEE0JN	14.1	**1.0

*Uses STAR 48 as additional upper stage.
**Delivers well under 2 Mg.

Table 4.5.: Neptune Trajectory Catalog: SLS Block 1B—Capture Outside Rings

Launch Date	Flyby Path	TOF, yrs	Mass, Mg	Prop. Mass, Mg
03/16/2020	*JN	14.02	**1.6	2.2
04/05/2021	*SN	14.55	**1.3	1.6
04/10/2022	*SN	13.83	**1.0	1.3
08/17/2026	VVE0JN	15.00	**1.5	25.0
12/20/2027	VVE0JN	14.73	**1.6	15.0
01/24/2028	VVE0JN	14.72	2.6	16.1
09/20/2029	VE0JN	14.31	**1.6	24.9
01/13/2030	JN	12.77	**1.6	7.1
01/13/2030	JN	14.46	2.7	6.0
02/12/2031	M0JN	12.89	2.2	8.4
02/27/2031	*M0JN	14.08	3.0	5.7
03/04/2031	*JN	13.28	2.1	5.1
03/23/2032	*JN	13.46	2.2	3.8
05/17/2033	*JN	14.27	**1.4	1.6
08/09/2039	VVE0JN	14.95	**1.6	19.1

Table 4.5.: *continued*

Launch Date	Flyby Path	TOF, yrs	Mass, Mg	Prop. Mass, Mg
11/06/2040	VVE0JN	14.54	2.9	17.8
01/25/2041	VVE0JN	13.83	2.4	20.3
07/19/2042	VVE0JN	13.07	2.0	14.6
07/29/2042	VVE0JN	13.97	4.4	14.3
03/01/2043	JN	12.92	1.9	6.8
03/01/2043	JN	14.55	3.0	5.8
04/09/2044	*JN	14.12	2.7	4.5
05/19/2045	*JN	14.16	2.1	2.7
06/23/2046	*JN	14.77	**1.1	1.2
11/02/2051	VEE0JN	14.84	**1.2	23.5
01/31/2052	VEE0JN	14.94	1.7	21.0
09/17/2053	VVE0JN	14.16	2.1	16.6
11/13/2053	VEE0JN	13.63	**1.5	17.1
02/16/2054	VEE0JN	14.27	2.0	18.7
04/17/2055	VEE0JN	14.74	1.8	18.8
06/06/2055	*SN	13.58	**1.0	2.0
04/01/2056	*JSN	13.00	1.8	5.4
05/06/2057	*JN	12.83	1.8	4.1
05/26/2057	*JSN	13.25	2.0	3.9
06/20/2058	*JN	14.30	1.7	2.1
12/03/2064	VMVE0JN	14.98	**1.3	25.2
02/18/2066	*JN	14.90	**1.4	5.8
07/23/2066	VV0JN	14.86	**1.6	17.1
03/15/2067	*JN	14.94	**1.1	2.6
04/13/2068	*JN	13.87	1.9	5.3
04/18/2068	*JN	14.96	2.5	4.7
05/28/2069	*JN	13.28	2.1	5.1
06/17/2070	*JN	13.54	1.8	3.0

*Uses STAR 48 as additional upper stage.

**Delivers well under 2 Mg.

Table 4.6.: Neptune Trajectory Catalog: SLS Block 1B—Capture Inside Rings

Launch Date	Flyby Path	TOF, yrs	Mass, Mg	Prop. Mass, Mg
03/21/2020	*JN	11.9	**1.6	2.2
04/05/2020	*JN	13.6	2.1	1.7
04/05/2021	*SN	14.5	1.7	1.2
04/10/2022	*SN	13.8	**1.3	1.0
05/10/2023	*SN	14.9	**1.1	0.7
05/09/2024	*SN	14.9	**1.1	0.7
09/06/2025	VEE0JN	14.9	1.9	18.8
08/27/2026	VEE0MJN	13.7	2.2	27.7
09/11/2026	VEE0JN	13.8	2.5	27.4
12/20/2027	VVE0JN	13.7	2.8	17.8
06/07/2028	VVE0JN	14.2	3.3	21.3
12/29/2029	VEE0JN	14.2	2.0	24.5
12/29/2029	*JN	11.9	**1.2	3.6
01/18/2030	JN	12.3	2.5	6.3
02/12/2031	*JN	11.6	2.1	5.1
03/28/2032	*JN	12.0	2.4	3.6
05/17/2033	*JN	14.3	1.8	1.2
12/12/2037	VEEE0JN	14.8	**1.0	25.5
12/12/2038	VEE0JN	14.2	2.0	26.2
08/14/2039	VVE0JN	13.8	2.2	20.5
11/16/2040	VVE0JN	13.3	2.2	18.5
01/20/2041	VVE0JN	12.8	2.7	19.9
07/19/2042	VVE0JN	12.0	3.3	13.3
03/11/2043	*JN	12.4	2.3	4.9
04/04/2044	*JN	11.3	2.1	5.1
05/14/2045	*JN	12.1	2.1	2.7
06/23/2046	*JN	14.8	**1.4	0.9
07/03/2047	*N	14.7	**1.1	0.7
07/07/2048	*N	14.5	**1.1	0.7
07/07/2049	*N	14.3	**1.1	0.7
07/12/2050	*N	14.3	**1.1	0.7
09/10/2050	VEE0SN	15.0	**1.6	23.1
09/10/2051	VEE0JN	14.4	2.2	18.5
06/16/2052	VVE0JN	13.9	2.5	16.1
12/03/2053	VEE0JN	13.1	2.6	20.1
01/17/2054	VEE0JN	13.2	2.7	17.9
01/25/2055	VE0JN	13.7	1.8	16.8
04/12/2055	VEE0JN	13.8	2.1	14.5

Table 4.6.: *continued*

Launch Date	Flyby Path	TOF, yrs	Mass, Mg	Prop. Mass, Mg
04/01/2056	*JN	12.5	2.5	4.7
04/16/2056	*JSN	11.5	1.9	5.3
05/06/2057	*JSN	12.0	2.3	3.6
06/25/2058	*JN	13.3	2.0	1.8
06/25/2058	*JSN	12.9	1.9	1.9
07/20/2059	*SN	14.8	**1.1	0.7
12/30/2059	VEE0N	15.0	**1.3	19.4
03/24/2060	VEE0N	14.7	**1.3	23.3
07/24/2060	*N	14.8	**1.1	0.7
08/08/2061	*N	13.9	**1.1	0.8
12/14/2061	VEE0N	15.0	1.8	24.7
01/08/2062	VEE0N	14.8	**1.2	21.5
07/29/2062	*N	14.3	**1.1	0.7
06/29/2063	VVEE0JN	14.8	**1.5	26.7
08/13/2063	*N	13.9	**1.0	0.8
12/28/2064	VEE0JN	13.8	2.7	25.6
01/22/2065	VEE0JN	13.6	2.4	25.9
03/10/2066	*JN	14.4	2.1	5.2
11/08/2066	VEE0JN	13.3	2.1	20.5
05/29/2067	0E0JN	14.1	1.8	14.0
04/08/2068	*JN	12.8	2.4	4.8
05/18/2069	*JN	11.1	1.8	5.4
05/28/2069	*JN	13.3	3.2	4.1
06/17/2070	*JN	13.5	2.5	2.3
07/07/2070	*JN	11.4	1.7	3.1

*Uses STAR 48 as additional upper stage.
**Delivers well under 2 Mg.

From the results in tables 4.1–4.6, the most attractive trajectories all use a Jupiter gravity assist. Jupiter is not available, however, for the years 2021–2024, 2034–2036, 2047–2050, and 2059–2062. During such time, the only solutions found that can deliver a spacecraft mass near 2000 kg are those that capture inside Neptune's rings. In 2021, Saturn is available, and the SN path provides about 1700 kg. Saturn is again available in 2050, delivering about 1600 kg using the gravity-assist path VEE0SN. For

many of the years that Jupiter is not available, Saturn can be used for gravity assist. In 2061, Venus and Earth are able to provide about 1800 kg, using the gravity-assist path VEE0N.

If the Delta IV Heavy launch vehicle is to be used, only a few trajectories are capable of delivering 2000 kg (or close to it), which occur in 2040, 2042, and 2053. The most attractive of these cases, is arguably the VVE0JN trajectory in 2042, as it is somewhat near-term, has the shortest TOF of 14 years, and delivers about 1800 kg (which can likely be increased to 2000 kg or more after optimization in MALTO, without much or any increase in TOF).

If the SLS Block 1B is used, several trajectory options are available that can deliver 2000 kg or more. Of the near-term solutions found for capture outside the rings (Table 4.5), a particularly attractive solution appears in 2031 using the gravity-assist path M0JN, which can deliver about 2200 kg in 12.9 years. This solution also has potential backup opportunities in surrounding years using the path JN, which can deliver similar mass, but requires longer flight times. Of the near-term solutions that capture inside Neptune's rings (Table 4.6), 2031 is also an attractive year; however, with the reduced capture ΔV from going inside the rings, the JN path provides sufficient mass with a reduced flight time compared to the M0JN trajectory— delivering about 2100 kg in about 12.6 years. (We will show in the next section however, that after optimization in MALTO, the 2031 M0JN trajectory's flight time can be reduced significantly.)

For a particular mission design, there will likely be a maximum amount of propellant that can be considered (which may vary from design to design). Since the propellant mass values for the SLS are large, we present two new trajectory catalogs in Tables 4.7 and 4.8 that launch with the SLS Block 1B and consider capture outside and inside the rings of Neptune, respectively, with an imposed maximum propellant mass of 5000 kg. As with the case for the trajectories to Uranus, most of the solutions one or zero flybys. The catalogs also show that with the propellant mass constraint,

capturing inside Neptune's rings dramatically increases the number of launch years for which trajectories to Neptune are available.

Table 4.7.: Neptune Trajectory Catalog: SLS Block 1B—Capture Outside Rings with 5 Mg or Less of Propellant

Launch Date	Flyby Path	TOF, yrs	Mass, Mg	Prop. Mass, Mg
04/05/2020	*JN	13.6	**1.5	2.3
01/08/2030	*JN	13.6	**1.5	4.5
01/13/2030	*JN	14.9	2.0	3.9
02/07/2031	*JN	13.5	1.8	4.1
03/14/2031	*M0JN	14.9	2.0	2.8
03/23/2032	*JN	13.5	2.2	3.8
03/28/2032	*JN	12.0	**1.5	4.4
02/19/2043	*JN	13.7	**1.6	4.3
04/09/2044	*JN	14.1	2.7	4.5
05/09/2045	*JN	12.4	**1.5	3.3
05/19/2045	*JN	14.2	2.1	2.7
02/11/2054	*JN	15.0	**1.5	3.3
05/06/2057	*JSN	12.0	**1.4	4.5
05/26/2057	*JSN	13.3	2.0	3.9
06/25/2058	*JN	13.3	**1.5	2.3
06/30/2058	*JSN	13.5	**1.5	2.3
04/18/2068	*JN	15.0	2.5	4.7
05/03/2068	*JN	14.2	1.7	4.2
06/17/2070	*JN	13.5	1.8	3.0

*Uses STAR 48 as additional upper stage.
**Delivers well under 2 Mg.

Table 4.8.: Neptune Trajectory Catalog: SLS Block 1B—Capture Inside Rings with 5 Mg or Less of Propellant

Launch Date	Flyby Path	TOF, yrs	Mass, Mg	Prop. Mass, Mg
03/26/2020	*JN	11.1	**1.4	2.4
04/05/2020	*JN	13.6	2.1	1.7
04/05/2021	*SN	14.5	1.7	1.2
04/10/2022	*SN	13.8	**1.3	1.0
04/20/2023	*SN	14.4	**1.1	0.7
05/14/2024	*SN	14.6	**1.1	0.7
01/04/2027	*JN	14.9	**1.4	4.6

Table 4.8.: *continued*

Launch Date	Flyby Path	TOF, yrs	Mass, Mg	Prop. Mass, Mg
01/09/2028	*JN	15.0	**1.0	2.0
12/29/2029	*JN	11.9	**1.2	3.6
01/03/2030	*JN	12.7	1.9	4.1
02/02/2030	*JN	13.2	2.6	4.6
02/12/2031	JN	11.6	2.0	4.9
03/04/2031	*M0JN	12.0	2.3	4.9
03/18/2032	*JN	11.0	**1.5	3.3
03/28/2032	*JN	12.0	2.4	3.6
05/12/2033	*JN	12.8	**1.5	1.5
05/17/2033	*JN	14.3	1.8	1.2
12/22/2038	*JN	14.9	**1.0	4.9
12/22/2039	*JN	14.8	**1.5	4.4
01/21/2040	*JN	14.8	**1.5	4.4
02/04/2041	*JN	14.9	**1.4	2.4
03/11/2043	*JN	12.4	2.3	4.9
03/30/2044	*JN	11.4	2.2	5.0
05/14/2045	*JN	12.1	2.1	2.7
06/23/2046	*JN	14.8	**1.4	0.9
07/03/2047	*N	14.7	**1.1	0.7
07/07/2048	*N	14.5	**1.1	0.7
07/07/2049	*N	14.3	**1.1	0.7
07/12/2050	*N	14.3	**1.1	0.7
07/12/2051	*N	13.9	**1.1	0.8
01/03/2052	*JSN	15.0	**1.3	4.6
02/11/2053	JSN	14.7	2.0	4.9
02/11/2054	*JN	15.0	2.2	2.6
06/06/2055	*SN	13.6	**1.4	1.6
04/01/2056	*JN	12.5	2.5	4.7
05/11/2057	*JSN	10.5	**1.5	4.5
05/06/2057	*JSN	12.0	2.3	3.6
06/25/2058	*JSN	12.9	1.9	1.9
06/25/2058	*JN	13.3	2.0	1.8
08/04/2059	*SN	13.9	**1.1	0.8
07/29/2060	*N	13.1	**1.0	0.9
08/03/2061	*N	13.1	**1.0	0.8
08/03/2062	*N	13.0	**1.0	0.9
08/08/2063	*N	13.0	**1.0	0.9
08/02/2064	*N	13.9	**1.1	0.8

Table 4.8.: *continued*

Launch Date	Flyby Path	TOF, yrs	Mass, Mg	Prop. Mass, Mg
02/28/2065	*JN	14.9	**1.5	4.4
03/05/2066	*JN	14.8	2.4	4.8
03/15/2067	*JN	14.9	1.7	2.1
04/08/2068	*JN	12.8	2.4	4.8
06/02/2069	*JN	11.1	**1.5	4.4
05/28/2069	*JN	13.3	3.2	4.1
06/22/2070	*JN	11.2	**1.6	3.2
06/17/2070	*JN	13.5	2.5	2.3

*Uses STAR 48 as additional upper stage.
**Delivers well under 2 Mg.

4.5 Neptune Probe and Orbiter Mission using the 2031 M0JN Trajectory

Of the attractive trajectories identified in the previous section, we select the M0JN trajectory in 2031 (of Table 4.5) for further investigation, since it is one of the most attractive trajectories that captured outside of Neptune's rings. The choice was made to select a trajectory that captures outside the rings, since (at the time of writing this document) it was unclear as to whether a capture inside the rings would be possible without damaging the spacecraft due to collisions with debris. The scenario assumed for this investigation is a mission to deliver an atmospheric probe at Neptune, as well as an orbiter.

First, we optimize the maneuver locations and encounter dates to maximize the delivered mass. The optimization is done using an optimization tool such as MALTO or EMTG, with the goal to minimize flight time, while obtaining a delivered mass of about 2200–2500 kg. After the optimized solution is obtained, the approach at Neptune is investigated to confirm that an atmospheric probe could be delivered before capture, without exceeding an atmosphere-relative entry speed of about 20 km/s. Such an entry speed is based on that used for Uranus in Ref. [22], which is

expected to be close to what is acceptable at Neptune; however, if it is not, the TOF can either be increased somewhat to reduce the probe entry speed, or in the extreme case, the probe can be released after capture.

For the 2031 M0JN trajectory, the optimization is done using EMTG, which substantially reduced the flight time to 11.7 years, and provided a greater delivered mass of 2500 kg. A plot of the trajectory is shown in Fig. 4.3 which also provides trajectory characteristics at each encounter. We note that the final mass reported in the figure, does not include the 12% propellant-mass penalty, which (for this trajectory) reduces the delivered mass value to 2500 kg.
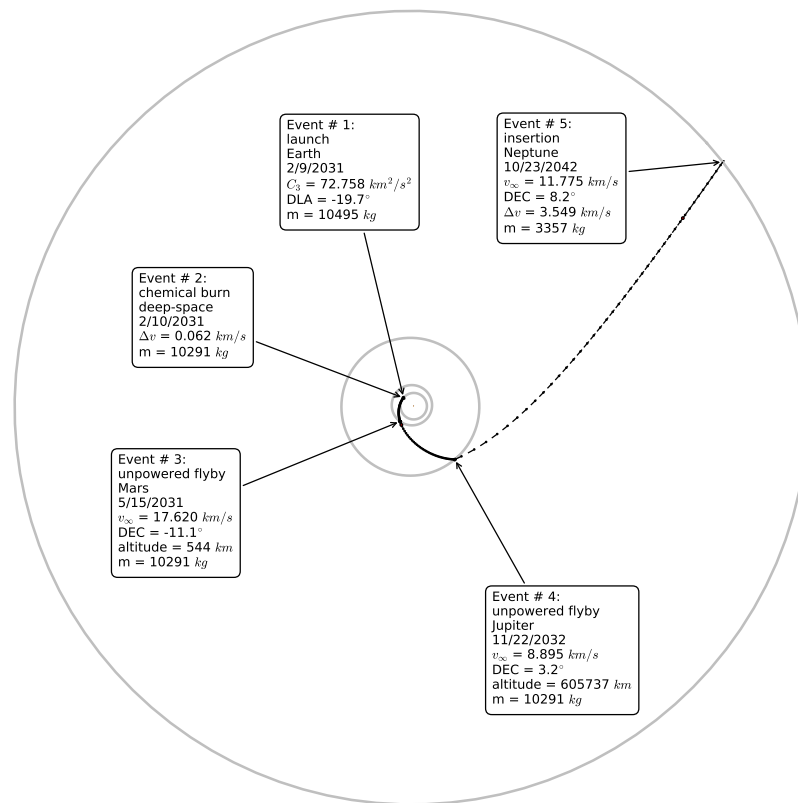
Figure 4.3.: Select candidate trajectory in 2031 for Neptune probe and orbiter mission, using the SLS Block 1B launch vehicle. Flybys occur at Mars and Jupiter, with a small DSM just after Earth launch.

Other attractive characteristics of the 2031 M0JN trajectory, are its launch and arrival declination angles. At launch, its declination angle magnitude is 19.6°, which

is less than 28.5°, and thus can launch from from Kennedy Space Center heading directly East, and take full advantage of Earth's spin (at KSC's latitude). The arrival declination angle at Neptune is also relatively small, at 8.24°, which is beneficial for any mission where an orbit in Neptune's equatorial plane is desired. An equatorial orbit will likely be desired in order to tour Neptune's moons, since an equatorial orbit provides much slower encounter velocities (in general) than are possible for a capture orbit highly inclined to the orbital plane of the moons.

The approach at Neptune is shown in Fig. 4.4, which is simulated using MATLAB. The prograde approach allows the probe to enter Neptune's atmosphere in the same direction as the atmosphere rotates, and thus reduce the atmosphere-relative entry speed which reduces heating on the probe during entry and thereby the TPS mass. For this prograde approach, the atmosphere-relative entry speed is 22.5 km/s for an entry flight path angle of -25.0°(both of which computed for an oblate-spheroid shaped atmosphere). This entry speed is comparable to the entry speed of 22 km/s in Ref. [22] for Uranus. The approach is very nearly at the minimum inclination solution (ψ value of $3\pi/2$) with a slight increase in inclination implemented (by decreasing ψ by 8.6°) so that the probe enters before crossing the ring plane. The orbiter approach is the minimum inclination solution. Using the same range of entry flight path angles as for Uranus (-40°to -25°), Table 4.9 provides a set of entry parameters that span the range of flight path angles.

For reference, the retrograde approach is also shown in Fig. 4.4. At Neptune, a retrograde approach will likely be preferable to a prograde approach, since Neptune's (arguably) most interesting moon Triton is in a retrograde orbit about the planet. Since an orbiter at Neptune will very likely be conducting flybys of Triton, a retrograde capture orbit (or even a polar orbit) about Neptune will significantly reduce the encounter velocities at Triton. The trouble with the retrograde approach however, is coordinating with the probe. If the probe approaches prograde while the orbiter approaches retrograde, the probe will loose line of sight with the orbiter during entry and will not be able to transmit its data. If the probe approaches retrograde near the
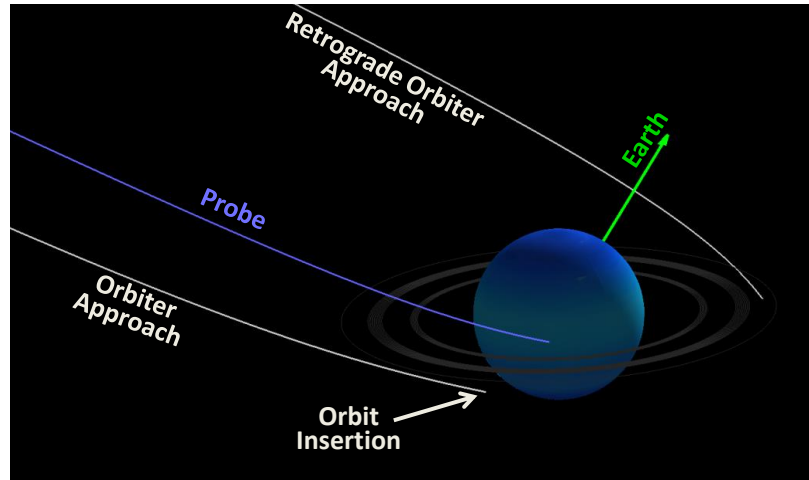
Figure 4.4.: Approach at Neptune with probe and orbiter entering prograde. The retrograde orbiter approach is also shown for comparison.

Table 4.9.: Feb. 9, 2031 Trajectory: Prograde Entry at Neptune

$V_{Inertial}$, km/s	FPA, deg	Heading, deg	Lat, deg	Long, deg	$V_{Atm-Rel}$, km/s
25.126	-40.007	85.398	10.949	-46.539	22.952
25.126	-38.689	85.020	10.782	-44.624	22.904
25.125	-37.345	84.641	10.600	-42.669	22.858
25.125	-35.971	84.259	10.401	-40.667	22.811
25.125	-34.564	83.876	10.183	-38.613	22.766
25.125	-33.117	83.490	9.944	-36.497	22.720
25.124	-31.624	83.102	9.684	-34.309	22.674
25.124	-30.077	82.710	9.398	-32.038	22.629
25.124	-28.468	82.314	9.084	-29.670	22.584
25.124	-26.782	81.913	8.738	-27.183	22.540
25.123	-25.005	81.506	8.353	-24.554	22.495

equatorial plane (i.e. in the plane of the retrograde orbiter approach), the atmosphere-relative entry speed will increase (for this trajectory) by about 6 km/s.

A compromise may be found in the retrograde design shown in Fig. 4.5, which has the probe enter in a near polar orbit (biased slightly to the retrograde side). This approach maintains line of sight between the orbiter and probe during entry, and allows the probe to avoid entering Neptune's atmosphere (as much as it can) in the

opposite direction of the planet's rotation. For this design, the probe enters with an atmospheric-relative entry speed of 25.8 km/s for an entry flight path angle of about -25.0°. This entry speed is significantly larger than the 22 km/s in Ref. [22], and determining whether this value (as well as that for the prograde solution) is acceptable, is beyond the scope of this work. However, with regards to the feasibility of using the M0JN trajectory for a probe and orbiter mission, the probe could be released after the orbiter captures at Uranus. In fact, since the removal of the probe's mass is not accounted for before the capture mass at Neptune is calculated, all delivered mass values at Neptune presented in this paper may be interpreted as mass delivered assuming the probe is released after capture. As for the case for the prograde probe-entry scenario, a set of entry parameters spanning a range of entry flight path angles from -40°to -25°is provided for the near-polar probe entry scenario in Table 4.10.
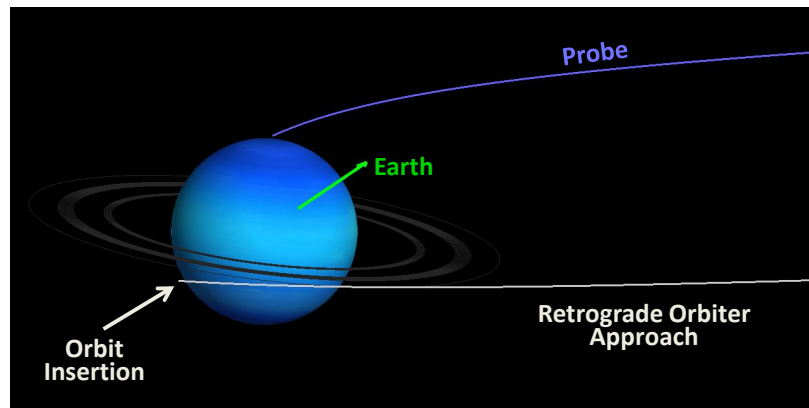
Figure 4.5.: Approach at Neptune with orbiter approaching retrograde, with probe entering in a near-polar orbit.

4.6 Candidate Trajectories for Aerocapture

As with the investigation of trajectories to Uranus, a preliminary analysis is done to identify candidate trajectories to Neptune that may be attractive for aerocapture. Such trajectories may allow for solutions with reduce the flight time, and increased delivered mass, for a given launch vehicle. In this work, we focus on the use of

Table 4.10.: Feb. 9, 2031 Trajectory: Near-Polar Entry at Neptune

$V_{Inertial}$, km/s	FPA, deg	Heading, deg	Lat, deg	Long, deg	$V_{Atm-Rel}$, km/s
25.259	-40.000	-137.923	73.037	-156.215	25.714
25.261	-38.676	-133.147	74.440	-161.178	25.722
25.262	-37.328	-127.328	75.738	-167.187	25.730
25.264	-35.952	-120.238	76.882	-174.471	25.739
25.265	-34.544	-111.695	77.807	176.786	25.747
25.265	-33.098	-101.686	78.431	166.570	25.755
25.266	-31.607	-90.523	78.664	155.195	25.763
25.265	-30.063	-78.906	78.438	143.357	25.772
25.265	-28.457	-67.714	77.720	131.933	25.780
25.263	-26.775	-57.645	76.520	121.620	25.788
25.261	-25.001	-49.015	74.872	112.731	25.797

aerocapture for trajectories launching with the Atlas V 551 and Delta IV Heavy launch vehicles, since aerocapture may allow these vehicles to provide trajectories that are comparably attractive to solutions found using the SLS Block 1B (without aerocapture). For all aerocapture trajectories found in this analysis, we uniformly assume that the TPS mass required for aerocapture is 50% of the arrival mass at Neptune. We also only consider solutions that have flight times of 12 years of less.

The catalogs of aerocapture trajectories for the Atlas V 551 and Delta IV Heavy are given in Tables 4.11 and 4.12. For the Atlas V 551, no solutions are found that can deliver near 2000 kg at Neptune; however, many of these solutions are likely capable of delivering more mass once optimized in a tool such as EMTG or MALTO. For the Delta IV Heavy, three trajectories ae found that deliver about 2000 kg or more. One of the more interesting solutions, with launch date in 2042, delivers over 2.1 Mg with a flight time of 9 years—over two years faster than any (non aerocapture) trajectory found that uses an SLS Block 1B.

Table 4.11.: Preliminary Neptune Aerocapture Trajectory Catalog: Atlas V 551

Launch Date	Flyby Path	TOF, yrs	Mass, Mg	$V_{\infty,Neptune}$, km/s
9/11/2026	VVEE0JN	11.8	1.1	24.2
9/8/2039	VEE0JN	11.6	1.3	22.2
12/26/2040	VEE0JN	11.0	1.1	19.8
1/25/2041	VEE0JN	11.6	1.0	17.7
7/29/2042	VVE0JN	9.0	1.1	21.1
11/19/2051	VEE0JN	11.7	1.1	24.9
12/13/2053	VEE0JN	10.8	1.0	20.2
1/7/2054	VEE0JN	10.7	1.0	20.3

Table 4.12.: Preliminary Neptune Aerocapture Trajectory Catalog: Delta IV Heavy

Launch Date	Flyby Path	TOF, yrs	Mass, Mg	$V_{\infty,Neptune}$, km/s
09/11/2026	VVEE0JN	11.8	1.9	24.2
12/10/2027	VEE0JN	11.2	1.0	21.4
01/14/2028	VEE0JN	10.8	1.1	22.4
05/03/2029	0E0JN	10.5	1.1	18.9
02/17/2031	M0JN	9.3	1.0	16.1
09/08/2039	VEE0JN	11.6	2.3	22.2
12/16/2040	VEE0JN	10.4	1.5	21.8
05/05/2041	0E0JN	10.4	1.2	20.7
07/29/2042	VVE0JN	9.0	2.1	21.1
11/22/2051	VEE0JN	11.6	1.1	25.4
01/08/2052	VEE0JN	11.5	1.5	25.4
12/18/2053	VEE0JN	10.0	1.2	23.0
01/10/2054	VEE0JN	9.9	1.2	23.1
12/25/2065	VEE0JN	11.8	1.1	19.6
04/19/2066	VEE0JN	10.9	1.1	21.7
08/02/2067	0E0JN	10.8	1.1	17.9

4.7 Conclusion

Several catalogs of trajectories to Neptune are presented for capture missions to Neptune for various mission constraints. If capture outside Neptune's rings is required, only the SLS Block 1B is capable of delivering a 2000 kg payload in orbit at

Neptune, unless an optimization program such as EMTG or MALTO can significantly improve upon the Atlas V 551 and Delta IV Heavy solutions. If capture inside Neptune's rings is found to be acceptable, the Delta IV Heavy was found to be capable of delivering near 2000 kg in the early 2040s, which may provide a case to attempt capture inside the rings (especially if the SLS is not available). If the SLS is available, many trajectories to Neptune are found for capture both outside and inside Neptune's rings. One catch with the SLS however is that many of the solutions require larger amounts of propellant mass, which can be avoided without much loss in flight time (but potentially a loss in delivered mass for some launch years) by launching on trajectories with high C_3 (often using a STAR 48) with fewer gravity assist.

In general, the most attractive solutions found use a Jupiter gravity assist; however, within the constraints of this study, Jupiter is not available for the launch years 2021–2024, 2034–2036, 2047–2050, and 2059–2062. During such times (except for 2034–2036) Saturn gravity assist, and often Venus and Earth gravity assists, can be used to deliver near 2000 kg of mass at Neptune. Direct launch to Neptune (with no gravity assists) may also be an option if smaller delivered mass values are acceptable for the mission, as optimization in EMTG or MALTO is not expected to significantly improve the direct launch solutions.

A candidate mission for a Neptune probe and orbiter mission is presented, which (after optimization in EMTG) delivers 2500 kg to Neptune in 11.7 years. The trajectory launches on February 9, 2031 and flies by Mars and Jupiter on route to Neptune. The declination for this trajectory is relatively small, at 8.2°, which is conducive for an equatorial orbiter to conduct science at Triton. A candidate approach trajectory is presented to allow for probe release as well as probe-orbiter communication during probe entry. Although a Mars flyby may limit the size of the launch window for such a trajectory, several Jupiter flyby solutions (without Mars) are found in neighboring years which may be sufficient for such a mission. In such a case, catching the window

when Mars is available may simple provide additional propellant for secondary science and extended mission options.

If the SLS is not available, aerocapture may be a viable option to get similar performance from the Delta IV Heavy for certain launch years. One particularly interesting case found launches on July 29, 2042, delivers 2100 kg of mass in only 9 years, using a Venus-Venus-Earth-Jupiter gravity assist combination, which outperforms the SLS in terms of flight time by over two years. Although not investigated in this study, technologies other than aerocapture may also provide attractive alternate trajectories if the SLS is not available. For example, solar electric propulsion (SEP), or electric propulsion powered by a nuclear (or some other) power source, such as a radioisotope thermoelectric generator (REP), may prove to be the best options if the SLS is not available, and may even prove to outperform the SLS. Nuclear powered electric propulsion in particular may be a very attractive option since the majority of the time spent on route to Neptune occurs beyond the orbit of Jupiter, where SEP is (generally) no longer effective.

5. FAST FREE RETURNS TO MARS AND VENUS WITH APPLICATION TO INSPIRATION MARS

Mars free-return trajectories are investigated, both with and without the use of Venus for gravity assist. Launch dates are searched from 2015 to 2060, and focus is placed on identifying opportunities that have a short total time of flight (i.e. that are "fast" among the available free-return opportunities), so that they may be used for a human mission to fly by Mars. Constraints on Earth launch V_∞ and Earth arrival V_∞ are based on those used for the nominal Inspiration Mars opportunity in 2018. All attractive Mars free-return candidates found are shown to be rare, with launch opportunities only repeating (approximately) every 15 years, or every 32 years if a Venus flyby is used. A set of near-term candidate trajectories are found using the gravity-assist path Earth-Venus-Mars-Earth, that may be suitable for backup to (or replacement for) the nominal Inspiration Mars free return. One such candidate, with launch date on November 22, 2021, has an Earth launch V_∞ of 4.50 km/s (C_3 of 20.25 km^2/s^2) and an arrival V_∞ of 6.53 km/s (entry speed of 12.85 km/s)—both lower than the nominal Inspiration Mars trajectory—with a total flight time of 582 days. Venus free-return opportunities are also found, with promising application for a human flyby mission to Venus. An entry analysis is done for select cases (including the 2018 and 2021 opportunities) and shown to be feasible using present-day or near-term technology. An opportunity in 2023 is also found, which may be feasible if aerocapture is available.

5.1 Introduction

In the last several decades, there have been many trajectory designs for human missions to Mars [58–83]. Despite this effort, humans have yet to stand on the surface of the red planet, and it remains a long-term goal for many nations.

In 2013, Tito et al. [79] proposed a US-lead human Mars flyby mission, dubbed "Inspiration Mars," that could be launched in 2018 with a two-person (one man and one woman) crew. This proposal was based on a trajectory reported by Patel et al. [67] who investigated Mars free-return trajectories (i.e. trajectories that flyby Mars and return to Earth, without the use of any deterministic maneuvers) with launch dates ranging from 1995 to 2020. In their paper, several notably "fast" trajectories were highlighted that had relatively short times of flight (TOF) of about 1.4 years. One of these fast trajectories, with a launch date on January 5, 2018, was selected by Tito et al. [79] because its 501-day flight time, launch energy, and Earth entry speed, were considered feasible (by their analysis) with near-term or present day technology.

In 1969, Hollister [84] (and Hollister and Menning in 1970 [85]) found special case free-returns between Earth and Venus that are capable of repeating indefinitely. Such trajectories are known as "cyclers," and were found by Rall and Hollister [68] to exist between Earth and Mars. Since their discovery, investigations of Earth-Mars cyclers have continued [69–75], and are usually proposed as a low-cost means (due to reusability) for transporting humans to Mars.

In 2002, Okutsu and Longuski [76] investigated Mars free-return trajectories that incorporate an intermediate flyby of Venus, with launch dates ranging from 2010 to 2025. A notable trajectory from their study was found (with launch date in 2014— clearly too soon for Inspiration Mars) that met all of the energy and TOF constraints within NASA's Design Reference Mission [63, 64], and was proposed as a candidate for a near term human mission to Mars.

In 2010, Foster and Daniels [78] investigated round-trip trajectories to Near-Earth objects (NEOs), Venus, and Mars (including trajectories to Mars with an intermedi-

ate Venus flyby). The trajectories found use impulsive maneuvers at each encounter (i.e. a powered flyby) and are therefore not *free* returns, but they do allow a spacecraft to return to Earth using maneuvers that are feasible with present day chemical propulsion systems.

In 2013, Bailey et al. [80] and Folta et al. [81] found fast round-trip trajectories with short stay-times in orbit at Mars. Their study includes trajectories that fly directly to and from Mars, as well as trajectories that use a Venus gravity assist before and/or after the Mars encounter. The trajectories found achieve short transfer times with the use of on-orbit staging. Many solutions were found with a total mission duration of about 1 year.

Trajectories for Mars flyby missions using low-thrust solar electric propulsion (SEP) were investigated in 2014 by De Smet et al. [82]. These trajectories were not free-returns, but were aimed for missions similar to Inspiration Mars, with the use of near-term low-thrust propulsion. In their study, low-thrust trajectories that use Venus for gravity assist were also found.

5.2 Methods

5.2.1 Satellite Tour Design Program (STOUR)

The STOUR program (developed by the Jet Propulsion Laboratory [28] and by Purdue University [3, 26]) was used to compute the free-return opportunities presented in this study. The STOUR program uses a patched-conic model with an analytic ephemeris (by Sturms [2]) to rapidly compute multiple gravity-assist trajectories. It imposes a search to find trajectories by stepping through specified launch dates and launch V_∞—thereby revealing all candidate trajectories within the search parameters. Free returns are found using a "vis viva matching" algorithm, as described by Longuski and Williams [26], to ensure that the incoming and outgoing V_∞ at an encounter are equal. Furthermore, this algorithm only stores solutions for which the required closest approach altitude (for the gravity assist) is at or above

the user-specified minimum value—providing only solutions that do not require a deterministic maneuver.

From the list of candidate trajectories found using STOUR, the most desirable trajectories are selected based on parameters such as launch date, launch V_∞, arrival V_∞, and TOF. Of these "best case" opportunities, free-returns that provide characteristics comparable to those for the Inspiration Mars mission can be identified as potential candidates for a similar, "IM-type," Mars flyby mission, or perhaps will provide a second chance opportunity for the Inspiration Mars mission itself.

The nominal Inspiration Mars trajectory (with launch date in 2018) is used as a baseline to determine the upper bounds for acceptable launch V_∞, arrival V_∞, and TOF values (as reported by Tito et al. [79]). Any trajectories found with launch V_∞, arrival V_∞, and TOF values within the upper bounds are considered candidates, however some trajectories are identified as (possibly) being more desirable than others. Table 5.1 shows the constraints used for the trajectory search in STOUR. In some cases, searches were performed with bounds set beyond those listed in Table 5.1, however, only trajectories that meet the Table 5.1 constraints are considered to be candidates for an IM-type mission. One possible exception is the listed value for maximum Earth arrival V_∞, which is an estimated upper bound (based on the nominal Inspiration Mars free return) and is investigated in detail in Sec. 5.3.3.

Table 5.1.: Trajectory Search Parameters

Parameter	Value
Max $V_{\infty,L}$ (C_3)	6.5 km/s (42.25 km^2/s^2)
Max $V_{\infty,A}$ (Entry Speed)	9.0 km/s (14.27 km/s)
Max TOF	600 days

The TOF for long-endurance space flight is difficult to put a constraint on. The current world record, held by cosmonaut Valeri Polyakov, is 437 consecutive days in low Earth orbit (LEO)—admittedly under the protection from space radiation by Earths magnetic field. The maximum TOF constraint of 600 days is chosen in this

study (somewhat arbitrarily) to include the fastest known TOF free-returns. From Bailey et al. [80] and Semones [86], a 600-day TOF would result in a 55-year-old male (and 60-year-old female) crew member to approximately reach their permissible exposure limit for their entire career (based on radiation exposure in LEO). However, research has yet to show that humans cannot tolerate radiation exposure in deep space for a mission of such duration.

The maximum launch V_∞ (or C_3) in Table 5.1 is based on the value used by Tito et al. [79], which is approximately the maximum achievable C_3 for a SpaceX Falcon Heavy to deliver the 10-metric ton payload mass estimated by Tito et al. for Inspiration Mars. This payload mass is based on the use of a SpaceX Dragon capsule (with a dry mass of about 4,200 kg), along with a proposed Environmental Control and Life Support System (ECLSS) with a mass estimated to be less than 6,000 kg [79]. For such a payload mass, the SpaceX Falcon Heavy launch vehicle can deliver a C_3 of approximately 39 km^2/s^2 (V_∞ of 6.25 km/s)—sufficient for the nominal Inspiration Mars trajectory. (In Table 5.1, the listed Max $V_{\infty,L}$ has been rounded up to the nearest half-km/s to ensure all free-returns near the nominal Inspiration Mars trajectory are found in the STOUR search.)

The 10 metric ton payload-mass estimate by Tito et al. [79] may be a bit optimistic. If the payload mass in the final Inspiration Mars design turns out to be larger than 10 metric tons, a larger launch vehicle will likely be needed. The Space Launch System (SLS), is expected to launch its first human crew in 2021 [87], and is estimated to be capable of launching a payload mass of over 20 metric tons with a C_3 of 40 km^2/s^2 (V_∞ of about 6.3 km/s) [35]. Such a launch capability depends on the choice of upper stage, but more importantly is more than sufficient for the expected payload mass of the Inspiration Mars mission. The SLS is not expected to be available by 2018, however, and therefore cannot be used for the nominal Inspiration Mars opportunity—making an alternate opportunity essential for the success of Inspiration Mars, or some other IM-type mission.

For the case of the traditional gravity-assist path Earth-Mars-Earth, launch dates are searched over a 100-year span, from December 1, 2014 to January 31, 2115. This extended search is to assess the rarity of the nominal Inspiration Mars opportunity over a broad time period. For all other gravity assist paths, a shorter span of launch dates is considered; however, it should be noted that (as stated by Okutsu et al. [76]) the inertial geometry of the planets Earth, Venus, and Mars (and therefore for Earth and Mars as well) approximately repeats every 32 years. Therefore, any search over 32 years is only expected to reproduce trajectories that are very similar to those found in the initial 32-year search. For the case of the traditional EME Mars free-return results, a span of 100 years was investigated to identify any small deviations in these repeated solutions, and assess how the nominal 2018 trajectory for Inspiration Mars compares to it's counterparts (when the inertial geometry repeats).

5.2.2 Pareto-Optimal Set

For the case of near-term trajectories, no single trajectory has a minimum of all three parameters: TOF, $V_{\infty,L}$, and $V_{\infty,A}$. Therefore, the Pareto-optimal set (or Pareto set) of trajectories are identified as the "best" candidates for backup to the Inspiration Mars (or similar IM-type) mission.

For a given trajectory, the design objectives (for this study) are TOF, $V_{\infty,L}$, and $V_{\infty,A}$. When comparing two trajectories (e.g. Trajectory A and Trajectory B) from the set of all near-term candidates, Trajectory A is said to "dominate" Trajectory B if all objectives in Trajectory A are less than or equal to (with at least one objective strictly less than) the objectives of Trajectory B. Otherwise, the two trajectories are "nondominated." For example, trajectories A and B are nondominated (with respect to each other) if Trajectory A has a lower TOF than Trajectory B, but Trajectory B has a lower launch V_{∞} than Trajectory A.

By comparing all trajectories found in STOUR, the remaining nondominated trajectories (i.e. the trajectories that are not dominated by any other trajectory in the

STOUR results) make up the Pareto-optimal set—any of which could be argued as the best case. A complete discussion of Pareto-optimal sets is given by Arora [88].

5.2.3 Earth Entry Parameters and Constraints

The ballistic coefficient β, of an entry vehicle is an important parameter and is defined by

$$\beta = m/SC_D \tag{5.1}$$

where m, C_D, and S are the vehicle mass, drag coefficient (at zero angle-of-attack), and reference surface area of the heat shield, respectively. An entry spacecraft with lower ballistic coefficient is desired as it helps to reduce the deceleration loads and peak stagnation point heat rates. However, ballistic coefficient is dictated by the volumetric constraints of a spacecraft.

In this study, two different entry vehicles are considered: the SpaceX Dragon [89], and NASA's Orion [90]. Since, the drag area, SC_D, of the Dragon entry vehicle is smaller than that of the Orion, the β value for Dragon is higher than that of Orion (for a given vehicle mass). However, until a detailed IM-type mission design is done with a master equipment list, the entry vehicle mass for both Dragon and Orion cannot be computed. Therefore, it is assumed in this analysis that the ballistic coefficients of both the Dragon and Orion vehicles are 362 kg/m^2 (similar to that of Apollo entry vehicles), with reference heat shield diameters of 3.7 m and 5.3 m, respectively.

The spacecraft hemispherical nose radius for the Dragon and Orion entry vehicles are 4.69 m and 6.0 m, respectively [89,90]. The entry vehicles fly at a nominal positive angle-of-attack which produces a modest maximum lift-to-drag (L/D) capability. The classical bank angle control method is used to modulate the lift vector that guides the entry vehicle to the desired landing site and at the same time maintain the deceleration load and peak heat-rate within tolerable limits. Therefore, limits of the control on the Dragon is such that $-0.18 \leq L/D \leq 0.18$ and that on the Orion is such

that $-0.24 \leq L/D \leq 0.24$. For the entry analysis at Earth, a strictly exponential atmospheric model is used with a scale height of 7.3 km and a surface atmospheric density of 1.225 kg/m^3.

The most important parameters for manned spacecraft entry trajectory design are the deceleration loads acting on the crew, peak heat rates and peak dynamic pressure on the heat shield, and the total heat load. The peak heat rates and peak dynamic pressure on the heat shield drive the choice in type of thermal protection system (TPS) material to be used, while the total heat load drives the value of total TPS mass.

Human body is sensitive to deceleration "loads" (i.e. the deceleration acting on a human body as a function of time), as well as on the rate of change of acceleration (i.e. the "jerk") expressed in m/s^3. Guided entry like in the case of Apollo and Mars Science Laboratory does not exhibit significant jerk except during events like parachute deployment, where momentary spikes in deceleration can be observed due to abrupt changes in ballistic coefficient.

In the US, studies on human tolerance of deceleration were done during the 1960s for the manned spaceflight program. Figure 5.1 shows a plot of deceleration versus time, and the limits of human tolerance. The tolerance of deceleration during atmospheric flight is greatest along the $\pm x$-directions. As a result, all crew are placed in a seated position for all entry spacecraft. The acceleration (or deceleration) experienced by the crew is called either "eyeballs out" or "eyeballs in", depending on the direction of the acceleration experienced by the crew. The upper bound for such acceleration on the human body is indicated in Fig. 5.1 by a solid line (with hash marks above) and labeled "Eyeballs Out or In."

Figure 5.1 shows that the human tolerance for time spent while experiencing an acceleration of 10 g's is 1 minute. For 8 g's, humans can tolerate 2 minutes, and for 7 g's, they can tolerate around 4 minutes. The decelerations beyond the limits in Fig. 5.1 do not necessarily result in death, but are not considered to be acceptable for crews returning from space missions. For both the Soyuz TMA-10 and TMA-11
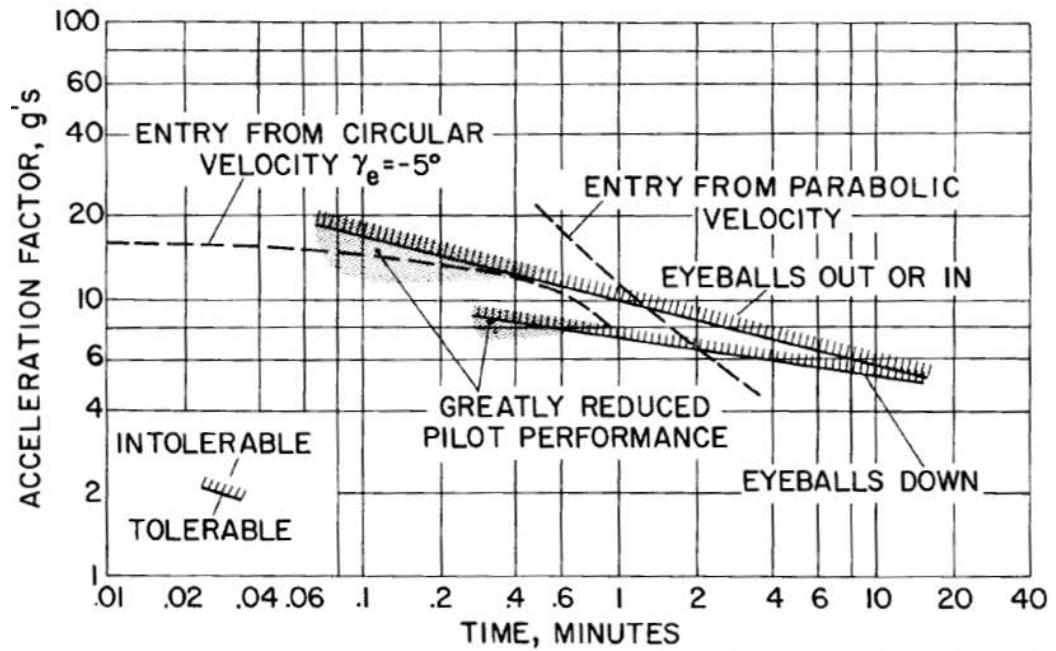
Figure 5.1.: Human tolerance limits of deceleration during spacecraft entry, descent, and landing [91]. The acceleration factor is expressed in Earth g's.

missions returning from the International Space Station (ISS) the crew pulled about 8 g's momentarily during its "unusual" ballistic entry [92]. During the Apollo program, crew experienced peak decelerations between 6.23 g's (Apollo 15) and 7.19 g's (Apollo 16) during entry.

In some cases, astronauts and cosmonauts have experienced more than 8 g's after living in microgravity for more than 200 days. However, it is not known what g-load can be tolerated after a mission exceeding 500 days—which is the case for many of the trajectories presented in this paper. Because of this uncertainty, and since only optimal entry trajectory solutions (without stochastic errors) are presented, only solutions with peak deceleration less than around 7 g's are considered to be acceptable.

The peak g-load experienced by the crew is largely dictated by the entry speed at Earth arrival, which is dictated by the interplanetary trajectory. Therefore, there is little that can be done to reduce the peak g-load beyond the minimization done by the Gauss Pseudospectral Optimization Software (described in the next section).

Additionally, if stochastic errors were to be considered for the solutions presented in this paper (a topic beyond the scope of this study), the peak g-loads would be even larger. Thus, it is clear that the Inspiration Mars (or other IM-type) mission will test the limits of the human body.

With regards to heating, the performance of the TPS during atmospheric flight is influenced by the total peak heat-rate (W/cm^2) and total heat load (J/cm^2), both defined at the stagnation-point. As stated previously, the peak heat rate (along with the peak dynamic pressure) determines the type of TPS material to be used, and the total heat load drives the thickness of the TPS (i.e. the TPS mass). During atmospheric flight, heat is transferred from the high temperature shock layer via the processes of convection and radiation. For hypervelocity entry (such as for the trajectories considered in this study), shock layer radiative heating dominates over convective heating.

The only hypervelocity entry performed to date was by that of NASA's Stardust spacecraft, which entered Earth (ballistically) at a speed of 12.9 km/s with a total stagnation-point heat rate of about 1200 W/cm^2. However, the nose radius of Stardust was about 0.22 m, which is very small compared to the nose radii of both the Dragon and Orion entry vehicles. Aerothermal conditions of the Stardust spacecraft are, therefore, not representative for Dragon and Orion. Furthermore, the entry speed of the nominal Inspiration Mars opportunity (of about 14 km/s) is greater than that of Stardust's entry speed.

The convective heating at the stagnation-point of the spacecraft is given by the Sutton-Graves relation for Earth entry [93]

$$\dot{q}_c = 18.8 V^3 \sqrt{\rho / R_n} \tag{5.2}$$

where V is the spacecraft speed in m/s, ρ is the freestream flow density in kg/m^3, and R_n is the spacecraft hemispherical nose radius in m.

The classical Tauber-Sutton correlation for radiative heating is valid in the speed range from 9 to 16 km/s and for freestream densities from 6.66×10^{-5} to 6.31×10^{-4}

kg/m³, or altitudes of about 72 to 54 km, respectively [94]. However, the correlation is only usable for nose radii from 0.3 to 3 m and thus not applicable to the baseline entry vehicles considered (with nose radii greater than 3 m). Therefore, a new correlation is used (developed by Brandis and Johnson [95]) for radiative heating at Earth entry, given by

$$\dot{q}_r = C R_n^a \rho^b f(V) \tag{5.3}$$

where $\dot{q}_r$ is the radiative heat flux in W/cm², C is a nondimensional constant with a value of 3.416×10^4, R_n is the spacecraft hemispherical nose radius in m, ρ is the freestream density in kg/m³, and V is the spacecraft speed in m/s. The exponent b is a nondimensional constant with a value of 1.261. The exponent a is a function of ρ and V, given by

$$a = \min\{3.175 \times 10^6 V^{-1.8} \rho^{-0.1575}, 0.49\} \tag{5.4}$$

and $f(V)$ is given by

$$f(V) = -53.26 + 6555/[1 + (16000/V)^{8.25}] \tag{5.5}$$

The correlation given by Eq. 5.3 is valid for velocities from 9.5 km/s to 17 km/s and for freestream densities from 1×10^{-5} to 5×10^{-3} kg/m³, or altitudes from approximately 83.5 to 38.5 km, and for nose radii from 2 to 10 m. The total stagnation-point heat rate, $\dot{q}$, is the sum of the convective and radiative heat-rates expressed in W/cm² (i.e. $\dot{q} = \dot{q}_c + \dot{q}_r$). The time integration of the total heat rate gives the total stagnation-point heat load, Q in J/cm², given by

$$Q = \int_0^t (\dot{q}_c + \dot{q}_r) dt \tag{5.6}$$

5.2.4   Gauss Pseudospectral Optimization Software (GPOPS)

Optimal Earth entry trajectories are computed using the Gauss Pseudospectral Optimization Software (GPOPS) [96]. For trajectories in this paper, GPOPS is used to find entry trajectories that minimize the total heat load (or equivalently the thermal protection system mass), while constraining peak g-loads experienced by the crew and peak stagnation-point heat rates to within acceptable levels, as discussed in Sec. 5.2.3 and Sec. 5.3.3 (Table 5.7), respectively.

GPOPS is a general purpose optimal control software which converts the continuous time-optimal control problem into a nonlinear programming problem, which is then solved using the Interior Point Optimizer (IPOPT) [96]. In GPOPS, a mesh tolerance of 10^{-6} is used. The preference in the search is for a direct entry trajectory, however, for cases where a feasible direct entry trajectory does not exist, aerocapture solutions are computed to find trajectories with reduced g-loads and peak heat rates. The trajectories are computed from an entry altitude of 122 km (a value conventionally used for entry interface [97]), to a final altitude of around 3 km, whereupon the speed reduces to around 95 m/s and the parachute deploys (which is not modeled in this study). These terminal conditions are similar to those encountered by the Apollo entry vehicles.

5.3   Results

The traditional Mars free-return gravity assist path Earth-Mars-Earth (EME) is first examined in this study to assess the rarity (and possible uniqueness) of the nominal Inspiration Mars opportunity. A search is then conducted for alternate Mars free-return candidates (in the near term) for Inspiration Mars (or some other IM-type mission) by incorporating a Venus gravity assist. The rarity of Venus flyby candidates is investigated, and a comprehensive discussion of all available near-term Mars free-return opportunities (within the constraints of this study) is given. For select Mars free-return candidates, the entry problem at Earth is analyzed in depth to charac-

terize the feasibility of each candidate regarding current and near-term technologies. Lastly, Venus free-return trajectories are investigated for human flyby missions to Venus (without a Mars flyby), in an attempt to account for all available opportunities for a near-term, human flyby mission to another planet (that is similar in scope to Inspiration Mars).

5.3.1 Rarity of the Nominal Inspiration Mars Free-Return Trajectory

To assess the nominal Inspiration Mars free-return with regards to how rarely such a launch opportunity occurs, traditional Mars free-returns (i.e. using the gravity assist path EME) are searched using the STOUR program for over a 100-year span of launch dates—from December 1, 2014 to January 31, 2115—with two-day time steps. The search steps through launch V_∞ values up to 7 km/s (C_3 of 49 km^2/s^2) with incremental steps of 0.1 km/s, and allows for TOF of up to 600 days, and Earth arrival V_∞ of up to 9 km/s (entry speed of 14.27 km/s). The results from this search are given in Fig. 5.2, where several opportunities over the next century are shown that meet the IM-type mission constraints. TOF is shown on the vertical axis and launch date is shown on the horizontal axis. Each data point on the plot (indicated by a numerical index) represents a Mars free-return trajectory, and the value of the numerical index corresponds to a launch V_∞ value, as indicated by the color bar to the right of the plot.

For clarity, the launch year is annotated for each set of trajectories in Fig. 5.2, where columns that show two consecutive years represent opportunities with launch windows spanning December of the earlier year through January of the later year. The only near-term opportunities are shown to have launch dates in December of 2017 through January of 2018—the window for the nominal Inspiration Mars opportunity.

One may expect the columns of opportunities to repeat every 2.135 years, since that is the synodic period of Earth and Mars (assuming circular, coplanar orbits). However, these results indicate that (in order to meet the constraints for an IM-type
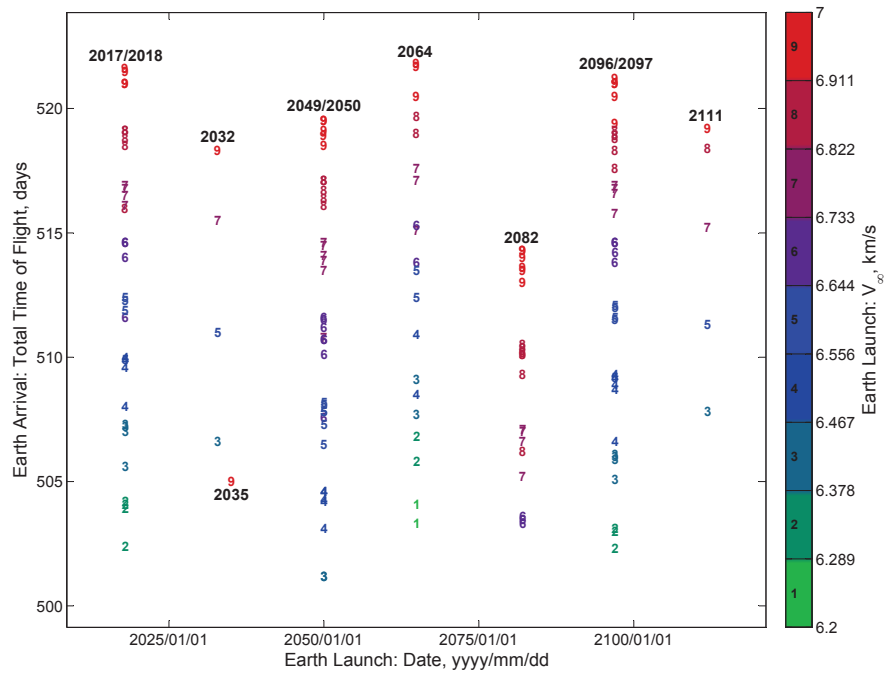
Figure 5.2.: EME free returns from December 1, 2014 to January 31, 2115. The launch year(s) for each "column" of solutions is annotated on the figure.

mission) non-circular, and possibly non-coplanar, aspects of the orbit geometries of Earth and Mars play a significant role in the computation of the candidate free returns.

In inertial space, the geometries (or positions) of Earth and Mars approximately repeat in 32 years, and therefore so do any trajectories between the two planets. That being the case, any inertially dependent characteristics of the planets' orbits (such as the non-circular and non-coplanar aspects) will approximately repeat in 32 years, as well as any free-return trajectories that are dependent on such characteristics (e.g. encounters at Mars during its passing through the ecliptic). This 32-year cycle occurs because Mars revolves around the Sun almost exactly an integer number of times (17.014) within 32 Earth revolutions about the Sun—leaving the two planets in almost exactly the same inertial positions 32 years later. Thus, although solutions

do not appear to repeat on a 2.135-year cycle in Fig. 5.2, most of the solutions shown in Fig. 5.2 do appear to repeat on a 32-year cycle. For example, the 2017/2018 opportunities appear to repeat 32 years later in 2049/2050, and then again in 2082. Similarly, the opportunities in 2032 appear to repeat in 2064 and 2096/2097. The opportunities in 2035 and 2111, however, do not appear to have any corresponding solutions in 32-year intervals (that is, not any corresponding solutions found within the constraints of this search). It is expected however that corresponding solutions would be found, if the constraints of the search were relaxed (i.e. if larger launch V_∞, arrival V_∞, and TOF values were allowed).

To determine which of the opportunities found in Fig. 5.2 are the most desirable (over the 100-year search), the Pareto-optimal set of solutions is found. Figure 5.3 shows the same set of trajectories from Fig. 5.2, but now the arrival V_∞ at Earth is shown on the horizontal axis, and thus all three parameters of interest (launch V_∞, arrival V_∞, and TOF) are visible on the same plot. The trajectories that make the Pareto set are indicated by a circle, and are arguably the "best" cases of the search. Since some of these Pareto-set solutions violate the constrains for an IM-type mission, Table 5.2 lists only those solutions that meet the constrains. The results in the table are therefore the best-case (EME) free-return candidates for an IM-type mission in 100 years (as computed by STOUR). With regards to launch for the trajectories listed in Table 5.2 (and all other trajectories discussed in this paper), it is known that when the declination of the launch V_∞ vector exceeds (in magnitude) the inclination of the launch site (28.5º for Cape Canaveral), there are losses in launch vehicle performance. These losses are not investigated in general for this study, with the exception of four select trajectories discussed in Sec. 5.3.6.

One exception to the best cases listed in Table 5.2 is the opportunity in 2032. This free-return trajectory is not a member of the Pareto-optimal set, but does meet the IM-type mission constraints, and is the next available opportunity after the window in 2017/2018. Therefore, if only the EME gravity-assist path is considered, another candidate opportunity is not available until 2032 (albeit less desirable).
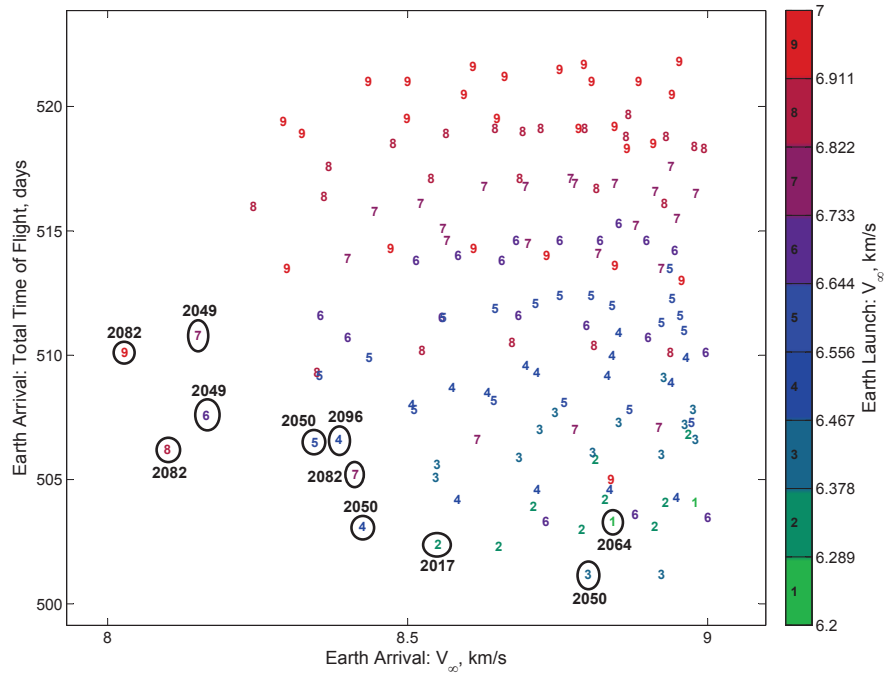
Figure 5.3.: Results from 100-year search of EME free returns with arrival V_∞ shown on the horizontal axis. The Pareto-optimal set of solutions (i.e. the "best" cases) are shown circled, along with the corresponding launch year.

Table 5.2.: Best Case EME Candidates for 100 Years

Launch Date	$V_{\infty,L}$, km/s	C_3, km^2/s^2	TOF, days	$V_{\infty,A}$, km/s	V_{Entry}, km/s
12/27/2017	6.30	39.69	502	8.55	13.99
*11/26/2032	6.40	40.96	507	8.98	14.26
01/10/2050	6.50	42.25	503	8.43	13.92
01/20/2050	6.40	40.96	501	8.80	14.15
12/18/2064	6.20	38.44	503	8.84	14.17
12/22/2096	6.50	42.25	507	8.39	13.89

*Candidate not in Pareto-optimal set

One interesting attribute of the opportunity in 2017 (in Table 5.2) is that the sum of its launch and arrival V_∞ values is the smallest of all Pareto-optimal set candidates, and therefore may be the closest to a minimum-energy transfer. Of course, (although

both of these values are preferably minimized) reducing the V_∞ at launch has a much different impact on the design than reducing the V_∞ arrival. Reducing the V_∞ at launch will lower the amount of propellant mass needed for the launch vehicle (for a given payload mass), and can possibly allow you to use a smaller launch vehicle—both of which reduce launch costs. For V_∞ at arrival however, the concern is related more to reducing the heating on the spacecraft upon atmospheric entry, as well as keeping the accelerations experienced by the astronauts to within tolerable amounts.

If the minimum launch energy is to be desired (with acceptable Earth entry speed and TOF), the best case in the near term remains the 2017 opportunity. Over the 100-year search however, the candidate found with lowest launch energy is the 12/18/2064 opportunity. (See Table 5.2.) Additionally, the fact that both launch and arrival velocity values for the entire Pareto-optimal set are near the constraint values, may be an indication that the imposed constraints are relatively difficult to meet. Forcing both launch and arrival V_∞ values to be small may, in turn, be restricting all solutions found to only those near the minimum-energy transfer. It is therefore of interest to investigate all Earth-Mars-Earth free returns near the theoretical minimum-energy transfer (in an attempt to identify the most desirable Earth-Mars geometries for an IM-type mission), and compare them to the solutions found in STOUR.

The Minimum-Energy Free Return

When transferring between two coplanar elliptical orbits (assuming collinear lines of apsides), Lawden [98] showed that for an impulsive ΔV-optimal transfer from one ellipse to another, the spacecraft must enter (and depart) the transfer arc tangentially, and at an apse (of the departure ellipse, transfer ellipse, and arrival ellipse). A special case of this theory is the Hohmann transfer, where the initial and final orbits are circular.

For ballistic Mars free-return trajectories, there is a complication due to the inclination of the orbit of Mars. Because of this inclination, a transfer angle of about

180º between Earth and Mars may result in a transfer arc that is inclined by nearly 90º with respect to the ecliptic. This near-90º transfer arc is caused by the Sun-Earth position vector (on the date of departure), and the Sun-Mars position vector (on the date of arrival) lying in a plane that is approximately normal to the ecliptic. Such a transfer between Earth and Mars may require an infeasibly large V_∞ at Earth launch (and possibly at Earth arrival for the Mars to Earth transfer). Additionally, if there is a large inclination difference between the transfer arcs before and after the Mars encounter, Mars may not be capable of providing sufficient gravity-assist (ballistically) to connect the two transfer arcs—rendering any such solution infeasible without the use of a maneuver (such as a broken-plane maneuver discussed in Sec. 5.3.2), and may therefore not appear in the ballistic trajectory search results from STOUR. The (possibly rare) trajectories that avoid this out-of-plane effect are those that encounter Mars as it passes through the ecliptic plane (at its ascending or descending node); placing Earth and Mars (and any connecting transfer arcs) in the ecliptic plane.

Therefore, the characteristics that will identify a minimum (or near minimum) energy free return, will have near 180º transfers (with Mars possibly near a node crossing at the time of the flyby), and will encounter Mars and Earth approximately tangentially, and near an apse (of both the planet's and the transfer arc's heliocentric trajectories).

Figure 5.4 shows the radial distance versus time for the 12/27/2017 free return candidate (given in Table 5.2). The lower and upper curves (that span the entire width of the plot) represent the orbits of Earth and Mars, respectively, and the central curve represents the spacecraft's free-return trajectory. The black dots on Mars' orbit represent the node crossings, where Mars passes through the ecliptic plane. All other dots represent an encounter at Earth or Mars. The inclination (relative to the ecliptic) for each leg of the free return is also indicated, and both are shown to be small.

The trajectory is shown to depart Earth near Earth's perihelion, flyby Mars near Mars' perihelion and node crossing, and (to a lesser extent) arrive at Earth near it's aphelion. The spacecraft trajectory is also very near its aphelion at the Mars

encounter. All of these attributes are characteristic of a (near) minimum-energy transfer.
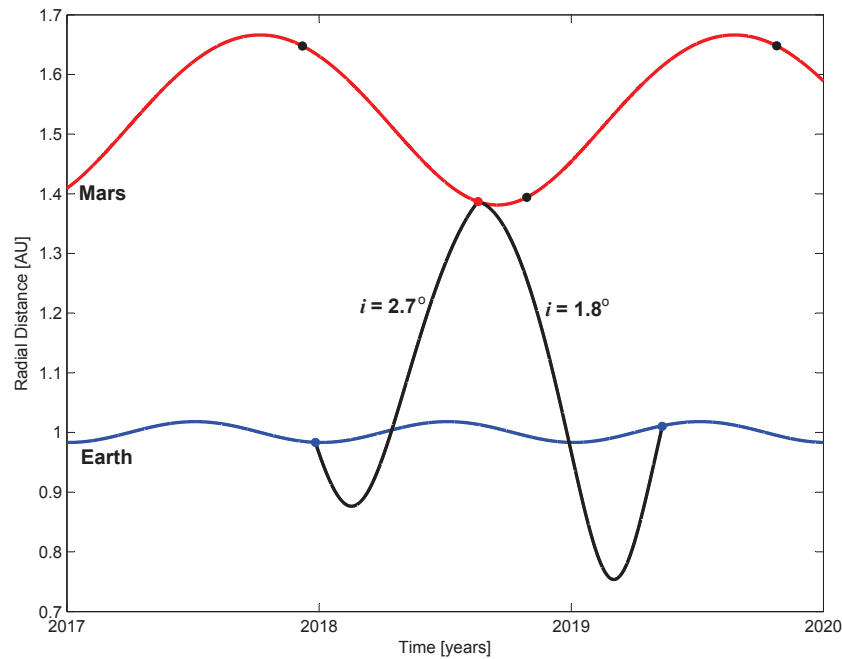
Figure 5.4.: Radial distance from the Sun shown over time for the 12/27/2017 free-return trajectory.

Deterministic Maneuvers

Part of the desirability of the 2018 opportunity for Inspiration Mars is that it is a *free* return, and therefore does not require any deterministic maneuvers to return the crew to Earth. Nevertheless, maneuvers are briefly investigated to determine if significant reductions in TOF, launch V_∞, and possibly arrival V_∞ can be achieved, for a moderately sized impulsive ΔV. Only powered flybys at Mars are considered for this investigation, and are implemented in STOUR using a subroutine that places the maneuver three days after the Mars encounter (i.e. three days after passage through hyperbolic periapsis). This three day delay is to allow time for navigators to

determine the spacecraft location after the flyby, before implementing a potentially large maneuver. Additionally, the delay forces STOUR to compute the maneuver outside of the gravity well of Mars. In practice, it may be the case that navigators need less than three days to determine the spacecraft states—allowing the maneuver to take some advantage of the gravity well of Mars—whereby the ΔV computed by STOUR is expected to be a conservative estimate. A full discussion of how this maneuver is implemented in STOUR is given in detail by Patel [29]. All maneuvers in this investigation are assumed impulsive and allowed a maximum ΔV size of 1 km/s.

Only near-term opportunities around the launch date of the nominal Inspiration Mars free return are considered in the STOUR trajectory search, which uses steps of 1 launch day and 0.25 km/s launch V_∞. Figure 5.5 shows the trajectory search results with regards to the impact of a maneuver on launch and arrival V_∞. (Note that due to the difficulty of viewing such a plot in three dimensions, TOF is not included in the figure.) Maneuver ΔV, arrival V_∞, and launch V_∞ are shown on the vertical axis, horizontal axis, and color bar (to the right of the figure), respectively.

The results show that, for more moderately sized maneuvers with ΔV below 0.5 km/s, an arrival V_∞ of 8.29 km/s (entry speed of 13.83 km/s) is achievable for a small 65 m/s maneuver, with launch V_∞ of 6.50 km/s (C_3 of 42.25 km^2/s^2). Overall, this is not much of a decrease from the nominal Inspiration Mars free return on 12/27/2017 (in Table 5.2), with entry speed of 13.99 km/s, which only requires a launch V_∞ of 6.30 km/s (C_3 of 39.69 km^2/s^2).

With regards to reducing TOF, it was found that a powered flyby at Mars has little to no effect, as the trajectories found in the search have TOF ranging from 497 days to 510 days—about the same as those found for the ballistic case (with no maneuver implemented), which ranged from 501 to 507 days. Specifically, to achieve a TOF of 497 days requires a fairly large maneuver of 0.41 km/s ΔV. The 497-day trajectory does however have a reduced launch V_∞ of 6.00 km/s (C_3 of 36.00 km^2/s^2),
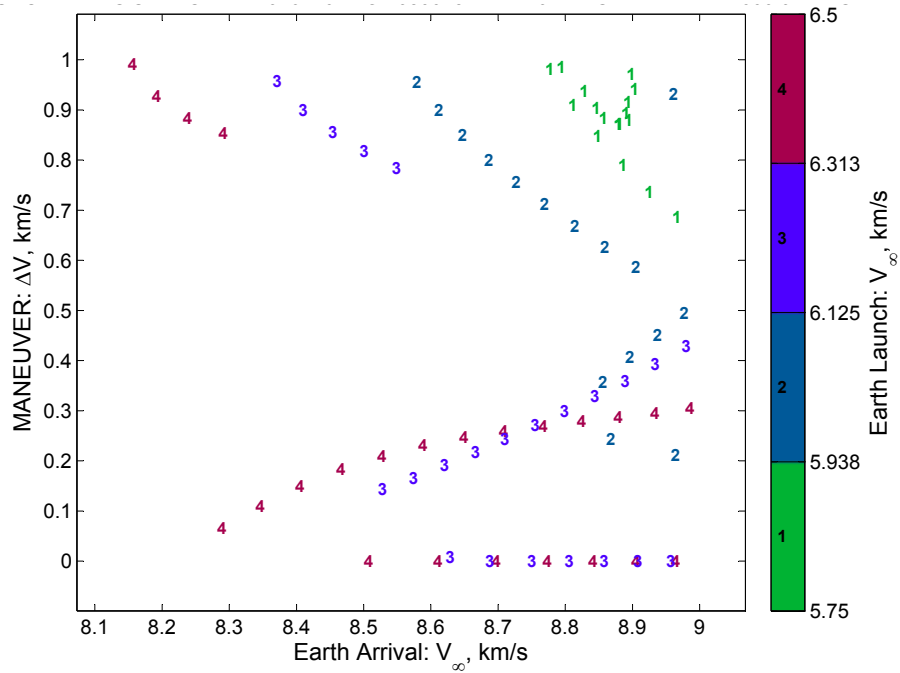
Figure 5.5.: STOUR results showing available opportunities in December 2017 to January 2018 with a powered flyby implemented at Mars.

compared to the nominal free-return on 12/27/2017 (see Table 5.2) with launch V_∞ of 6.30 km/s (C_3 of 39.69 km^2/s^2).

To compare these two trajectories, the maximum delivered payload mass is estimated. For the 497-day trajectory (with C3 of 36 km^2/s^2), Tito et al. [79] estimate that the Falcon Heavy can launch about 10 metric tons of payload (assuming launch from Cape Canaveral into a 28.5°-inclined orbit). Using this as the initial mass, an impulsive maneuver of 0.41 km/s requires about 1.4 metric tons of propellant (assuming an Isp of 300s and adding 10% to the propellant mass to estimate the mass of the propellant tanks), leaving about 8.6 metric tons for the remainder of the spacecraft. For the nominal free-return in 2017 (with C3 of 39.69 km^2/s^2), the Falcon Heavy can launch about 9.5 metric tons (as estimated by Tito et al. [79]), delivering about 900 kg more payload dry mass (payload mass less the mass of propellant and tanks) than that capable by the 497-day trajectory. (In the feasibility study conducted by Tito et

al., the nominal free return is optimized to find a local minimum C_3 solution of 38.8 km^2/s^2, which is able to deliver a payload dry mass of 9.8 metric tons.)

As with all of the powered-flyby maneuvers presented in Fig. 5.5, the computed ΔV may be a conservative estimate since it is not computed in the Mars gravity well. This however may bias the previous comparison since the benefits of such a maneuver may be diminished. With this in mind, an equivalent to the 0.41 km/s maneuver (computed for the 497-day trajectory) was estimated for the case where this maneuver is placed at the hyperbolic periapsis of the Mars flyby at a closest approach altitude of 200 km. This calculation assumes that the 0.41 km/s maneuver (placed three days after the flyby) is approximately along the outgoing hyperbolic asymptote (and thus the outgoing V_∞ is simply 0.41 km/s larger than the incoming V_∞). For the 497-day trajectory, the incoming V_∞ is 5.23 km/s, and the equivalent ΔV at hyperbolic periapsis is estimated to be 0.30 km/s. Using this value for the maneuver ΔV, the 497-day trajectory can still only deliver 8.9 metric tons of payload dry mass—600 kg less than the nominal 2017 free return.

With regard to reducing launch V_∞, the results in Fig. 5.5 indicate that maneuvers of at least 0.69 km/s are required to obtain a launch V_∞ of 5.75 km/s (C_3 of 33.01 km^2/s^2). For this trajectory, the Falcon Heavy can launch about 10.5 metric tons, but a ΔV of 0.69 requires 2.2 metric tons of propellant (including the mass for the propellant tanks) laving 8.3 metric tons for the payload (dry mass)—1.2 metric tons less than the 9.5 metric tons provided by the nominal 2017 free return. Even if the maneuver is performed in the gravity well of Mars (with incoming V_∞ of 4.92 km/s), the equivalent maneuver size at hyperbolic periapsis is approximately 0.51 km/s, which results in a payload dry mass of 8.7 metric tons—800 kg less than that of the nominal 2017 free return. Additionally, the trajectories that have lower launch V_∞ of 5.75 km/s all have relatively large arrival V_∞; approaching 9 km/s (entry speed of 14.27 km/s).

Therefore, be it for reducing launch V_∞, TOF, or arrival V_∞, the use of a powered flyby at Mars seems to provide very little to no advantage over the purely ballistic, nominal free-return in 2017.

5.3.2 Investigation of Fast Mars Free-Returns with Venus Gravity Assist

Using the STOUR program, Mars free-return trajectories for the gravity-assist paths Earth-Venus-Mars-Earth (EVME), Earth-Mars-Venus-Earth (EMVE), and Earth-Venus-Mars-Venus-Earth (EVMVE) are investigated. In all cases, the span of launch dates searched is over a 45-year period, from December 1, 2014 to January 31, 2060. The results for the path EVME are shown in Fig. 5.6. The search includes Earth launch V_∞ from 2.5 km/s to 6.5 km/s (in steps of 0.25 km/s), with a minimum allowed altitude of 200 km at both Venus and Mars.

Venus flybys with minimum altitudes less than 300 km would need further investigation, for concerns of interaction with the atmosphere of Venus. (Minimum altitudes of 200 km and 300 km for Mars and Venus, respectfully, are commonly chosen by convention to avoid the perturbative effect of atmospheric drag at these planets. For example, see Diehl and Myers [99].) However, of the EVME trajectories highlighted in this study (in Tables 5.3 and 5.4) all Venus flybys were found to have closest approach distances well above 300 km (the lowest being the 12/19/2021 opportunity in Table 5.4 with a closest approach of about 5580 km). Additionally, all of the EVME trajectories in Tables 5.3 and 5.4 have a closest approach to the Sun of about 0.7 AU. One exception is the 6/24/2036 EVME in Table 5.3, which has a closest approach distance of 0.54 AU. (The EME free returns in Table 5.2 all have closest approach distances to the Sun of 0.73 AU or larger.) It is not expected that this close perihelion will present technological challenges, since several unmanned spacecraft (e.g. Galileo, Cassini, and MESSENGER) have successfully flown as close as 0.7 AU (and closer). For example, the Galileo spacecraft (which flew by Venus on its way to Jupiter) only required multi-layer insulation (MLI) for solar thermal-

radiation protection. The MESSENGER spacecraft, which flew much closer to the Sun at about 0.38 AU, was successfully kept at room temperature using MLI, optical solar reflectors (OSRs), and a ceramic-cloth sunshade. Thus, for the case of the 2036 EVME, such a close perihelion will likely require additional thermal protection (over that needed for 0.7 AU).

The results shown in Fig. 5.6 allow a TOF as long as 700 days for purposes of observing the broader design space, however, only opportunities with TOF of 600 days or less are considered candidates for an IM-type mission.
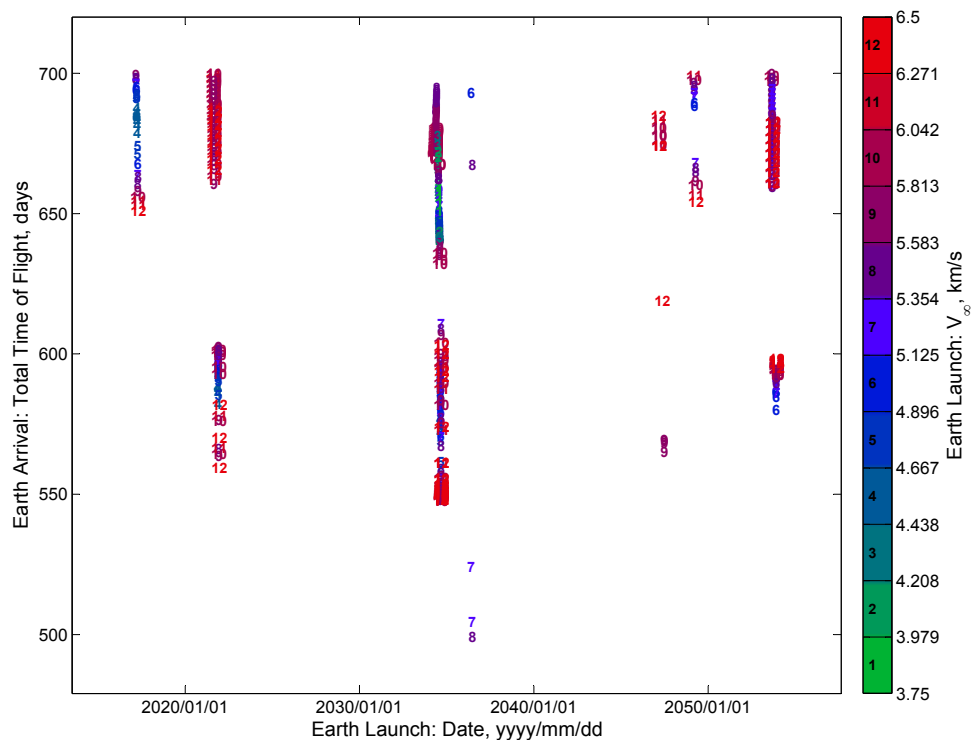
Figure 5.6.: Mars free-return trajectories with intermediate Venus flyby before the Mars encounter (gravity assist path EVME). All results shown have an Earth arrival V_∞ less than or equal to 9 km/s.

Although the STOUR program is stepping through launch dates with 1-day increments (a relatively small step size for trajectory design), the results of Fig. 5.6 show trajectories clustered around specific launch dates. This clustering implies that, in order to meet the imposed constraints, the design space is sensitive to launch date.

The clusters of trajectories appear as seven distinct vertical stripes, occurring (from left to right in the figure) in 2017, 2021, 2034, 2036, 2047, 2049, and 2053. Of these opportunities, none in 2017 nor 2049 have any solutions with TOF below 600 days, and are therefore not candidates for an IM-type mission.

With several EVME candidate trajectories available, the results of Fig. 5.6 are investigated further with regard to Earth arrival V_∞ (since this is a key parameter not explicitly shown in Fig. 5.6). Figure 5.7 shows Earth arrival V_∞ on the horizontal axis, with TOF and Earth launch V_∞ on the vertical axis and color bar, respectively. Because the figure no longer shows launch date, the launch year for notable trajectories (with emphasis on reduced Earth arrival V_∞) is indicated in the figure for 2021, 2034, 2036, 2047, and 2053. The notable trajectories in 2021, 2034, and 2053 appear to have similar characteristics, and for the 2021 and 2053 trajectories, the 32-year time difference in launch date is consistent with the time for the inertial geometry of Earth, Mars, and Venus, to repeat (as discussed by Okutsu et al. [76]). Thus, the trajectories in 2053 are essentially a recurrence of the opportunities in 2021. (A more detailed discussion of these reoccurring trajectories is given in Sec. 5.3.2.)

The opportunities in 2021 from Figs. 5.6 and 5.7 are the only realistic EVME candidates for a second chance to the Inspiration Mars mission since they are the only opportunities that occur in the near term (apart from the nominal EME Inspiration Mars opportunity in late 2017 to early 2018). Furthermore, the 2021 EVME trajectories are likely the only practical candidates for some other IM-type mission, as the purpose of such a mission is to pave the way for humans to explore Mars, and therefore is more significant if undergone in the near term.

It should also be noted that, as indicated in Fig. 5.7, the opportunities in 2036 and 2047 are near the maximum allowed Earth arrival V_∞ of 9 km/s, and may therefore be less desirable when compared to other notable candidates in 2021, 2034, and 2053, which have much lower entry speeds. The key characteristics of the trajectories identified in Fig. 5.7 are given in Table 5.3.
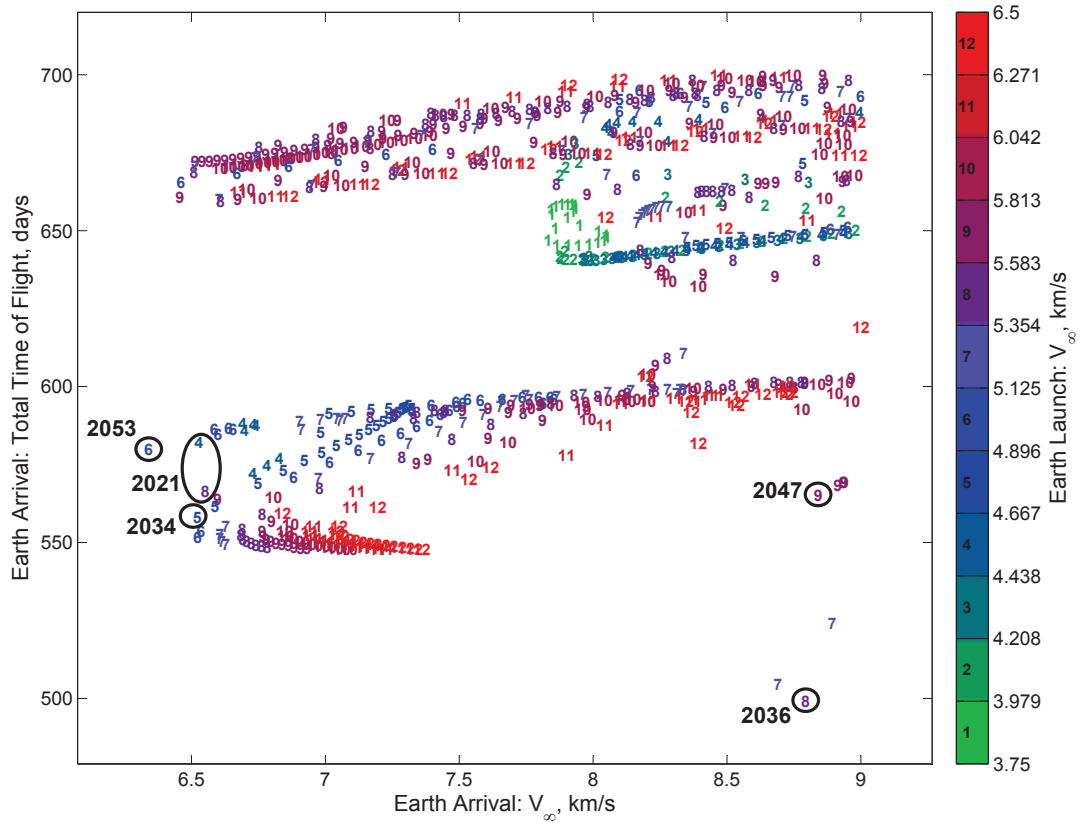
Figure 5.7.: Mars free-return trajectories with gravity assist path EVME. Trajectories shown in this plot are the same as those shown in Fig. 5.6, with Earth launch date exchanged for Earth arrival V_∞ on the horizontal axis.

Table 5.3.: Notable EVME Trajectories from Broad 45-Year Search

Launch Date	$V_{\infty,L}$, km/s	C_3, km^2/s^2	TOF, days	$V_{\infty,A}$, km/s	V_{Entry}, km/s
11/22/2021	4.50	20.25	582	6.53	12.85
12/08/2021	5.50	30.25	566	6.55	12.87
08/28/2034	4.75	22.56	558	6.52	12.85
06/24/2036	5.50	30.25	499	8.79	14.14
07/02/2047	5.75	33.06	565	8.84	14.17
11/28/2053	5.00	25.00	580	6.34	12.76

The free-return search results for the gravity-assist path Earth-Mars-Venus-Earth (EMVE) are very sparse in comparison to EVME. Because of the extremely low num-

ber of trajectories found, the search parameters were expanded slightly to accommodate a launch V_∞ of up to 7.0 km/s (C_3 of 49.00 km^2/s^2). All other parameters in the search were kept the same as those used to obtain the EVME results. Despite the increase in allowable launch V_∞ values, only 2 trajectories were found—both of which exhibited a TOF greater than 600 days. Thus, no trajectories from the EMVE search satisfied the constraints; thereby leaving EMVE an unlikely gravity-assist path for an IM-type mission.

For the gravity-assist path Earth-Venus-Mars-Venus-Earth (EVMVE), only near-term solutions were investigated, with launch dates ranging from 1/1/2018 to 1/1/2030. The constraints on launch and arrival V_∞ imposed on the search were the same as those listed in Table 5.1. The search results produced many solutions in 2021 and 2028, however, all of these solutions had TOF greater than 600 days, and therefore are not suitable candidates for an IM-type mission.

Feasibility of Gravity-Assist Paths

When considering the addition of a Venus gravity assist for a Mars free-return trajectory, the feasibility of the gravity-assist combination (or *path*) can first be investigated with the use of a Tisserand graph. The Tisserand graph is a plot of orbital specific energy (or orbital period) versus radius of periapsis (assuming all planets have circular and coplanar orbits), and provides a graphical means of identifying (from an energy perspective) the feasibility of a gravity-assist path. A flyby of a gravitational body (e.g. Mars) is represented on the Tisserand graph, by plotting a curve (for a chosen value of V_∞) for all possible gravity-assist turn angles. Thus, for a set of bodies (e.g. Earth, Mars, and Venus), the Tisserand graph provides a plot of curves (each of constant V_∞) for each body. These curves of constant V_∞ are also of constant Tisserand parameter—hence the name Tisserand graph.

A derivation of the Tisserand graph and how it is used for investigating candidate gravity-assist paths is given by Strange and Longuski [4] and Labunsky et al. [5].

This graphical tool has since been adapted for aerogravity-assist trajectories in 2002 by Johnson and Longuski [6], and for low-thrust gravity-assist trajectories in 2008 by Chen et al. [7]. In 2010, Campagnola and Russell adapted the Tisserand Graph for gravity-assist trajectories that implement a V_∞-leveraging maneuver [100], as well as for application to the circular-restricted three-body problem [101].

To illustrate the use of the Tisserand graph for assessing the feasibility of a path, an example is shown in Fig. 5.8 for the path Earth-Venus-Mars-Earth (EVME). Each curve in the plot is of constant V_∞, for odd integer values (e.g. 1 km/s, 3 km/s, 5 km/s, etc.) from right to left on the plot. The dots shown on each curve represent the maximum amount of energy change possible for a minimum flyby altitude of 200 km. The bold line traced-out on the plot represents the EVME trajectory.

To follow the bold path shown on the graph, Earth launch with V_∞ of 5 km/s occurs along the third (from the right) "Earth" curve. The intersection of the bold "Venus" curve indicates that a trajectory exists from Earth to Venus with an arrival V_∞ at Venus of 7 km/s. Following along the bold Venus curve represents the energy increase gained through the Venus gravity assist. The intersection of the bold Venus and "Mars" curves indicates the existence of a trajectory between Venus and Mars, with arrival V_∞ at Mars of 5 km/s. The gravity assist at Mars (following the bold Mars curve) shows that a return trajectory to Earth is possible since the Mars curve intersects Earth's curve with an Earth arrival V_∞ of 5 km/s (coincidentally the same as the V_∞ at Earth launch).

The Tisserand graph is also useful to evaluate the feasibility of (and to compare from an energy perspective) the path EVME versus EMVE. As shown in Fig. 5.8, the path EVME can provide trajectories with Earth launch V_∞ of 5 km/s (C_3 of 25.00 km^2/s^2) and return to Earth with arrival V_∞ as low as 5 km/s, which is not unlike the trajectories found in STOUR. (See Figs. 5.6 and 5.7 and Table 5.3.) Therefore, it is clear from the Tisserand graph (and from the STOUR results) that the path EVME is a promising candidate for providing free-return trajectories within the IM-type mission constraints.
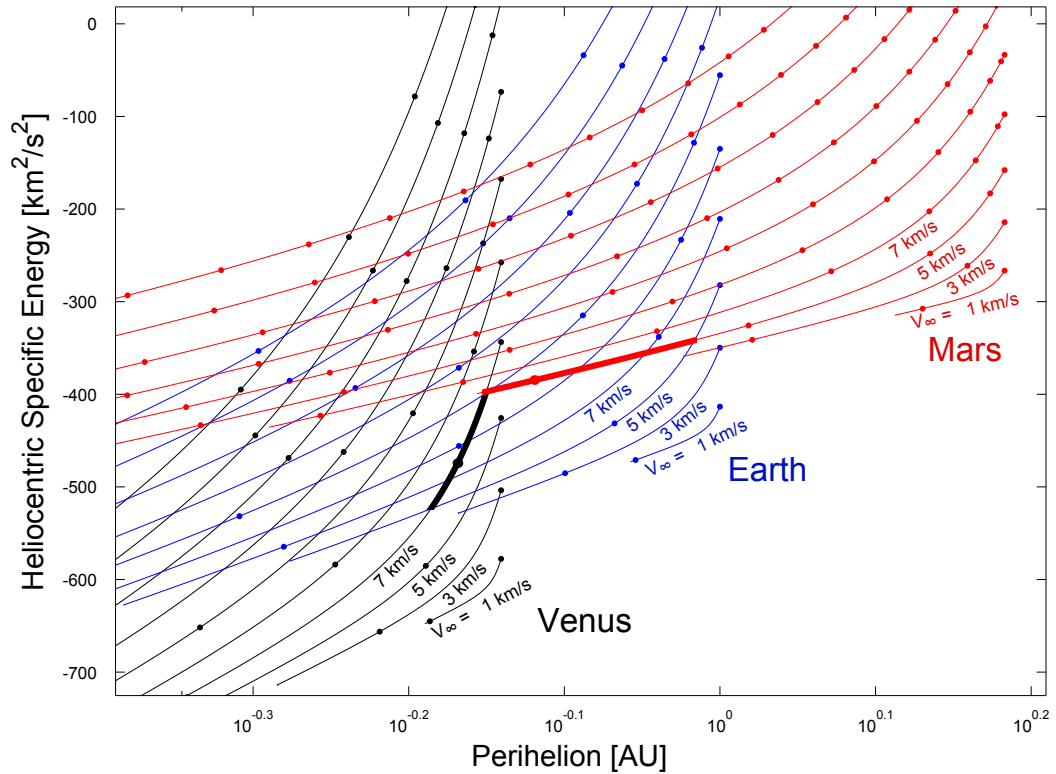
Figure 5.8.: Tisserand graph for heliocentric trajectories, with example EVME trajectory (in bold). The plot shows that for an Earth launch V_∞ of 5 km/s, Venus can be reached (from an energy assessment), then Mars, and finally back to Earth with an arrival V_∞ of 5 km/s.

The concerning issue is that the path EMVE can also be viewed in Fig. 5.8 by simply following the bold lines in reverse. Thus, the Tisserand graph shows that the path EMVE is also feasible with an Earth launch V_∞ of 5 km/s (C_3 of 25.00 km²/s²) and Earth arrival V_∞ of 5 km/s. The STOUR results however clearly show that EVME is the more feasible path with regards to satisfying the constraints set for this study. One key constraint however that the Tisserand graph does *not* show is TOF, which is a possible indication that the flight time required for the EMVE trajectories is simply too long. To investigate this idea further, a new STOUR trajectory search was conducted for EMVE trajectories with TOF of up to 5 years (about 1826 days)—well beyond the set constraint of 600 days. The results in Fig. 5.9 show that by only extending TOF (and holding the launch and arrival V_∞ constraints the same) many

trajectories appear with comparable launch and arrival V_∞ values to those found in the EVME search. All of the EMVE results however, have TOF longer than about 800 days—leaving no suitable EMVE candidates for an IM-type mission.
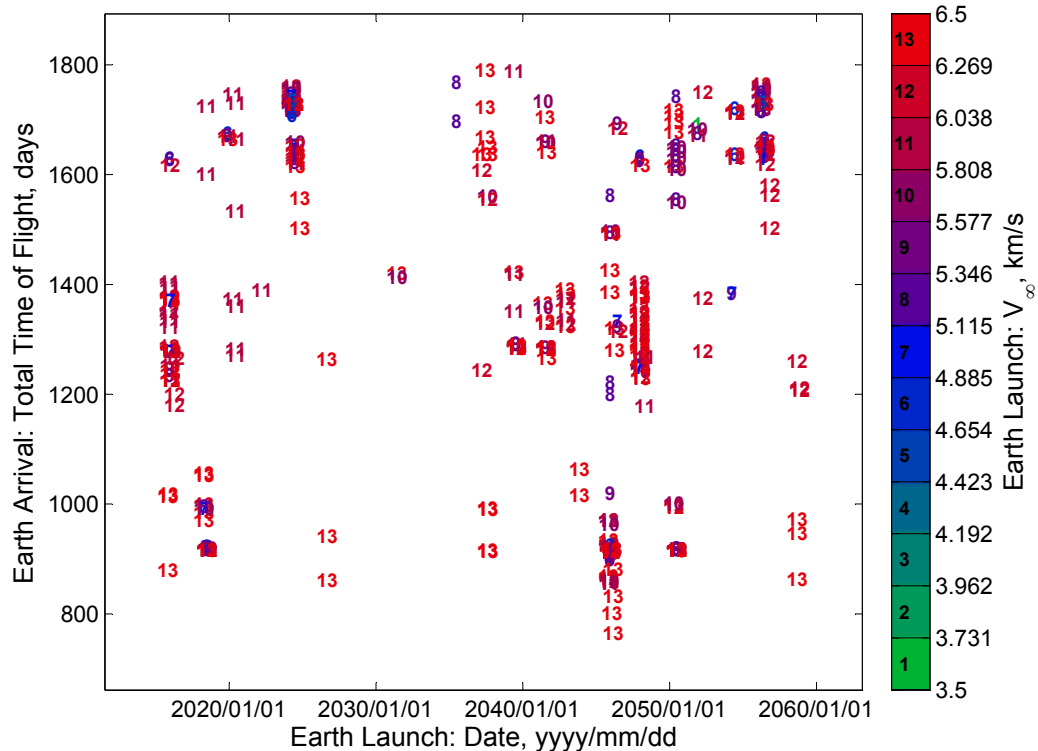
Figure 5.9.: Mars free-return trajectories for the gravity assist path EMVE. The longer TOF solutions (up to 5 years) allow for trajectories with similar launch and arrival V_∞ compared to the EVME results (as indicated by the Tisserand graph).

Since time is not represented on the Tisserand graph, Earth launch dates and stay times at Mars are also not visible from the Tisserand graph. The issue of Earth launch date not being shown can be disregarded since the STOUR simulations search over a span of launch dates beyond the 32 years estimated for the geometry of Earth, Mars, and Venus to repeat in inertial space. With regards to stay times at Mars, several studies that incorporate stay times (such as Walberg [62], Casalino et al. [65], Bailey et al. [80], and Folta et al. [81]) have found solutions with the path EMVE; however, such opportunities use a maneuver to capture into orbit at Mars, and are not suitable for an IM-type mission.

Near-Term Opportunities

Of the opportunities found (shown in Figs. 5.6 and 5.7), all launch dates near or beyond 2034 are too distant for a mission like Inspiration Mars, since the primary purpose of such a mission is to send humans to Mars in the *near* future. The remaining near-term opportunities all have launch dates in 2021, which all occur within about a one-month time span (from November 18, 2021 to December 21, 2021). Such near-term opportunities are essential if an IM-type mission is to serve as a catalyst for human missions to Mars, and provide a key stepping stone for subsequent missions that will land on the Red Planet.

Figures 5.10 and 5.11 show the near-term opportunities, with relatively small search step sizes (one day for launch date and 0.1 km/s for launch V_∞) to show more precisely the available opportunities in the near term. Since all launch dates in these figures occur around the same day, Fig. 5.11 shows arrival V_∞ on the horizontal axis in place of launch date.

In Figs. 5.10 and 5.11, no single opportunity exists in the data set that minimizes TOF, Earth launch V_∞, and Earth arrival V_∞ simultaneously. Therefore, the Pareto set (as discussed in Sec. 5.2.2) is found to characterize the set of "best" cases. The trajectories that make up the Pareto set are circled in Fig. 5.11, and since none are dominated by any other trajectories shown in the near-term results, are all arguably the "best" near-term opportunities. The near-term Pareto-set trajectories are listed in Table 5.4. The circled opportunity with an index of 20 (found near the lower left corner of Fig. 5.11) is not included in Table 5.4 because its TOF (when rounded to the nearest day) is equal to the TOF of the 12/17/2021 opportunity (which is the dominating trajectory).

Of the best opportunities listed in Table 5.4, some stand out as potentially more desirable. For example, the opportunity on 11/22/2021 has the lowest launch V_∞ and nearly the lowest arrival V_∞, but has the longest TOF. Conversely, the opportunity on 12/19/2021 has the shortest TOF, but has the largest launch V_∞ and nearly
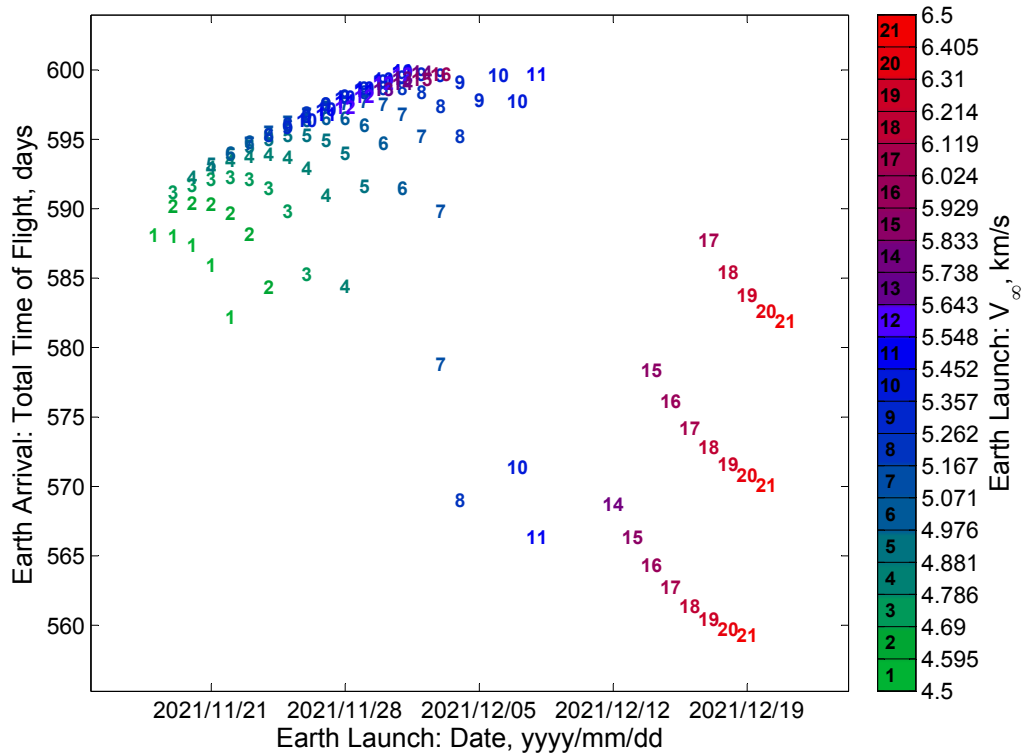
Figure 5.10.: Near-term EVME Mars free-return trajectories with launch dates spanning from November 18 to December 21 of 2021. All results shown have an Earth arrival V_∞ less than or equal to 9 km/s.

Table 5.4.: Best Near-Term EVME Opportunities

Launch Date	$V_{\infty,L}$, km/s	C_3, km^2/s^2	TOF, days	$V_{\infty,A}$, km/s	V_{Entry}, km/s
11/22/2021	4.50	20.25	582	6.53	12.85
12/03/2021	5.10	26.01	579	6.95	13.07
12/04/2021	5.20	27.04	569	6.46	12.82
12/08/2021	5.50	30.25	566	6.55	12.87
12/14/2021	6.00	36.00	564	6.81	13.00
12/15/2021	6.10	37.21	563	6.78	12.99
12/16/2021	6.20	38.44	561	6.77	12.98
12/17/2021	6.30	39.69	560	6.78	12.99
12/19/2021	6.50	42.25	559	6.84	13.02
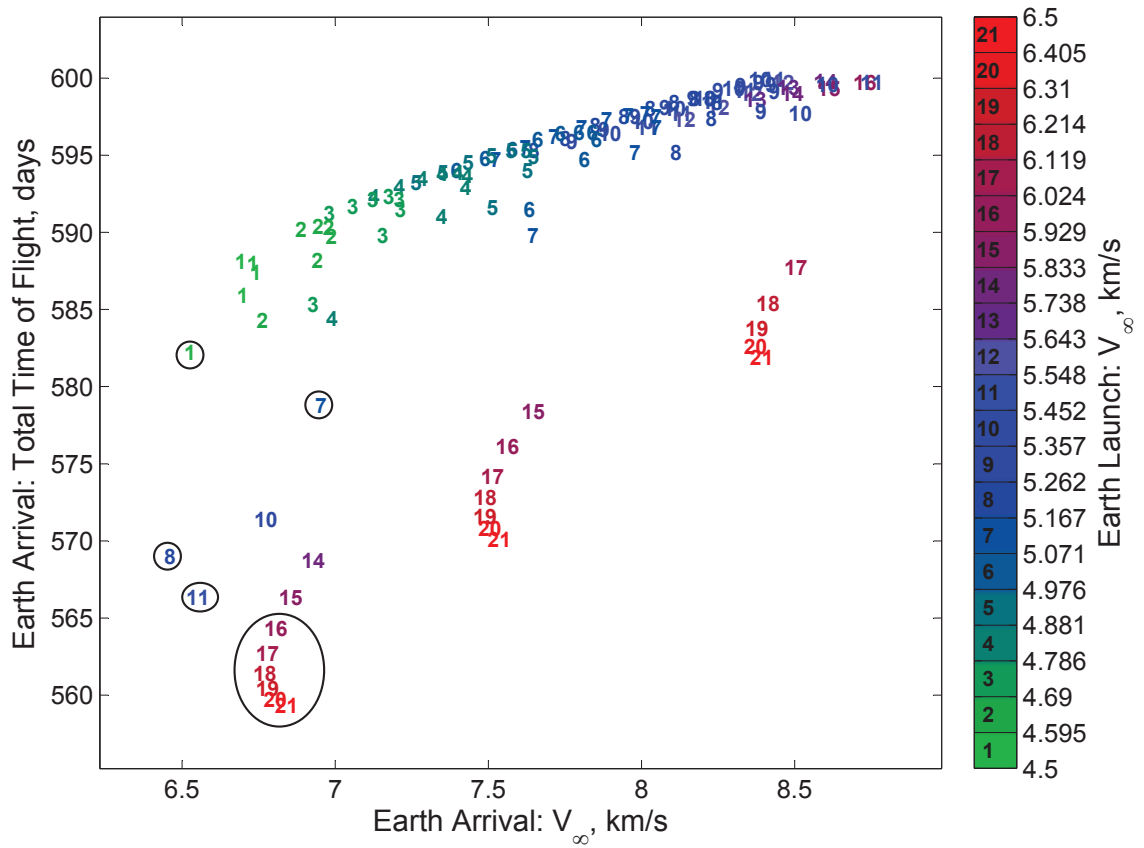
Figure 5.11.: Near-term EVME Mars free-return trajectories. Circled trajectories are considered to be the best near-term candidates (as defined by a Pareto-optimal set), and are listed explicitly in Table 5.4.

the largest arrival V_∞. The opportunity with the smallest arrival V_∞ (occurring on 12/04/2021) has launch V_∞ and TOF values that lie near the middle of the spread of launch V_∞ and TOF values listed in the Pareto set. The truly most desirable near-term opportunity will ultimately depend on how the importance of minimizing each parameter is weighted in the final mission design.

The trajectory with launch date on 11/22/2021 is shown in Fig. 5.12, and is representative of all trajectories in the near-term Pareto set. All trajectories in the Pareto set exist primarily in the ecliptic plane, where the only arc with notable inclination (in each trajectory) occurs on the Earth-Venus legs with a value of approximately

5.4°. The closest approach to the Sun is also shown to be near the orbit of Venus (at approximately 0.7 AU).
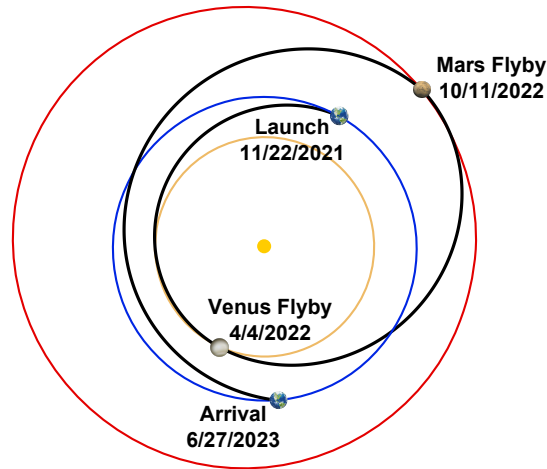
Figure 5.12.: Desirable EVME opportunity generated by STOUR, with launch date on 11/22/2021. (See Table 5.4.) The launch, encounter, and arrival dates are annotated on the figure.

To demonstrate that the EVME trajectories generated by STOUR (using patched conics with an analytic ephemeris) are valid in a high-fidelity model (such as considering the gravity force due to multiple bodies simultaneously), the STOUR trajectory with launch date on 11/22/2021 was reproduced using AGI's Systems Tool Kit (STK) with the propagator Astrogator [102]. In the vicinity of Earth (at both launch and arrival), the high-fidelity STK propagation accounts for the gravity of the Earth, Moon, and Sun. The Moon and Sun are modeled as point masses, and an eighth-degree, eighth-order gravity model is used for Earth. Outside of Earth's vicinity, the interplanetary, high-fidelity propagation uses STK's default heliocentric propagator, which models all planets in the solar system, the Sun, the Moon, and Pluto—all as point masses. Forces due to solar radiation pressure are not taken into account for any part of the STK trajectory propagation. The high-fidelity STK trajectory is shown in Fig. 5.13 and clearly resembles the STOUR trajectory in Fig. 5.12.
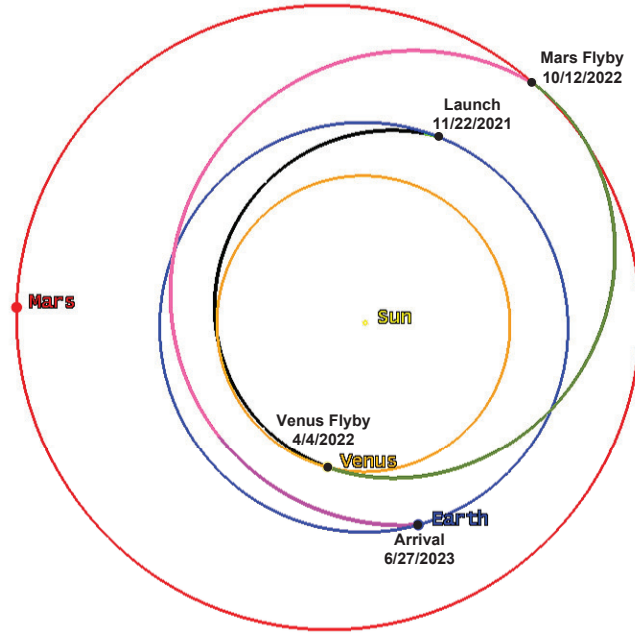
Figure 5.13.: STK plot of EVME opportunity (propagated using STK's Astrogator), with launch date on 11/22/2021. By comparison with the STOUR-generated trajectory in Fig. 5.12, the STK trajectory is clearly similar.

Parameters from the STK trajectory are shown in Table 5.5 along with those from the STOUR solution for comparison. The similarity of the STK and STOUR solution values indicates that (for the gravity-assist trajectories found in this study) the patched-conic method with analytic ephemeris (as used in STOUR) provides solutions that closely approximate the true dynamic motion. The similarity of the results in Table 5.5 also validates the use of STOUR-generated trajectories as initial guesses for targeting high-fidelity solutions in tools such as STK.

Table 5.5.: High-Fidelity Comparison of 11/22/2021 EVME Opportunity

Propagator	$V_{\infty,L}$, km/s	C_3, km^2/s^2	h_V, km	h_M, km	TOF, days	$V_{\infty,A}$, km/s	V_{Entry}, km/s
Astrogator	4.511	20.35	11097	363	582.5	6.459	12.87
STOUR	4.500	20.25	10868	346	582.2	6.526	12.85

Physical Behavior and Rarity of Candidate Trajectories

For each leg (i.e. each trajectory arc between bodies) of the near-term Pareto-set trajectories in Table 5.4, the transfer angle is nearly 180º—a characteristic resemblant of a minimum-energy transfer—and is visible in Fig. 5.12 (with a slightly larger than 180º transfer shown on the Mars-Earth leg). Such behavior may (as with the EME cases) indicate that the solutions found are near the lowest achievable V_∞ at Earth launch and arrival. However, it may also indicate (as with the EME cases) that approaching the minimum energy transfer is necessary to meet the imposed constraints, and may explain the relatively short span of available launch dates for near-term opportunities. Having 180º transfers between each encounter may also explain why the lowest found launch and arrival V_∞ candidates all have similar TOF— around 570 days.

As mentioned previously, the 32-year time difference between the 2021 and 2053 opportunities agrees with the estimate of Okutsu et al. [76] as the approximate time for the orientations of Earth, Venus, and Mars to repeat in inertial space. Thus, it is expected that the same physical factors are in play for both the 2021 and 2053 opportunities, and by the same logic, that opportunities similar to those in 2034 will reoccur 32 years later, in 2066. This repetition cycle suggests that the opportunities found in 2021, 2034, and 2053, are dependent on some inertially fixed characteristics (such as eccentricity, inclination, and ascending and descending node locations) of the Earth, Venus, and Mars orbits, and that these inertial characteristics are also playing a significant role in reducing the V_∞ at Earth launch and arrival.

One means to observe what role (if any) inertial characteristics of the planets' orbits plays on a gravity-assist trajectory, is in a radial distance plot. Figures 5.14 and 5.15 show radial distance plots for the 11/22/2021 and 8/28/2034 opportunities, respectively. The figures show the radial distance (with respect to the Sun) of each planet (Earth, Venus, and Mars), as well as for the spacecraft's trajectory, plotted against time. To investigate the node crossings of Venus and Mars, the ascending

and descending nodes for each planet's orbit are indicated by the black dots shown along the curves for Venus and Mars. All other dots shown indicate where in the spacecraft's trajectory the gravity assist occurs. Additionally, the inclination of each leg of the spacecraft's trajectory is annotated next to the corresponding curve on the plot.
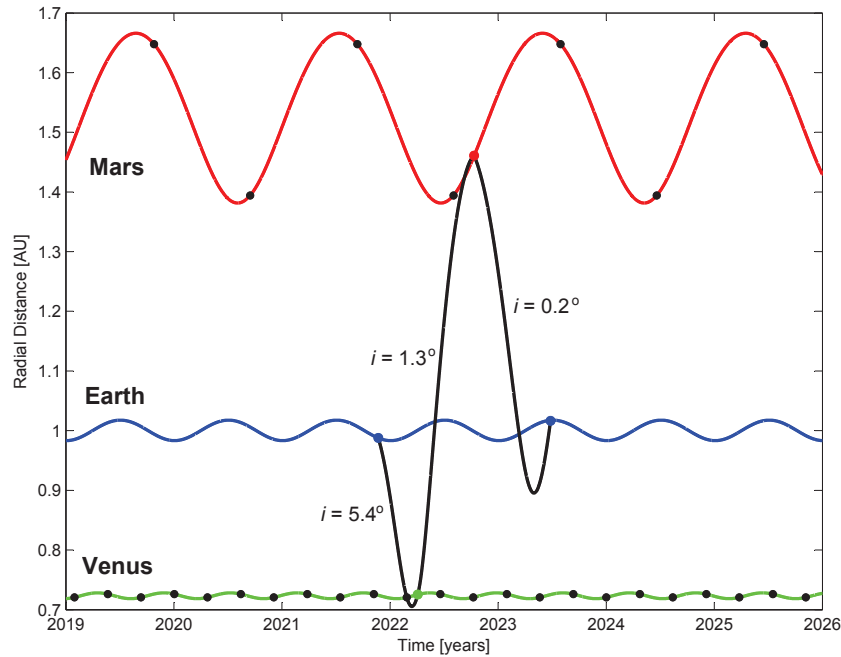
Figure 5.14.: Radial distance plot of 11/22/2021 EVME opportunity. The plot shows the eccentric orbits of Venus, Earth, and Mars along with the spacecraft trajectory. The black dots on the Venus and Mars curves indicate a node crossing. All other dots indicate an encounter.

When looking at each radial distance plot, it is important to consider the two key characteristics that are known to reduce the energy required for a transfer between two bodies. The first involves the concept discussed by Lawden [98], where the minimum-energy transfer between two elliptical orbits is found by starting and ending the transfer arc at an apse. The second characteristic being the high-inclination issue for transfer arcs at or near 180° between inclined target bodies, which may be damped out (or eliminated) if the encounter occurs when the departure and target bodies are in the same plane (i.e. when Mars and Venus are at a node crossing). A trajectory
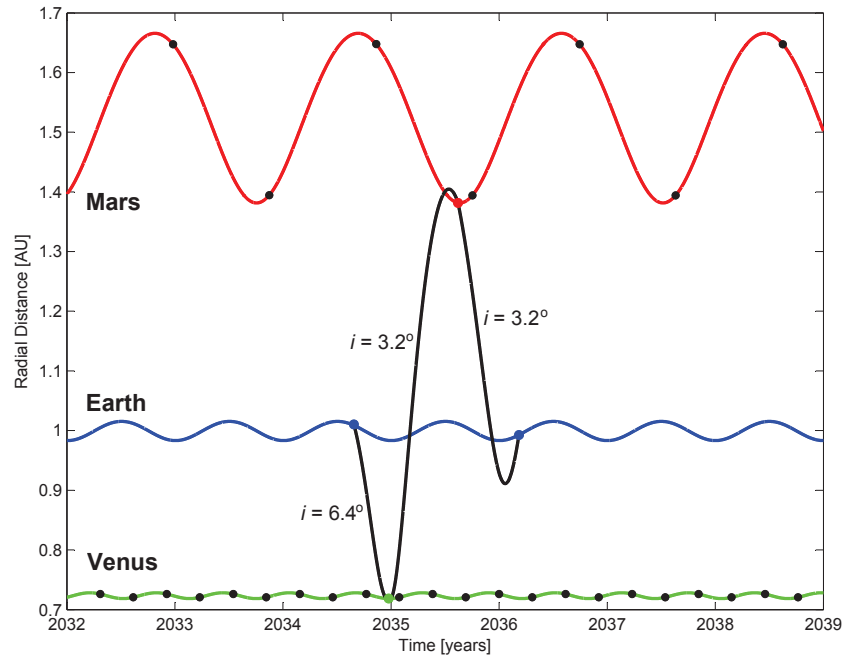
Figure 5.15.: Radial distance plot of 8/28/2034 EVME opportunity.

that has these geometric characteristics may be on (or near) a minimum-energy free return.

Figure 5.14 shows (from left to right on the plot) that the spacecraft departs Earth near Earth's perihelion, encounters Venus near the spacecraft's perihelion, encounters Mars near the spacecraft's aphelia (both on the arrival and departure transfer arcs), and finally encounters Earth at Earth's aphelion. Additionally, the figure shows that the Venus and Mars encounters both occur near their respective node crossings, which may explain why the transfer arcs with nearly 180° transfer angles can exist with relatively small inclination. The Venus and Mars encounters also do not occur very near to either the perihelion or aphelion of Venus' or Mars' orbits, nor does the spacecraft depart Earth or arrive at Earth near either apse of the transfer arcs. Nevertheless, several transfers do begin and end near an apse, and both encounters occur near Venus' and Mars' node crossings.

Figure 5.15 shows no apse at Earth departure (neither from Earth's nor the spacecraft's orbits), but at the Venus encounter, all three orbits (the spacecraft's arrival

and departure arcs, and that of Venus) are at their respective perihelia. At the following Mars encounter, Mars is at perihelion and the spacecrafts arrival arc is near aphelion. The final arrival at Earth however does not occur near an apse. The figure also shows that the Venus and Mars encounters occur very near the node crossings, which may explain (as with the 2021 case) why such low transfer arc inclinations can exist with near 180° transfer angles. To better illustrate that the 2034 trajectory has near 180° transfer arcs (with a slightly larger transfer angle for the Mars-Earth leg), its trajectory is shown in Fig. 5.16.
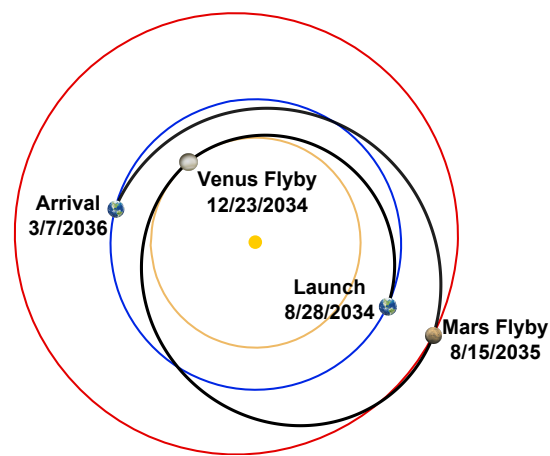
Figure 5.16.: Trajectory plot of 8/28/2034 EVME opportunity. The plot shows that all transfer arcs have transfer angles that are near 180° (although slightly larger on the Mars-Earth leg).

Broken-Plane Maneuver

It should be noted that the issue of 180° transfer angles producing highly inclined trajectories can be resolved with the use of a broken-plane maneuver. Such a maneuver is typically small (particularly if applied to this problem since the inclinations of Venus' and Mars' orbits are small), however, the use of a broken-plane maneuver

prevents the resulting EVME trajectory from being a true *free* return, and is therefore less desirable for an IM-type mission.

Nevertheless, a broken-plane maneuver could potentially allow for transfers closer to a true 180º-transfer, and thereby (potentially) provide lower Earth launch and arrival V_∞ values than those found in Table 5.4. Such trajectories are not investigated in this paper, as the primary goal of this study is to find trajectories for an IM-type mission that are purely ballistic—allowing those aboard the spacecraft to return to Earth without the need of deterministic maneuvers.

5.3.3   Earth Entry Analysis

In the previous sections, the arrival V_∞ constraint was chosen to be 9 km/s, which was based on the arrival V_∞ for the nominal Inspiration Mars mission. Now, a more in-depth entry analysis is conducted to determine whether or not direct entry can be used with current technologies, and if not, what is required of new technologies to make such an entry speed achievable.

Two key trajectories are considered for this entry analysis: the EME free-return with launch date on 11/27/2017 (the nominal Inspiration Mars trajectory), and the EVME free-return on 11/22/2021. For the 2017 opportunity, the SpaceX Dragon capsule [89] parameters were used for a baseline entry vehicle, since Dragon is expected to be ready for human cargo by the time of launch. (Additionally, Dragon was the capsule considered in the Inspiration Mars feasibility study by Tito et al. [79].) For the 2021 opportunity, the Orion capsule [90] is expected to be ready for human cargo as well. Therefore, both Orion and Dragon were considered for use as baseline entry vehicles for the 2021 EVME free-return. These three vehicle-opportunity combinations will hereafter be addressed as Dragon-2018, Dragon-2021, and Orion-2021, respectively. The label "2018" is used for the 11/27/2017 opportunity to remain consistent with other literature for the nominal inspiration Mars free-return, which refer to a later launch date of the same opportunity in January of 2018. It is important to

note that the 2018 trajectory mentioned in other literature (such as Tito et al.) and the 11/27/2017 trajectory are nearly identical, with minor variations in launch V_∞, arrival V_∞, and TOF.

The optimal direct entry trajectories that minimize the total heat load (i.e. TPS mass) of the spacecraft are computed (using GPOPS), such that the deceleration loads are within human tolerance after a long duration spaceflight, and peak stagnation-point heat rates are within the performance limits of the TPS materials.

For cases where g-loads exceed the allowed limits for human tolerance, or peak stagnation-point heat rates exceed that of TPS materials currently available, aerocapture trajectories are considered. Since aerocapture has yet to be demonstrated (at the time of writing this paper), direct entry trajectories (if achievable) are preferred over aerocapture. For all aerocapture trajectories considered in this work, the orbit post-aerocapture is designed such that the periapsis is within Earth's atmosphere; allowing entry to occur on the return leg of the capture orbit. Although, in practice, a correction maneuver may be necessary after the spacecraft enters its capture orbit, it is assumed in this study that no deterministic maneuver is required to de-orbit the spacecraft.

From the GPOPS analysis, it was found that direct entry trajectories are feasible in terms of g-loading on the crew, using bank-angle control for guided entry. Figures 5.17 (a) and (b) shows the altitude-speed profile and deceleration, respectively, for the direct-entry solutions of both the 11/27/2017 trajectory (using Dragon) and the 11/22/2021 opportunities (using both Dragon and Orion). The entry speed for the 11/27/2017 free return is 14.2 km/s, which is significantly higher than the entry speed for the 11/22/2021 opportunity, of 12.8 km/s. For the three cases: Dragon-2018, Dragon-2021, and Orion-2021, the peak deceleration and corresponding time duration are denoted by G_A, G_B, and G_C, respectively. For the Dragon-2018 case, G_A is 5.5 g's for a maximum duration of 30 seconds, whereas for the Dragon-2021 case, G_B is 5.2 g's for about 3 minutes. On the other hand, for the same 11/22/2021 opportunity, G_C is only 4 g's for a duration of 4.5 minutes, due to higher lift capability of the Orion. By

comparing G_A, G_B, and G_C with Fig. 5.1, it is apparent that the peak decelerations for all three vehicle-opportunity combinations are within acceptable human tolerance limits for missions of (at least) about 200 days. However, as mentioned in Sec. 5.2.3, it is not yet known what g-loads humans may be able to tolerate after more than 500 days in microgravity.
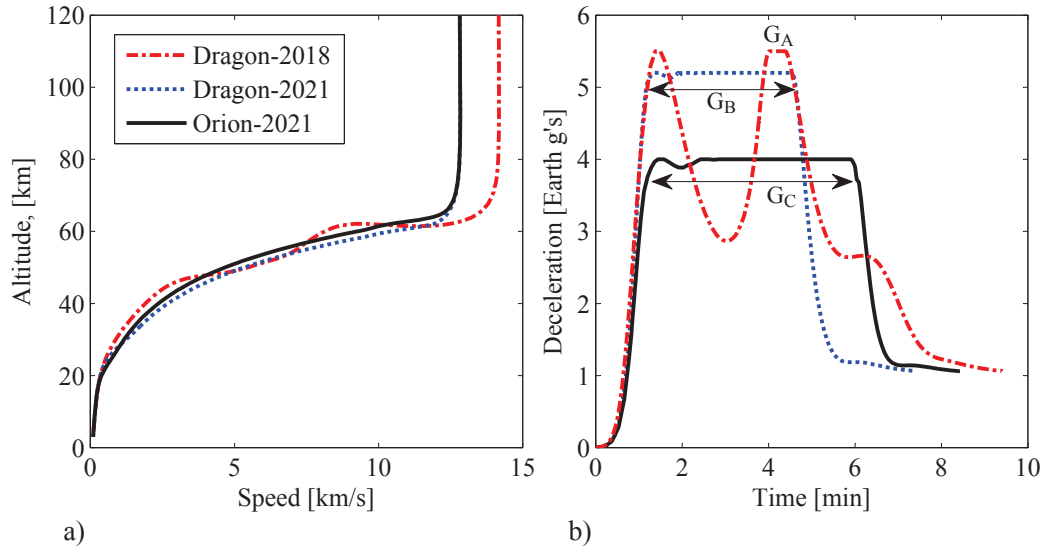
Figure 5.17.: a) Altitude vs speed, and b) deceleration load, for the three vehicle-opportunity combinations: Dragon-2018, Dragon-2021, and Orion-2021, using bank-angle control.

The corresponding total stagnation-point heat rate and the total stagnation-point heat load for the three vehicle-opportunity combinations: Dragon-2018, Dragon-2021, and Orion-2021 are shown in Figs. 5.18 (a) and (b). For the Dragon-2018 case, the total stagnation-point peak heat rate and heat load are 1866 W/cm² and 36.6 kJ/cm², respectively. Since, in the Dragon-2021 case, the entry speed is lower, the total stagnation-point peak heat rate and heat load are 1219 W/cm² and 25.3 kJ/cm²— less than the 2018 case. For Orion-2021, the total stagnation-point peak heat rate is 967 W/cm², due to the higher lift capability of Orion.
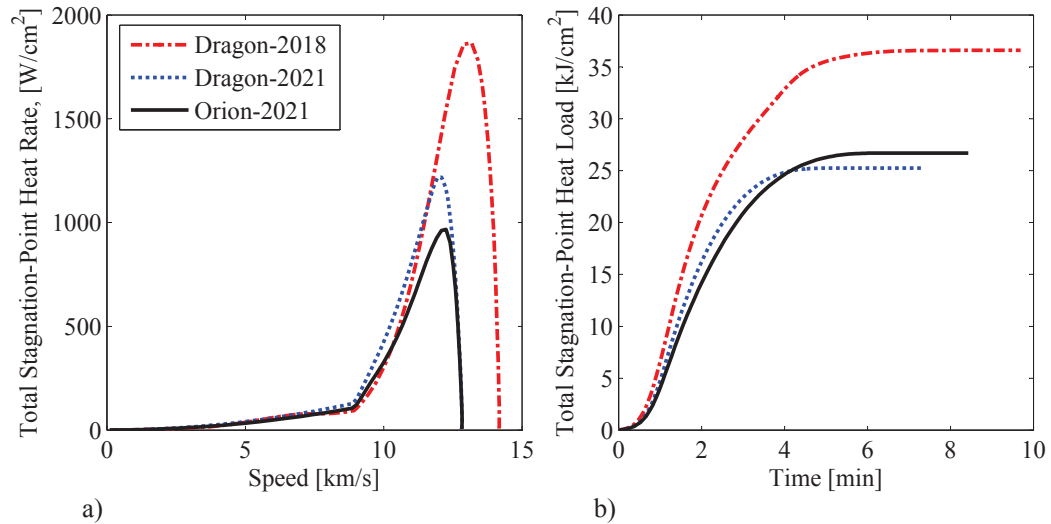
Figure 5.18.: a) Total stagnation-point heat rate, and b) total stagnation-point heat load, for the three vehicle-opportunity combinations: Dragon-2018, Dragon-2021, and Orion-2021, using bank angle control.

The Orion entry vehicle flies a shallower trajectory, which reduces the heat rate, but increases the entry and descent timeline. For the 11/22/2021 opportunity, Fig. 5.18 (b) shows that while the Dragon entry vehicle takes around 7.3 minutes for entry and descent (from 122 km to 3 km), the Orion entry vehicle takes longer, at about 8.4 minutes. This increase in time for entry and descent to occur brings about an increase in the total stagnation-point heat load for the Orion-2021 case—reaching 26.7 kJ/cm^2. For reference, it is worth noting that a typical Apollo capsule entering Earth's atmosphere at around 10.8 km/s, the peak heat rate is about 400 W/cm^2, and the corresponding stagnation-point heat load is about 20 kJ/cm^2 [103].

For hypervelocity entry, shock layer radiative heating dominates over convective heating, and therefore, the driver of the total stagnation-point heat rate is radiative heating. This radiative-heating dominance is evident in Fig. 5.19, which shows the total, radiative, and convective heat rates, for the 11/22/2021 opportunity using (a) Dragon and (b) Orion. For Dragon-2021, the peak stagnation-point radiative heat rate is about 994 W/cm^2 (82% of the total) and the remainder (225 W/cm^2) is due to convective heating. Similarly, for the Orion-2021 case, the peak stagnation-point

radiative heat rate is about 971 W/cm^2 (81% of the total) and the convective heat rate is 187 W/cm^2.
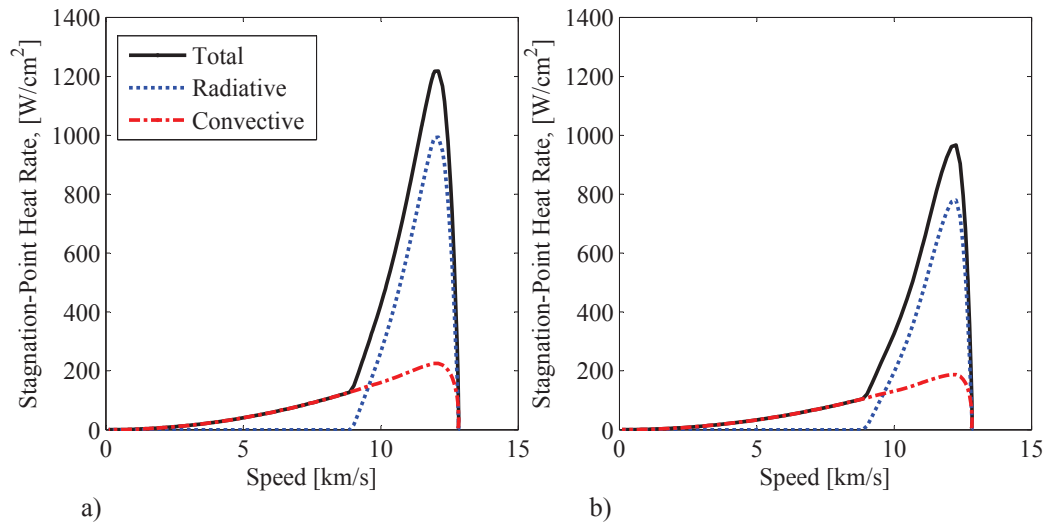
Figure 5.19.: Total, radiative, and convective heat rates for a) Dragon-2021, and b) Orion-2021.

Brandis-Johnston [95] provides a correlation for radiative heat rate in terms of parameters such as freestream density, shock speed, gas composition, and vehicle size, and is only valid for limited ranges of these parameters. As seen in Figs. 5.19 (a) and (b), the radiative heating correlation is invalid (and therefore set equal to zero) for either speeds less than 8.8 km/s, or altitude less than 57 km and 59 km, respectively, for the Dragon-2021 and Orion-2021 cases.

Along with the stagnation point heat rate, the peak dynamic pressure on the heat shield due to the entry vehicle's motion is important in determining the TPS material. The dynamic pressure is a function of the free stream density and speed of an entry spacecraft, given by $q_{dyn} = \rho V^2/2$. The peak dynamic pressure for the Dragon-2018 case is 0.19 atm (19.4 kPa). For the 2021 opportunity, the peak dynamic pressures are 0.18 atm (18.5 kPa) and 0.14 atm (14.2 kPa) for the Dragon and Orion entry vehicles, respectively.

The aerothermal conditions and deceleration of the three cases are summarized in Table 5.6. It should be noted that the true peak heat rate and peak dynamic pressure values will, in practice, likely deviate from the values listed in the table. This deviation will inevitably arise from various errors due to uncertainly in the arrival conditions (e.g. from navigation errors), atmospheric model, and vehicle aerodynamics, to name a few. The goal of this analysis is therefore to merely assess the feasibility of entry for the free-return trajectories found in this paper, since these cases exhibit exceptionally high entry speeds compared to previous human missions. A statistical assessment of the effects of dispersions on these entry trajectories is not the intent of this study.

Table 5.6.: Direct Entry Aerothermal Conditions for Key Free-Return Opportunities

Case	Peak $\dot{q}$, W/cm^2	Peak $\dot{q}_{dyn}$, atm	Q, kJ/cm^2	Peak Decel., Earth g's
Dragon-2018	1866	0.19	36.6	5.5
Dragon-2021	1219	0.18	25.3	5.2
Orion-2021	967	0.14	26.7	4

The TPS mass fraction of an entry vehicle is strongly correlated to the total stagnation-point heat load given in Eq. 5.6. The Dragon entry vehicle uses a SpaceX variant of Phenolic Impregnated Carbon Ablator (PICA) for its TPS material called PICA X [103], and Orion uses a variant of Avcoat [103]. These TPS materials, however, may not be suitable for the trajectories of interest in this study. Thus, once the aerothermal conditions are determined from the GPOPS simulation, a suitable TPS material is identified (which may or may not match the material currently being used by Dragon and Orion).

TPS materials are often characterized by their density (high, mid, or low) and capability to withstand various heat rates at a particular stagnation pressure [103]. Table 5.7 summarizes the currently available (or near-term) ablative TPS materials, as well as their projected performance in terms of heat rate and stagnation pressure. Flight heritage or Technology Readiness Level (TRL) is also listed.

Table 5.7.: Ablative TPS Material Properties (Adapted from Kolawa et al. [103])

TPS	Density	Heritage or TRL	$\dot{q}_r$, W/cm^2	Pres., atm
PhenCarb Family	Low-Mid	TRL $4-5$	$800-10000$	> 1
Adv. Carbon-Carbon (ACC)	Low-Mid	Genesis	> 2000	> 1
PICA and PICA X	Low-Mid	Stardust	~ 1200	< 1
Avcoat	Low-Mid	Apollo, Orion	~ 1000	~ 1
Carbon Phenolic (CP)	High	Galileo, Pioneer-Venus	~ 100000	$>>1$
Chopped Molded CP (CMCP)	High	Galileo, Pioneer-Venus	~ 100000	$>>1$
Tape Wrapped CP (TWCP)	High	Galileo, Pioneer-Venus	~ 100000	$>>1$
3 DQP	High	TRL 3	~ 5000	> 1

Observe that for all three trajectory cases, Dragon-2018, Dragon-2021, and Orion-2021, both PhenCarb and ACC are suitable TPS materials for withstanding their peak heat rates of 1866, 1219, and 967 W/cm^2, respectively. For Orion-2021, PICA and PICA X will also work, and possibly Avcoat. The peak heating of Orion-2021 is very near Avcoat's listed limit however, and more qualification testing would be needed to account for deviations from the optimal trajectory found in this study. A similar situation is true if PICA or PICA X are to be considered for Dragon-2021, since its peak rate of 1219 W/cm^2 is slightly over PICA's qualified limit and must be qualified for aerothermal conditions beyond the current limit. In all cases, PhenCarb will need further development to become flight-ready, due to its current TRL.

For Dragon-2018, ACC may also need to be qualified beyond the listed limit in Table 5.7, since deviations from the optimal entry trajectory found in this study may result in a larger heat rate than the 1866 W/cm^2, which is already close to the current qualified limit for ACC. Additionally, the flight-ready carbon phenolic (used on the Galileo probe to Jupiter and Pioneer Probe to Venus) would be able to easily withstand all heat rates encountered from the trajectories in this study. However, carbon phenolic is a high-density TPS material, and will have a significant mass penalty. It is more likely therefore, that the low-mid density TPS options are a more attractive choice (pending further trade studies).

5.3.4   The 2023 EVME High Entry-Speed Free-Returns

From the Earth entry results in the previous section, it seems that opportunities with Earth arrival V_∞ greater than the 9 km/s constraint may be feasible if carbon phenolic or aerocapture is used. Of course, these high entry-speed solutions will only be usable if the g-loads experienced by the crew are kept within acceptable levels. The goal of such a study being to find near-term opportunities that occur on dates other than those in 2017, 2018 and 2021, with particular interest in any opportunities occurring later than 2021.

To find such near-term opportunities, free returns (from STOUR) are identified that have arrival V_∞ as large as 11 km/s. These high entry-speed cases are investigated for all gravity-assist paths considered in this study: EME, EVME, EMVE, and EVMVE. For the paths EME, EMVE, and EVMVE, no near-term opportunities were found with characteristics significantly different from those already found in 2017, 2018 and 2021 (apart from the larger entry speed). Of these paths, the closest opportunity to meeting the constraints (with high entry speed), is an EVMVE on 12/07/2021, with launch V_∞ of 5.5 km/s, arrival V_∞ of 10.76 km/s, but TOF of 632 days—a month longer than the 600-day constraint.

Using the gravity assist path EVME however, a group of high entry-speed opportunities were found that occur in September and October of 2023. These trajectories all have arrival V_∞ near 11 km/s, but have launch V_∞ as low as 5 km/s (C_3 of 25.00 km^2/s^2), and TOF as low as 483 days. The Pareto-optimal set (i.e. best cases) from the 2023 EVME free returns found is listed in Table 5.8.

Table 5.8.: 2023 EVME Pareto-Set Opportunities

Launch Date	$V_{\infty,L}$, km/s	C_3, km^2/s^2	TOF, days	$V_{\infty,A}$, km/s	V_{Entry}, km/s
09/09/2023	5.00	25.00	501	10.92	15.55
09/22/2023	5.50	30.25	486	10.96	15.58
09/25/2023	5.70	32.49	483	10.98	15.59
10/06/2023	6.00	36.00	500	10.74	15.43

Another attribute of the opportunities listed in Table 5.8 is that they have a relatively close approach to the Sun (compared to the other trajectories highlighted in this study) of about 0.5 AU. Any risk associated with such a solar distance was not investigated in this study. However, it is not expected that such a close approach will be problematic (as discussed in Sec. 5.3.2), and will likely require additional thermal protection (over the other notable trajectories in this paper, with minimum solar distances of about 0.7 AU).

The high entry speeds listed in Table 5.8 are of greater concern (at least from a trajectory standpoint) since they are on the order of 1.5 km/s greater than that of the nominal Inspiration Mars opportunity, and are further analyzed using GPOPS. To capture all 2023 opportunities found, the GPOPS analysis is done using an arrival V_∞ of 11 km/s (entry speed of 15.6 km/s). Both direct entry and aerocapture are investigated (using Dragon and Orion as baseline entry vehicles) to determine if this high speed entry is feasible with regards to human deceleration tolerance and stagnation-point heat rate.

Using Dragon, no feasible direct entry trajectory was found to exist with a peak deceleration less than 7.2 g's. Even when aerocapture was implemented in GPOPS, a trajectory was not found to exist with peak deceleration less than 7 g's. Using Orion however, both direct entry and aerocapture trajectories were found with decelerations within human tolerances.

Feasible direct entry and aerocapture trajectories of Orion with peak deceleration of about 6.2 g's are shown in Figs. 5.20 (a) and (b). For aerocapture, a single peak in deceleration is shown, whereas for the direct entry there are two peaks shown, where the crew must withstand the peak g-loads for a longer period of time (about 1 minute) during the second peak. In both cases however, the g-loads are well below the maximum allowed peak values (and duration) for human tolerance. The two-peak behavior from direct entry is called a skip-type trajectory, and is a product of the bank-angle modulation working to satisfy the deceleration constraint.
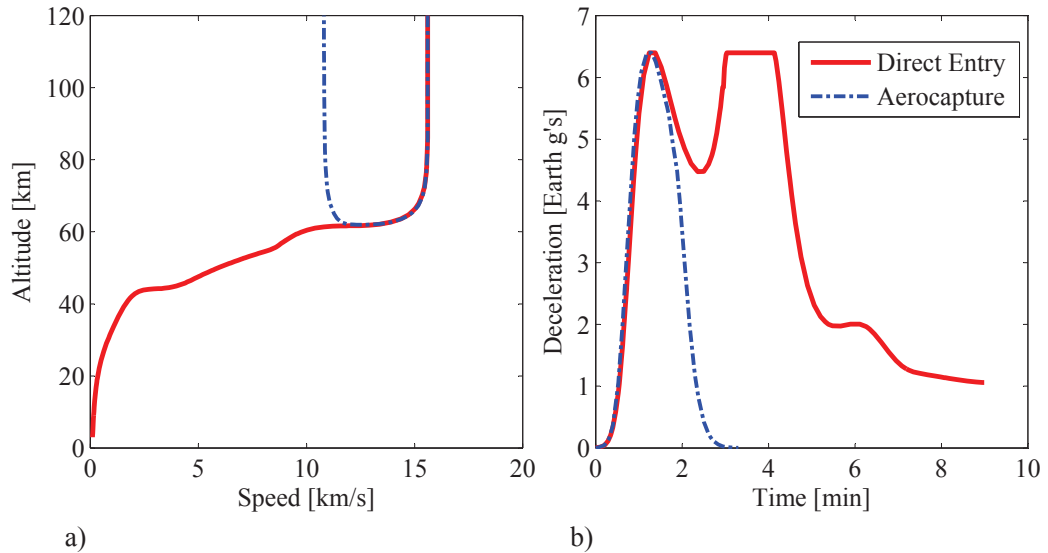
Figure 5.20.: Orion entry analysis for 2023 EVME free returns for both direct entry and aerocapture. The speed profile is shown plotted against altitude in (a), and the deceleration over time is shown in (b).

For the case of aerocapture, Fig. 5.20 (a) shows the trajectory altitude decrease to just above 60 km, before exiting with a speed of 10.8 km/s (at an altitude of 120 km). The important factor here is that escape velocity at 120 km altitude is 11.1 km/s, and therefore a trajectory with a speed of 10.8 km/s is captured in an orbit about Earth. The design of the capture orbit post aerocapture is a two-dimensional problem, and can be determined from various combinations of parameters that define an orbit in the two-body problem, such as the exit speed and exit flight-path angle, apoapsis and orbital period, etc. These capture orbit parameters are specified in GPOPS, which impose additional constraints on the optimal entry solution—thereby changing the result. Therefore, as different capture orbit parameters are specified, GPOPS will find solutions with differences in deceleration profiles. As a result, a more thorough analysis of aerocapture constitutes a more in-depth trade study of possible final capture orbits. Such a trade is not included in this paper, since the primary interest in this brief investigation is to merely determine if there exists a feasible entry solution for the 2023 free-returns.

The aerocapture trajectory in Fig. 5.20 results in a capture trajectory with an apoapsis of 125,500 km (nearly 1/3 the lunar distance) with an orbital period of about 2 days. A larger capture orbit could be chosen to even further reduce the exit speed, as well as the peak g-loads experienced by the crew. Likewise, the opposite holds true for smaller capture orbits. The 2-day capture orbit chosen here provides sufficiently low g-loads for this feasibility analysis, however further trades may prove to find a more desirable solution.

Figure 5.21 shows the total stagnation-point heat rate and heat load (plotted against speed and time, respectively) for the same two entry trajectories given in Fig. 5.20. The total heat rates for the direct entry and aerocapture cases are very similar, with peak heat rates reaching 3040 W/cm^2 and 3088 W/cm^2, respectively. For both of these cases, (as observed in Table 5.7) the low-mid density TPS material PhenCarb would be suitable (pending further development and qualification testing to become flight ready). ACC may also be suitable, pending further tests to qualify it for heat rates beyond its current qualified limit.
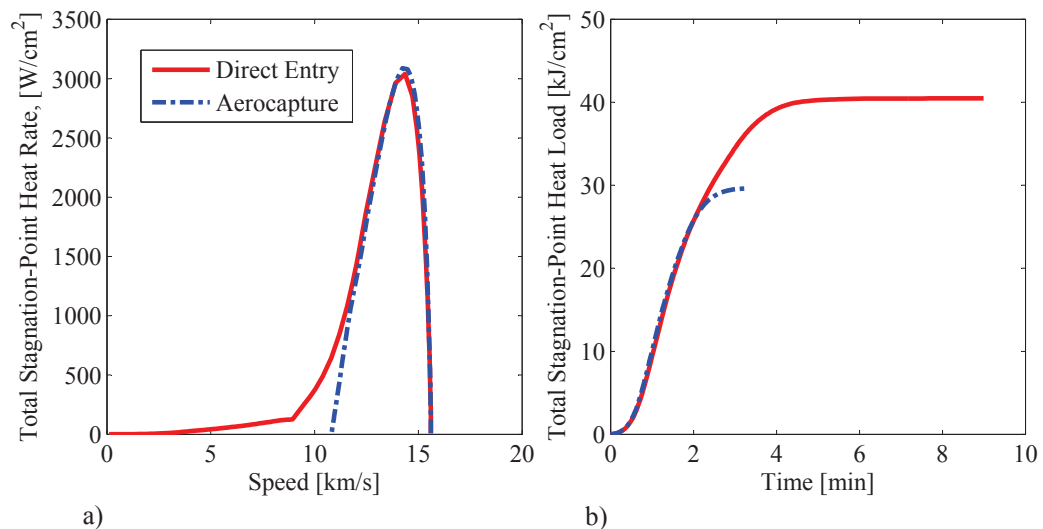
Figure 5.21.: Direct entry and aerocapture results for the 2023 free-return opportunity. Total stagnation-point heat rate (a) and head load (b) are shown, and correspond to the same entry trajectories given in Fig. 5.20.

There is however a substantial difference in total heat load between the direct entry and aerocapture cases. For aerocapture, the total heat load is 29.6 kJ/cm^2, and for direct entry, the total heat load is 40.5 kJ/cm^2. This direct entry heat load is nearly double that of what the Apollo command modules encountered, which had a TPS mass-fraction of about 14% [103] (of the total spacecraft mass). The direct entry trajectory for the 2023 free-return is estimated to require a TPS mass fraction of about 22.0% (much larger than that of Apollo), and may provide an argument for the use of aerocapture, which requires a TPS mass fraction of 18.4%. The increased heat load for the direct entry case can be attributed to the fact that lift is used to fly a more shallow trajectory, which is done to reduce the g-loads experienced by the crew. Flying such a shallow trajectory, however, increases the time that the spacecraft must be in the atmosphere, which increases the total heat load.

5.3.5 The Case for Venus

Free-return trajectories to Venus have also been investigated. In 1969 Hollister [84], and in 1970 Hollister and Menning [85], found free-return trajectories that repeatedly encounter Earth and Venus (also known as Earth-Venus cycler trajectories). In 2000, Bonfiglio et al. [104] investigated Venus free returns using aerogravity assists. In general however, far less attention has been paid on human missions to Venus as it has been for Mars. Nevertheless, the case for Venus has been proposed (or at least addressed) by some [105–109].

For Inspiration Mars, the results of this study indicate that, apart from the nominal Inspiration Mars opportunity in December of 2017 to January of 2018 (and apart from the high entry-speed cases in Table 5.8), the only near-term IM-type mission candidates are the 2021 EVME trajectories listed in Table 5.4. However, as the 2018 nominal launch date nears, it may turn out that the 2021 EVME opportunity becomes the new "nominal" case, and if so, there would be no near-term backup for such a mission. Since a primary goal of Inspiration Mars is to push human spaceflight

into deep space, many of the mission objectives could still be met with a human flyby of Venus alone—albeit an *Inspiration Venus* mission.

To investigate such an option, the Venus free-return gravity-assist path Earth-Venus-Earth (EVE) was searched using STOUR, and many near-term opportunities were found. Because this is proposed as an alternate for Inspiration Mars (or some other IM-type mission), the same constraints were imposed on this STOUR search with regard to Earth launch and arrival V_∞ and TOF. Therefore, any vehicle designed for the EVME 2021 trajectory, should be capable of flying a candidate EVE trajectory.

Figure 5.22 shows the search results over launch dates spanning from 1/1/2019 through 1/1/2027 with steps of one day, and all with Earth arrival V_∞ at or below 9 km/s. These dates were chosen as the most relevant near-term launch dates for backup to the nominal Inspiration Mars trajectory, as well as to the 2021 EVME opportunities. An eight-year span of launch dates was chosen as it is the approximate time for the Earth-Venus geometry to repeat in inertial space (approximately 8 Earth and 13 Venus revolutions about the Sun). A minimum flyby altitude of 300 km at Venus was also imposed for this search. The figure shows five columns of opportunities whose launch dates each span about six months. The distance between columns is consistent with the Earth-Venus synodic period (assuming circular-coplanar orbits) of about 1.6 years, which repeats approximately five times in the eight years shown. From the results in the figure, it is clear that many EVE candidates are available for an IM-type mission.

To identify the most desirable EVE near-term candidates, Fig. 5.23 shows the same candidate trajectories as shown in Fig. 5.22, but with Earth launch date exchanged for Earth arrival V_∞ on the horizontal axis. The trajectories that make up the Pareto set have been circled, and are mostly made up of opportunities in 2026, although those that exhibit lower arrival V_∞ have launch dates in 2019 and 2021 (as annotated on the figure).

A representative subset of the Pareto-set EVE trajectories is given in Table 5.9. The cases listed include a case with the overall lowest Earth launch V_∞, Earth arrival
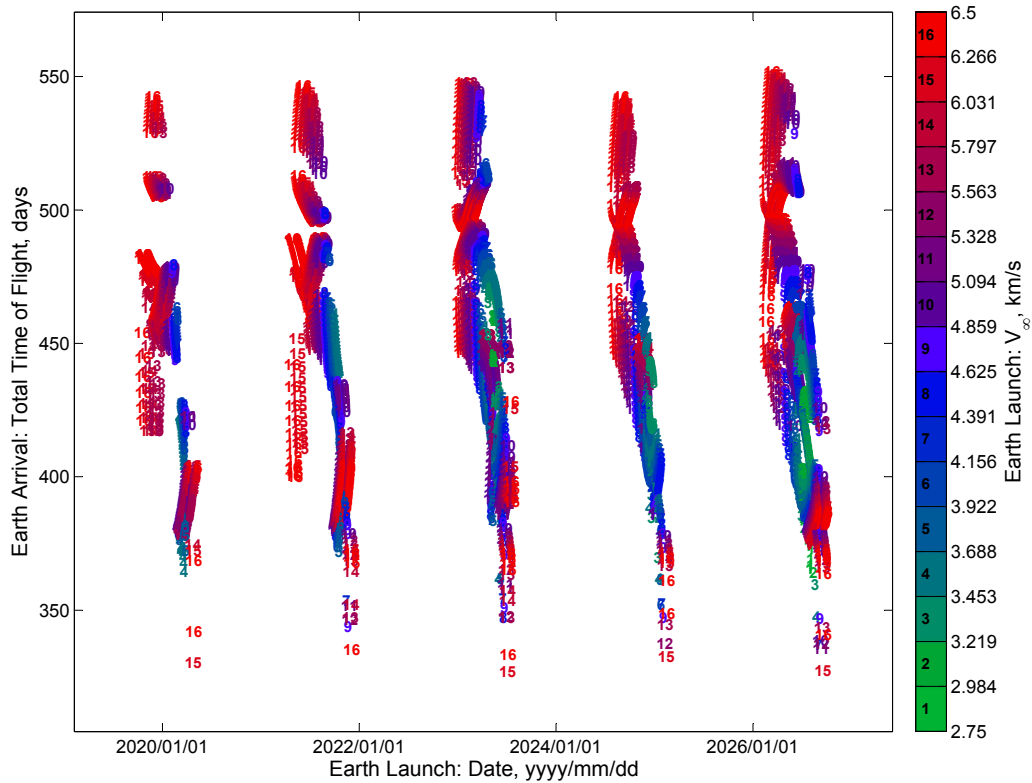
Figure 5.22.: Venus free-return trajectories (gravity assist path Earth-Venus-Earth) with launch dates spanning eight years, from January 1, 2019 to January 1, 2027. All results shown have an Earth arrival V_∞ less than or equal to 9 km/s.

V_∞, and TOF, respectively. Since the Pareto set does not include many of the candidates from other launch years, the case from 2019 is included in the list. Additionally, candidates that more closely follow the 2021 EVME launch dates (such as in 2023) are not included in the Pareto set, but due to more convenient launch dates, may be of interest for backup to the EVME candidates in 2021. Therefore, one such EVE case with launch date in 2023 is also included in Table 5.9. (All trajectories listed in Table 5.9 have a minimum solar distance no smaller than that of the orbit of Venus; at about 0.72 AU.)

One immediate observation of the results in Table 5.9 is that the EVE trajectories are capable of providing much lower launch and arrival V_∞ and TOF values than the EVME cases. The difference is even more extreme when compared to the nominal
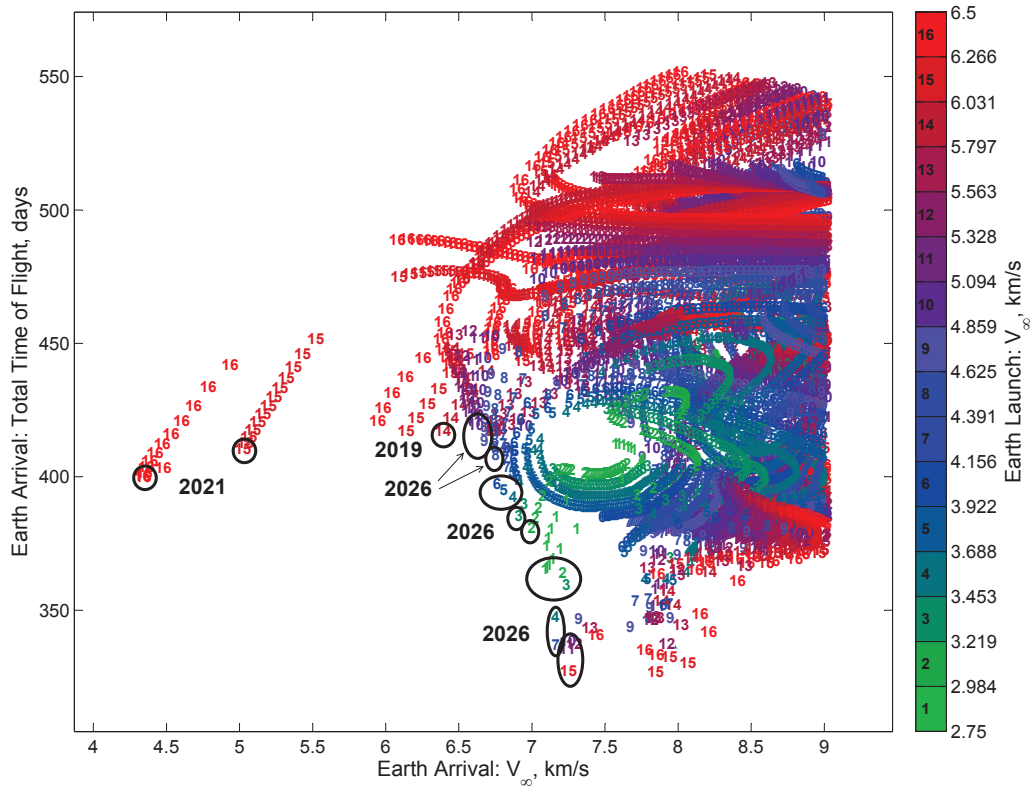
Figure 5.23.: Venus free-return trajectories. Candidates in the Pareto set are shown circled and annotated with corresponding launch year. Most Pareto-set candidates are shown to occur in the year 2026.

Table 5.9.: Subset of Best Near-Term EVE Opportunities

Launch Date	$V_{\infty,L}$, km/s	C_3, km^2/s^2	TOF, days	$V_{\infty,A}$, km/s	V_{Entry}, km/s
07/31/2026	2.75	7.56	366	7.09	13.15
05/07/2021	6.50	42.25	400	4.34	11.90
09/18/2026	6.25	39.06	327	7.25	13.24
11/18/2019	6.00	36.00	417	6.39	12.79
*07/02/2023	5.75	33.06	347	7.83	13.56

*Not in Pareto-optimal set of trajectories from Fig. 5.23.

2018 Inspiration Mars trajectory. In fact, the EVE trajectories appear so attractive that a Venus-only flyby mission may be more desirable than the EVME opportunity as a backup, or in the extreme case, a replacement for the nominal Inspiration Mars trajectory in early 2018. Additionally, a set of desirable EVE trajectories similar

to those in 2026 will also occur in 2018 (since the Earth-Venus inertial geometry approximately repeats every 8 years).

Regarding Earth entry, the nominal Inspiration Mars opportunity was found to undergo direct entry within acceptable g-loads for the crew, and nearly acceptable heat rates. Since (among the best cases) the maximum EVE arrival V_∞ found of 7.83 km/s (entry speed of 13.56 km/s) is more than 1 km/s less than that of the nominal Inspiration Mars EME opportunity, direct entry for the EVE was (to within the scope of this study) deemed feasible, and a separate entry analysis for the EVE cases was not done.

5.3.6 Feasibility of Launch

For both launch vehicles suspected to be used for such an IM-type mission (the Falcon 9 Heavy and SLS), the launch site location will be at Kennedy Space Center (KSC). To avoid flying over populated areas, KSC has a maximum allowable inclination of 57º relative to Earth's equatorial plane [110]. If the desired orbit has an inclination larger than 57º (and if launch must occur at KSC), then a plane change maneuver is required [111], which may have a prohibitively large ΔV. The minimum possible inclination is limited by the latitude at KSC of 28.5º.

For a given interplanetary trajectory, there is also the geometric constraint [111]

$$i \geq |\delta| \tag{5.7}$$

where i is the inclination of the desired departure hyperbolic trajectory, and δ is the declination angle of the Earth departure V_∞ vector (i.e. the angle between the vector and the equatorial plane). These inclination constraints must be satisfied for a trajectory (launching from KSC) to be feasible, without the need of a plane change maneuver. Thus, the declination angle for a particular interplanetary trajectory can (if larger than 57º) render that trajectory infeasible if launch is to take place from KSC. Additionally, any trajectory launching from KSC that requires an inclination

larger than 28.5º will suffer further losses in launch vehicle performance by not taking full advantage of Earth's rotational velocity [112].

The declination angles (found using STOUR) for a select set of free returns to Mars and Venus are are listed in Table 5.10. By applying Eq. 5.7 and the constraint for KSC that $57º \leq i \leq 28.5º$, Table 5.10 shows that nearly all listed trajectories can launch due east from KSC, with 28.5º inclination. The exception is the EVME opportunity on 11/22/2021, which will require an inclination of at least 56.6º. This inclination would normally be of some concern since it is larger than 28.5º and is nearly reaching the 57º-limit for KSC; however, a recent study by Post and Loucks [113] shows that such a launch is feasible (for this EVME opportunity) using the SLS, with a payload mass of approximately 25.3 metric tons.

Table 5.10.: Declination of Select Free Returns to Mars and Venus

Path	Launch Date	δ, deg
EME	12/27/2017	-9.8
EVME	11/22/2021	-56.6
EVME	09/09/2023	-21.5
EVE	07/02/2023	7.0

5.4 Conclusion

The nominal Inspiration Mars trajectory, with launch date in December 2017 to January 2018, was shown to be one of the best achievable free returns, if Venus is not to be used for gravity assist. A caveat to this statement however is that direct entry for this trajectory (of 14 km/s) has a total heat rate that nearly reaches that of the flight ready ACC TPS material, and may need additional qualification testing to be used for Inspiration Mars.

This study has also found key alternate opportunities, such as the EVME Mars free-return on November 22, 2021, for application to Inspiration Mars (or similar

IM-type) mission. These trajectories were found to possess significantly lower V_∞ values at Earth launch and arrival (with a moderate increase in TOF) compared to those exhibited by the nominal Inspiration Mars trajectory (with launch date in late 2017 – early 2018). One major advantage to the 2021 free return being that the flight-ready TPS material ACC is suitable for direct entry using Dragon. If Orion is used instead, ACC, PICA, and possibly Avcoat (pending further qualification testing) can be used—making the 2021 opportunity achievable (from a trajectory standpoint) using present-day technology.

All trajectories of the gravity-assist path EMVE were found to provide similar launch and arrival V_∞ values, but all with TOF greater than about 800 days—much too long for an IM-type mission. Similarly, the path EVMVE produced solutions with acceptable launch and arrival V_∞, but all with TOF longer than the 600-day constraint.

The existence of the low launch and low arrival V_∞ values found from the EVME search results can be attributed to the near-minimum-energy transfer arcs between the bodies. The Earth-Venus-Mars geometry that allows for such opportunities occurs in 2021 and 2034, whereupon each set of solutions approximately reoccurs every 32 years thereafter.

An EVME opportunity could also serve as a replacement for the nominal Inspiration Mars trajectory in 2018. In fact, the November 22, 2021 opportunity was proposed to the United States House of Representatives Committee on Science, Space, and Technology, on February 27, 2014. The proposal was for an IM-type mission (using the November 2021 opportunity) to be the first human-crew, deep-space mission for the Orion and Space Launch System.

For the Inspiration Mars mission, if the 2021 EVME free-return becomes the new nominal opportunity, a backup will be needed. EVME trajectories with high entry speeds were found in 2023, that may serve as a suitable backup. The feasibility of such a trajectory will depend on further development of PhenCarb TPS materials, or qualification of other heritage TPS materials (such as ACC) at increased heat rates

on the order of 3000 W/cm^2. Additionally, if the TPS mass fraction for direct entry (of 22.0%) is found to be unacceptably high, aerocapture must be developed for the 2023 opportunity to be feasible (presuming its TPS mass fractions of 18.4% is found to be acceptable).

Venus free-return opportunities (using the gravity-assist path Earth-Venus-Earth) were also found with the same search constraints on Earth launch and arrival V_∞, and TOF as those for the Mars free-return cases. Many candidate EVE opportunities were found with either lower launch V_∞, arrival V_∞, or TOF than any found for the EME or EVME Mars flyby opportunities. Although Mars is the ultimate goal, the EVE opportunities may prove to be essential for an IM-type mission, with Venus as the primary flyby target, if a mission to flyby Mars becomes unobtainable by the desired launch dates. A Venus free-return would allow for a human deep-space mission, and thereby meet many of the primary mission objectives of Inspiration Mars.

There is a need for a second-chance opportunity to the nominal Inspiration Mars trajectory in late 2017 to early 2018. Several near-term EVME opportunities found in this study are suitable candidates to (and with regards to launch and arrival V_∞, more desirable than) the nominal trajectory. If the launch date in early 2018 cannot be met, the EVME gravity-assist path provides this opportunity in 2021—essential for keeping the Inspiration Mars mission alive. Be it with the 2018 or the 2021 opportunity, if an IM-type, human-crewed, Mars-flyby mission is to happen before the mid 2030's, we must go now!

6. VERIFICATION OF TRAJECTORIES TO ESTABLISH EARTH-MARS CYCLERS

6.1 Introduction

In the late 1960s and early 1970s, Hollister [84, 114] and Hollister and Menning [115, 116] discovered trajectories that use gravity-assists to repeatedly encounter the Earth and Venus. Rall [117] and Rall and Hollister [118] were the first to show that these types of trajectories also exist between Earth and Mars.

Trajectories that repeatedly encounter the same planets on a regular schedule without stopping are now known as cycler trajectories, or *cyclers*. Two varieties of such trajectories are ballistic cyclers and powered cyclers. Powered cyclers, however, require large propellant expenditures compared to ballistic cyclers. Another variety of cycler (known as a "semi-cycler") involves occasional stops (or stay times) at a planet, but requires an expenditure of propellant to capture into (and depart from) an orbit about that planet [119].

The advantage of a ballistic cycler is that the vehicle can be more massive than a powered cycler. Massive vehicles are preferable for long human missions because they allow for increased space, and therefore comfort, for the crew. Cycler vehicles can also be made safer by adding a significant amount of material between the source and the crew for radiation protection.

Perhaps the simplest and most famous of the Mars cyclers is the Aldrin cycler, named for Buzz Aldrin [120–122]. Several other types of cycler trajectories have been offered as possible solutions by Niehoff [123, 124]; Friedlander et al. [125]; Brynes et al. [126]; McConaghy et al. [127]; and Russell and Ocampo [128]. Each of these have their advantages and disadvantages, but the problem of getting cycler vehicles into

their cycler orbits is significant, and establishing these transfer trajectories has not been investigated.

The simplest way to get onto the desired cycler trajectory is to perform a single, large maneuver at Earth, but this method would be expensive with regards to propellant consumption. In light of this, a more efficacious method of constructing "establishment trajectories" is attempted by Rogers et al. [83]. In their paper, the term "establishment-cycler" is introduced to designate the two combined trajectories, namely the establishment trajectory and the cycler trajectory.

6.2 V_∞ Leveraging

V_∞ leveraging is the use of a small deep-space maneuver to modify the V_∞ at a body. This maneuver, when used in conjunction with a gravity assist maneuver to get onto the desired cycler orbit, reduces the overall ΔV for the mission. Figure 6.1 illustrates the concept of V_∞ leveraging, and a detailed description of it (as well as an introduction to the notation used in this section) is given by Sims et al. [32] as follows:

First, a nominal orbit is chosen that has a period that will intercept the Earth after an integer number of periods. To find such nominal orbits, one chooses the number of Earth orbit revolutions (K) and the number of spacecraft orbit revolutions (L). If the spacecraft is on this orbit and no other maneuver is performed, the spacecraft would intercept the Earth tangentially in K years.

Next, an initial tangential ΔV is performed so that the resulting V_∞ is slightly larger than the V_∞ required to get onto the nominal orbit.

On some revolution number (M) of the orbit, a retrograde maneuver is performed at aphelion. This maneuver causes the orbit of the spacecraft to intersect the orbit of the Earth non-tangentially at two locations. The notation used to specify a given V_∞-leveraging technique is K:L(M)$^\pm$. The trajectory after the flyby is determined by
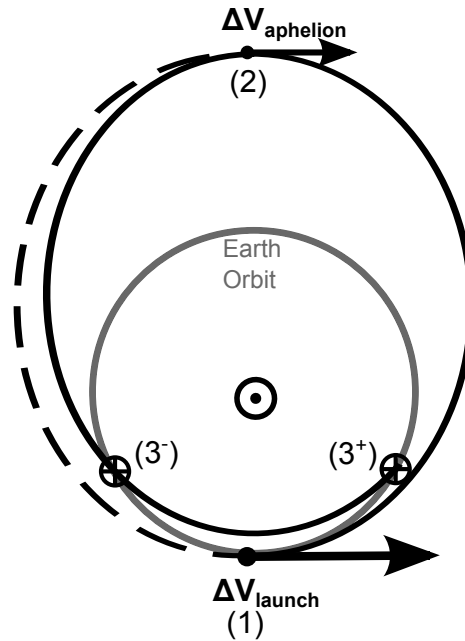
Figure 6.1.: The V_∞-leveraging maneuver consists of a (1) ΔV_{launch} followed by a (2) $\Delta V_{aphelion}$ to increases the V_∞ at the subsequent Earth flyby, which may be chosen to occur before (3^-) or after (3^+) perihelion. It should be noted that the crew does not board the cycler vehicle until the Earth flyby.

whether the encounter is selected to be before $(-)$ or after $(+)$ perihelion and by the altitude of the flyby.

The maneuver is performed at aphelion because the shape of the orbit is the most efficiently altered when the velocity is the lowest. Therefore, performing the maneuver at aphelion produces the largest encounter angle between the Earth and the spacecraft [129]. Sims found [32] that for aphelion radii at the orbital distance of Mars, flybys before perihelion require less total ΔV. The trajectories considered in this paper will all have aphelia close to Mars.

6.2.1 Selected Cyclers and Their Characteristics

The trajectories considered for establishment via V_∞ leveraging are the Aldrin Cycler [121], the VISIT cyclers [123–125], and various two synodic period cyclers [126, 127]. The orbital elements of the first legs of the various cycling trajectories are

presented in Table 6.1. To illustrate an example of a cycler trajectory, the Aldrin Cycler is shown in Figure 6.2.

Table 6.1.: Orbital Elements and Number of Vehicles for Selected Cycler Trajectories

Type	Number of vehicles	Semimajor axis, AU	Eccentricity	Aphelion, AU	Perihelion, AU
Aldrin Cycler	2	1.60	0.393	2.23	0.97
VISIT-1	14[a]	1.17	0.193	1.40	0.94
VISIT-2	14[a]	1.31	0.275	1.67	0.95
Case 1	4	1.22	0.238	1.51	0.93
Case 2	4	1.21	0.202	1.45	0.96
Case 3	4	1.30	0.268	1.65	0.95
S1L1	4	1.30	0.257	1.64	0.97
U0L1	4	2.05	0.563	3.20	0.90

[a] These cyclers repeat every 7 Earth-Mars synodic periods, which usually means that 14 vehicles are needed. However, the VISIT cyclers encounter Earth and Mars more often than once every 15 years, so fewer vehicles could be used [127].

Several of the trajectories have multiple legs that change orbit characteristics after flybys of the Earth. However, to establish the cycler vehicle, only the characteristics of the first leg are used (i.e. E1 to M2).

The number of cycler vehicles is the amount needed to take advantage of each opportunity on both the outbound cycler (ascending or up escalator) and inbound cycler (descending cycler or down escalator). Each cycler trajectory passes through Earth orbit and Mars orbit at least twice each, so it is crucial to know at which passage the spacecraft would encounter each planet. The Aldrin and Case 1 cyclers launch from Earth before perihelion, and all of the cyclers, with the exception of Case 1, encounter Mars before aphelion.
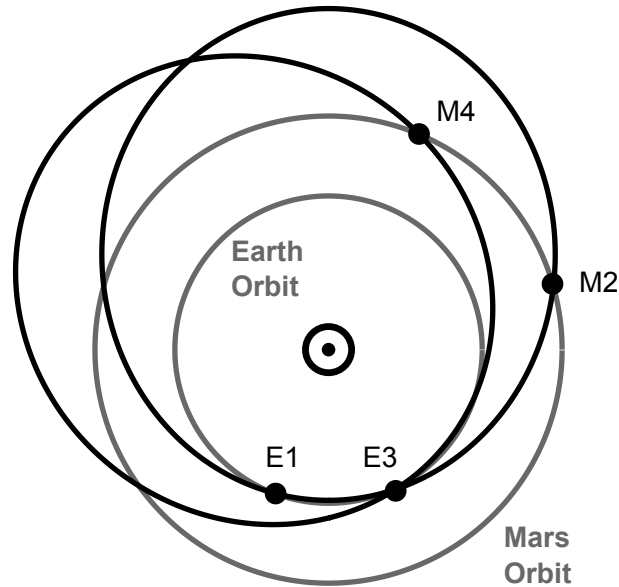
Figure 6.2.: The Aldrin Cycler. The cycler vehicle launches from Earth (E1) and travels to Mars (M2). The spacecraft next encounters Earth (E3), one synodic period after launch. A gravity assist is performed, which rotates the line of apsides by 1/7 of a revolution. The cycler vehicle continues on to Mars (M4), and repeats the process ad infinitum. After 7 Earth-Mars synodic periods (15 years), the Earth is at the same inertial position as launch.

6.3 Patched Conic Propagator Analysis

Establishment-cycler trajectory solutions were found by Rogers et al. [83] using a genetic algorithm method and assuming a circular, coplanar model. These circular-coplanar model solutions can be verified using STOUR (i.e. a patched-conic model with analytical ephemeris) which provides a higher order of fidelity compared to the circular-coplanar model.

Incorporating the V_∞-leveraging maneuver in STOUR was achieved using the ΔV-EGA subroutine [31]. The subroutine allows the user to specify launch date, nominal orbit, approximate deviation in launch V_∞ from the nominal, location of the maneuver in terms of true anomaly, and number of heliocentric spacecraft and

Earth revolutions between the maneuver and the Earth flyby. With the parameters of the V_∞-leveraging maneuver specified, STOUR then finds all possible patched-conic trajectories to the subsequent Mars encounter. To ensure that the desired cycler trajectory is found, launch dates were searched over a three-year period in order to encompass the $2\frac{1}{7}$ year Earth-Mars synodic period. The starting launch date was chosen to be no sooner than 2022. For cycler trajectories with aphelion radii near that of the perihelion of Mars, search windows larger than three years were required, as the relative orientation between Earth and Mars must occur when Mars is near its perihelion.

Once STOUR calculates the trajectories for the specified span of launch dates, those trajectories that have orbit characteristics similar to the cycler trajectory of interest are identified. First, trajectories with the desired cycler shape are found by matching the aphelion and perihelion radii for the Earth to Mars arc to the theoretical aphelion and perihelion radii of the cycler (in the circular, co-planar model). The trajectory then must be checked to ensure the transfer occurs on the correct segment of the orbit. For example, on the Earth-to-Mars leg of the outbound Aldrin cycler, the spacecraft must encounter Earth (at E1) just before perihelion and arrive at Mars (at M2) before reaching aphelion. The final trajectories chosen from the STOUR output over the three-year search were those that most closely matched the desired cycler orbit shape (i.e. aphelion and perihelion radii) while also providing the desired orbit segment on the trip from Earth to Mars for the first leg of the trajectory.

6.4 Low-Thrust Analysis

An alternative to using the impulsive methods described above to place the cycler vehicle into the desired orbit is low-thrust propulsion. Electric propulsion systems employ low thrust in order to increase the mass delivered or reduce the time of flight compared to chemical propulsion systems that use impulsive maneuvers [130, 131].

For this application, low thrust can be used to shape an orbit so that it acts similar to the V_∞-leveraging trajectories. Instead of using two impulsive maneuvers, there are thrusting arcs spread out over large portions of the orbit.

The low-thrust establishment trajectories were constructed by Rogers et al. [83] using MALTO [37], assuming that the V_∞ of launch from Earth is 0 km/s. A series of low-thrust maneuvers are performed in order to encounter the first Earth flyby of the cycler trajectory at the proper time and with the correct V_∞ and to continue on the cycler trajectory to Mars. Unlike the case using the V_∞-leveraging technique, multiple encounters during the establishment phase are allowed, and these encounters are added until the launch V_∞ is reduced to 0 km/s.

MALTO approximates continuous thrust by dividing each planet-planet leg of the trajectory into segments with an impulsive ΔV at each of the midpoints. The propagation of the trajectory between these impulsive maneuvers assumes conic trajectories and also assumes that all flybys are instantaneous and modeled by the rotation of the V_∞ vectors. This method results in a constrained nonlinear optimization problem, which MALTO solves by using the nonlinear programming software Sparse Nonlinear OPTimizer (SNOPT) [132,133]. MALTO solves for the cycler trajectory in which the final mass is maximized.

6.5   Results

6.5.1   STOUR Verification of V_∞-Leveraging Establishment Trajectories

STOUR trajectory data for the given establishment-cycler trajectories are shown in Table 6.2. According to NASA's Mars Design Reference Architecture [134], the Earth-to-Mars time of flight should be 180 days or less for the health of the crew. The results from STOUR confirm that the Aldrin, Case 2, and U0L1 cyclers have times of flight that satisfy this requirement. The 4:3(2)$^-$ Case 3 and 4:3(2)$^-$ S1L1 establishment-cycler trajectories have the smallest Earth launch V_∞ values, as well as some of the smallest maneuver ΔV values. The lowest maneuver ΔV values come

from the $4:3(2)^-$ VISIT-1 and $4:3(2)^-$ Case 2 establishment-cycler trajectories, 0.043 km/s and 0.059 km/s, respectively. Unfortunately, the VISIT-1 cycler requires more than 180 days to reach Mars, and, requires a large number of cycler vehicles (up to 14 for missions that return the crew back to Earth). The $4:3(2)^-$ Case 2 establishment-cycler trajectory, on the other hand, has an Earth launch V_∞ of only 2.522 km/s, and has an Earth-Mars flight time of 171 days. Another notable establishment-cycler trajectory is the $4:3(2)^-$ Aldrin cycler, which has a time of flight of 161 days, an Earth launch V_∞ of 2.608 km/s, and a maneuver ΔV of 0.568 km/s. It should also be noted that for all of the trajectories considered in Table 6.2, the closest approach flyby altitude is well above the safe altitude of 300 km.

Table 6.2.: STOUR Results for the Selected Cyclers in the Analytic Ephemeris

Type	K:L(M)	LD	TOF[a] days	r_p AU	r_a AU	$V_{\infty,L}$ km/s	ΔV_{DSM} km/s	$V_{\infty,flyby}$ km/s	h_{flyby} km
Aldrin	$4:3(2)^-$	01/03/2023	161	0.983	2.229	2.608	0.568	5.509	10,483
	$3:2(1)^-$	12/09/2023	172	0.964	2.229	3.449	0.530	6.546	20,745
VISIT-1	$4:3(2)^-$	06/12/2046	201	1.012	1.470	2.540	0.043	2.834	120,625
VISIT-2	$4:3(2)^-$	12/27/2022	207	0.985	1.670	2.503	0.221	3.878	7,696
Case 1	$4:3(2)^-$	12/14/2024	365	0.946	1.503	2.558	0.346	4.526	140,286
Case 2	$4:3(2)^-$	04/22/2029	171	0.997	1.433	2.522	0.059	2.910	56,068
Case 3	$4:3(2)^-$	12/20/2022	216	0.988	1.651	2.492	0.187	3.688	13,291
S1L1	$4:3(2)^-$	12/20/2022	221	0.987	1.635	2.492	0.182	3.657	12,965
U0L1	$3:2(1)^-$	11/25/2025	97	0.960	3.189	3.702	0.794	8.049	6,633

[a] Time of flight from Earth flyby to Mars.

The savings from V_∞ leveraging, in terms of both launch V_∞ and overall ΔV (compared to launching the cycler directly into its orbit) are discussed in detail by Rogers et al. [83] An example of the $4:3(2)^-$ Aldrin establishment-cycler trajectory (produced using STOUR) is illustrated in Figure 6.3.

When the establishment-cycler trajectories given in Table 6.2 were determined, the aphelion of the cycler trajectories was usually the first parameter examined to find a match to a particular cycler trajectory (out of the many trajectories found in STOUR). Once a match was found for the aphelion (usually to within a hundredth of an AU), the cycler trajectory with the closest to the desired perihelion was chosen

as the candidate match. Because of this selection order (aphelion first, perihelion second), the aphelion values tend to match more closely to those determined by the circular, co-planar model than do the perihelion values, as observed in Table 6.2 and Table 6.1.
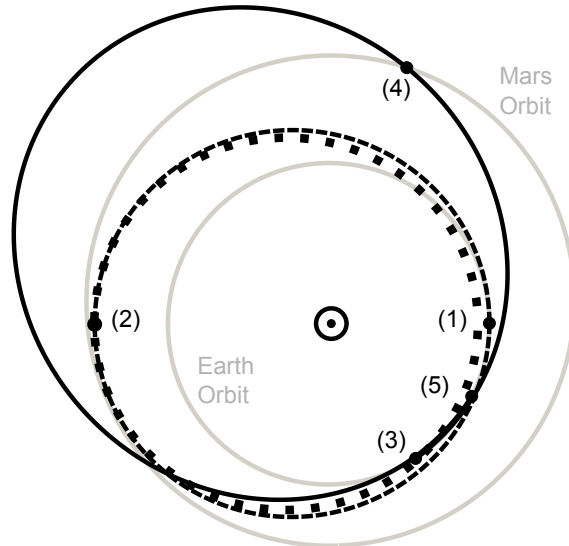

Figure 6.3.: The $4{:}3(2)^-$ Aldrin establishment-cycler trajectory. The spacecraft launches (1) from the Earth onto the *dashed* orbit and completes one and a half orbits. At aphelion (2) of this orbit, a maneuver is performed to lower the perihelion and get onto the *dotted* orbit. The spacecraft completes one full orbit and returns to aphelion. The spacecraft continues inbound toward perihelion and flies (3) by the Earth. This flyby raises the heliocentric energy of the orbit and puts the vehicle on the cycler trajectory (the *solid* line). Mars is encountered (4), but does not significantly affect the trajectory. The spacecraft completes its orbit and encounters the Earth (5) once more in order to continue on the cycler trajectory.

6.5.2 Validation of Low-Thrust Establishment Trajectories

One concern with the low-thrust establishment-cycler trajectories designed by Rogers et al. [83], is that the time taken for the spacecraft to fly by Earth is relatively long compared to other missions. In this analysis, the spacecraft is considered to be in Earth's vicinity when it is within Earth's Hill sphere (of radius 1.5×10^6 km or 0.01 AU). For the Aldrin establishment-cycler trajectory, the spacecraft is within

the Earth's Hill sphere for about 80 days at launch, 14 days at the next flyby, and then about 6 days at the final establishment flyby. (For comparison, the Galileo spacecraft spent only about 4 days inside Earth's Hill sphere for its two Earth flybys, and the Cassini spacecraft's Earth flyby only took about 3 days.) The 80 days at launch is considered to be a simple targeting problem and it is assumed for this study that the states upon exit of the Earth's Hill sphere could indeed be targeted using the given propulsion system. The other two Earth flybys however could prove to be problematic.

The issues come from the model assumptions used in the solutions generated by MALTO. The low-thrust trajectories produced by MALTO use patched-conics to model each gravity assist, and therefore the effect of Earth's gravity during a flyby is assumed to occur instantaneously. In practice of course, flybys take time!

This long flyby time also occurs for the S1L1 establishment trajectory, where the first Earth flyby takes approximately 18 days (the longest of all encounters considered in this study), and the second Earth flyby takes approximately 6 days. The VISIT-2 establishment trajectory's single Earth flyby is less of a concern as it takes only about 8 days. For illustrative purposed the S1L1 low-thrust establishment-cycler trajectory is shown in Figure 6.4.

To verify that the low-thrust establishment trajectories generated by MALTO are indeed feasible, the solution for the S1L1 establishment trajectory (the 'worst' case with regards to long flyby times) was recomputed with the additional considerations of both the time spent during the Earth encounters and the gravitational effects of the Sun during these encounters. This simulation was carried out in the following way:

1. Upon entry into Earth's Hill sphere (at the start of an Earth encounter), the position and velocity states from the MALTO solution were propagated in MATLAB using the Sun-Earth circular-restricted three-body (CR3B) model. The propagation continued until the vehicle exited the Hill sphere, and the final states were compared to the states from the MALTO trajectory.
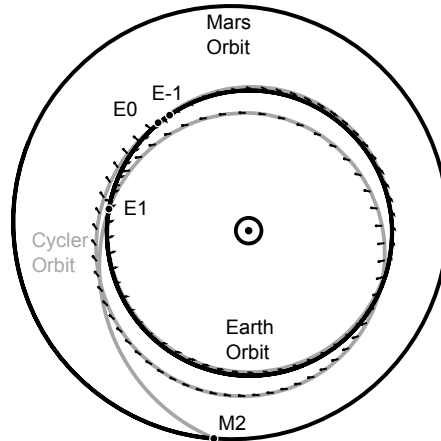
Figure 6.4.: Establishment of the S1L1 and Case 3 cyclers using low thrust. Launch from Earth begins at E-1, a gravity assist occurs at E0, and placement into the cycler orbit occurs at E1. Between E-1 and E0, slightly more than one full revolution of the Sun is completed. More than one full revolution occurs between E0 and E1. The E1-to-M2 leg is the first leg of the S1L1 and Case 3 cyclers. The next Earth-to-Mars leg (E3-to-M4) occurs two synodic periods later.

2. To aid in targeting the exit states of the MALTO trajectory, constant low-thrust (with respect to the Sun-Earth rotating frame) was applied to the propagated three-body model trajectory. The amount of constant thrust applied was found via trial and error.

3. Using the exit states from the propagated circular-restricted three-body trajectory (with constant low thrust), a new MALTO trajectory leg was found (i.e. the leg from E0 to E1). To ensure that the newly found MALTO trajectory remained 'close' to the originally found MALTO trajectory, the entry states for the next Earth encounter (from the originally found MALTO trajectory at E1) were targeted.

This process was then repeated for the second Earth encounter (at E1), and a new MALTO trajectory leg was found (from E1 to M2), where the states from the original MALTO trajectory at M2 were targeted.

To interface the patched conic model with the CR3B model, the coordinate frame that each model is computed in must be related. In this case, the patched conic solution in MALTO is computed in the Sun-centered J2000 ecliptic frame, and the CR3B model in MATLAB is computed in the Sun-Earth rotating frame.

The two frames are illustrated in Fig. 6.5, where

$$\mu = m_{Earth}/m^* \tag{6.1}$$

$$m^* = m_{Sun} + m_{Earth} \tag{6.2}$$

and m_{Earth} and m_{Sun} are the masses of the Earth and Sun, respectively.
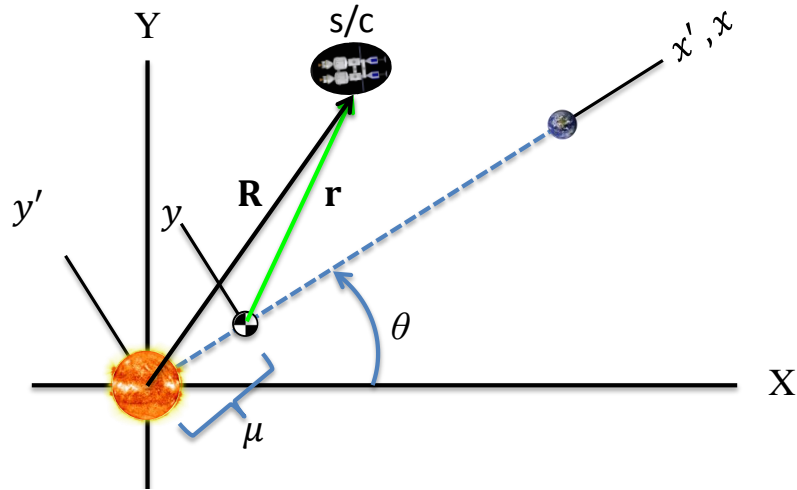
Figure 6.5.: Position of the cycler vehicle shown in both the Sun-centered J2000 ecliptic frame (with axes X-Y-Z) and the Sun-Earth rotating frame (with axes x-y-z).

In the figure, the Sun-centered J2000 frame, which we denote as the I frame, has axes X-Y-Z, and the Sun-Earth rotating frame, which we denote as the B frame, has axes x-y-z. To relate the I and B frames, we first relate values in x-y-z coordinates to coordinates in the intermediate-frame, B', with axes x'-y'-z', given by

$$
\begin{aligned}
x &= x' - \mu \\
y &= y' \\
x &= z'
\end{aligned}
\tag{6.3}
$$

where x, y, z, x', y', and z' are expressed in nondimensional units, by dividing each by the Sun-Earth distance. To nondimensionalize distance and time units, values are divided by l^* Sun-Earth distance and t^*, respectively, when appropriate, which are given by

$$
\begin{aligned}
l^* &= \text{Sun-Earth distance} \\
t^* &= \sqrt{(l^*)^3/(Gm^*)}
\end{aligned}
\tag{6.4}
$$

where G is the gravitational constant.

We denote the position of the spacecraft in the I and B frames as, $\mathbf{R}$ and $\mathbf{r}$, respectively, giving

$$
\begin{aligned}
\mathbf{R} &= R_x \hat{X} + R_y \hat{Y} + R_z \hat{Z} \\
\mathbf{r} &= r_x \hat{x} + r_y \hat{y} + r_z \hat{z}
\end{aligned}
\tag{6.5}
$$

The I and B frames can then be related by first rotating from X-Y-Z to x'-y'-z' about the Z=z' axis by angle θ, and then converting from B' to B coordinates using Eq. (6.3), giving

$$
\begin{aligned}
r_x &= R_x \cos\theta + R_y \sin\theta - \mu \\
r_y &= R_y \cos\theta - R_x \sin\theta \\
r_z &= R_z
\end{aligned}
\tag{6.6}
$$

or more compactly as

$$
\mathbf{r} = {}^I\mathbf{C}^{B'}\mathbf{R} + \begin{bmatrix} \mu \\ 0 \\ 0 \end{bmatrix}
\tag{6.7}
$$

where $\mathbf{r}$ and $\mathbf{R}$ are expressed as column vectors, and the direction cosine matrix, $^I\mathbf{C}^{B'}$ is given by,

$$^I\mathbf{C}^{B'} = \begin{bmatrix} \cos\theta & \sin\theta & 0 \\ -\sin\theta & \cos\theta & 0 \\ 0 & 0 & 1 \end{bmatrix} \tag{6.8}$$

Thus, given position states from MALTO in Sun-centered J2000 coordinates (i.e. given $\mathbf{R}$), Eqs. (6.6) and (6.7) can be used to compute the equivalent position vector in the Sun-Earth rotating frame.

To compute relate the velocity states, we use the basic kinematic equation (BKE), giving

$$\frac{^I d}{dt}\mathbf{R} = \frac{^B d}{dt}\mathbf{R} + {}^I\omega^B \times \mathbf{R} \tag{6.9}$$

where $^I\omega^B$ is the rotation (i.e. angular velocity vector) of the B frame with respect to the I frame, given in nondimensional units (revolutions per time) by

$$^I\omega^B = 1\hat{Z} = 1\hat{z} \tag{6.10}$$

The time derivative $\frac{^I d}{dt}\mathbf{R}$ represents the derivative of $\mathbf{R}$ with respect to the I frame, and $\frac{^B d}{dt}\mathbf{R}$ represents the derivative of $\mathbf{R}$ with respect to the Sun-Earth rotating frame. By expressing R as,

$$\mathbf{R} = \mu\hat{x} + \mathbf{r} \tag{6.11}$$

and plugging into Eq. (6.9), and noting that the derivative of the constant μ with respect to time is zero, gives

$$\frac{^{I}d}{dt}\mathbf{R} = \frac{^{B}d}{dt}\mathbf{r} + {^{I}\omega^{B}} \times (\mu\hat{\mathbf{x}} + \mathbf{r}) \tag{6.12}$$

Noting that $\frac{^{I}d}{dt}\mathbf{R}$ is the spacecraft velocity with respect to the Sun-centered J2000 ecliptic frame, and $\frac{^{B}d}{dt}\mathbf{r}$ is the velocity of the spacecraft with respect to the Sun-Earth rotating frame, Eq. (6.12) can be written as

$$\nu = {^{I}\mathbf{C}^{B'}}\mathbf{V} - {^{I}\omega^{B}} \times (\mu\hat{\mathbf{x}} + \mathbf{r}) \tag{6.13}$$

where ν is the spacecraft velocity with respect to the Sun-Earth rotating frame written in nondimensional B-frame coordinates, and $\mathbf{V}$ is the spacecraft velocity with respect to the Sun-centered J2000 ecliptic frame written in nondimensional I-frame coordinates (and thus is left multiplied by $^{I}\mathbf{C}^{B'}$ to convert to B-frame coordinates).

Thus, given the velocity states from MALTO in Sun-centered J2000 ecliptic frame, the corresponding velocity states in the Sun-Earth rotating frame can be computed using Eq. (6.13).

Once in the Earth's Hill sphere and the position and velocity states are converted into the Sun-Earth rotating frame, the CR3B model can be propagated by integrating the CR3B equations of motion with the modification of the added nondimensional acceleration due to the applied thrust, with components a_{T_x}, a_{T_y}, and a_{T_z}. The equations of motion (in nondimensional units) are given by

$$\begin{aligned}
\ddot{r}_x &= 2\dot{r}_y + r_x - \frac{(1-\mu)(r_x+\mu)}{d^3} - \frac{\mu(r_x-1+\mu)}{\tilde{r}^3} + a_{T_x} \\
\ddot{r}_y &= -2\dot{r}_x + r_y - \frac{(1-\mu)r_y}{d^3} - \frac{\mu r_y}{\tilde{r}^3} + a_{T_y} \\
\ddot{r}_z &= -\frac{(1-\mu)r_z}{d^3} - \frac{\mu r_z}{\tilde{r}^3} + a_{T_z}
\end{aligned} \tag{6.14}$$

where

$$\begin{aligned}
d &= \sqrt{(r_x + \mu)^2 + r_y^2 + r_z^2} \\
\tilde{r} &= \sqrt{(r_x - 1 + \mu)^2 + r_y^2 + r_z^2}
\end{aligned} \tag{6.15}$$

An example of a flyby at E1 propagated (using MATLAB) in the CR3B model for the S1L1 cycler trajectory is shown in Fig. 6.6 as viewed in the Sun-centered J2000 ecliptic frame. The size of Earth shown is not to scale, but the grey circular region around the Earth, which represents the Hill sphere, is shown to scale. The CR3B propagation with low thrust is shown in red, and without thrust (labeled as "ballistic" in the figure) is shown as the dashed black line. The MALTO solution is also shown. The flyby begins at the top right of the figure, where the spacecraft enters the Hill sphere, and ends at the bottom left of the figure, where the spacecraft departs the Hill sphere (during which time Earth is moving faster than the spacecraft and "overtakes" it). The figure clearly shows that the CR3B propagated flyby matches much more closely with the MALTO solution when constant low-thrust is applied. We also note that the MALTO solution has a "kink" in the middle of the flyby, which is attributed to MALTO's modeling of low thrust as discrete impulses (one of which occurs at the kink).
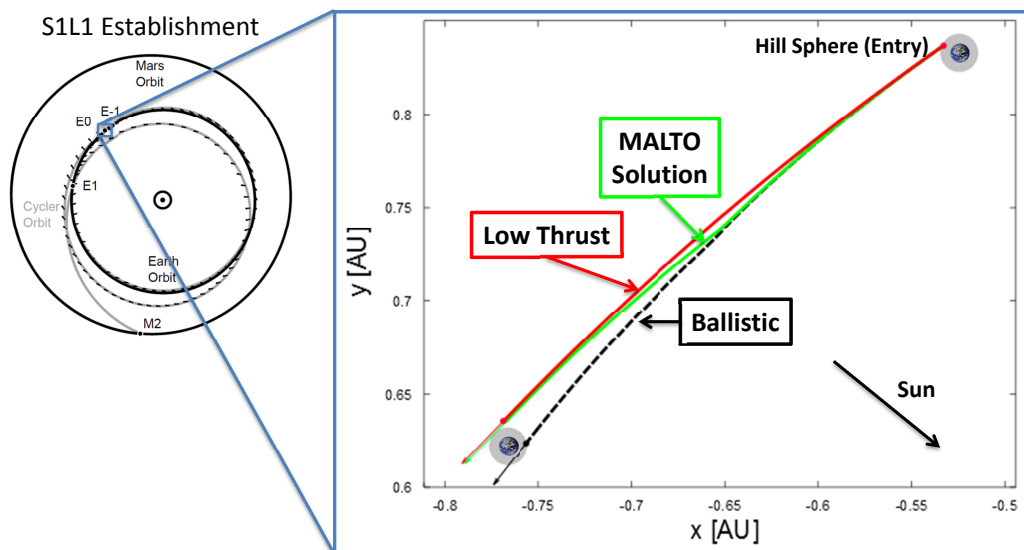

Figure 6.6.: Flyby at E1 for the S1L1 establishment trajectory viewed in Sun-centered J2000 ecliptic frame. The low-thrust and ballistic trajectories are both propagated in the Sun-Earth CR3B model, where the low-thrust arc as constant applied thrust.

Using the verification method presented in this section, the position and velocity states at each encounter of the original MALTO solution (i.e. the solution assuming instantaneous flybys) were successfully targeted, with negligible variance in spacecraft mass upon departure of the Hill sphere at E1—on the order of 10s of kg for a 75 Mg spacecraft. Much of this propellant mass agreement may be attributed to the robust nature of low-thrust trajectories, which may adjust for perturbations over months (or even years) of burn time, and effectively wash out the effects of such perturbations with little to no cost in propellant mass. Additionally, by thrusting with constant thrust through the flyby, the low-thrust burn takes advantage of burning through closest approach (where the velocity is greatest). Thrusting through the flyby makes the burn more efficient for the higher-fidelity flyby model, than for the patched conic MALTO solution, and may make up for any propellant that would otherwise be lost due to the slow flyby (if any is to be lost at all). In the patched conic model, the gravity of the flyby body is ignored (other than computing the bending of the velocity vector). For the S1L1 establishment trajectory used for this verification, the required propellant mass for the higher-order flyby model solution is found to be slightly less (by a few 10s of kg) than that found by the original MALTO solution, which may be attributed to the increased efficiency of the low-thrust burns taking place throughout the flyby and within Earth's gravity well.

6.6   Conclusion

It was found by Rogers et al. that, from the perspective of propellant savings, low-thrust establishment is superior to V_∞-leveraging establishment trajectories; however, V_∞-leveraging establishment trajectories can have times of flight that are several years shorter than low-thrust establishment.

The use of the circular-coplanar model to find suitable V_∞-leveraging establishment trajectories proved to be accurate. This validation was achieved using the JPL program STOUR, which uses a patched-conic model with analytic ephemeris.

By modeling the flybys using the CR3B model, perturbations in the low-thrust establishment trajectories (constructed using JPL's MALTO) due to the extended amount of time taken for the Earth flybys to occur were shown to be correctable (for the case of the S1L1 establishment trajectory) with the given low-thrust engine and with a negligible difference in required propellant mass.

7. CONCLUDING REMARKS

7.1 Contribution of Work

The primary contribution of this work are the candidate trajectories found for various missions to Mars, Venus, and the Ice Giants, which are intended to be a convenient source for mission designers, systems engineers, and scientists, to quickly assess the trajectory characteristics and derived mission requirements for relevant mission concepts. Rare free-return trajectories are identified for a near-term human flyby mission to either Mars, Venus, or both. Additionally, several broad-search trajectory catalogs (for chemical missions) are provided for a future orbiter mission to Uranus and Neptune, which will hopefully contribute to future decadal studies for such a mission. In particular, this investigation is one of the first to look closely at the benefits provided by the SLS for outer-planet science missions, one of which found in this work is the ability to do probe science at multiple outer-planet targets (such as the Saturn-Uranus mission opportunity proposed in Ch. 3).

The techniques and corresponding tools developed for this work are also a contribution to the field of astrodynamics. In previous studies, trajectories found using STOUR required designers to sort through the results of each gravity assist path separately. Using the post-processing python script (the STOUR Utility) developed for this work allows designers to compile the STOUR data from all gravity-assist paths, as well as incorporate various launch vehicles and thruster models, and compute relevant trajectory parameters (not computed by STOUR) such as delivered mass at the target body. This structure will enable future designers to incorporate other systems-level factors, such as a communications link analysis during probe entry.

For select cases, the development of the MATLAB script to model the approach trajectory at the target body, allows designers to visually modify the approach and

quickly assess the feasibility of a particular trajectory design before committing to a high-fidelity tool such as STK or GMAT. The formulation of the approach trajectory computations in this work is also intended on being a more convenient (and conceptually more understandable) approach than that presented in Ref. [111]. The formulation of the probe entry parameters on a rotating, oblate-spheroid atmosphere, is also intended on being a direct and convenient means to quickly estimate probe entry parameters to be shared with probe entry modeling specialist to model the probe entry and design the TPS. The calculation is fast and, when used in combination with the approach visualization, allows the designer to easily modify the approach while keeping in mind constraints such as ring avoidance, and is conducive for an iterative design environment between the mission designer and the probe entry modeling specialist. (For this work, the parameters for entry are specifically suited for the probe entry specialists at Ames Research Center, but may be easily adapted to compute any entry analysis parameters that are needed.)

7.2   Potential Advancement of Work

Most of the research presented in this thesis is based on solving a larger portion of the gravity-assist trajectory design space in a grid-like fashion, using patched-conics with an analytic ephemeris. Select cases can then be optimized using tools such as MALTO or EMTG; however, this occurs after the unoptimized has been sorted to identify the most attractive candidates for optimization. A potential issue with this technique is that the optimization process may dramatically improve the select cases, but the amount of improvement varies depending on how close to the optimal solution the STOUR solution happens to be. Solutions that are farther from their optimized performance may not make it through the initial sorting filter when select cases are identified, and the most attractive solution may be lost. Future work should automate the process of optimizing trajectories from STOUR in MALTO or EMTG before the solutions are sorted.

Future work may also incorporate more systems-level parameters and constraints into the STOUR Utility post processing script. A simplified form of the approach trajectory calculation could be implemented for a chosen approach ψ value (or inclination) to estimate the feasibility of the interplanetary trajectory for probe missions. With this information, a link analysis could also be incorporated to estimate the amount of data that could be transmitted (if any link is possible) from the probe to the spacecraft (and Earth) for a give trajectory. This will allow such mission components to be considered at the initial trajectory design phase, and potentially eliminate the need to trajectory redesigns later on in the design process.

For any outer-planet orbiter mission, a tour of the planet's moons is likely going to be desired. A moon-tour design is typically done as a point design separate of the interplanetary design, but has some common characteristics that are generally desirable. To keep the encounter velocities at each moon small, near-equatorial orbits are typically desired, which (to reduce propellant) need a low declination angle and low V_∞ at arrival. If low declination is not possible, a maneuver strategy must be implemented (after capture) to get the spacecraft into an equatorial orbit with minimal propellant. Future work could incorporate these constraints into the STOUR Utility, to improve the designers ability to find attractive and relevant trajectories for a moon tour.

In this work, any trajectories considered for aerocapture uniformly assumed a TPS mass fraction of 50%. Future work could incorporate a low- to mid-fidelity aerocapture model into the STOUR Utility, to more accurately estimate the TPS mass required, to more precisely identify attractive trajectory candidates for aerocapture. Options for a hybrid capture could also be implemented, where the atmosphere is used to dramatically reduce the planet-relative velocity, but then a thruster is used to implement the final ΔV needed for capture.

Lastly, for some trajectories, perturbations from third bodies (such as trajectories in a planet-moon system), non-spherical gravity terms (such as J_2), and solar radiation pressure (SRP), may significantly influence an interplanetary trajectory. Future

work for select cases could include a medium-high fidelity integrated form of the patched conic solution, which may include influences of third bodies, J_2, and SRP. If perturbations need to be considered during the initial trajectory sweep, computational speed could be improved by only integrating sections of the trajectory where the perturbation is most significant (e.g. only integrating the trajectory with SRP during times when the spacecraft is within 1 AU of the Sun). Such integrated, or patched-integrated, solutions may be necessary to improve a patched-conic solution in a high-perturbation environment, in order for it to serve as a suitable initial guess for a high-fidelity tool such as STK or GMAT.

REFERENCES

REFERENCES

[1] Lancaster, E. R. and Blanchard R. C., "A Unified Form of Lambert's Theorem," NASA Technical Note, No. NASA TN D-5368, Goddard Space Flight Center, Greenbelt, MD, Sept., 1969.

[2] Sturms, F. M. "Polynomial Expressions for Planetary Equators and Orbit Elements with respect to Mean 1950.0 Coordinate System," NASA Technical Report, JPL 32-1508, Pasadena, CA, Jan. 15, 1971.

[3] Williams, S. N., "Automated Design of Multiple Encounter Gravity-Assist Trajectories," M.S. Thesis, School of Aeronautics and Astronautics, Purdue University, West Lafayette, IN, Aug. 1990.

[4] Strange, N.J. and Longuski, J.M., "Graphical Methods for Gravity-Assist Trajectory Design," *Journal of Spacecraft and Rockets*, Vol. 39, No. 1, Jan.–Feb. 2002.

[5] Labunsky, A., Papkov, O., and Sukhanov, K., "Multiple Gravity Assist Interplanetary Trajectories," Earth Space Institute Book Series, Gordon and Breach, London, 1998, pp. 33–68.

[6] Johnson, W.R. and Longuski, J.M., "Design of Aerogravity-Assist Trajectories," *Journal of Spacecraft and Rockets*, Vol. 39, No. 1, Jan.–Feb. 2002.

[7] Chen, K.J., Kloster, K.W., and Longuski, J.M., "A Graphical Method for Preliminary Design of Low-Thrust Gravity-Assist Trajectories," AIAA Paper No. 2008-6952, AIAA/AAS Astrodynamics Specialist Conference, Honolulu, HI, Aug. 18–21, 2008.

[8] Campagnola, S. and Russell, R.P., "Endgame Problem Part 1: V_∞-Leveraging Technique and the Leveraging Graph," *Journal of Guidance, Control, and Dynamics*, Vol. 33, No. 2, March–April 2010.

[9] Campagnola, S. and Russell, R.P., "Endgame Problem Part 2: Multibody Technique and the Tisserand-Poincaré Graph," *Journal of Guidance, Control, and Dynamics*, Vol. 33, No. 2, March–April 2010.

[10] Archinal, B. A., A'Hearn, M. F., Bowell, E., Conrad, A., Consolmagno, G. J., Courtin, R., Fukushima, T., Hestroffer, D., Hilton, J. L., Krasinsky, G. A., Neumann, G., Oberst, J., Seidelmann, P. K., Stooke, P., Tholen, D. J., Thomas, P. C., Williams, I. P., "Report of the IAU Working Group on Cartographic Coordinates and Rotational Elements: 2009," *Celestial Mechanics and Dynamical Astronomy*, Vol. 109, pp. 101–135, 2011.

[11] Orbital ATK, "Space Propulsion Products Catalog," OSR No. 12-S-1902, Sept. 2012.

[12] Squyres S., "Vision and voyages for planetary science in the decade 2013–2022," National Research Council Publications, 2011.

[13] Green, J. L., "Planetary Science Division Status Report," Presentation at the Aug. 2015 Meeting of the Outer Planets Assessment Group.

[14] Spreen, C.M., Mueterthies, M.J., Kloster, K.W., and Longuski, J.M., "Preliminary Analysis of Ballistic Trajectories to Uranus Using Gravity-Assists from Venus, Earth, Mars, Jupiter, and Saturn," AAS Paper No. 11-623, AAS/AIAA Astrodynamics Specialist Conference, Girdwood, AK, July 31–Aug. 4, 2011.

[15] Dankanich, J. W. and McAdams, J., "Interplanetary Electric Propulsion Uranus Mission Trades Supporting the Decadal Survey," AAS Paper No. 11-189, AAS/AIAA Astrodynamics Specialist Conference, Girdwood, AK, July 31–Aug. 4, 2011.

[16] Landau, D., Lam, T., and Strange, N., "Broad Search and Optimization of Solar Electric Propulsion Trajectories to Uranus and Neptune," *Advances in the Astronautical Sciences*, Vol. 135, Part 3, No. AAS 09-428, 2009, pp. 2093–2112.

[17] Bocanegra-Bahamón, T., Bracken, C., Sitjà, M. C., Dirkx, D., Gerth, I., Konstantinidis, K., Labrianidis, C., Laneuville, M., Luntzer, A., MacArthur, J. L., Maier, A., Morschhauser, A., Nordheim, T. A., Sallantin, R., and Tlustos, R., "MUSE – Mission to the Uranian System: Unveiling the Evolution and Formation of Ice Giants," *Advances in Space Research*, Vol. 55, 2015, pp. 2190–2216.

[18] Agrawal, P., Allen, G. A. Jr., Sklyanskiy, E. B., Hwang, H. H., Huynh, L. C., McGuire, K., Marley, M. S., Garcia, J. A., Aliaga, J. F., and Moses, R. W., "Atmospheric Entry Studies for Uranus," IEEE Aerospace Conference, Paper No. 978-1-4799-1622-1, 2014.

[19] Saikia, S. J., et al., "MUSEings on Uranus: An Enhanced New Frontiers Class Mission to Uranus," Presentation at 11th International Planetary Probe Workshop, Pasadena, CA, June 16–20, 2014.

[20] Okutsu, M., Yam, C. H., Longuski, J. M., and Strange, N. J., "Cassini Saturn-Escape Trajectories to Jupiter, Uranus, and Neptune," *Acta Astronautica*, Vol. 79, 2012, pp. 157–167.

[21] McAdams, J., Scott, C., Guo, Y., Dankanich, J., and Russell, R., "Conceptual Mission Design of a Polar Uranus Orbiter and Satellite Tour," AAS Paper No. 11-188, AAS/AIAA Astrodynamics Specialist Conference, Girdwood, AK, July 31–Aug. 4, 2011.

[22] Hubbard, W.B., "Ice Giants Decadal Study," Planetary Science Decadal Survey: Mission Concept Study Final Report, National Aeronautics and Space Administration, June 2010, SDO-12345.

[23] Yam, C. H., McConaghy, T. T., Chen, K. J., and Longuski, J. M., "Design of Low-Thrust Gravity-Assist Trajectories to the Outer Planets," International Astronautical Congress, Paper No. IAC-04-A.6.02, Oct. 4–8, 2004.

[24] Yam, C. H., McConaghy, T. T., Chen, K. J., and Longuski, J. M., "Preliminary Design of Nuclear Electric Propulsion Missions to the Outer Planets," AIAA/AAS Astrodynamics Specialist Conference, Paper No. AIAA 2004-5393, Providence, RI, Aug. 16–19, 2004.

[25] Heaton A. F. and Longuski, J. M., "The Feasibility of a Galileo-Style Tour of the Uranian Satellites," AAS/AIAA Astrodynamics Specialist Conference, Paper No. AAS 01-464, Quebec City, Quebec, Canada, July 30–Aug. 2, 2001.

[26] Longuski, J.M. and Williams, S.N., "Automated Design of Gravity-Assist Trajectories to Mars and the Outer Planets," *Celestial Mechanics and Dynamical Astronomy*, Vol. 52, No. 3, Aug. 1991, pp. 207 – 220.

[27] Kohlhase, C. E. and Penzo, P. A., "Voyager Mission Description," *Space Science Reviews*, Vol. 21, 1977, pp. 77–101.

[28] Rinderle, E. A., "Galileo Users Guide, Mission Design System, Satellite Tour Analysis and Design Subsystem," Jet Propulsion Laboratory, Report JPL D-263, California Institute of Technology, Pasadena, CA, July 1986.

[29] Patel, M. R., "Automated Design of Delta-V Gravity-Assist Trajectories for Solar System Exploration," M.S. Thesis, School of Aeronautics and Astronautics, Purdue University, West Lafayette, IN, Aug. 1990.

[30] Petropoulos, A.E., Longuski, J.M., and Bonfiglio, E.P., "Trajectories to Jupiter via Gravity Assists from Venus, Earth, and Mars," *Journal of Spacecraft and Rockets*, Vol. 37, No. 6 Nov.–Dec. 2000.

[31] Staugler, A.J., "STOUR (Satellite Tour Design Program) User's Guide for the ΔV-EGA and V_∞-Leveraging Routines," School of Aeronautics and Astronautics, Purdue University, West Lafayette, IN, June 1996.

[32] Sims, J.A., Longuski, J.M., and Staugler, A.J., "V_∞ Leveraging for Interplanetary Missions: Multiple-Revolution Orbit Techniques," *Journal of Guidance, Control, and Dynamics*, Vol. 20, No. 3, 1997, pp. 409–415.

[33] Sims, J.A., "Delta-V Gravity-Assist Trajectory Design: Theory and Practice," PhD Thesis, School of Aeronautics and Astronautics, Purdue University, West Lafayette, IN, 1996.

[34] Marley, M. S., "Planetary Science Decadal Survey, JPL Rapid Mission Architecture: Neptune-Triton-KBO Study Final Report," NASA-JPL Mission Concept Study, Feb. 2010.

[35] NASA, "Space Launch System (SLS) Program Mission Planner's Guide (MPG) Executive Overview," Version 1, No. SLS-MNL-201, Aug. 22, 2014.

[36] Sims, J. A., and Flanagan, S. N., "Preliminary Design of Low-Thrust Interplanetary Missions," AAS/AIAA Astrodynamics Specialist Conference, AAS Paper No. 99-338, Girdwood, AK, August 1999.

[37] Sims, J. A., Finlayson, P. A., Rinderle, E. A., Vavrina, M. A., and Kowalkowski, T. D., "Implementation of a Low-Thrust Trajectory Optimization Algorithm for Preliminary Design," AIAA/AAS Astrodynamics Specialist Conference, AIAA Paper No. 2006-6746, Keystone, CO, Aug. 21–24, 2006.

[38] Englander, J. A., Conway, B. A., and Williams, T., "Automated Mission Planning via Evolutionary Algorithms, Journal of Guidance, Control, and Dynamics, Vol. 35, Nov. 2012, pp. 1878–1887.

[39] Englander, J. A., "Automated Trajectory Planning for Multiple-Flyby Interplanetary Missions," PhD thesis, University of Illinois at Urbana-Champaign, April 2013.

[40] Englander, J. A. and Englander, A. C., "Tuning Monotonic Basin Hopping: Improving the Efficiency of Stochastic Search as Applied to Low-Thrust Trajectory Optimization," 24th International Symposium on Space Flight Dynamics, Laurel, MD, May 2014.

[41] Englander, J. A., Ellison, D. H., and Conway, B. A., "Global Optimization of Low-Thrust, Multiple-Flyby Trajectories at Medium and Medium-High Fidelity," AAS/AIAA Space-Flight Mechanics Meeting, Santa Fe, NM, January 2014.

[42] Englander, J. A. and Conway, B. A., "An Automated Solution of the Low-Thrust Interplanetary Trajectory Problem, Journal of Guidance, Control, and Dynamics, 2016. Accepted.

[43] Vavrina, M. A., Englander, J. A., and Ghosh, A., "Coupled Low-Thrust Trajectory and Systems Optimization via Multi-objective Hybrid Optimal Control," AAS/AIAA Space Flight Mechanics Meeting Williamsburg, Virginia, January 2015.

[44] Englander, J. A., Vavrina, M. A., Ghosh, A.R., "Multi-objective Hybrid Optimal Control for Multiple-Flyby Low-Thrust Mission Design," AAS/AIAA Space Flight Mechanics Meeting, Williamsburg, Virginia, January 2015.

[45] Englander, J. A., and Vavrina, M. A., "Multi-Objective Hybrid Optimal Control For Multiple-Flyby Interplanetary Mission Design Using Chemical Propulsion," AAS/AIAA Astrodynamics Conference, Vail, Colorado, August 2015.

[46] Vavrina, M. A., Englander, J. A., and Ellison, D. H., "Global Optimization of N-Maneuver, High-Thrust Trajectories Using Direct Multiple Shooting," AAS/AIAA Spaceflight Mechanics Meeting, AAS Paper No. 16-272, Napa, CA, Feb. 14–18, 2016.

[47] Beebe, R., "Planetary Science Decadal Survey: Saturn Atmospheric Entry Probe Trade Study," NASA-JPL Mission Concept Study, Sept. 2010.

[48] Beebe, R., "Planetary Science Decadal Survey: Saturn Atmospheric Entry Probe Mission Study," NASA-JPL Mission Concept Study, April 2010.

[49] Kolencherry, N., Mansell, J. R., Hughes, K. M., Mudek, A. J., Podesta, L. P., Libben, B., Chye, H. S., Millane, J., Fulton, S., Shibata, E., Coleman, K., Arora, A., Lu, Y., Tackett, B., Elliott, J., Smith, G., Ukai, T., Pouplin, J., Hobar, N., Witsberger, P., and Saikia, S. J., "A Multi-Planet, Multi-Spacecraft Flagship Class Mission Concept to Explore a Gas Giant and an Ice Giant Planet," 13th International Planetary Probe Workshop, Laurel, MD, June 13–17, 2016, Paper and Poster Presentation.

[50] Lockwood, M. K., "Neptune Aerocapture Systems Analysis," AIAA Atmospheric Flight Mechanics Conference and Exhibit, AIAA Paper No. 2004-4951, Providence, RI, Aug. 16–19, 2004.

[51] Longuski, J.M. and Williams, S.N., "The Last Grand Tour Opportunity to Pluto," *The Journal of the Astronautical Sciences*, Vol. 39, No. 3, July – Sep. 1991, pp. 359–365.

[52] Sims, J.A., Staugler, A.J., and Longuski, J.M., "Trajectory Options to Pluto via Gravity Assists from Venus, Mars, and Jupiter," *Journal of Spacecraft and Rockets*, Vol. 34, No. 3, May–June 1997, pp. 347–353.

[53] Petropoulos, A.E., Longuski, J.M., and Bonfiglio, E.P., "Trajectories to Jupiter via Gravity Assists from Venus, Earth, and Mars," *Journal of Spacecraft and Rockets*, Vol. 37, No. 6 Nov.–Dec. 2000.

[54] Melman, J., Orlando, G., Safipour, E., Mooij, E., and Noomen, R., "Trajectory Optimization for a Mission to Neptune and Triton," AIAA Paper No. 2008-7366, AIAA/AAS Astrodynamics Specialist Conference, Honolulu, HI, Aug. 18–21, 2008.

[55] Casalino, L., Colasurdo, G., and Pastrone, D., "Optimal Low-Thrust Escape Trajectories Using Gravity Assist," *Journal of Guidance, Control, and Dynamics*, Vol. 22, No. 5, Sep.–Oct. 1999.

[56] Zimmer, S. and Ocampo, C., "Use of Analytical Gradients to Calculate Optimal Gravity-Assist Trajectories," *Journal of Guidance, Control and Dynamics*, Vol. 28, No. 2, March–April 2005.

[57] Yam, C.H., Di Lorenzo, D., and Izzo, D., "Constrained Global Optimization of Low-Thrust Interplanetary Trajectories," IEEE Congress on Evolutionary Computation, Barcelona, Spain, July 18–23, 2010.

[58] Hollister, W. M., "Mars Transfer via Venus," AIAA/ION Astrodynamics Guidance and Control Conference, Los Angeles, CA, Aug. 24–26, 1964, AIAA 64-647.

[59] Sohn, R.L., "Manned Mars Trips Using Venus Flyby Modes," *Journal of Spacecraft and Rockets*, Vol. 3, No. 2, 1966, pp. 161–169.

[60] Wilson, S., "Fast Round Trip Mars Trajectories," AIAA/AAS Astrodynamics Conference, Portland, OR, Aug. 20–22, 1990, AIAA 90-2934.

[61] Wolf, A. A., "Free Return Trajectories for Mars Missions," AAS/AIAA Annual Spaceflight Mechanics Meeting, Houston, TX, Feb. 11–13, 1991.

[62] Walberg, G., "How Shall We Go to Mars? A Review of Mission Scenarios," *Journal of Spacecraft and Rockets*, Vol. 30, No. 3, March–April 1993.

[63] Hoffman, S.J. and Kaplan, D.I. (eds.), "Human Exploration of Mars: The Reference Mission of the NASA Mars Exploration Study Team," NASA SP 6107, Houston, TX, March 1997.

[64] Drake, B.G. (ed.), "Reference Mission Version 3.0 Addendum to the Human Exploration of Mars: The Reference Mission of the NASA Mars Exploration Study Team," NASA SP-6107-ADD, EX13-98-036, Houston, TX, June 1998.

[65] Casalino, L., Colasurdo, G., and Patrone, D., "Mission Opportunities for Human Exploration of Mars," *Planetary and Space Science*, Vol. 46, No. 11/12, pp. 1613–1622, 1998.

[66] Lyne, J. E., and Townsend, L. W., "Critical Need for a Swingby Return Option for Early Manned Mars Missions," *Journal of Spacecraft and Rockets*, Vol. 35, No. 6, 1998, pp. 855, 856.

[67] Patel M.R., Longuski, J.M., and Sims, J.A., "Mars Free Return Trajectories," *Journal of Spacecraft and Rockets*, Vol. 35, No. 3, May–June 1998.

[68] Rall, C. and Hollister, W., "Free-Fall Periodic Orbits Connecting Earth and Mars," 1971, AIAA 71-92.

[69] Friedlander, A. L., Niehoff, J. C., Byrnes, D. V., and Longuski, J. M., "Circulating Transportation Orbits Between Earth and Mars," AIAA/AAS Astrodynamics Conference, Williamsburg, VA, Aug. 1986, AIAA 86-2009-CP.

[70] Byrnes, D. V., Longuski, J. M., and Aldrin, B., "Cycler Orbit Between Earth and Mars," *Journal of Spacecraft and Rockets*, Vol. 3, 1993, pp. 334–336.

[71] McConaghy, T. T., Longuski, J. M., and Byrnes, D. V., "Analysis of a Broad Class of Earth-Mars Cycler Trajectories," AIAA/AAS Astrodynamics Specialist Conference, Monterey, CA, Aug. 5–8, 2002, AIAA 2002-4420.

[72] Russell, R. P. and Ocampo, C. A., "Systematic Method for Constructing Earth-Mars Cyclers Using Free-Return Trajectories," *Journal of Guidance, Control, and Dynamics*, Vol. 27, No. 3, May–June 2004, pp. 321-335.

[73] Russell, R. P. and Ocampo, C. A., "Global Search for Idealized Free-Return Earth-Mars Cyclers," *Journal of Guidance, Control, and Dynamics*, Vol. 28, No. 2, March–April 2005, pp. 194-208.

[74] Landau, D.F. and Longuski, J.M., "Trajectories for Human Missions to Mars, Part I: Impulsive Transfers," *Journal of Spacecraft and Rockets*, Vol. 43, No. 5, Sept.–Oct. 2006, pp. 1035–1042.

[75] Landau, D. F., Longuski, J. M., and Aldrin, B., "Continuous Mars Habitation with a Limited Number of Cycler Vehicles," *Journal of the British Interplanetary Society*, Vol. 60, No. 4, April 2007, pp. 122–128.

[76] Okutsu, M. and Longuski, J.M., "Mars Free Returns via Gravity Assist from Venus," *Journal of Spacecraft and Rockets*, Vol. 39, No. 1, Jan.–Feb. 2002.

[77] Landau, D.F. and Longuski, J.M., "Trajectories for Human Missions to Mars, Part II: Low-Thrust Transfers," *Journal of Spacecraft and Rockets*, Vol. 43, No. 5, Sept.–Oct. 2006, pp. 1043–1047.

[78] Foster, C. and Daniels, M., "Mission Opportunities for Human Exploration of Nearby Planetary Bodies," AIAA SPACE Conference and Exposition, Anaheim, CA, Aug.–Sept. 2010.

[79] Tito, D.A., Anderson, G., Carrico, J.P., Clark, J., Finger, B., Lantz, G.A., Loucks, M.E., MacCallum, T., Poynter, J., Squire, T.H., and Worden, S.P., "Feasibility Analysis for a Manned Mars Free-Return Mission in 2018," IEEE Aerospace Conference, Big Sky, MT, March 2013.

[80] Bailey, L., Folta, D., Barbee, B., Vaughn, F., Kirchman, F., Englander, J., Campbell, B., Thronson, H., and Lin, T.Y., "A Lean, Fast Mars Round-Trip Mission Architecture: Using Current Technologies for a Human Mission in the 2030s," AIAA SPACE Conference and Exposition, San Diego, CA, Sept. 10–12, 2013, AIAA 2013-5507.

[81] Folta, D., Barbee, B. W., Englander, J., Vaughn, F., and Lin, T.Y., "Optimal Round-Trip Trajectories for Short Duration Mars Missions," AAS/AIAA Astrodynamics Specialist Conference, Hilton Head, SC, Aug. 11–15, 2013, AAS 13-808.

[82] De Smet, S., Parker, J.S., Herman, J., and Noomen, R., "Preliminary Mission Design for a Crewed Earth-Mars Flyby Mission Using Solar Electric Propulsion (SEP)," AAS/AIAA Space Flight Mechanics Meeting, Santa Fe, NM, Jan. 2014, AAS 14-366.

[83] Rogers, B.A., Hughes, K.M., Longuski, J.M., and Aldrin, B., "Establishing Cycler Trajectories between Earth and Mars," *Acta Astronautica*, Vol. 112, 2015, pp 114–125.

[84] Hollister, W., "Periodic Orbits for Interplanetary Flight," *Journal of Spacecraft and Rockets*, Vol. 6, No. 4, April 1969, pp. 366–369.

[85] Hollister, W. and Menning, M., "Periodic Swing-By Orbits between Earth and Venus," *Journal of Spacecraft and Rockets*, Vol. 7, No. 10, Oct. 1970, pp. 1193–1199.

[86] Semones, E., "Radiation Limits for Astronauts," NASA Technical Report, JSC, Houston, TX, Dec. 2011.

[87] May, T. A. and Creech, S. D., "NASA's Space Launch System (SLS) Program: Mars Program Utilization," Proceedings from the Concepts and Approaches for Mars Exploration workshop, Houston, TX, June 12–14, 2012, Paper No. 4098.

[88] Arora, J. S., "Introduction to Optimum Design," Third Edition, Elsevier Inc., Waltham, MA, 2012, pp. 663–667.

[89] Trevino, L., "SpaceX Dragon Re-Entry Vehicle: Aerodynamics and Aerothermodynamics with Application to Base Heat-Shield Design," 6th International Planetary Probe Workshop, June 21–27, 2008, Atlanta, GA.

[90] Bibb, K.L., Walker, E.L., Brauckmann, G.J., and Robinson, P.E., "Development of the Orion Crew Module Static Aerodynamic Database, Part I: Hypersonic," 29th AIAA Applied Aerodynamics Conference, June 27–30, 2011, Honolulu, HI, AIAA 2011-3506.

[91] Creer, B.Y., Smedal, H.A., and Wingrove, R.C., "Centrifuge Study of Pilot Tolerance to Acceleration and the Effects of Acceleration on Pilot Performance," NASA Ames Research Center, NASA TN D-337, Moffett Field, CA, Nov. 1960.

[92] Morring, F., "Soyuz Ballistic Re-entry Explained," Aviation Week and Space Technology, 2008.

[93] Sutton, K. and Graves Jr., R., "A General Stagnation-Point Convective Heating Equation for Arbitrary Gas Mixtures," NASA TR-R-376, Hampton, VA, Nov. 1971.

[94] Tauber, M. and Sutton, K., "Stagnation-Point Radiative Heating Relations for Earth and Mars Entries," *Journal of Spacecraft and Rockets*, Vol. 28, No. 1, 1991, pp. 40–42.

[95] Brandis, A. M. and Johnston, C. O., "Characterization of Stagnation-Point Heat Flux for Earth Entry," 45th AIAA Plasmadynamics and Lasers Conference, June 2014, Atlanta, GA,

[96] Rao, A. V., Benson, D. A., Darby, C. L., Francolin, C., Patterson, M. A., Sanders, I., and Huntington, G. T., "Algorithm 902: GPOPS, A Matlab Software for Solving Multiple-Phase Optimal Control Problems Using the Gauss Pseudospectral Method," ACM Transactions on Mathematical Software, Vol. 37, No. 2, April–June 2010.

[97] Griffin, M.D. and French, J.R., "Space Vehicle Design," Second Edition, American Institute of Aeronautics and Astronautics, Inc., Reston, VA, 2004, p. 277.

[98] Leitmann, G. (Editor), "Optimization Techniques With Applications to Aerospace Systems," Academic Press, London, 1962, pp. 323–351.

[99] Diehl, R.E. and Myers, M.R. "Gravity-Assist Trajectories to the Outer Solar System," Jet Propulsion Laboratory, JPL Publication D-4677, Pasadena, CA, Sept. 1987.

[100] Campagnola, S. and Russell, R.P., "Endgame Problem Part 1: V_∞-Leveraging Technique and the Leveraging Graph," *Journal of Guidance, Control, and Dynamics*, Vol. 33, No. 2, March–April 2010.

[101] Campagnola, S. and Russell, R.P., "Endgame Problem Part 2: Multibody Technique and the Tisserand-Poincaré Graph," *Journal of Guidance, Control, and Dynamics*, Vol. 33, No. 2, March–April 2010.

[102] Carrico, J. and Fletcher, E., "Software Architecture and Use of Satellite Tool Kits's Astrogator Module for Libration Point Orbit Missions," Proceedings of the Conference Libration Point Orbits and Applications, Aiguablava, Spain, June 10–14, 2002. Edited by Gomez, G., Lo, M.W., and Masdemont, J.J., Published by World Scientific, 2003.

[103] Kolawa, E., Balint, T.S., Birur, G., Brandon, E., Del Castillo, L., Hall, J., Johnson, M., Kirschman, R., Manvi, R., Mojarradi, M., Moussessian, A., Patel, J., Pauken, M., Peterson, C., Whitacre, J., Martinez, E., Venkatapathy, E., Newdeck, P., and Okojie R., "Extreme Environment Technologies for Future Space Science Missions," NASA Technical Report, JPL D-32832, Pasadena, CA, Sept. 19, 2007.

[104] Bonfiglio, E. P., Longuski, J. M., and Vinh, N. X., "Automated Design of Aerogravity-Assist Trajectories," *Journal of Spacecraft and Rockets*, Vol. 37, No. 6, Nov. – Dec. 2000. pp. 768–775.

[105] Lowe, R. E. and Gervais, R. L., "Manned Entry Missions to Mars and Venus," *ARS Journal*, Vol. 32, No. 11, 1962, pp. 1660–1668.

[106] Sagan, C., *Pale Blue Dot: A Vision of the Human Future in Space*, Random House, Nov. 1994.

[107] Landis, G. A., "Colonization of Venus," Conference on Human Space Exploration, Space Technology and Applications International Forum, Albuquerque, NM, Feb. 26, 2003. AIP Conference Proceedings, 654, pp. 1193–1198.

[108] Landis, G. A., Lamarre, C., and Colozza, A., "Atmospheric Flight on Venus: A Conceptual Design," *Journal of Spacecraft and Rockets*, Vol. 40, No. 5, Sept.–Oct. 2003, pp. 672–677.

[109] Landis, G. A., "Astrobiology: The Case for Venus," NASA Technical Memorandum 2003-212310, Cleveland, OH, July 2003.

[110] Wertz, J. and Wiley L., Editors, *Space Mission Analysis & Design*, 3rd Edition, Microcosm, 1999.

[111] Sergeyevsky, A.B., Snyder, G.C., and Cunniff, R.A., "Interplanetary Mission Design Handbook," Vol. 1, Pt. 2, Jet Propulsion Laboratory, JPL Publication 82-43, Pasadena, CA, Sept. 15, 1983.

[112] Curtis, H.D., *Orbital Mechanics for Engineering Students*, Elsevier Butterworth-Heinemann, 2005.

[113] Post, K. and Loucks, M., "Inspiraiton Mars 2021 Mission Design," 65th International Astronautical Congress, Sept. 29–Oct. 3, 2014, Toronto, Canada, IAC-14,A3,3B,1,x22690.

[114] Hollister, W., "Periodic Orbits for Interplanetary Flight," *Journal of Spacecraft and Rockets*, Vol. 6, No. 4, April 1969, pp. 366 – 369.

[115] Hollister, W. and Menning, M., "Interplanetary Orbits for Multiple Swingby Missions," August 1969, AIAA Paper 69 – 931.

[116] Hollister, W. and Menning, M., "Periodic Swing-By Orbits between Earth and Venus," *Journal of Spacecraft and Rockets*, Vol. 7, No. 10, October 1970, pp. 1193 – 1199.

[117] Rall, C., "Free-Fall Periodic Orbits Connecting Earth and Mars," Sc.D. dissertation, Department of Aeronautics and Astronautics, Massachusetts Institute of Technology, Cambridge, MA, October 1969.

[118] Rall, C. and Hollister, W., "Free-Fall Periodic Orbits Connecting Earth and Mars," AIAA Paper 71-92, January 1971.

[119] Landau, D. F., Longuski, J. M., and Aldrin, B., "Continuous Mars Habitation with a Limited Number of Cycler Vehicles," *Journal of the British Interplanetary Society*, Vol. 60, No. 4, April 2007, pp. 122 – 128.

[120] Aldrin, B., "Cyclic Trajectory Concepts," SAIC presentation to the Interplanetary Rapid Transit Study Meeting, Jet Propulsion Laboratory, Pasadena, CA.

[121] Byrnes, D. V., Longuski, J. M., and Aldrin, B., "Cycler Orbit Between Earth and Mars," *Journal of Spacecraft and Rockets*, Vol. 3, 1993, pp. 334 – 336.

[122] Aldrin, B. and David, L., *Mission to Mars: My Vision for Space Exploration*, National Geographic, Washington, D.C., 2013.

[123] Niehoff, J., "Manned Mars Mission Design," Steps to Mars, Joint AIAA/Planetary Society Conference, National Academy of Sciences, Washington, DC, 1985.

[124] Niehoff, J., "Integrated Mars Unmanned Surface Exploration (IMUSE), A New Strategy for the Intensive Science Exploration of Mars," Space Science Board, Woods Hole, MA, July 1985.

[125] Friedlander, A. L., Niehoff, J. C., Byrnes, D. V., and Longuski, J. M., "Circulating Transportation Orbits Between Earth and Mars," AIAA/AAS Astrodynamics Conference, Williamsburg, Virginia, August 1986, AIAA 86-2009-CP.

[126] Byrnes, D. V., McConaghy, T. T., and Longuski, J. M., "Analysis of Various Two Syndoic Period Earth-Mars Cycler Trajectories," AIAA/AAS Astrodynamics Specialist Conference, Monterey, CA, August 5 – 8 2002, AIAA 2002-4423.

[127] McConaghy, T. T., Longuski, J. M., and Byrnes, D. V., "Analysis of a Broad Class of Earth-Mars Cycler Trajectories," AIAA/AAS Astrodynamics Specialist Conference, Monterey, CA, August 5 – 8 2002, AIAA 2002-4420.

[128] Russell, R. P. and Ocampo, C. A., "Systematic Method for Constructing Earth-Mars Cyclers Using Free-Return Trajectories," *Journal of Guidance, Control, and Dynamics*, Vol. 27, No. 3, May – June 2004, pp. 321 – 335.

[129] Sweetser, T. H., "Jacobi's Integral and ΔV-Earth-Gravity-Assist (ΔV-EGA) Trajectories," AAS/AIAA Astrodynamics Specialist Conference, Victoria Canada, August 1993, AAS Paper 93-635.

[130] Williams, S. N. and Coverstone-Carroll, V.,"Benefits of Solar Electric Propulsion for the Next Generation of Planetary Exploration Missions," *Journal of the Astronautical Sciences*, Vol. 45, No. 2, April – June 1997, pp. 143 – 159.

[131] Sauer, Jr., C. G. and Yen, C.-W. L., "Planetary Mission Capability of Small Low Power Solar Electric Propulsion Systems," IAA International Conference on Low-Cost Planetary Missions, No. IAA-L-0706, April 1994.

[132] Gill, P., Murray, W., and Saunders, M., "SNOPT: An SQP Algorithm for Large-Scale Constrained Optimization," *SIAM Journal on Optimization*, Vol. 12, 2002, pp. 979 – 1006.

[133] McConaghy, T. T., Debban, T., Petropoulos, A., and Longuski, J. M., "Design and Optimization of Low-Thrust Trajectories with Gravity Assists," *Journal of Spacecraft and Rockets*, Vol. 40, No. 3, May – June 2003, pp. 380 – 387.

[134] Drake, B. G., "Human Exploration of Mars Design Reference Architecture 5.0," Tech. rep., NASA, 2009, NASA/SP-2009-566.

VITA

VITA

Kyle Hughes earned his Bachelor of Science in Aeronautical and Astronautical Engineering from the University of Washington, where he graduated Magna Cum Laude in 2008. He earned his Master of Science in Aeronautics and Astronautics from the University of Washington in 2010, where he also worked as a Teaching Assistant in the Aeronautics and Astronautics Department throughout his M.S. studies. In the following fall, Kyle began his Ph.D. graduate studies in astrodynamics at Purdue University under the advisement of Professor Jim Longuski. During his Ph.D. studies, Kyle worked as an instructor for the Department of Mathematics at Purdue from 2010–2013, where he taught algebra, trigonometry, and calculus. From 2014–2016 Kyle was a Graduate Assistant for the College of Engineering, where he planned and organized the Summer Undergraduate Research Fellowship (SURF) program. In 2014, Kyle worked on high-fidelity SRP modeling for the Origins Spectral Interpretation Resource Identification Security Regolith Explorer (OSIRIS-REx) mission at NASA-Goddard Space Flight Center. Currently, Kyle is working at NASA Goddard in the Navigation and Mission Design Branch, where he designs chemical and low-thrust trajectories for various missions and mission proposals, with a focus on destinations in the outer solar system.